Investigating neurovascular and metabolic function in healthy and Multiple Sclerosis populations using multi-modal neuroimaging (MEG and fMRI)

Rachael Stickland

A thesis submitted to Cardiff University for the degree of Doctor of Philosophy.

October 2018

Declarations and Statements

DECLARATION

This work has not been submitted in substance for any other degree or award at this or any other university or place of learning, nor is being submitted concurrently in candidature for any degree or other award.

Signed …… (candidate) Date ……..……

STATEMENT 1

This thesis is being submitted in partial fulfilment of the requirements for the degree of PhD.

Signed …… (candidate) Date ……..……

STATEMENT 2

This thesis is the result of my own independent work/investigation, except where otherwise stated, and the thesis has not been edited by a third party beyond what is permitted by Cardiff University's Policy on the Use of Third-Party Editors by Research Degree Students. Other sources are acknowledged by explicit references. The views expressed are my own.

Signed …… (candidate) Date ……..……

STATEMENT 3

I hereby give consent for my thesis, if accepted, to be available online in the University's Open Access repository and for inter-library loan, and for the title and summary to be made available to outside organisations.

Signed …… (candidate) Date ……..……

STATEMENT 4: PREVIOUSLY APPROVED BAR ON ACCESS

I hereby give consent for my thesis, if accepted, to be available online in the University's Open Access repository and for inter-library loans **after expiry of a bar on access previously approved by the Academic Standards & Quality Committee.**

Signed …… (candidate) Date ……..……

Acknowledgments

Thank you to *Wellcome* for the funding that facilitated this research. It has been brilliant and challenging. Thanks to my main supervisor, Richard Wise, for all the support and guidance, and the calm and open-minded approach. Thanks also to Krish Singh and Valentina Tomassini, who supervised parts of my research. I was fortunate to have supervision from three great researchers, with a diverse set of skills and perspectives.

There are too many people to thank individually from *CUBRIC*, where this research was carried out. A great bunch of researchers that helped with many of my coding and analysis queries and stimulated good discussion. And of course, the regular cake helped too. Thanks to many in the MEG lab. Thanks to Ilona Lipp and Hannah Furby for getting me started with neuroimaging at the beginning of my PhD. Thanks very much to Marek Allen, Catherine Foster, Eleonora Patitucci, and Mike Germuska for all the work they've contributed. Thanks to Hannah Chandler, who was a pleasure to work closely with in my last year.

Thank you to my family, in particular: Mum & Dad, Becky & Steve, Amy & Rory, Leah & Tim, Andy & Cathy, Kit & Charlie, who have given me much support. Big thanks to my colourful Cardiff friends; you made this fun. Thank you to Willow, Emony, Lashek, Kin, and Dal for keeping me sane, and helping me live a little.

Finally, thanks to my partner Jonathan who has challenged and supported me with patience, love and humour all throughout this process.

Contributors

Thank you to everyone that contributed to the research presented in this thesis. Specific names relating to each research chapter are given below (of researchers outside the supervisory team).

The study design and data collection presented in **Chapter 4** were carried out by Marek Allen. I analysed the data and wrote-up the manuscript.

For data presented in **Chapters 5 and 6**, I did the participant recruitment, scanning, data analysis and write-up. Catherine Foster was involved in study design and set-up. The researchers and clinicians at CUBRIC that were involved in the scanning sessions: Hannah Chandler, Eleonora Patitucci, Neeraj Saxena and Sharmila Khot. Data analysis presented in Chapter 5 was done by me, except for the voxel-wise comparisons by Hannah Chandler, and lesion drawing by Shona Bhome-Dhaliwal. Mike Germuska developed the MRI sequence and the analysis pipeline applied in Chapter 5, and acknowledgment is given through-out the chapter where appropriate.

I collected, analysed and wrote up the data presented in **Chapters 7, 8, 9** and **Appendix 1.** Some data presented in **Chapter 7**, to compare with my own, was collected and analysed by Phoebe Asquith, Bethany Routley, Simon Rushton and Krish Singh. Chapter 7 is a replication and extension of their research design, using analysis code from Krish Singh.

Thesis Summary

The brain requires a constant supply of glucose and oxygen to meet metabolic needs at rest and during increased activity. If blood flow is disrupted, or if tissue has difficulty extracting or metabolising nutrients, cell damage or death may occur. Vascular and metabolic impairments in Multiple Sclerosis (MS) are hypothesised to contribute to disease progression. This thesis develops empirical measures of neurovascular coupling using the relationship between magnetoencephalography (MEG) and functional Magnetic Resonance Imaging (fMRI). Visual MEG and fMRI responses were reduced in MS. The relationship between them was unchanged suggesting preserved neurovascular coupling. Addressing the same questions with a naturalistic movie stimulus in MS, no coupling differences were found. In a healthy population, results show neurovascular coupling is dependent on brain region and frequency of neural oscillations. Under the hypothesis of reduced cerebral metabolic rate of O_2 ($CMRO_2$) contributing to damage in MS, we quantified baseline $CMRO_2$ and cerebral blood flow (CBF), amongst other parameters. This is the first application of dual-calibrated fMRI in MS, involving biophysical modelling of fMRI signals in response to changing inspired CO_2 and O_2. Reduced baseline CBF and $CMRO_2$ were found in MS, correlating with lesion and grey matter volumes. Relative visual-induced CBF and $CMRO_2$ signals were investigated in MS; a reduction in CBF was found in a small visual region but no visual $CMRO_2$ changes were found, or differences in CBF-$CMRO_2$ coupling. Baseline CBF and $CMRO_2$ signals predicted visual stimulus responses, in both groups. As an alternative to externally supplied gases, we used a breath-hold design to create a $CMRO_2$ movie time-series but report no significant relationships between $CMRO_2$ and MEG. Quantitative functional imaging can detect impairments in resting and stimulus-induced neural oscillations, blood flow and oxygen metabolism in MS, which should be explored further to understand their exact role in disease progression.

Abbreviations

Frequently used shown in bold	
ATP	Adenosine Triphosphate
ADP	Adenosine Diphosphate
ASL	**Arterial Spin Labelling**
BBB	Blood Brain Barrier
B_0	Static Magnetic Field
BH	Breath-Hold
BOLD	**Blood Oxygen Level Dependent**
CaO_2	Arterial oxygen content
CBF	**Cerebral Blood Flow**
CBV	Cerebral Blood Volume
CNS	Central Nervous System
$CMRO_2$	**Cerebral Metabolic Rate of Oxygen**
CO_2	**Carbon Dioxide**
CvO_2	Venous oxygen content
CVR	Cerebrovascular Reactivity
D_c	Effective Oxygen Diffusivity
DEXI	Dual-Excitation
DMT	Disease Modifying Treatment
DOF	Degrees of Freedom
DSC	Dynamic Susceptibility Contrast
EEG	Electroencephalography
EDSS	Expanded Disability Status Scale
ET-1	Endothelin-1
FDR	False Discovery Rate
FLAIR	Fluid Attenuated Inversion Recovery
fMRI	**Functional Magnetic Resonance Imaging**
FSMC	Fatigue Scale for Motor and Cognitive Functions
GG	Greenhouse-Geisser
GM	**Grey Matter**
GRE	Gradient Echo
Hg	Haemoglobin
ISC	Inter-Subject correlation
IQR	**Interquartile range**
LFP	**Local Field Potential**
LCMV	Linearly Constrained Minimum Variance
MAR	MAgnification Requirement
MEG	**Magnetoencephalography**
mmHg	Millimetre of mercury
MS	**Multiple Sclerosis**
MSIS-29	Multiple Sclerosis Impact Scale 29
MTT	Mean Transit Time
NAWM	Normal Appearing White Matter
NMV	Net Magnetisation Vector
NO	Nitric Oxide

NVC	**Neurovascular Coupling**
O_2	**Oxygen**
OEF	Oxygen Extraction Fraction
$P_{ET}CO2$	End-tidal partial pressure of CO_2
$P_{ET}O2$	End-tidal partial pressure of O_2
PASL	**Pulsed Arterial Spin Labelling**
PASAT	Paced Auditory Serial Addition Test
pCASL	**pseudo-Continuous Arterial Spin Labelling**
PD	Proton Density
PET	Positron Emission Tomography
PLD	Post Labelling Delay
PSP	Postsynaptic Potential
PVE	**Partial Volume Estimate**
RF	Radio Frequency
RMSE	Root Mean Square Error
ROI	**Region Of Interest**
RRMS	Relapsing Remitting Multiple Sclerosis
SD	**Standard Deviation**
SDMT	Symbol Digit Modalities Test
SEM	Standard Error of the Mean
SNR	**Signal to Noise Ratio**
T25-FW	Time 25 Foot Walk
TE	**Echo Time**
TFCE	Threshold-Free Cluster Enhancement
TI	Inversion Time
TR	**Repetition Time**
VEF	Visual Evoked Field
WM	**White Matter**
9-HPT	9 Hole Peg Test

Table of Contents

Aims of Thesis

This thesis uses non-invasive neuroimaging methods to measure the energy demands of neural activity, and the coupling between neural activity and blood flow. The main aims of this thesis are to:

1. **Investigate neurovascular coupling (NVC) mechanisms using the relationship between magnetoencephalography (MEG) and functional Magnetic Resonance Imaging (fMRI) signals.** The relationship between MEG signals (neural activity) and fMRI signals (blood flow response to neural activity) in response to the same stimulus is used as an empirical measure of NVC. NVC is not fully understood but is crucial to how the brain replenishes energy in active areas, as well as underpinning how the fMRI signal is interpreted.

2. **Develop more quantifiable and interpretable measures of vascular and metabolic brain function.** The calibrated fMRI methods used in this thesis aim to parcellate out the commonly used Blood Oxygen Level Dependent (BOLD) fMRI signal into more quantifiable and interpretable signals, for example blood flow and oxygen metabolism. Importantly, blood flow and oxygen metabolism signals are quantified at baseline in this thesis, as well as relative signal changes to a stimulus. Characterising the baseline state is important for the interpretation of stimulus-induced changes, particularly when studying patient populations where this baseline state may be altered.

3. **Apply these MEG and fMRI methods to the investigation of vascular and metabolic impairment in Multiple Sclerosis (MS).** Vascular and metabolic impairments are present in MS, but it is not clear when and how they contribute to the disease. We need more non-invasive ways of investigating these mechanisms in MS and therefore the methods described in aims (1) and (2) are used. This thesis presents the first application of a dual-calibrated fMRI study in MS, allowing baseline oxygen metabolism to be quantified, alongside baseline blood flow and many other relevant physiological parameters. Blood flow and oxygen metabolism changes are also investigated in response to visual stimuli, and the MEG-fMRI relationship is used to assess impairments in NVC. It is important to establish the practicality and utility of these methods in MS.

   This thesis contributes to the development of these methods, as well as their application to disease populations.

Structure of Thesis

Introductory Chapters (1-3): Chapter 1 introduces the biological signals and mechanisms of interest and Chapter 2 introduces the methods used to investigate these signals and mechanisms (see figure below). Chapter 3 gives a background to MS and explains the relevance of investigating these mechanisms in this disease.

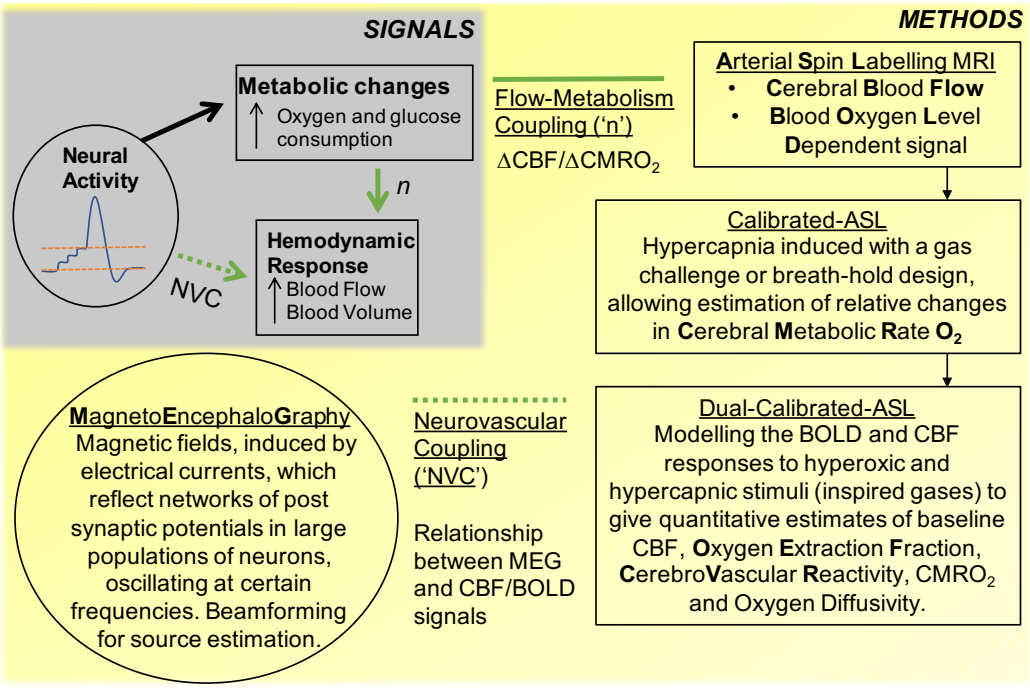

Research Chapters (4-9)

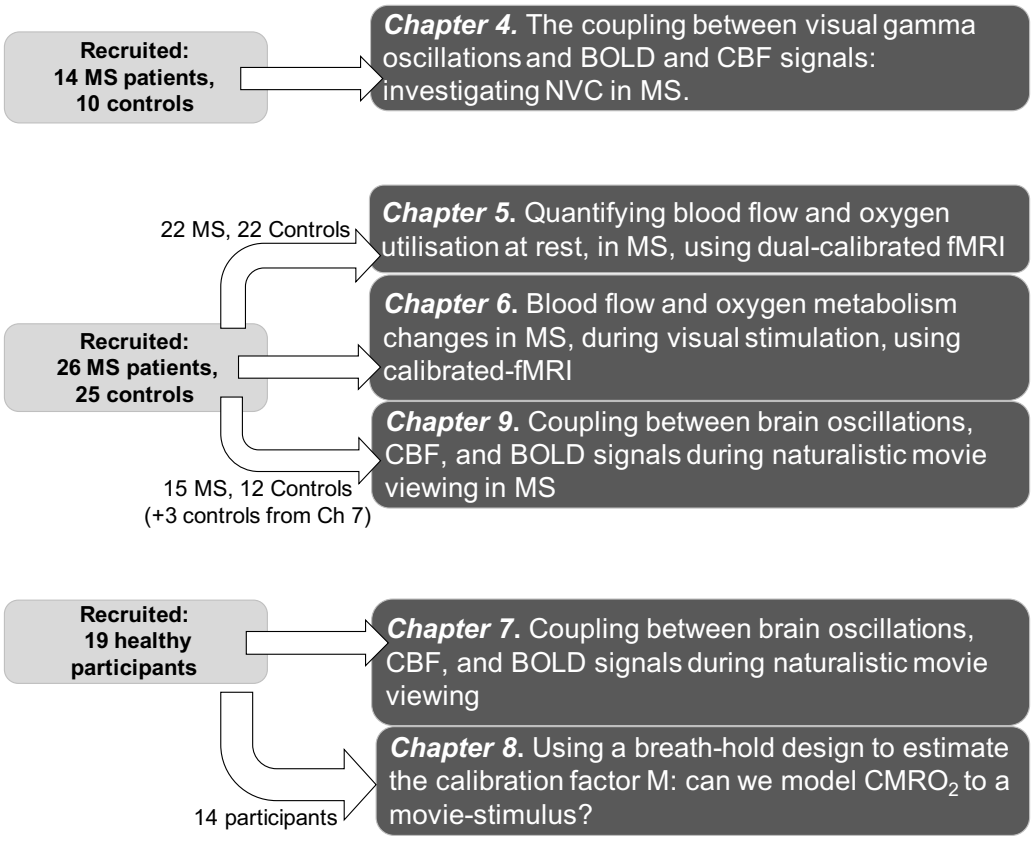

1 Introduction to Biological Signals

1.1 Neural Oscillations

1.1.1 What are neural oscillations?

In this thesis, neural activity is studied at the population level, via the oscillating electrical activity of large populations of neurons. These oscillations represent synchronous rhythmic neural activity. This synchronisation, in time, causes a summation of amplitude in space, measured over a certain area of the brain. Neural oscillations are typically described by their amplitude, frequency and phase, displayed in Figure 1-1. The first observations of neural oscillations in humans were reported by Hans Berger in the 1920s (Millett, 2001). He made the electroencephalography (EEG) recording in a human, showing that fluctuations in voltage amplitude, at a frequency of ~10Hz measured over the occipital cortex, varied with the participant's attention to their visual environment. For example, when participants closed their eyes this produced large increases in the amplitude of these oscillations. To measure these neural oscillations non-invasively we can use EEG or MEG. Whereas EEG measures electrical currents at scalp level, MEG measures magnetic field fluctuations, produced by electrical currents, outside the head. These electrical currents are caused by the flow of transmembrane ionic currents in large populations of neurons. In this thesis, neural oscillations are measured non-invasively with MEG (see Chapter 2.1).

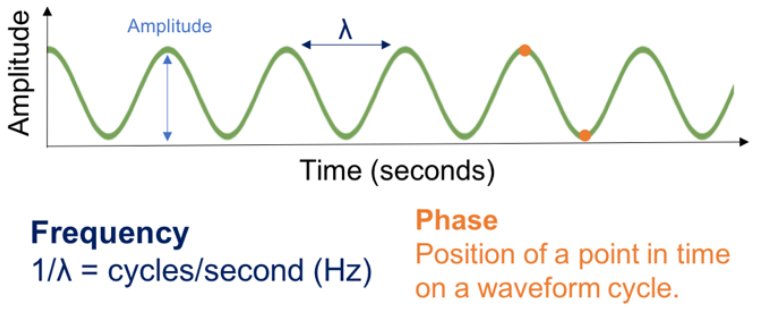

Figure 1-1. A diagram displaying the amplitude, frequency and phase information of an oscillating wave.

1.1.2 Biological origin of neural oscillations

Neural oscillations are thought to represent rhythmic fluctuations of the local field potential (LFP). The LFP is a measured signal reflecting the summed electrical current over a volume of tissue, generated by transmembrane ionic current flow (Einevoll,

Kayser, Logothetis, & Panzeri, 2013). Ionic currents are thought to arise from two main types of activity: axonal and post-synaptic. Axonal activity involves the rapid depolarisation of the membrane, resulting in an action potential that propagates along the axon. Post-synaptic activity is the electrical input at the level of dendrites, contributing to an action potential but distinct in space and time. When an action potential reaches the presynaptic membrane, this leads to an excitatory (E) or inhibitory (I) postsynaptic potential (PSP), dependent on the type of neurotransmitters released and the type of receptors present. The summed effect of these EPSPs and IPSPs will contribute to whether an action potential is triggered.

It is thought that LFPs, and therefore neural oscillations measured with EEG or MEG, predominantly originate from the post-synaptic current flow (Cohen, 2017; Hall, Robson, Morris, & Brookes, 2014). This is mainly due to the magnitude of the signal we detect. A single axonal or dendritic current flow is not sufficient to detect a signal outside the head; for a detectable field, tens of thousands of currents would need to flow in synchrony. The temporal duration of dendritic current is greater than an action potential and dendrites are also greater in number. As to the type of neuron, it is argued that stellate neurons, which have dendritic processes radiating from all around the cell body, are unlikely to contribute significantly to the magnetic field measured with MEG as their ESPS will not sum cumulatively. Therefore, apical dendrites of pyramidal cells, in parallel columns, are the most likely origin of MEG signals. Furthermore, these apical dendrites need to be oriented in parallel (tangential orientation) to the cortical surface for them to project detectable magnetic field components outside the head; neurons in gyri that are perpendicular (radial orientation) to the cortical surface do not project outside the head and cannot be measured with MEG (Ahlfors, Han, Belliveau, & Hämäläinen, 2010).

Simultaneous measurements of invasive electrophysiology and MEG (Zhu et al., 2009), show that LFPs (mostly post-synaptic in origin) better match the MEG signal changes than multi-unit activity (largely axonal origin). However, although PSPs make the biggest contribution to the LFP, other neural processes also contribute. Importantly, a transmembrane current in any excitable membrane (dendrite, soma, axon, axon terminal) can contribute to the LFP (Buzsáki, Anastassiou, & Koch, 2012; Einevoll et al., 2013) as it is the temporal and spatial accumulation of all ionic processes that is being measured.

1.1.3 How are neural oscillations typically studied?

When resting activity is examined, the brain exhibits a 1/frequency power spectrum; the lower the frequency the higher the amplitude, see part A of Figure 1-2. This remains the case when brain networks are activated (Jia & Kohn, 2011) but to a smaller degree, as the power of higher frequency oscillations often increases and low frequency oscillations decrease. This is why studies of neural oscillations typically look at changes relative to baseline, to characterise frequency components that are task-driven (part B of Figure 1-2). A wide range of frequencies of neural oscillations have been studied and linked to behaviour, typically catergorised into these approximate frequency bands: 'delta' (<4Hz), 'theta' (4-8Hz), 'alpha' (8-13Hz), 'beta' (13-30Hz), and 'gamma' (> 30Hz), (Buzsáki & Draguhn, 2004; Ward, 2003). The functional significance of each band is still an active area of research, but they all have been linked to perception, cognition or memory in some way. For example, there is much animal literature, and some human, linking theta oscillations to episodic memory processes in the hippocampus, e.g. (Lega, Jacobs, & Kahana, 2012). Alpha is typically linked to attentional and inhibitory control (Mathewson et al., 2011), beta to sensorimotor control (Kilavik, Zaepffel, Brovelli, MacKay, & Riehle, 2013), and gamma to attention, perception, and mediation of information transfer across cortical areas (Fries, 2009; Jia & Kohn, 2011).

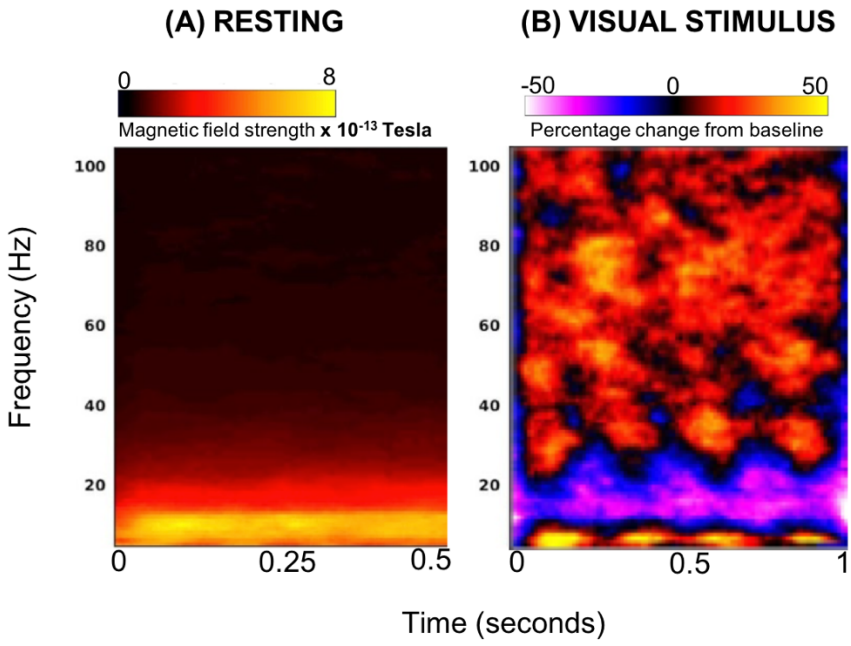

MEG recordings from primary visual cortex. The visual stimulus refers to reversing checkerboard stimulus with four reversals.

Figure 1-2. Time-frequency spectrogram showing power at rest (A) and during a visual stimulus (B). (A) displays the typical 1/f power spectrum at rest, and (B) shows the relative change in power, in different frequency bands, elicited by a visual stimulus.

Changes in oscillatory frequency rarely happen in one frequency band alone; the amplitude of the signal in different frequencies change together in dynamic ways. This can be seen in Figure 1-2. In response to a reversing checkerboard (stimulus onset 0) a clear power increase in the gamma band is seen (a *synchronisation*) and a decrease in alpha and beta (a *desynchronisation*). The slower visual evoked response can also be seen as a synchronisation in the delta/theta band. This plot displays both *evoked* and *induced* oscillatory components; it is therefore useful to explain their distinction. For evoked oscillations, the phase of the wave is locked to the stimulus, which is not the case for induced oscillations (David, Kilner, & Friston, 2006; Tallon-Baudry & Bertrand, 1999). To estimate evoked power only, an E/MEG signal is averaged over trials in the experiment, then the time-frequency components are examined. If a power increase related to the stimulus is not phase locked, this signal will therefore not remain in the average. For induced oscillations, time-frequency decomposition is performed at each trial first, then the power is averaged, as is summarised in Figure 1-3. To visualise induced activity only, the power of evoked signals can be subtracted (not the case in Figure 1-2).

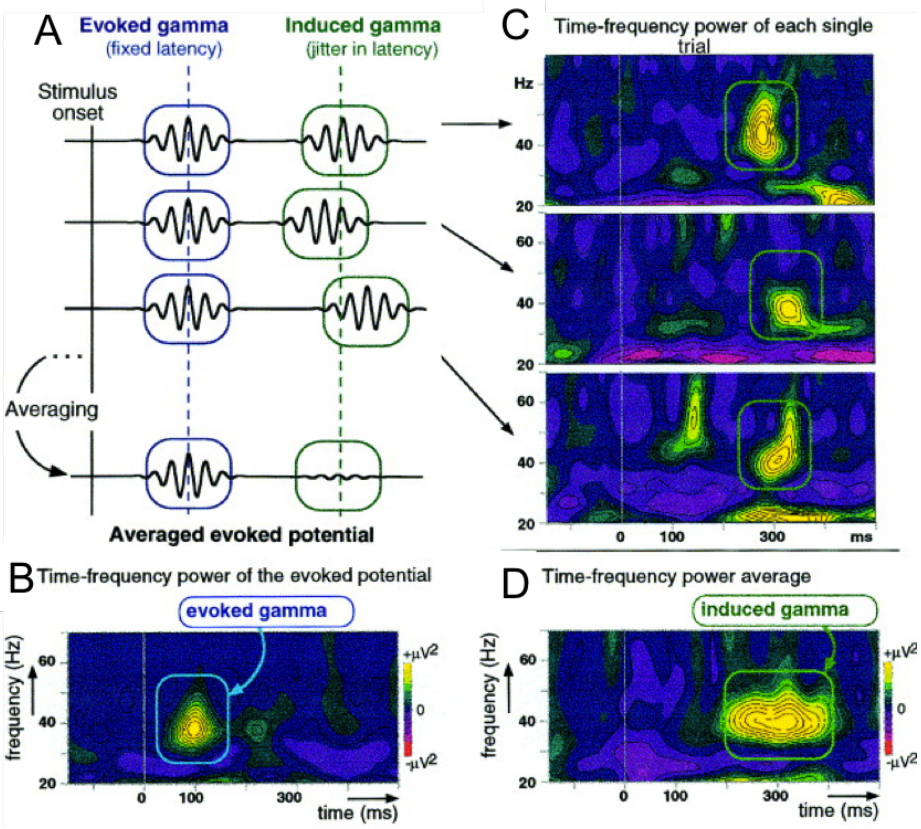

Figure 1-3. (A) Distinction between evoked and induced responses. (B) Time-frequency power of the evoked response after averaging over each trial. (C) Time-frequency power of each trial. (D) Average of each in C to give the induced gamma response. ***Figure from Tallon-Baudry & Bertrand (1999).***

1.1.4 Functional relevance of neural oscillations

Despite a large variability in brain volume across mammalian species, the intermittent and oscillatory patterns of LFPs, and even their behavioural correlates, are very closely preserved across species (Buzsáki, Logothetis, & Singer, 2013). Therefore, it seems neural oscillations constitute a fundamental biological mechanism in the mammalian brain. The features of neural oscillations are determined by the physical architecture of neural networks; the frequency of oscillation is constrained by the size of the neural population involved, with faster oscillations typically confined to more local networks, and slower oscillations reflecting larger spatial networks (Buzsáki & Draguhn, 2004). With the evoked response, we assume there is the same brain response at each trial, with surrounding fluctuating noise. They are often studied clinically, for example the visual evoked field (VEF) is thought to reveal integrity of the afferent visual pathway (Kothari, Bokariya, Singh, & Singh, 2016). Induced oscillations are thought to be generated by higher-order processes, with synchronisation of ionic current flows reflecting functional coherence. There is building evidence for neural oscillations being impaired in neurodegenerative diseases (Nimmrich, Draguhn, & Axmacher, 2015), and particularly in schizophrenia (Uhlhaas & Singer, 2010).

1.2 Energy demands of neural activity: the response of the cerebrovasculature

1.2.1 Energy demands of neural activity

Neural oscillations, and neural activity in general, are very energy demanding processes. Energy is needed to restore ionic gradients to their baseline, after they change due to action potentials and PSPs, and also for the uptake and recycling of neurotransmitters at the synapse, particularly glutamate (Attwell & Laughlin, 2001; Shulman, Rothman, Behar, & Hyder, 2004). In order to do this, neurons, like other cells, need a source of free energy in the form Adenosine Triphosphate (ATP), a molecule that can store and transport chemical energy. When ATP is consumed due to metabolic processes, it converts to either Adenosine Diphosphate (ADP) or adenosine monophosphate. In the brain, the most efficient way to convert ADP back to ATP is through the oxidative metabolism of glucose (Buxton, 2009). Glucose and oxygen are converted to water, carbon dioxide (CO_2) and energy; energy that can be used to convert ADP molecules to ATP. First, the process of *glycolysis* in the cytosol involves the breakdown of glucose into pyruvate molecules. These can be further broken down in the mitochondria (through the *Krebs cycle*) to form CO_2 and energy, and eventually water and energy to convert ADP to ATP. A small amount of ATP is formed during

glycolysis in the cytoplasm, without the use of oxygen. However, a much larger amount of ATP is produced in the mitochondria with the aid of oxygen (Du et al., 2008). For example, breaking down glucose into 2 molecules of pyruvate is coupled to the conversion of 2 molecules of ADP to ATP, whereas metabolism of 1 pyruvate and 3 oxygen molecules is coupled to the conversion of 18 ADP to ATP (Buxton, 2009). Therefore, the energy demands of neural activity are greatly dependent on the direct supply of oxygen and glucose.

In this thesis, the fMRI methods used do not measure changes in glucose directly but changes reflective of oxygen metabolism. Although it is the metabolism of glucose that provides the brain with the required ATP, this is strongly aided by the supply of oxygen. Therefore, oxygen and glucose metabolism are intrinsically coupled, both reflecting the energy demands of neural activity.

1.2.2 Delivery of nutrients by blood flow

Blood flow delivers the required oxygen and glucose to the brain. In proportion to its size, the resting metabolic demands of the brain are large; it represents approximately 2% of body weight but requires 20% of cardiac output to deliver oxygen and glucose (Raichle & Gusnard, 2002). The brain does not store glucose and oxygen so requires a continuous supply to allow it to produce enough ATP. This makes the brain very vulnerable to tissue death if blood flow is disrupted. Both glucose and oxygen are carried in the blood first by arteries (large blood vessels) entering the brain, which branch into smaller arteries called arterioles, and end up at capillaries, very small blood vessels where the oxygen and glucose is exchanged with tissue. Waste products from neural activity (such as CO_2) also exchange at the capillary level, and are carried away by venules, small blood vessels that carry blood to veins, which return the blood and waste products to the lungs. This is displayed in Figure 1-4.

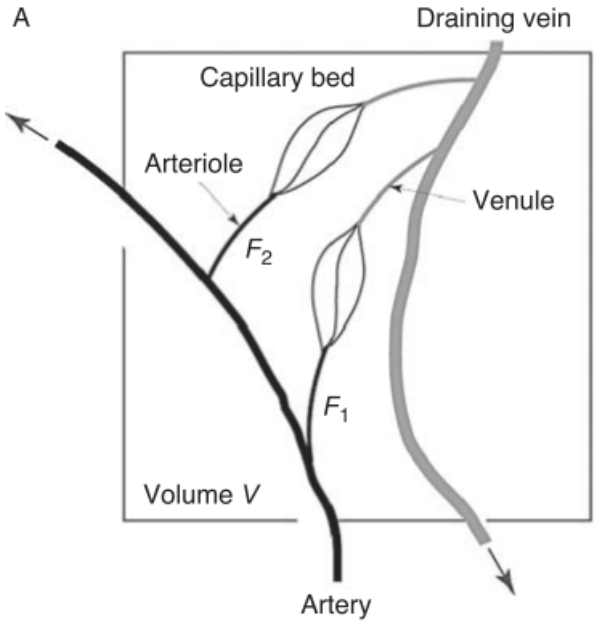

Figure 1-4. Blood vessels within a volume of tissue. Arterial blood delivered through the arteries and then the arterioles, ends up at the capillary beds (F1 + F2). Once oxygen and glucose are extracted into the tissue, by-products are drained away in the venules. ***Figure from Buxton (2009).***

Glucose, carried in blood plasma, does not easily cross the blood-brain barrier, but diffuses down its concentration gradient from the higher blood concentration to the lower tissue concentration, through transporters in the capillary wall (Buxton, 2009). The oxygen carried in the blood is mostly bound to the protein haemoglobin, although a small amount (~2%) is carried as dissolved gas in the plasma. This plasma concentration is important, as oxygen diffuses down its concentration gradient from dissolved gas in capillary plasma to dissolved gas in the active tissue (Dunn, Mythen, & Grocott, 2016), which is then quickly replaced by the release of haemoglobin-bound oxygen. We will return to glucose and oxygen metabolism below, but first will focus on how blood is delivered to an area of the brain.

Perfusion is a general term for the arrival of arterial blood to the capillary bed. With fMRI measures, we refer to cerebral blood flow (CBF), which is expressed as the amount of blood volume flowing into a certain mass of tissue, over a given time. Typically, the units are expressed as ml per 100g of tissue per minute (ml/100g/min). Despite changes in arterial pressure (the pressure of blood on the walls of blood vessels) the brain is extremely good at maintaining a constant resting CBF, by a process known as *autoregulation* (Duffin et al., 2018). Autoregulation happens via the control of vascular smooth muscle (multiple layers of smooth muscle cells in the large pial arteries and a single layer in the arterioles). This smooth muscle can contract to constrict the vessel or relax to dilate it, therefore changing the vascular resistance. In general,

autoregulation maintains a constant resting blood flow despite variations in pressure, but blood flow also needs to change in response to metabolic demand (Duffin et al., 2018).

1.2.3 Neurovascular coupling and the neurovascular unit

Neural activity and CBF have a close spatial and temporal relationship; increases in oxygen and glucose consumption, due to an increase in neural activity, is followed by a local increase in CBF. The processes relating local neural activity and subsequent changes in vessel tone, and therefore local CBF, is termed *neurovascular coupling* (NVC). This spatial and temporal coupling is the basis of fMRI, relying on blood flow changes to map neural activity.

It was initially thought that NVC was controlled directly by a negative-feedback system, with changes in ATP producing a metabolic signal that increased blood flow (Attwell et al., 2010; Girouard & Iadecola, 2006). As well as blood replenishing oxygen and glucose, a flow increase clears the brain of potentially toxic by-products of neural activity, for example lactate and CO_2, as well as regulating the brain's temperature (Iadecola, 2017). In fact, both lactate and CO_2, as well as other by-products, are potent vasodilators (Ainslie & Duffin, 2009; Dienel, 2012). However, this negative-feedback mechanism is thought to be an oversimplified account. One reason is that CBF response is not altered by experimentally reducing glucose and oxygen (Mintun et al., 2001; Powers, Hirsch, & Cryer, 1996). Another reason is that the small transient reduction in oxygen consumption at the active site cannot account for the sustained increases in CBF. This is covered in more detail in Section 2.3.1 but, in brief, the increase in CBF is much greater than the increase in oxygen metabolism, in response to neural activity. These findings suggest that depletion of these metabolic substrates is not the only mechanism causing this increase in CBF after neural activity.

NVC is also mediated by a feed-forward system, supported by what is termed the *neurovascular unit*, see Figure 1-5. The neurovascular unit involves the interaction of neuronal, glial, and vascular cells. Neurons can signal directly to blood vessels (Attwell & Iadecola, 2002), or signal to astrocytes to release vasoactive agents which then act on blood vessels (Petzold & Murthy, 2011). Neurotransmitter signalling is involved in both of these routes, particularly glutamate which activates calcium dependent signalling pathways and results in the realise of vasoactive components (Iadecola, 2017). Many by-products of synaptic activity, such as potassium, nitric oxide (NO), and

prostanoids (Attwell et al., 2010) are vasoactive, therefore able to trigger vasodilation or vasoconstriction of the local blood vessels.

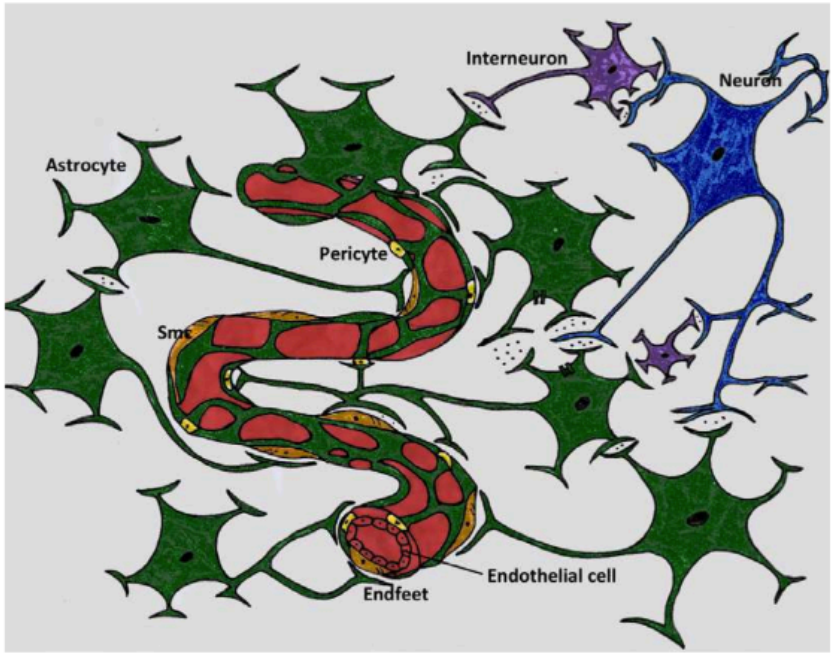

Figure 1-5. Synapses between neurons (blue), interneurons (purple) and astrocytes (green). Astrocytes signal to blood vessels at the astrocytic end-feet, in direct contact with endothelial cells (red), pericytes (yellow) and myocytes/Smc (orange). ***Figure from Muoio et al (2014).***

These feed-forward and feed-backward mechanisms are not mutually exclusive; it is likely that both may be involved in NVC. Summarised by Iadecola (2017), the relative involvement of each mechanism may depend on "the timing, intensity, and duration of the activation as well as the brain region and the brain's developmental stage." Regardless of the direction of signalling, the traditional view of *where* the regulation of blood happens is at the level of the arterioles, but there is an emerging idea that regulation can also happen at the level of the capillaries, due to the contractile properties of cells called the pericytes, which line the capillary wall (Hamilton, Attwell, & Hall, 2010). There is much to still understand about NVC: the contribution of feedforward and feedback mechanisms, the cellular basis of the signalling pathways, the regional variations across the brain, the upstream propagation of vasoactive signals and the exact role of the capillaries (Iadecola, 2017). There is also a lot to learn about how sensitive our neuroimaging techniques are to measuring these processes, hence why a focus of some of the research questions in this thesis is to investigate NVC mechanisms.

1.2.4 Functional relevance of neurovascular coupling

The health of the neurovascular unit is extremely important, considering its role in replenishing nutrients that have been used up by neural activity, as well as removing potentially toxic by-products. An impaired blood flow response to an area can lead to tissue hypoxia, and eventually tissue death. Although this can occur rapidly in cases such as stroke or other traumatic brain injury, damage to blood vessels or disruption of NVC pathways can also build up over time in many neurodegenerative conditions (Girouard & Iadecola, 2006; Phillips, Chan, Zheng, Krassioukov, & Ainslie, 2015; Stanimirovic & Friedman, 2012). There also may be cases where the blood flow response to an area is adequate, but mitochondrial impairment leads to the brain being unable to metabolise oxygen appropriately (Aboul-Enein & Lassmann, 2005; Lindroos et al., 2009). The neuroimaging field is developing metrics to help non-invasively assess some of these impairments and help understand their role in the progression of many diseases. For example, by quantifying regional blood flow, oxygen metabolism and the reactivity of blood vessels. These are all explained in the next section.

2 Introduction to Methods

2.1 Magnetoencephalography (MEG)

Neural oscillations are measured in this thesis using MEG. Despite being around since the late 1960s (Cohen, 1968) it is only in the last two to three decades that MEG has started to be fully utilised as a technique to investigate neural activity. This is partly due to development of larger arrays of sensors (200+), measuring from the whole cortex. An electrical current generated by one neuron is too weak to be measured with MEG; tens of thousands of neurons need to synchronously fire to generate a signal large enough to be detected (Hansen, Kringelbach, & Salmelin, 2010). Hansen et al (2010) describe how 50,000 synchronous firing neurons would correspond to a patch of cortex approximately 0.63 mm^2, with a diameter of 0.9mm assuming the cortical patch has a circular form. These values are based on estimating the diameter of cortical mini-columns, and the density of neurons contained within. Despite the spatial scale at which a signal can be generated estimated at <1mm^3, MEG signals are estimated at a much coarser spatial resolution due to limitations in source localisation (explained below and in section 2.1).

MEG is sensitive to neural activity due to the laws of electromagnetism: all electrical currents generate a magnetic field perpendicular to their direction (Figure 2-1).

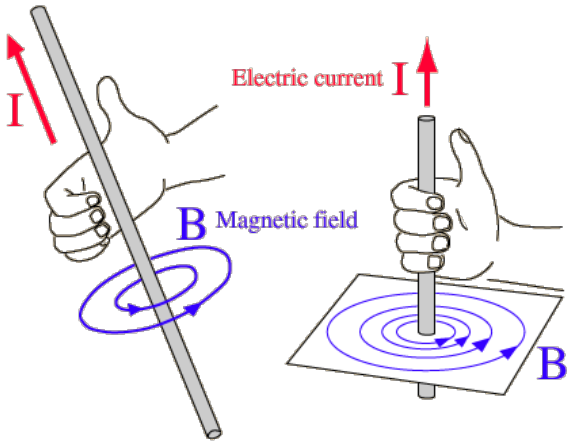

*Figure 2-1. The 'Right hand rule' shows the direction of the magnetic field **B** (following the curvature of the fingers and shown by the lines in blue) caused by the electrical current I (the direction of the thumb and shown by the red arrows). Public domain image from Wikipedia.*

The electrical current induced by the activity of a group of neurons is called the 'primary current', and this is what the MEG signal is most sensitive to (Senior, Russell, & Gazzaniga, 2006, Chapter 12). EEG, in contrast, is sensitive to the secondary currents (or 'volume currents') generated from this primary current; they flow outside the cell in the opposite direction, forming irregular patterns because they take the path of least electrical resistance to get to the head surface, where they can be recorded as voltage differences (Cheyne & Papanicolaou, 2015). Magnetic fields are not distorted as they

pass through different tissue layers. However, volume currents still contribute to the externally measured magnetic field (Cheyne & Papanicolaou, 2015) and have to be taken into account during forward modelling (estimating the electrical/magnetic fields recorded at the sensors given a particular pattern of current sources in the brain).

Magnetic field strength rapidly decreases as distance increases from the source, making it challenging to accurately measure activity from sources deep in the brain (Hillebrand & Barnes, 2002). However progress is being made to study oscillations in areas such as the hippocampus (Pu, Cheyne, Cornwell, & Johnson, 2018). As the magnetic field fluctuations measured with MEG are so weak (in the femtotesla range, 10^{-15} tesla), modern MEG systems are housed in magnetically shielded rooms, to block out magnetic signals from the environment, including the earth's magnetic field. Super Conducting Quantum Interference Devices (SQUIDs) allow such magnetic fields to be measured. They are small rings of material that are superconducting when immersed in liquid helium (at ~4.2 Kelvin), with the capability of sensitively measuring tiny magnetic fields (Senior, Russell, & Gazzaniga, 2006, Chapter 12). These SQUIDS are attached to larger pickup coils (arranged in an array over the participant's head) which funnel the magnetic flux into the smaller SQUID. There are lots of different types of pick-up coils, with the broad categories being 'magnetometers' and 'gradiometers'. Magnetometers simply measure any orthogonal field, whereas gradiometers (pairs of coils that are close together and wound in opposite directions) can measure *gradients* in the magnetic field over space, therefore being able to better separate noise from the environment (same effect on each coil from distant sources) and signals from the brain (different effect on each coil from the nearby source), (Proudfoot, Woolrich, Nobre, Turner, & Turner, 2014).

The biggest strength of MEG is that it measures signals that directly relate to electrical brain activity. The temporal resolution of MEG is only limited by the sampling rate, allowing magnetic fields to be characterised on the millisecond level, the timescale of neural activity. The biggest weakness of MEG is the precision with which it can locate the source in space. The goal is to relate the magnetic field fluctuations measured at the level of the sensors to the location of the currents in the brain. This is referred to as the 'inverse problem' and there is no unique solution i.e. there are an infinite number of possible current distributions in the brain that could generate one pattern of magnetic fields at the sensors. To solve this inverse problem, we introduce prior constraints on the solutions, and find the solution that best describes the data. In this thesis, beamforming techniques are used to solve the inverse problem, explained below.

2.1.1 Beamforming source localisation

The magnetic fields measured with MEG are often modelled as current dipoles which have a position, orientation and strength. Estimates of the current dipole at each brain location come from some weighted contribution from each sensor. Beamformer techniques measure the contribution of a single brain location to the measured field at each sensor, by constructing a spatial filter to 'tune in' to each location independently. First, a volumetric grid of target locations is defined, and for each location an optimum set of beamformer weights is determined (Hillebrand, Singh, Holliday, Furlong, & Barnes, 2005). This volumetric grid (typically around 5mm in resolution) is based on each participant's anatomical MRI, which is co-registered to the MEG data by recording the location of three fiducial coils during MEG scanning, placed at three anatomical landmarks. Therefore, if we match these coil positions to the MEG data *and* the anatomical MRI, it follows that we can superimpose the MEG data onto this anatomical space. For each location in the brain, the signal is taken from each of the sensors multiplied by the beamformer weight, and all of these products summed to give a single time-series that represents the estimate of the current dipole at that location (see Figure 2-2). For each grid location we need to find the weights that maximise the contribution of that location to the sensor array and suppress the others. In order to do this, beamforming algorithms make the assumption that any two distant cortical areas are not perfectly correlated (Hillebrand & Barnes, 2005). i.e. they do not generate coherent LFPs over long time scales. Empirical data has shown this to be a reasonable assumption (Hillebrand & Barnes, 2005).

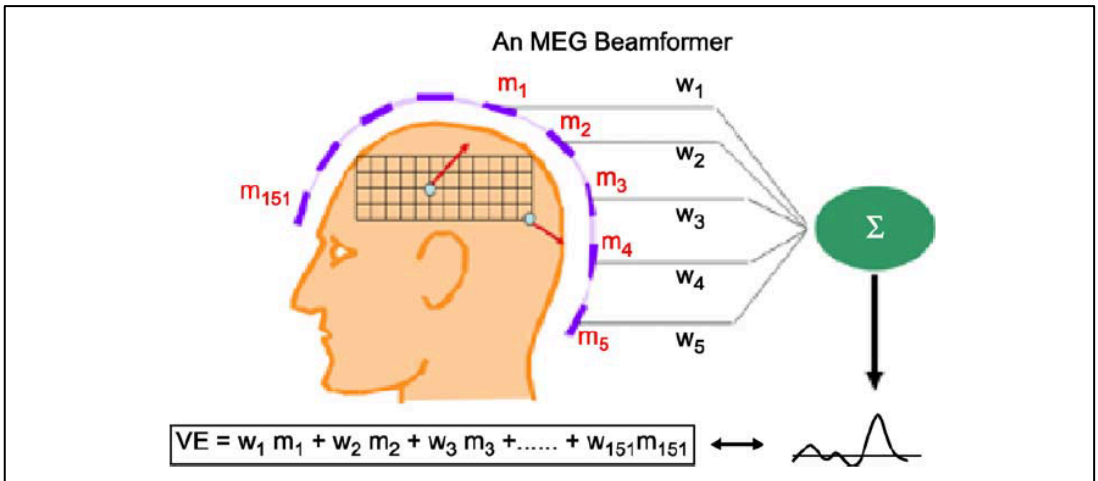

FIG. 1. Illustration of the main idea behind beamforming. The neuronal signal at a location of interest is constructed as the weighted sum of the MEG channels ($m_1 \ldots m_{151}$), forming a so-called virtual electrode (VE). The weights ($w_1 \ldots w_{151}$) are chosen so that only the signal from the location of interest contributes to the beamformer output, whereas the signal from noise sources is suppressed. A different set of weights is computed sequentially for each location in the brain, Figure courtesy of Dr. D. Cheyne, University of Toronto (modified).

Figure 2-2. MEG beamforming technique for source localisation. ***Figure taken from (Hillebrand & Barnes, 2005).***

2.2 The physics of MRI: A brief recap

Before a more detailed description of the functional MRI methods, the main focus of this thesis, a brief description of MRI physics is given.

Magnetic moments of hydrogen nuclei. MRI relies on the magnetic properties of hydrogen nuclei, which are positively charged protons spinning on their axes. These properties induce a magnetic moment (Figure 2-3). When placed in a large static magnetic field (B_0) the magnetic moments of hydrogen go from being randomly orientated (part A Figure 2-3) to aligning parallel or antiparallel with B_0 (part B Figure 2-3). A small excess of low-energy nuclei aligning parallel causes a net magnetic moment, the net magnetisation vector (NMV) of hydrogen (part C Figure 2-3), (Westbrook, Roth, & Talbot, 2011).

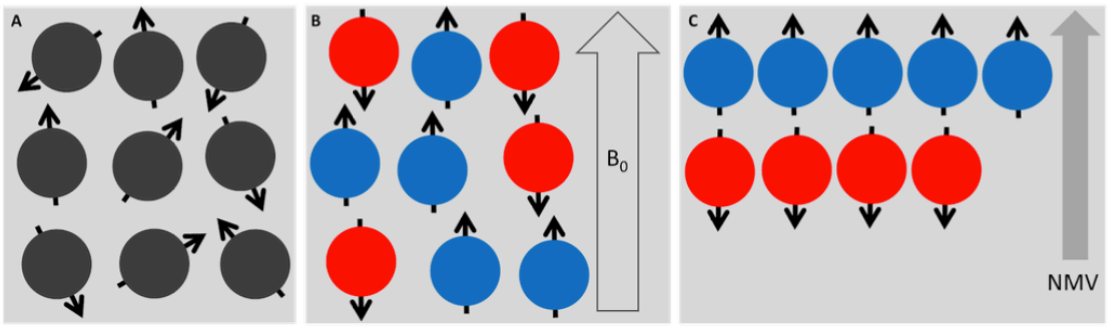

Figure 2-3. Hydrogen nuclei = coloured circles; magnetic moments = black arrows; B0 = static field; NMV = net magnetic vector. Blue nuclei aligning parallel to B0 are low energy 'spin-up'. Red nuclei aligning anti-parallel to B0 are high energy 'spin-down'. ***Figure is my own but based on figures from Westbrook, Roth, & Talbot (2011).***

Precession. Being placed in B_0 causes this magnetic moment to precess in a circular path around B_0 (direction of small orange arrows in Figure 2-4). The Larmor equation explains the frequency at which a specific nucleus precesses: $\omega_0 = \gamma B_0$. Where the precessional frequency of the nucleus (ω_0) is related to B_0 by the constant γ, termed the gyromagnetic ratio. At typical MRI field strengths, hydrogen precesses in the radio frequency (RF) band.

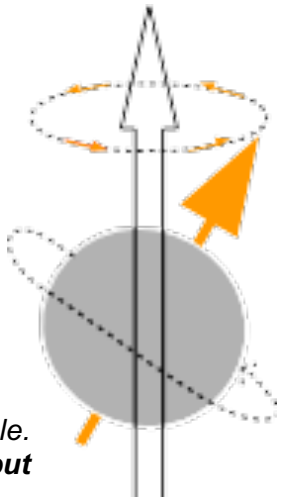

Figure 2-4. B0 = large white arrow. Hydrogen proton = grey circle. Magnetic moment = large orange arrow. ***Figure is my own but based on figures from Westbrook, Roth, & Talbot (2011).***

Resonance. A RF pulse of energy at the larmor frequency must be applied in order for energy to be absorbed, a process termed resonance. Resonance has two effects on the NMV. Firstly, the energy absorption causes the NMV to no longer align perfectly with B_0, as more nuclei join the high energy population. The angle of misalignment depends on the amplitude and duration of the RF pulse, termed the flip angle. The second effect of resonance is related to the phase of the magnetic moments of hydrogen (their position along the processional path around B_0 at a specific time, for example the four small orange arrows on Figure 2-4). Resonance causes all the magnetic moments to eventually move to the same position along this processional path, referred to as being 'in phase.'

The MR signal. Magnetic field fluctuations inside an MR receiver coil induce an electrical voltage, and this is the MR signal. These magnetic field fluctuations will depend on the amount of magnetisation in the transverse plane (i.e. the amount of in-phase magnetisation) at the larmor frequency. Once perturbed from the longitudinal direction, the NMV starts to realign back with B_0, as hydrogen nuclei lose energy. This is known as relaxation. Magnetization in the longitudinal plane increases ('recovery'), and the amount of magnetisation in the transverse plane decreases ('decay'). This evolution of the signal in the MR receiver coil is referred to as free induction decay (FID). The recovery of the longitudinal magnetization is due to nuclei giving up energy to their surrounding environment (lattice) and is termed 'spin-lattice relaxation'. The magnetization recovers exponentially over time, with the *T1 relaxation* time being the time it takes for 63% of the longitudinal magnetization to recover. Decay of coherent transverse magnetisation is due to magnetic fields of near-by nuclei interacting, termed 'spin-spin relaxation'. This rate of decay is also an exponential process, with the *T2 relaxation time* being the time it takes for 63% of transverse magnetization to decay.

The amount of T1 and T2 relaxation allowed is manipulated with the choice of RF pulse timing parameters. The *repetition time (TR)* is the time between one excitation RF pulse to the next excitation RF pulse, determining how much T1 relaxation has occurred when reading the signal. The *echo time (TE)* is the time between the RF pulse and the peak of the signal in the receiver-coil, determining how much T2 relaxation has occurred when reading the signal. As different tissue types have differing amounts and arrangements of hydrogen, this means the magnetic moments of hydrogen nuclei in these different tissues take a different amount of time to lose their transverse magnetisation, after the RF pulse has been turned off, and therefore induce different levels of magnetic field fluctuation. This is the basis of contrast in an MR image.

The spin-spin relaxation, characterised by T2 relaxation time, causes dephasing of the transverse magnetisation that is irreversible. Dephasing is also caused by macro- and mesoscopic magnetic field inhomogeneities and this is termed T2* relaxation. These field inhomogeneities mainly occur due to magnetic susceptibility of different tissues, (Chavhan, Babyn, Thomas, Shroff, & Haacke, 2009). fMRI, explained below, depends on this T2* relaxation as the basis of the signal contrast. When reading out the image using gradient-echo (GRE) sequences, transverse magnetisation is based on both spin-spin relaxation as well as these magnetic field inhomogeneities which cause dephasing and increase the transverse relaxation. Therefore, as these sequences are sensitive to T2 relaxation and these extra dephasing effects, they are said to have T2*-weighting, with T2* always being shorter than T2. Using a different method of image read-out, spin-echo sequences, can eliminate these dephasing effects, making the contrast dependent on T2 relaxation only, by using a refocusing RF pulse with a flip angle of 180° (Chavhan et al., 2009).

2.3 Functional MRI (fMRI)

2.3.1 The BOLD signal

The Blood Oxygen Level Dependent (BOLD) signal was discovered in the early 1990s, first demonstrated in rat brains then shortly after in humans (Ogawa, Lee, Kay, & Tank, 1990; Ogawa & Lee, 1990). Since then, a very large number (hundreds of thousands) of studies in cognitive neuroscience, clinical psychology, and presurgical planning have utilised this technique as a way to localise changes in brain activity (Glover, 2011). The principles of the BOLD signal rely on the fact that de-oxyhaemoglobin and oxyhaemoglobin have different magnetic susceptibilities. At rest, the arterial blood is almost fully saturated with oxygen i.e. the arterial oxygen content (CaO_2) is close to 1. In the healthy brain, the amount of oxygen extracted from the blood is consistently reported to be around 40% at rest, making the Oxygen Extraction Fraction (OEF) 0.4 (Leithner & Royl, 2014). We can model the Cerebral Metabolic Rate of Oxygen ($CMRO_2$) if we know the delivery of oxygen (by oxygenated blood) and the amount extracted by the tissue:

$$CMRO_2 = CaO_2 \times OEF \times CBF \quad \textit{(Equation 2-1)}$$

During activation, CBF increases from its baseline state in much larger proportions than $CMRO_2$ increases from baseline. This is characterised by the coupling ratio ‘n’ normally reported to be around 2-4, meaning the relative CBF response is typically 2-4 times

larger than the relative $CMRO_2$ response (Buxton, 2009; Leithner & Royl, 2014). Assuming CaO_2 is the same as it is at rest, it follows that OEF *decreases* with activation. This seems unintuitive, that the fraction of oxygen extracted from the blood goes down during activation. This is due to the increased rate of delivery of oxygenated blood, so the tissue extracts a lower proportion of oxygen from the blood at a given time.

How does this lead to the BOLD signal? As the capillary and venous blood are more oxygenated, less deoxyhaemoglobin is present in the voxel that is being imaged. Oxyhaemoglobin is diamagnetic, meaning it is has similar magnetic properties to the surrounding tissue. Deoxyhaemoglobin is paramagnetic, meaning it distorts the surrounding magnetic field, causing shorter T2 and T2* relaxation times, and making the MR signal decay faster. Put another way, when the amount of deoxyhaemoglobin decreases in the imaged voxel, as is the case with increases in neural activity, the T2 and T2* relaxation times become longer and the signal measured with a T2 or T2*-weighted sequence slightly increases. Due to the most commonly acquired BOLD signal contrast being dependent on the T2* relaxation time (from GRE acquisition), it is particularly susceptible to signal drop-out in regions that are near air cavities (e.g. sinuses) as macroscopic susceptibility-induced magnetic field gradients cause de-phasing and therefore signal loss.

The BOLD response indexes only relative changes in neural activity, as it does not provide information about the concentration of deoxyhaemoglobin in the resting state, only the difference between rest and stimulus. The BOLD response not only reflects the relative increases in CBF and $CMRO_2$, but also a local increase in cerebral blood volume (CBV), see Figure 2-5. The increases in CBV and $CMRO_2$ cause a decrease in the BOLD signal, whereas an increase in CBF causes an increase in the BOLD signal; this CBF effect is typically dominant causing a net increase. As well as this, the maximum BOLD response is dependent on the resting physiological state of the tissue, determined by blood haematocrit (ratio of volume of red blood cells to total volume of blood), the resting OEF and the resting CBV. The maximum possible BOLD response increases when these resting parameters increase.

Due to the BOLD response reflecting all these changes, its utility as a sole marker of brain activity in studies investigating diseases and pharmacology has been questioned (Iannetti & Wise, 2007). In any circumstance where two populations being compared have a different baseline state, the comparison of BOLD signal changes may not be a valid reflection of differences in neural activity. Furthermore, if the couplings between the CBF, $CMRO_2$ and CBV responses are altered in disease, this could result in a

different BOLD response when the neural activity is the same, or no BOLD change when the neural activity is different. The focus of this thesis is to partial out these signals that contribute to the BOLD response, allowing us to more meaningfully interpret how the brain is responding to neural activity. This is the focus of the next sections: using Arterial Spin Labelling (ASL) to measure CBF and using calibrated-fMRI to model the $CMRO_2$ response, as well as to estimate the baseline tissue physiology.

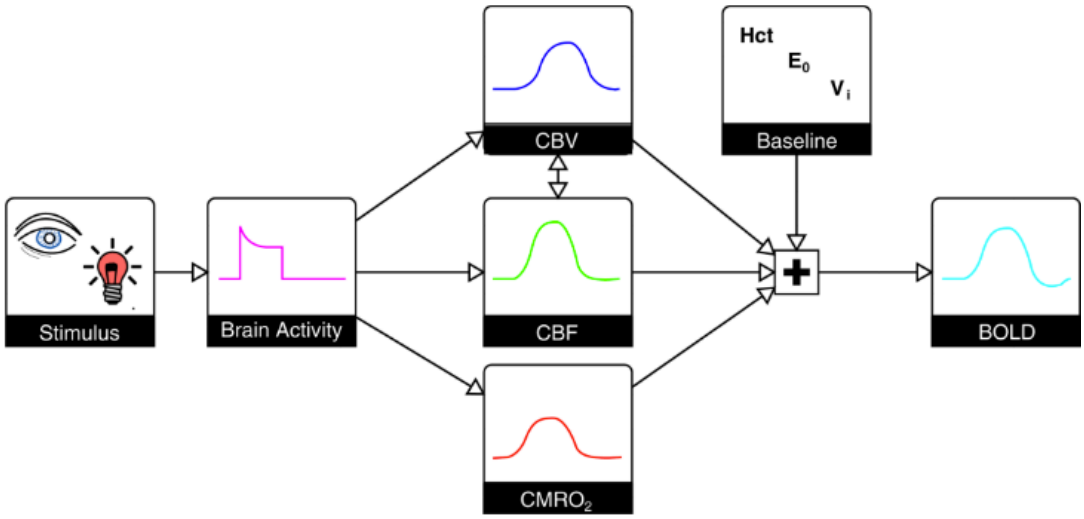

Figure 2-5. Overview of the BOLD response, showing its dependence on changes in CBV, CBF and CMRO2, in response to a stimulus. The baseline state (levels of haematocrit, resting OEF and resting CBV) affect the maximum possible BOLD response. ***Figure taken from (Blockley et al., 2013).***

2.3.2 Arterial Spin Labelling for CBF measurements

There have been many techniques developed, used in research and clinical practice, to measure CBF: perfusion CT-scan, dynamic susceptibility contrast-MRI (DSC-MRI), single-photo emission computed tomography and positron emission tomography (PET), (Ferré et al., 2013). However, these techniques require the injection of exogenous contrast media or ionizing radiation, making them invasive and challenging to use repeatedly on the same subject. This thesis focuses on non-invasive ways to study the brain, and therefore uses a non-invasive fMRI technique to measure CBF, called Arterial Spin Labelling (ASL). Compared to BOLD-fMRI, ASL directly measures the delivery of arterial blood, therefore the signal is more localised to the capillary beds, whereas the BOLD signal is more influenced by venous oxygenation changes (Buxton, 2009).

Imaging techniques such as PET monitor the kinetics of an injected agent as it passes through the tissue, therefore reflecting the rate of blood flow. ASL works on similar

principles but uses an endogenous tracer. With ASL, the blood water is magnetically labelled to flip the magnetization of hydrogen protons within water molecules carried by arterial blood. After waiting a certain time to allow the labelled blood to travel to the slice of interest, a 'labelled' image is acquired. A 'control' image is acquired using the exact same imaging parameters, but without labelling the blood. The differences between the label and control images (repeated many times to get enough signal through averaging) is proportional to the blood flow into the slice of interest, under the assumption that static signal from the tissue subtracts out, leaving just the signal that represents the flow of the magnetically labelled blood into the tissue. The signal decays with the T1 relaxation rate; as the relaxation time for water in blood or tissue is 1-2 seconds only a small amount of labelled water contributes to this 'difference' image, with the inflowing labelled blood only accounting for 0.5 – 1.5% of the full tissue signal (Petcharunpaisan, Ramalho, Castillo, & Carmichael, 2010). Therefore, ASL as a technique has a low signal to noise ratio (SNR), and lower temporal resolution than standard BOLD-fMRI considering both a label and a control image have to be acquired, as well as labelling of the blood. However, this label-control subtraction makes the CBF signal robust against slow drifts of the MR signal, making it more suitable for long task-designs (Wang et al., 2003) than BOLD-fMRI.

There are different options for labelling the blood. Two of the most common, pulsed ASL (PASL) and pseudo-continuous (pCASL), are displayed in Figure 2-6.

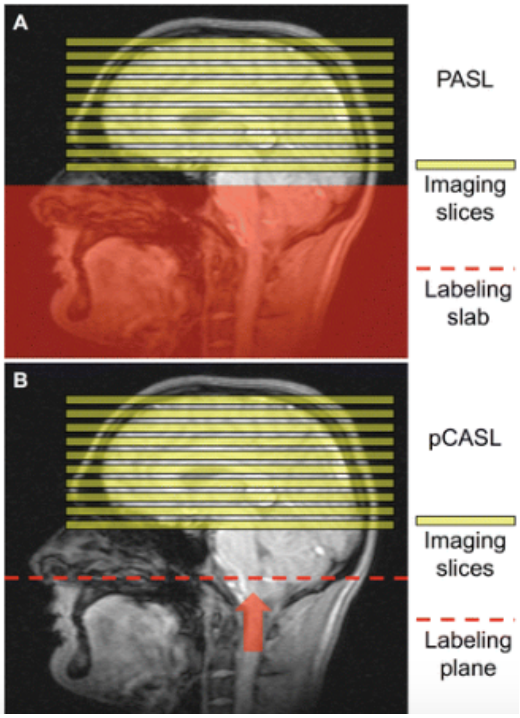

Figure 2-6. Figure taken from (Haller et al., 2016) showing two different ASL labelling schemes. (A) shows pulsed ASL and (B) shows pseudo-continuous ASL.

In this thesis, both PASL and pCASL are used. With PASL, arterial blood water is labelled in an inversion slab below the imaging volume, labelling the blood in the arteries supplying the brain. All the blood in this slab is inverted simultaneously, in about 10 milliseconds, and the time from labelling to acquiring the image is termed the inversion time (TI), (Haller et al., 2016). With pCASL the magnetisation of the blood water is continuously inverted as it flows through a much narrower labelling plane, typically for 1-2 seconds (Haller et al., 2016), with a train of very short (~1ms) pulses. The post label delay (PLD) is the amount of time after the end of the labelling that passes before acquiring the image. PASL has lower SNR than pCASL because the arterial blood inverted with PASL undergoes T1 relaxation as it travels through the inversion slab and to the slice of interest. With pCASL, the blood is continuously inverted, meaning all blood that arrives at the tissue has the same amount of T1 decay regardless of when it was labelled (Haller et al., 2016), if a constant arrival time is assumed. In terms of the labelling inversion efficiency, in pCASL this is affected by the velocity of blood (Wu, Fernández-Seara, Detre, Wehrli, & Wang, 2007), whereas this is not a problem with the very short labelling duration used in PASL.

Comparing the difference between labelled and control acquisitions during stimulus and baseline periods can give relative CBF changes. However, the great advantage of ASL techniques is that the signal can be quantified in units of ml/100g/min (Alsop et al., 2015). Using PCASL as an example, this can be calculated in each voxel by:

$$CBF\ (ml/100g/min) = \frac{6000 \,.\, \lambda \,.\, \left(SI_{Control} - SI_{Tag}\right) . e^{\frac{PLD}{T_{1,blood}}}}{2 \,.\, \alpha \,.\, T_{1,blood} \,.\, SI_{PD} \,.\, \left(1 - e^{-\frac{\tau}{T_{1,blood}}}\right.} \quad \textit{(Equation 2-2)}$$

where λ is the brain/blood partition coefficient (typically assumed to be 0.9 ml/g), $SI_{Control}$ and SI_{Tag} are the signal intensities of the control and labelled images, $T_{1,blood}$ is the longitudinal relaxation time of blood in seconds (typically assumed to be 1650ms at 3Tesla), α is the labelling efficiency (typically 0.85 for PCASL), SI_{PD} is the signal intensity of water in a proton density image acquired with the same characteristics as the CBF images (typically referred to as the *M0* image in this thesis), and τ is the label duration. The 6000 simply converts the units from ml/g/s to ml/100g/min, which is how CBF is typically reported in the literature.

For both PASL and PCASL CBF quantification, some assumptions are made in order to do this CBF quantification step. These assumptions (summarised by (Alsop et al., 2015)) are: (1) The entire amount of labelled blood is delivered to the target tissue

(determined by the important choice of PLD in PCASL and TI in PASL), (2) There is no outflow of labelled blood water, and (3) T1 of blood only determines the relaxation of labelled spins, which is not likely to be completely true due to the difference between the T1 of blood and tissue. This is thought to only introduce small errors.

The ASL scans used in this thesis allow the estimation of both CBF and BOLD weighted images. The specifics of each sequence are explained in each chapter but the general approach is described here. Using one RF excitation pulse, two read-outs can follow: one with a short TE (~3ms) for CBF time series with little BOLD weighing, and a later TE (~30ms) for the BOLD-weighted time series. A slightly different approach involves using an interleaved acquisition, with two RF excitation pulses. This results in a repeating sequence of 4 image volumes: ASL labelled image with short TE, BOLD image with long TE, ASL control image with short TE, BOLD image with long TE. Use of background suppression and a short TE reduces the BOLD weighted signal in the ASL time series (Warnock et al., 2018) and reduces noise contributions from static tissue. The dual excitation approach gives less ASL contamination to the BOLD time-series, compared with the single excitation method. However, in both cases a 'surround average' processing approach is taken to isolate the BOLD time series, analogous to the 'surround subtraction' approach used to generate CBF time series (Liu & Wong, 2005; Warnock et al., 2018). ASL provides a set of *n* control (C) and label (L) images: $[C_1, L_1, C_2, L_2, C_3, L_3, C_n, L_n]$. With surround subtraction, the perfusion (P) time-series can be calculated by taking the difference between the control image and its two surrounding label images (except for the first volume where only pair-wise subtraction occurs):

$$[P_1, P_2, P_3, P_{n/2}] = [C_1 - L_1, C_2 - ((L_1 + L_2)/2), C_3 - ((L_2 + L_3)/2) \ldots]$$

A similar approach can be taken for the BOLD-time series using surround averaging, where the average between the control image and its two surrounding label images is taken, to remove ASL contamination.

2.3.3 Calibrated-fMRI

Acquiring both BOLD and CBF time-series in the same sequence is useful for modelling the $CMRO_2$ response, when some physiological manipulations are administered, and some assumptions made. Calibrated fMRI refers to measuring BOLD and CBF signals during hypercapnia to 'calibrate' the BOLD signal, then allowing a change in the relative $CMRO_2$ response to a stimulus to be calculated. This approach was introduced by

Davis, Kwong, Weisskoff, & Rosen (1998) and later adapted by (Hoge et al., 1999). As described in Figure 2-5 the BOLD response can be expressed in terms of changes in CBF, CBV and $CMRO_2$ changes:

$$\frac{\Delta BOLD}{BOLD_0} = M\left(1 - \left(\frac{CBV}{CBV_0}\right)\left(\frac{CBF}{CBF_0}\right)^{-\beta}\left(\frac{CMRO_2}{CMRO_{2_0}}\right)^{\beta}\right) \quad \textit{(Equation 2-3)}$$

Here, the Δ symbol means change from baseline and the 0 subscript refers to the baseline state. There is a power-law relationship between BOLD and deoxyhaemoglobin concentration, represented by the β parameter. This parameter varies with field strength and is dependent on vessel size distribution. It is typically assumed to be 1.3 when scanning with 3 Tesla MRI (Kennan, Zhong, & Gore, 1994). CBV is not commonly measured directly, as is the case in this thesis. Therefore, CBV changes are inferred from changes in CBF assuming the power law relationship

$$\left(\frac{CBV}{CBV_0}\right) = k.\left(\frac{CBF}{CBF_0}\right)^{\alpha} \quad \textit{(Equation 2-4)}$$

where k is a constant and α has typically been assumed to be 0.38, based on early animal work (Grubb, Raichle, Eichling, 1974). However, recent studies have started to use lower values, based on evidence showing this coupling to be closer to ~0.2 in human fMRI calibration studies (Chen & Pike, 2009, 2010; Mark & Pike, 2012).The modelled BOLD signal now becomes:

$$\frac{\Delta BOLD}{BOLD_0} = M\left(1 - \left(\frac{CBF}{CBF_0}\right)^{\alpha-\beta}\left(\frac{CMRO_2}{CMRO_{2_0}}\right)^{\beta}\right) \quad \textit{(Equation 2-5)}$$

In order to model $CMRO_2$ the only remaining unknown in this equation is therefore the *M* value. *M* is a scaling parameter often described as the maximum BOLD signal change that would occur if all deoxyhaemoglobin were washed out of the venous blood vessels, and therefore reflects the baseline physiological state of the tissue. We do not measure *M* directly like BOLD and CBF signals, but we can estimate it using a gas calibration manipulation.

CO_2 is a vasoactive stimulus that increases blood flow by dilating the blood vessels, normally as a by-product to neural activity. The principles of calibrated-fMRI involves administering a hypercapnic (increased CO_2) gas mixture to the subject to increase CBF (and therefore also increase BOLD), with the assumption that there is no change in $CMRO_2$ (Davis et al., 1998), This has been carried out in many research studies with healthy volunteers (Liu, De Vis, & Lu, 2018), and shown to be safe, well tolerated and feasible in patient populations (Spano et al., 2013). Typically, a gas mixture of 5% CO_2, 21% oxygen and 74% nitrogen is used. Assuming there is no change in $CMRO_2$, the

relative $CMRO_2$ term in Equation 2-5 equates to 1 so the modelled BOLD signal becomes:

$$\frac{\Delta BOLD}{BOLD_0} = M\left(1 - \left(\frac{CBF}{CBF_0}\right)^{\alpha-\beta}\right) \quad \textit{(Equation 2-6)}$$

As we measure the BOLD and CBF change to the hypercapnic stimulus, and we assume values for α and β, we can simply re-arrange Equation 2-6 to get the *M* value in that region. In the same scanning session, in the same subject, if we collect BOLD and CBF response to a task or stimulus, we can then re-arrange Equation 2-5 to give relative changes in $CMRO_2$ to the stimulus:

$$\frac{CMRO2}{CMRO2_0} = \left(\frac{CBF}{CBF_0}\right)^{1-\frac{\alpha}{\beta}} \cdot \left(1 - \frac{\frac{\Delta BOLD}{BOLD_0}}{M}\right)^{\frac{1}{\beta}} \quad \textit{(Equation 2-7)}$$

Another way CO_2 inhalation is commonly used in the fMRI literature is to characterise the reactivity of the blood vessels. As CO_2 is a vasodilator it will increase blood flow all across the brain. A response to CO_2 therefore gives an indication of the ability of the blood vessels to dilate or constrict, informing about vascular health and reserve (Liu et al., 2018). This metric is referred to as *Cerebrovascular Reactivity* (CVR) in the literature. Concentrations of the inhaled and exhaled CO_2 are recorded through-out the experiment via a face-mask or nasal cannula. As arterial blood gas measurements are invasive, end-tidal partial pressure of CO_2 ($P_{ET}CO_2$), the partial pressure of CO_2 at the end of the exhalation, is used as a surrogate measure of arterial CO_2 (McSwain et al., 2010). Gas measurements are typically quantified in units of millimetres of mercury (mmHg), a unit of pressure. The measured BOLD or CBF response can then be expressed in percentage or absolute change in BOLD/CBF per mmHg change in $P_{ET}CO_2$.

Instead of a gas-paradigm, a breath-hold (BH) task where participants hold their breath typically for 10-20 seconds can also act as a hypercapnic stimulus, in order to characterise CVR (Urback, MacIntosh, & Goldstein, 2017). An estimate of *M* can also be gained from a BH task, to model $CMRO_2$ the same way as explained above. Developing such methodology is the focus of Chapter 8 of this thesis.

2.3.4 Dual Calibrated-fMRI

Calibrated-fMRI gives relative $CMRO_2$ changes to a stimulus, which we expect to offer a closer reflection of the metabolic demands of brain activity compared to BOLD-fMRI alone. An extension of this technique has been recently developed (Bulte et al., 2012; Gauthier, Desjardins-Crépeau, Madjar, Bherer, & Hoge, 2012; Wise, Harris, Stone, &

Murphy, 2013) showing that information about baseline $CMRO_2$ can also be estimated, by adding a second calibration step. In the original calibrated-fMRI design, the baseline physiological state is summarised by the *M* parameter, and its effect on the BOLD signal is considered. With dual-calibrated designs, the models attempt to separate out the different physiological contributions to *M* and estimate the baseline physiological state. Characterising baseline $CMRO_2$ measurements, alongside other parameters such as baseline CBF, has potential valuable information to help understand the cause of a disease, including what mechanisms might relate to disease progression. As with BOLD and CBF signals, interpreting relative $CMRO_2$ signal changes still may be confounded if baseline $CMRO_2$ is altered in disease (Iannetti & Wise, 2007), therefore it is also useful to consider the baseline in the interpretation of any stimulus-induced changes.

The BOLD response modelled by (Davis et al., 1998) and (Hoge et al., 1999) can be expressed in terms of CBV (CBV substituted with CBF by Equation 2-4) and venous deoxyhaemoglobin concentration [dHb] in response to changes in partial pressure of O_2 and CO_2:

$$\frac{\Delta BOLD}{BOLD_0} = M\left(1 - \left(\frac{CBF}{CBF_0}\right)^{\alpha}\left(\frac{dHb}{dHb_0}\right)^{\beta}\right) \textit{(Equation 2-8)}$$

where the subscript 0 represents the baseline (normoxic and normocapnic) conditions (Wise et al., 2013). As explained in the Calibrated-fMRI section, M can be calculated with a hypercapnic stimulus. The aim with dual-calibrated fMRI is to estimate the $[dHb_0]$ which is not possible with hypercapnia alone. The change in [dHb] concentration, with respect to baseline, when arterial oxygen content is increased and/or CBF altered is given by:

$$\frac{dHb}{dHb_0} = \frac{CBF_0}{CBF} - \frac{1}{dHb_0}\left\{\frac{1}{\emptyset}\left(CaO_2 - \left(\frac{CBF_0}{CBF}\right)CaO_{2|0}\right) + [Hb]\left(\frac{CBF_0}{CBF} - 1\right)\right\} \text{(Equation 2-9)}$$

where [Hb] is haemoglobin in g/dL (grams per decilitre of blood), ϕ is the O_2 carrying capacity of [Hb] in mlO_2/g_{Hb}, and CaO_2 is the oxygen content of arterial blood. Subsisting Equation 2-9 into 2-8 leaves the only unknown term as $[dHb_0]$, therefore this can be obtained from measurement and estimation of all the other physiological parameters. Full derivation of equations can be found in Wise et al (2013).

This dual-calibrated design includes a hypercapnic stimulus to increase CBF as before, and a hyperoxic stimulus to increase the BOLD signal, to first approximation, without a

CBF change. As with hypercapnia, the hyperoxia is assumed to be isometabolic (no change in $CMRO_2$), just leading to an increase in the BOLD response due to more oxygen being bound to haemoglobin in the blood and dissolved in blood plasma on the arterial side of the supply. With CBF and $CMRO_2$ constant, this hyperoxia produces an increase BOLD signal. The fraction of inspired O_2 is typically increased to 50%, a trade-off between maximising the BOLD response during hyperoxia and avoiding artefacts (Germuska & Wise, 2018). Under the assumption that $CMRO_2$ is the same under hypercapnia and hyperoxia, estimates of the baseline venous deoxyhaemoglobin concentration can obtained. Once we have an estimate of [dHb_0] baseline OEF can be estimated as OEF is simply the difference between the CaO_2 and the CvO_2 (venous blood content), and [dHb_0] determines the venous blood oxygen saturation. CaO_2 is the total amount of oxygen transported in the blood, either bound to haemoglobin or dissolved in plasma. The amount of haemoglobin bound to oxygen can be estimated with an assumed or measured value of haemoglobin and the amount dissolved in plasma is based on the partial pressure of O_2 estimated from the end-tidal physiological traces. Once we have a value for resting OEF, resting $CMRO_2$ can be calculated using Equation 2-1, alongside ASL measurements of CBF and estimates of CaO_2.

In the original implementations of this dual-calibrated model (Bulte et al., 2012; Gauthier et al., 2012; Wise et al., 2013) the CBF and BOLD data were analysed independently, to separately estimate the M and the baseline [dHb]. In later adaptations, and what is implemented in this thesis, all physiological parameters are estimated together (Germuska et al., 2016). This helps create more stable solutions due to less error propagation along different steps of the analysis pipeline and allows the CBF to inform the modelling of the BOLD signal changes and vice versa. This is done by finding the set of parameters that minimises the error between a forward model (describing how the BOLD and CBF are expected to respond to the CO_2 and O_2 manipulations) and the acquired data (Germuska et al., 2016). This is the implementation used in Chapter 5, with a new addition to the modelling which uses the CBF and OEF observations to model the exchange of oxygen between the capillaries and the tissue (the effective oxygen diffusivity), (Germuska et al., 2019).

2.4 The relationship between MEG and fMRI: an empirical measure of neurovascular coupling

In this thesis, the relationship between MEG and fMRI signals is used as an empirical measure of NVC. The rationale of why NVC is an important physiological mechanism

has already been covered; this section will briefly cover the practicalities of characterising it with MEG and fMRI.

NVC is characterised by quantifying how much the fMRI signal changes relative to the MEG signal change. The obvious limitation to this approach is the need to carry out two scans separated in time. Therefore, an assumption made in order to characterise this MEG-fMRI relationship is that the brain is responding in a similar way in both scanning modalities. Both MEG and fMRI signals are thought to largely reflect post-synaptic (dendritic) rather than axonal activity (Hall et al., 2014; Logothetis, 2002; Logothetis, Pauls, Augath, Trinath, & Oeltermann, 2001; Zhu et al., 2009), and literature shows good spatial coherence between MEG and fMRI signals (Muthukumaraswamy & Singh, 2008; Singh, Barnes, Hillebrand, Forde, & Williams, 2002). Most findings show negative correlation between BOLD and low frequency neural oscillations (e.g. alpha and beta), and a positive correlation with higher frequency bands (e.g. gamma), (Logothetis, 2002; Mukamel et al., 2005; Zumer, Brookes, Stevenson, Francis, & Morris, 2010). From manipulating stimulus parameters, commonly visual, some have suggested BOLD signals are most reflective of gamma oscillations. However, the picture is complex. BOLD signals and visual gamma oscillations seem to be tuned similarly by some stimulus features (i.e. visual contrast, (Muthukumaraswamy & Singh, 2009; Scheeringa et al., 2011)) but some seem to greatly influence the visual gamma response but not the BOLD response (i.e. spatial frequency (Muthukumaraswamy & Singh, 2008, 2009) and colour (Swettenham, Muthukumaraswamy, & Singh, 2013). It is therefore not clear how stable these coupling behaviours are under different stimulus conditions, and across different brain areas.

Compared to MEG, and other neuroimaging methods, fMRI has superior spatial resolution, providing information about the location of neural activity at millimetre resolution. However, the temporal resolution of BOLD and CBF is limited by the restrictions in acquiring the signals but predominantly by low frequency nature of the signals themselves: the CBF response to neural activity is typically delayed by 1-2 seconds, peaks at around 5 seconds, and takes a similar amount of time to return to baseline. This is opposite to MEG, which has superior temporal resolution, at the level of milliseconds. However, MEG suffers from the mathematically ill-posed 'inverse problem', when trying to locate the neural origins of signals measured at scalp, which limits spatial resolution. Any choice of stimulus design to investigate common MEG and fMRI signals will therefore be a trade-off between these very different temporal and spatial resolutions.

Previous non-invasive studies have predominantly looked at the relationship between BOLD-fMRI signals and neural activity. There are a few studies collecting both MEG and CBF data in the same participants, for example resting state dynamics in stroke and aging (Kielar et al., 2016; Sakamoto et al., 2016) and in response to LSD (Carhart-Harris et al., 2016). There is also some work comparing EEG and CBF responses to a visual stimulus (Mayhew, Macintosh, Dirckx, Iannetti, & Wise, 2010). There are some invasive recordings carried out in somatosensory cortex of rodents showing relationships between neural activity and CBF, for example: correlations between the LFPs and CBF which depended on frequency of electrical forepaw stimulation (Ureshi, Matsuura, & Kanno, 2004), a power law function describing the relationship between LFPs and CBF during whisker stimulation (Hewson-Stoate, Jones, Martindale, Berwick, & Mayhew, 2005), and findings that show CBF and $CMRO_2$ signals more directly correlate with neural activity than BOLD signals during forepaw stimulation (Masamoto, Vazquez, Wang, & Kim, 2008). To the best of our knowledge, the coupling between MEG and CBF signals have not been compared in the context of NVC, as they are in this thesis. As explained in the earlier sections, CBF directly reflects blood flow to an area. The BOLD signal gives better SNR but can be difficult to interpret under any conditions where the baseline state may be altered. Therefore, in this thesis both BOLD and CBF signals are compared with MEG signals, with the aim of increasing the understanding of NVC mechanisms, in both the healthy brain and in MS (explained in Chapter 3).

2.5 Software and statistics

Pre-processing of structural and functional MR images was performed with FSL (Jenkinson, Beckmann, Behrens, Woolrich, & Smith, 2012) or MATLAB (The MathWorks Inc), unless otherwise stated.

In FSL:

- *fslmaths* function was uses to combine, binarise and threshold images
- *fslstats* function used to get descriptive statistics
- Registration of images were carried out with FLIRT (Jenkinson & Smith, 2001)
- Non-brain removal with BET (Smith, 2002)
- Segmentation of tissue performed with FAST (Zhang, Brady, & Smith, 2001)
- Task-responses were modelled with FEAT Version 6 (Jenkinson et al., 2012).

Statistical analysis was performed with MATLAB (The MathWorks Inc), IBM SPSS Statistics (Versions 20-25), or R software (R Core Team, 2017). For Man-Whitney U-

tests, the non-parametric version of the independent t-test, an exact sampling distribution was used for *U*. For each comparison, if the shape of the distribution between the two groups was similar (by visual inspection) medians between groups were compared.

Assumptions of statistical tests were met, unless otherwise stated. Outliers were classed as 3 standard deviations (SD) above or below the mean. Data was also visualised as boxplots and checked for extreme outliers. The use of boxplots to visualise the distribution of data (Tukey, 1977) is implemented in SPSS. The interquartile range (IQR) is the upper quartile (Q3, 75th percentile) minus the lower quartile (Q1, 25th percentile). Possible outliers are classed as 1.5xIQR below Q1 and 1.5xIQR above Q3 (outside the 'inner fence'). Extreme outliers are classed as 3xIQR below Q1 and 3xIQR above Q3 (outside the 'outer fence'). With a normal probability distribution, it is estimated that approximately 99.2% of values fall within the inner fence (equivalent to $\pm$ 2.67 SD from the mean) and 99.99% of values within the outer fence (equivalent to $\pm$ 4.67 SD from the mean), (Dawson, 2011). In reality, with smaller sample sizes, it is reasonable to assume a smaller percentage of values fall within these inner and outer fences, as is assumed with the Student's *t* distribution.

3 Introduction to Multiple Sclerosis

3.1 Overview

3.1.1 Etiology

MS is the leading cause of non-traumatic neurological disability in young adults, estimated to affect 2.3 million people worldwide (Aarli et al., 2014). Symptom onset peaks between 20-40 years. For common forms of adult MS, higher prevalence rates are reported in women compared to men (~2:1 ratio), as well as in people living in higher latitudes, although this has decreased over recent decades (Kamm, Uitdehaag, Polman, & Kamm, 2014). Smoking, Vitamin D exposure and viral infections are all risk factors, yet the etiology of MS is unknown (Kamm et al., 2014). Although many genetic variants have been found, MS is not considered hereditary and there is extensive overlap between genetic risk variants for MS and other autoimmune diseases (Baranzini & Oksenberg, 2017).

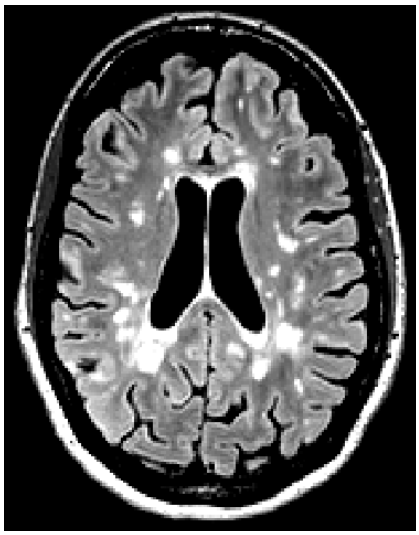

Figure 3-1. An axial slice from a T2-FLAIR image showing widespread white matter hyperintensities. This data is an example MS patient from Chapter 5.

3.1.2 MS pathology

MS is classed as a chronic inflammatory autoimmune disease of the central nervous system (CNS), with the hallmark pathological feature being focal demyelination of white matter (WM) in the CNS (Noseworthy, Lucchinetti, Rodriguez, & Weinshenker, 2000), see Figure 3-1. These areas of demyelination are referred to as WM lesions or 'plaques'. It is thought that this damage is caused by autoreactive immune cells from the periphery crossing the blood-brain barrier (BBB) into the brain and spinal cord (Dendrou, Fugger, & Friese, 2015).

The BBB separates the blood from neural cells in the CNS; it is a made up of endothelial cells that line the micro-vessels to form a physical barrier impermeable to large molecules and immune cells, maintaining a regulated environment for neuronal signalling (Abbott, Rönnbäck, & Hansson, 2006). There is evidence that immune cells (T cells/lymphocytes) react against components within the myelin sheaths (e.g. myelin basic protein, proteolipid protein and myelin oligodendrocyte glycoprotein). Once the T-cells are activated they rapidly divide and secrete proinflammatory cytokines (small signalling proteins) which promote microglia and macrophage activity (Dendrou et al., 2015). This leads to damage to the myelin sheaths and therefore a slowing of the signal propagation along the axon, leading to functional impairments. The exact process of how and why the immune cells infiltrate the BBB is still not known although many environmental factors have been proposed (O'gorman, Lucas, & Taylor, 2012).

MS has been traditionally viewed as a disease of WM, with myelin loss proposed as the key cause of functional impairments, however there is clear evidence that grey matter (GM) inflammation, demyelination and degeneration occur. This dysfunction of GM, both cortical and subcortical, is present from the early stages of MS and changes with disease progression (Crespy et al., 2011; Klaver, De Vries, Schenk, & Geurts, 2013b; Lucchinetti et al., 2011). Post-mortem studies show significant GM demyelination and microglial activation. However, there is some evidence for less extensive influx of immune cells and BBB leakage in GM compared to WM (Bø, Vedeler, Nyland, Trapp, & Mørk, 2003; Bø, Vedeler, Nyland, Trapp, & Mørk, 2003; Klaver, De Vries, Schenk, & Geurts, 2013). Another challenge to the traditional view of MS pathology is the evidence that axonal injury, thought to be responsible for progressive neurological deficits (Neumann, 2003), is present at sites of active inflammation and demyelination early in the disease (Bitsch, Schuchardt, Bunkowski, Kuhlmann, & Brück, 2000; Ferguson, Matyszak, Esiri, & Perry, 1997). Axonal injury and GM atrophy have been typically regarded as secondary to myelin damage, however this may not be the case. There is much debate over whether one mechanism is solely responsible for initiating MS pathology, or whether there are parallel multiple mechanisms, and whether autoimmunity leads to cytodegeneration or vice versa (Dendrou et al., 2015; Stys, Zamponi, van Minnen, & Geurts, 2012), see Figure 3-2.

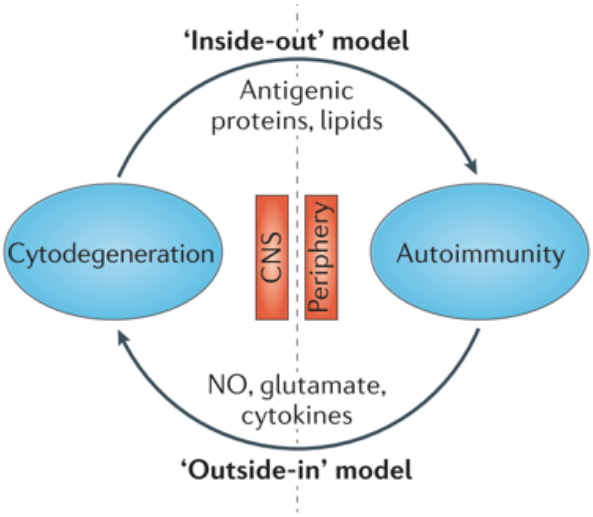

Figure 3-2. Traditional theories say that dysregulation of the immune system is the initial event, eventually leading to tissue injury (Outside-In). Alternatively, cytodegeneration may happen first, promoting an autoimmune and inflammatory response (Inside-Out).

3.1.3 Symptoms and disease course

Symptoms depend on stage of disease, and the location of damage across the brain or spinal cord and are therefore very varied. However, initial symptoms typically include: limb weakness, sensory disturbances, monocular visual loss (optic neuritis), double vision, gait instability and ataxia (Kamm et al., 2014). Later in the disease, bladder dysfunction, fatigue, heat sensitivity, vertigo, weakness or pain and spasms are often reported. Cognitive deficits (Guimarães, Sá, & Massano, 2012) and depression (Siegert, 2005) are also commonly reported. MS is classified into different disease subtypes or courses (Lublin et al., 2014). About 85% of cases are Relapsing Remitting MS (RRMS), characterised by periods of increased disability due to an immune attack (a relapse), interspersed with periods of functional recovery (a remission), see part A of Figure 3-3.

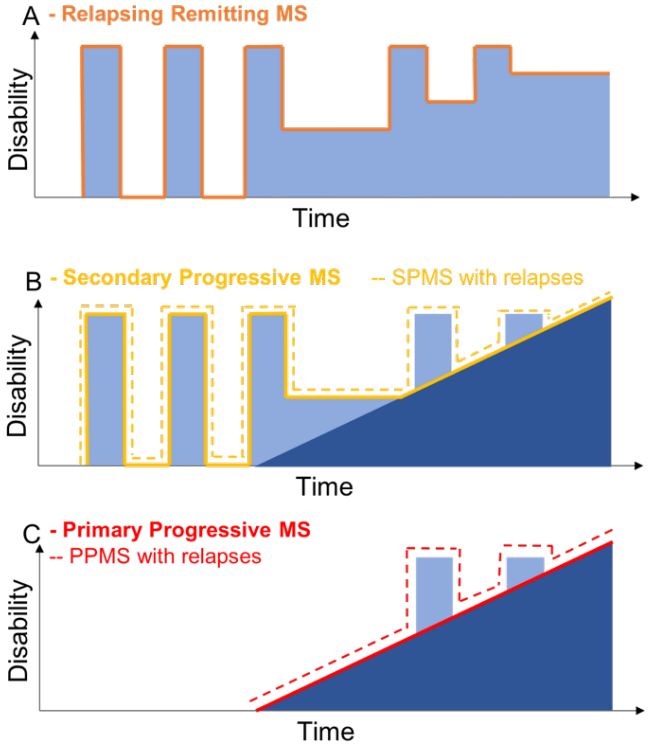

Figure 3-3. Disability progression for different MS subtypes. The height of the light blue bars and dark blue triangles indicate functional disability, and the solid and dotted lines mark the course of this disability over time.

During relapses, peripheral immune cells infiltrate the CNS due to BBB breakdown and target myelin proteins, as explained earlier. During a remission, remyelination occurs (Franklin & Goldman, 2015). Earlier on in the disease course, this can often lead to full functional recovery. For remyelination to occur, oligodendrocyte progenitor cells have to migrate to the damaged area then differentiae into mature oligodendrocytes to form new myelin sheaths (Brück, Kuhlmann, & Stadelmann, 2003). This remyelination process becomes less efficient as the disease progresses (Franklin, 2002), and functional recovery during remissions lessens. Approximately 75% of people with RRMS transition onto Secondary Progressive MS, a steady worsening of disability, relapses remaining in 40% of cases, see part B of Figure 3-3. Less common types of MS present with progressive disability from onset (15% with Primary Progressive MS, of which 40% have relapses), see part C of Figure 3-3.

3.1.4 Diagnosis

The most recently revised McDonald criteria for diagnosis of MS was last updated in 2017 and is discussed by (Thompson et al., 2018). The key diagnostic criteria for MS are the dissemination in space and dissemination in time, which can apply to lesions (i.e. across different areas of the CNS) or to symptoms tracked by clinical assessments. A diagnosis of MS will be given based on clinical history being suggestive of MS and when there is no better clinical explanation i.e. alternative diagnoses must be ruled out. When a patient without an existing diagnosis of MS presents with symptoms alongside evidence of inflammatory demyelinating activity (duration of at least 24 hours), the diagnosis of Clinically Isolated Syndrome is given. This diagnosis of Clinically Isolated Syndrome, without the full criteria being met, is classed as possible MS.

A neurologist will perform physical examinations to check for changes in weakness, coordination, balance, and sensation. Sometimes latency and amplitude of evoked potentials are examined, an impairment of which can indicate slowing of signal propagation along axons. This can be done for visual, auditory, sensory and motor systems. Visual is most common, considering optic neuritis is a common initial symptom in MS, as well as broader visual problems (Graham & Klistorner, 2017). The Expanded Disability Status Scale (EDSS) (Kurtzke, 1983) is a commonly used clinical metric to represent the degree of disability, and monitor changes over time. Scores range from 0 to 10 (in 0.5 increments) and are based on clinical assessment of 8 systems: pyramidal (limb movement), cerebellar (co-ordination or tremor), brainstem, (speed and swallowing), sensory (loss or numbness), bowel or bladder function, visual function and

cerebral (cognitive) function. EDSS of less than 5 means the patient can walk without a walking aid.

Conventional structural MRI can non-invasively detect lesions and therefore plays a big role in demonstrating disseminating symptoms in space and time. Typical sequences include T2-weighted and pre and post contrast T1-weighted images. Gadolinium-enhancing lesions indicate BBB breakdown, i.e. areas of active inflammation. Importantly for a diagnosis of MS, there needs to be no alternative diagnosis that can better explain the clinical presentation, and blood and CSF samples help rule out other diagnoses. Analysis of a CSF sample (via a lumbar puncture) can contribute to MS diagnosis by looking for the presence of oligoclonal bands (bands of antibodies called immunoglobins) in the CSF compared to blood, and higher levels of other proteins evident of myelin breakdown (e.g. neurofilaments).

3.1.5 Treatment

There is no cure for MS. Drugs typically prescribed for MS can be divided into relapse, disease-modifying and symptomatic treatment (Kamm et al., 2014). Corticosteroids (typically methylprednisolone) are used to treat relapses, suppressing the immune system and decreasing inflammation. Disease Modifying Treatments (DMTs) are used to alter the disease course (mainly CIS, RRMS) by reducing the likelihood of relapses. Available first-line therapies include Interferon beta, Glatiramer acetate, Teriflunomide and Dimethyl fumarate. Some patients transition onto second-line therapies (or start on this, if the MS is very active), if disease activity remains, which include Fingolimod, Natalizumab, Ocrelizumab and Alemtuzumab (Torkildsen, Myhr, & Bø, 2016). In general, these drugs work to inhibit the proliferation and migration of inflammatory cells into the CNS, and to shift the cytokine response from an inflammatory response to an anti-inflammatory profile, although many of the drug mechanisms are not completely known (Torkildsen et al., 2016). There are also many drug treatments prescribed based on specific symptoms experienced, for example for depression or spasticity. Symptomatic treatments are particularly important for people with progressive forms of MS, to limit the impact of disability on daily activities.

3.2 Neurovascular and metabolic dysfunction in MS

GM damage undeniably plays a role in MS pathology. In fact, as GM damage is not typically a part of the diagnostic process, this may go some way to explain the clinic-radiological paradox (Barkhof, 2002; Chard & Trip, 2017), i.e., the observation that the

number and volume of WM lesions only explain a small amount of variability in clinical outcomes. However, despite recent advances in characterising GM damage with MRI, challenges with the sensitivity of these techniques remain (reviewed by Amiri et al., 2018). Further, the mechanism that leads to GM damage, and the cause of MS pathology in general, is not fully known. Therefore, it is important that neuroimaging research also studies functional signals, as well as structural tissue characteristics, to try to further the understanding of causal mechanisms. Below, the evidence for neurovascular and metabolic dysfunction in MS is summarised, followed by a discussion of the mechanisms.

3.2.1 Neuroimaging Evidence

Vascular and metabolic impairments are acknowledged to be a pathological feature of MS (D'haeseleer et al., 2015; Lapointe, Li, Traboulsee, & Rauscher, 2018; Paling, Golay, Wheeler-Kingshott, Kapoor, & Miller, 2011; Spencer, Bell, & DeLuca, 2018). Perfusion alterations within lesions, normal appearing WM (NAWM) and GM have been widely reported and some key findings are summarised below. In the studies below, perfusion and oxygen metabolism have mostly been measured with ASL-MRI imaging or with DSC-MRI (where an intravenous paramagnetic contrast agent is administered, and the brain is scanned with a rapid T2-weighted imaging technique). There are a few studies using PET imaging and Dynamic Contrast-Enhanced MRI, which uses T1-shortening due to a contrast agent to detect area of BBB disruption (Lapointe et al., 2018).

MS Perfusion changes in Normal Appearing Brain Tissue

Grey matter. In GM, a reduction in CBF and CBV is seen in both cortical and deep GM structures, mostly reported for RRMS subtypes but also for Secondary Progressive MS and PPMS (Aviv et al., 2012; Brooks et al., 1984; D'haeseleer et al., 2013; Debernard et al., 2014; Hojjat et al., 2016; Inglese et al., 2007, 2008; Lycke, Wikkelsö, Bergh, Jacobsson, & Andersen, 1993; Ota et al., 2013; Papadaki et al., 2012; Rashid et al., 2004; Steen et al., 2013; Sun, Tanaka, Kondo, Okamoto, & Hirai, 1998; Vitorino et al., 2016). There is some evidence, in RRMS, that reduced CBF in many GM regions is seen in the absence of atrophy (Debernard et al., 2014). In support of this, another study reported decreases in CBF and CBV in frontal regions for cognitively impaired patients compared to unimpaired patients, after adjusting for volumetric differences (Vitorino et al., 2016).

White matter. In NAWM, DSC and PET studies have mostly reported decreases in CBF and CBV, and increases in mean transit time (MTT), in MS patients (Adhya et al., 2006; Debernard et al., 2014; Ge et al., 2005; Guo, Jewells, & Provenzale, 2001; Inglese et al., 2008; Narayana et al., 2014; Papadaki et al., 2012; Steen et al., 2013; Sun et al., 1998). However, these CBF and CBV reductions in NAWM appear less consistent in the literature compared to the GM findings. A study by Rashid et al (2004) reported an increased CBF in 60 patients with mixed subtypes, and Paling et al (2013) reported increased CBF in NAWM of RRMS patients. This inconsistency could be due to varying levels of inflammation in these patients populations; Bester et al (2015) characterised RRMS into a high or low inflammatory group depending on the number of new contrast enhancing lesions and found that the high inflammatory group had higher CBV and CBF values in NAWM. There is also evidence that patients with CIS have higher CBV, CBF and MTT values in deep GM and NAWM, compared to RRMS patients (Papadaki et al., 2012).

These reductions of CBF and CBV have been shown to correlate with neurological disability (Lycke et al., 1993), fatigue (Inglese et al., 2007), cognition (Inglese et al., 2008) and memory (Debernard et al., 2014). However, in the review by Lapointe et al (2018), they argue that "Despite compelling and reproducible perfusion abnormalities in MS, their relation to clinical measures of disability and disease severity has not been strongly established", giving an overview of the studies that have addressed this.

Perfusion changes in MS Lesions

In active WM lesions, evidence points towards increased perfusion, mostly likely due to increased metabolic activity at the site of active inflammation. This increase was demonstrated in a longitudinal study by Wuerfel et al (2004). In 20 RRMS patients, they tracked the formation and progression of gadolinium-enhancing lesions. They showed regional increases in CBF and CBV 3 weeks before gadolinium enhancement. They saw a further increase at the time of gadolinium enhancement, and a decline to baseline during the 20 weeks after. Their study provides evidence for the role of the vasculature preceding BBB breakdown (or at least before this is measured with gadolinium enhancement). Other DSC or DCE studies also found CBV and CBF increased in contrast-enhancing lesions compared with NAWM (Ge et al., 2005; Haselhorst et al., 2000; Ingrisch et al., 2012). For chronic WM lesions, looking at T1-hypointense, there is evidence for a reduction in CBF (Haselhorst et al., 2000; Li et al., 2014) presumably due to axonal loss therefore having less metabolic activity. There are very few studies looking at perfusion in cortical lesions, due to the technical challenges, however one

DSC study reports lower CBF and CBV in cortical lesions, in RRMS patients, compared to normal appearing GM (Peruzzo et al., 2013). A small subset of cortical lesions did show increased CBF and CBV, as with WM, suggestive of acute inflammation. A very recent ASL study (Dury et al., 2018) was the first to quantify CBF in cortical lesions using 7 Tesla MRI, showing the majority of cortical lesions to be hypoperfused compared to normal appearing GM.

Cerebrovascular Reactivity in MS

There is some evidence for impaired reactivity of blood vessels to a CO_2 stimulus in MS, termed CVR, introduced in Chapter 2.3.3. PASL was used to measure the CBF response to hypercapnia, compared to normocapnia, finding decreased global GM CVR in patients in multiple brain regions, and a negative correlation between GM CVR and lesion load (Marshall et al., 2014). No baseline CBF differences between groups were reported in this study. The same research group reported, in a different MS cohort, decreases in CVR in different functional networks (default mode, frontoparietal, somatomotor, and ventral attentional), and again correlations with lesion load and GM atrophy (Marshall, Chawla, Lu, Pape, & Ge, 2016). A study by a different research group reported no significant difference in CVR in patients with RRMS across three different time points (first two days after a relapses but pre-treatment, just after steroid treatment, and one month later), as well no differences with healthy controls at one time point (Uzuner, Ozkan, & Cinar, 2007). This study used transcranial Doppler imaging to asses vasomotion in response to a BH task, so there are many methodological factors that could explain their different findings to Marshall et al (2014; 2016).

Oxygen Utilisation in MS

Many studies have used the BOLD-fMRI contrast to demonstrate functional connectivity deficits in MS (e.g. Sbardella, Petsas, Tona, & Pantano, 2015), altered task responses which relate to disability or structural damage (Hubbard et al., 2016; Rocca & Filippi, 2007) and as a way to assess functional reorganisation of the cortex (Tomassini et al., 2012). This research contributes to the evidence that there is a strong hemodynamic impairment in MS. However, as explained in Chapter 2.3.1, the BOLD response alone can be hard to interpret in a patient group; despite it reflecting changes in oxygen usage, it is a relative composite signal that depends on CBF, CBV, oxygen metabolism changes, and the baseline tissue activity. Therefore, research is needed to measure and quantify more specific and interpretable signals, such as the fraction of oxygen extracted from the blood (OEF) or rate of oxygen metabolism in the tissue ($CMRO_2$).

Very few studies have characterised such signals in an MS group. Some early papers using PET and MRI did show reductions in $CMRO_2$ and CBF in both WM and GM, with correlations with atrophy, cognition, vision, EDSS and number of relapses (Brooks et al., 1984; Lycke et al., 1993; Sun et al., 1998). One MRI studying characterised $CMRO_2$ at rest in an MS population using a T2-relaxation-under-spin-tagging (TRUST) technique, which gives a global estimate of oxygen consumption (Ge et al., 2012). They found increased global venous oxygen saturation, decreased OEF and decreased $CMRO_2$, which significantly correlated with EDSS and lesion load.

3.2.2 Discussion of the mechanisms

Finding both increases and decreases in perfusion within lesioned tissue can be partly explained by the levels of inflammation and metabolic activity at that stage of the lesion's development. What is less clear is why there are alterations in BOLD, CBF, CBV and $CMRO_2$ in normal appearing WM and GM. It is thought that this reduced perfusion and oxygen metabolism may contribute to the progressive neurodegeneration seen in MS, due to tissue hypoxia (Trapp & Stys, 2009), yet the mechanisms are unclear.

It is possible that perfusion to the active tissue is restricted in some way, as there is increased cardiovascular risk reported in MS, but this increased risk appears to be small (Christiansen et al., 2010; D'haeseleer, Cambron, Vanopdenbosch, & De Keyser, 2011). A simple explanation for reduced perfusion is reduced metabolic demand: if there is neuronal loss, less blood will need to flow to the area as less energy is being used. However, as discussed in section 2.7.1, there is evidence for perfusion changes before neuronal loss. Furthermore, reduced blood flow and oxygen metabolic changes are often reported as widespread changes across the brain, and not just localised near lesioned areas. Some studies report increases in CBF and CBV in NAWM and decreases in GM in the same patients (e.g. Rashid et al., 2004), as well as correlations between T2 lesion load and global cortical CBF (e.g. Amann et al., 2012) and CVR (e.g. Marshall et al., 2014). It is of course possible that there is more extensive damage across the GM and WM that is not being measured, however it still appears that focal BBB disruption occurs alongside widespread functional perfusion changes.

Another proposed mechanism is the increase of different vasoactive agents circulating in the blood, released from reactive astrocytes near lesions, or upregulated due to the presence of many proinflammatory cytokines. NO has been shown to be elevated in MS lesions (Smith & Lassmann, 2002a), and has been proposed as a potential mediator

leading to hypoperfusion. It is a strong vasodilator, and therefore its overproduction could desensitise smooth muscle function over time, resulting in decreased vascular capacity (Marshall et al., 2014). Furthermore, NO is synthesized by endothelial cells (which make up the BBB), and one study showed patients with endothelial dysfunction to have decreased cerebrovascular reactivity (Lavi, Gaitini, Milloul, & Jacob, 2006). A different vasoactive agent, Endothelin-1 (ET-1), has also been proposed as a potential mediator (D'haeseleer et al., 2013). ET-1 is a vasoconstrictor secreted by endothelial cells. D'haeseleer et al (2013) reported higher plasma ET-1 levels in patients, from both the internal jugular vein and a peripheral vein, and only in patients was the internal jugular ET-1 plasma levels higher than the ET-1 levels in the peripheral vein. They interpreted this as evidence that ET-1 is released from the brain into circulation. They also reported, with data from an ASL acquisition, that CBF was lower in MS patients, but increased to control levels after an ET-1 antagonist administration. They included post-mortem immunohistochemistry analysis of WM tissue, from different patients, suggesting reactive astrocytes to be the likely source of ET-1 increase. Increased NO and ET-1 are just two examples of ways in which the inflamed environment can have a direct effect on blood vessels, potentially changing how they respond to metabolic demands of neural activity.

There is evidence for mitochondrial dysfunction in MS (Paling et al., 2011) and this has been proposed as a potential mechanism leading to the neurodegeneration seen, with the mitochondria not able to make sufficient ATP in response to energy demands. Ge et al (2012) explain how NO may also play a role in this, as NO inhibits oxygen binding to mitochondria, affecting ATP synthesis. They explain how this is termed 'metabolic hypoxia' – even if there is enough blood flow to an area, the cells and tissue may be unable to use it properly.

3.2.3 MS and MEG literature

Compared to fMRI, there is a small amount of literature using MEG imaging to investigate neural oscillations in MS, as done in this thesis. Studies have mostly focused on MEG connectivity, from resting state paradigms. For theta band, there are reports of increased connectivity in MS (Schoonheim et al., 2013; Tewarie et al., 2014). For the alpha band, there are reports of decreased connectivity in MS (Cover et al., 2006; Tewarie et al., 2013, 2014), but some studies split their analysis into smaller frequency bands and show increased connectivity in lower (8-10Hz) alpha bands and decreased connectivity in upper (10-13Hz) alpha bands, (Schoonheim et al., 2013; Van der Meer et al., 2013). For beta bands, increased network strength has been reported

(Schoonheim et al., 2013; Tewarie et al., 2013) and decreased functional connectivity (Tewarie et al., 2014). Thalamic volumes have been linked to network disruption in MS (Tewarie et al., 2013, 2015). Although it is difficult to pull out consistent directional trends, there is clear evidence showing abnormal functional network connectivity in MS, and many of these alterations in connectivity where shown to correlate with impaired cognition or disease severity. There are a few recent studies showing impaired visual and motor task-based MEG responses (Arpin et al., 2017; Barratt et al., 2017a) and these are discussed in Chapter 4.

As explained earlier, one explanation for reduced CBF or $CMRO_2$ in MS is simply reduced demand from the tissue. However, in these studies that looked at flow or oxygen metabolic changes in MS, neural activity was not directly measured. In order to address this mechanism more directly, we need to establish if there is a decrease in flow or oxygen metabolism *above and beyond* any decrease in neuronal activity. This is the rationale for measuring MEG signals in MS, in order to correlate with fMRI signals as a measure of NVC. Studying the amplitude and frequency of brain oscillations with MEG can also be informative for understanding disease mechanisms in MS.

4 The coupling between visual gamma oscillations and BOLD and CBF signals: investigating neurovascular coupling in Multiple Sclerosis

The work presented in this chapter has been published as a part of a peer-reviewed journal article:

Stickland, R., Allen, M., Magazzini, L., Singh, K. D., Wise, R.G., Tomassini, V. (2018). Neurovascular Coupling During Visual Stimulation in Multiple Sclerosis: A MEG-fMRI Study. *Neuroscience (in press)*. Available online from 23rd March 2010.
DOI: doi.org/10.1016/j.neuroscience.2018.03.018

4.1 INTRODUCTION

There is abundant evidence showing vascular and metabolic impairments in MS and this was covered in detail in Chapter 3.2. In summary, there is evidence for reduced blood flow, less reactive blood vessels, altered levels of vasoactive compounds, and reductions in oxygen metabolism in MS. NVC, the mechanism responsible for ensuring local blood flow increases to an area with increased neural activity, is affected by many of these processes. Therefore, NVC may be altered in MS, which would likely contribute to tissue dysfunction and damage.

In this chapter, we investigated NVC in MS using two complementary non-invasive imaging modalities: MEG and fMRI. Commonly, when cortical networks are activated there is an increase in the signal power of faster oscillations, i.e. in the gamma band (Demanuele, James, & Sonuga-Barke, 2007; Jia & Kohn, 2011). Most findings show a positive correlation between changes in gamma band activity (typically >30Hz) and haemodynamic responses (Mukamel et al., 2005; Niessing et al., 2005; Zumer et al., 2010), as well as good spatial coherence between these signals (Muthukumaraswamy & Singh, 2008; Singh et al., 2002). By displaying the same reversing checkerboard stimulus at five levels of contrast, we probed neural oscillations, BOLD and CBF responses in the visual cortex, expecting them to increase monotonically with increasing contrast (Goodyear & Menon, 1998; Hall et al., 2005; Henrie & Shapley, 2005; Muthukumaraswamy & Singh, 2009; Perry, Randle, Koelewijn, Routley, & Singh, 2015). We used the positive relationship between gamma power (30 – 80Hz) and fMRI signals as an empirical measure of NVC. This design addresses the question of whether there are vascular and metabolic alterations in MS above and beyond alterations in

neural activity.

At the time of this research, no studies had reported on gamma oscillatory changes in MS. Given possible GM dysfunction and damage, we predicted a reduction in gamma power in the MS group. Based on the vascular and metabolic impairments reported in MS, we predicted that the MS group would have a reduced haemodynamic response to stimulation, and that NVC in the visual cortex would be altered.

4.2 METHODS

Participants

Patients with a diagnosis of MS (Polman et al., 2011) were recruited at the University Hospital Wales, Cardiff. Patients were treatment naïve, but eligible to start first line disease-modifying treatment and had not experienced a relapse in the last 3 months. Age and gender matched healthy controls were recruited. Written consent was obtained according to the protocol approved by Research Ethics Committee, Wales, UK.

Data Collection

All participants had a behavioural session, a MEG and a MRI scan performed on the same day, except for one control who returned on a different day for the MRI scan.

Behavioural Testing. Patients' disability was assessed using the *EDSS* score (Kurtzke, 1983). Tests from the MS Functional Composite (Cutter et al., 1999) were carried out on the patients and controls: *9 Hole Peg Test (9-HPT)* for upper limb motor function, the *Timed 25-Foot Walk (T25-FW)* for mobility and walking, and the *Paced Auditory Serial Addition Test (PASAT) 2 and 3 seconds* as a measure of sustained attention. Visual acuity was assessed, in each eye separately, with a SLOAN letter chart (Precision Vison) at 100%, 25%, 10%, 2.5%, 1.25% and 0.6% contrast, expressed as a decimal that represented viewing distance divided by the letter size (in M-units). All participants except five required corrective lenses for daily use and wore them throughout the testing sessions.

Visual paradigm during scanning. Identical stimulation parameters were used for fMRI and MEG. The visual stimulus consisted of a black and white checkerboard, polarity reversing every 250ms. Checks were squares, with a spatial frequency of 1 cycle per degree. The checkerboard was displayed on a mean luminance background,

with a small red fixation circle in the centre. The rest conditions consisted only of this background and fixation. For both scanning modalities, the entire stimulus field was 16x16° of visual angle and the stimulus was projected on screens with a 1024 x 768 resolution and 60 Hz refresh rate. The checkerboard was displayed at 5 Michelson contrast levels: 6.25%, 12.5%, 25%, 50% and 100%. Stimuli were displayed in 30 s blocks and each contrast level was presented 4 times. The rest blocks were also 30 s long and were presented 8 times. The block order was pseudorandomised across participants, but for each participant the same block order was used for both MEG and fMRI. The task lasted for 14 minutes and was repeated twice, once for each eye, with the untested eye covered with a cotton pad. We tested separate eyes because a common initial presentation of MS is optic neuritis, an acute, often unilateral, visual impairment characterised by a reduction in visual acuity and connectivity in visual pathways (Polman et al., 2011; Toosy, Mason, & Miller, 2014) The experiments were programmed in MATLAB, using the Psychophysics Toolbox extensions.

MEG data acquisition. A 275-channel CTF axial gradiometer system was used to obtain whole-head MEG recordings, sampled at 1200 Hz (0-300 Hz band-pass). An additional 29 reference channels were recorded for noise cancellation, and 3 of the 275 channels were turned off due to excessive sensor noise. Fiduciary coils were placed at fixed distances from three anatomical landmarks (nasion, left, and right pre-auricular) and the positions of the coils were monitored continuously. For co-registration, these landmarks were later identified on the subject's structural MRI and also verified with digital photographs. The MEG data were acquired continuously and epoched offline.

MRI data acquisition. MRI data were acquired on a 3T GE HDx MRI system using an eight-channel receiver head coil. A 3D T1-weighted structural scan was obtained for each participant: fast-spoiled gradient recalled echo (FSPGR): acquisition matrix = 256 x 256 x172, 1x1x1 mm voxels, TE = 2.9ms, TR = 7.8ms.

During the visual task, a PASL scan sequence was acquired with a dual GRE spiral k-space readout (TR/TE1/TE2 = 2200/3/29ms, 64 x 64 x 12 slices, voxels 3.4 x 3.4 x 7 mm, 1mm inter-slice gap, ascending order, 22cm field of view in-plane, flip angle 90°), the first echo being used to estimate CBF changes and the second echo being used for BOLD time series analysis. The proximal inversion and control for off-resonance effects (PICORE) labelling scheme was used, with a label thickness of 20cm (TI1 = 700ms, TI2 = 1600ms for most proximal slice) and 10mm gap between labelling slab and bottom slice. An adiabatic hyperbolic secant inversion pulse was used with quantitative imaging of perfusion using a single subtraction (QUIPSS II), with a 10cm saturation band

thickness (Wong, Buxton, & Frank, 1998). 191 tag-control pairs resulted in 382 volumes being acquired over the 14-minute task. Whilst the participant was at rest, two single echo multi TI PASL scans (Chappell et al., 2010) were acquired in order to estimate baseline perfusion (scan 1, TIs: 400, 500, 600, 700ms, scan 2, TIs: 1000, 1100, 1400, 1700 and 2000ms). The same PICORE labelling sequence was used as explained above, with a QUIPSS II cut of at 700ms for TIs > 700ms. A variable TR was used in order to minimise scan time. 16 tag-control pairs for each TI were acquired.

Before both PASL scans, a calibration scan was acquired in order to obtain the equilibrium magnetisation (M_0) of cerebrospinal fluid for the purposes of perfusion quantification: a single volume with the same acquisition parameters but without the ASL preparation and with an effectively infinite TR (so magnetization fully relaxed). Additionally, a minimum contrast scan was acquired to correct for received image intensity variation with the same previous parameters, except TE = 11ms, TR = 2s, and 8 interleaves.

Data analysis

Behavioural data analysis. The 9-HPT, T25-FW, PASAT-2, and PASAT-3 were all scored with the 'Brief Repeatable Battery of Neuropsychological Tests in Multiple Sclerosis' manual. Responses from 9-HPT and the T25-FW were measured in seconds to complete, and the PASAT in number of correct trials. For visual acuity, the MAR value (MAgnification Requirement – the inverse of the visual acuity score) was calculated. Values were then expressed in log(MAR) units, which indicate "visual acuity loss". A value of 0 indicates no loss so is equivalent to visual acuity at the reference standard (20/20), and an increment increase of 0.1 log(MAR) indicates one line of loss.

MEG data analysis. The analysis of MEG data was performed in MATLAB using the Fieldtrip toolbox (Oostenveld, Fries, Maris, & Schoffelen, 2011). First, data segments including large muscle artefacts were identified semi-automatically (by applying individual z-value thresholds to the z-transformed sensor time-series, band-pass filtered between 110-140 Hz) and excluded. Second, eye-movement artefacts and cardiac signals were projected out of the data using independent component analysis. The 30 s stimulus blocks were then epoched into 1 s long trials (4 reversals within one trial) and the 30 s rest blocks were also epoched into 1 s trials.

For source localisation, each participant's anatomical MRI was divided into an irregular grid by warping the individual MRI to the MNI template brain and then applying the

inverse transformation matrix to the regular MNI template grid (5mm isotropic voxel resolution), allowing source estimates at brain locations directly comparable across participants. For each grid location inside the brain, the forward model (i.e. the lead field) was calculated for a single dipole orientation by singular value decomposition, using a single-shell volume conduction model (Nolte, 2003). Source power at each location was estimated using an LCMV (linearly constrained minimum variance) beamformer (Van Veen, Van Drongelen, Yuchtman, & Suzuki, 1997). The weights were computed using a covariance matrix calculated after band-pass filtering the data between 30 and 80 Hz, combining trials from all conditions. For each participant, the voxel of greatest increase in gamma power (30-80 Hz) was located within either the Calcarine sulcus (primary visual cortex) or two adjacent regions (cuneus and lingual gyrus), found by contrasting the 1 s stimulus epochs with the 1 s baseline epochs (as a percentage change from baseline). Anatomical masks were created using the AAL atlas (Tzourio-Mazoyer et al., 2002). At this peak location, the source-level time-series were reconstructed by multiplying the sensor-level data by the beamformer weights. Trials were represented in the time-frequency domain by calculating the amplitude envelope of analytic signal obtained with the Hilbert transform. Stimulus-induced peak gamma power was extracted, separately for each visual contrast condition. This analysis was performed separately for the left and right eye acquisitions. The analysis steps are summarised in Figure 4-1.

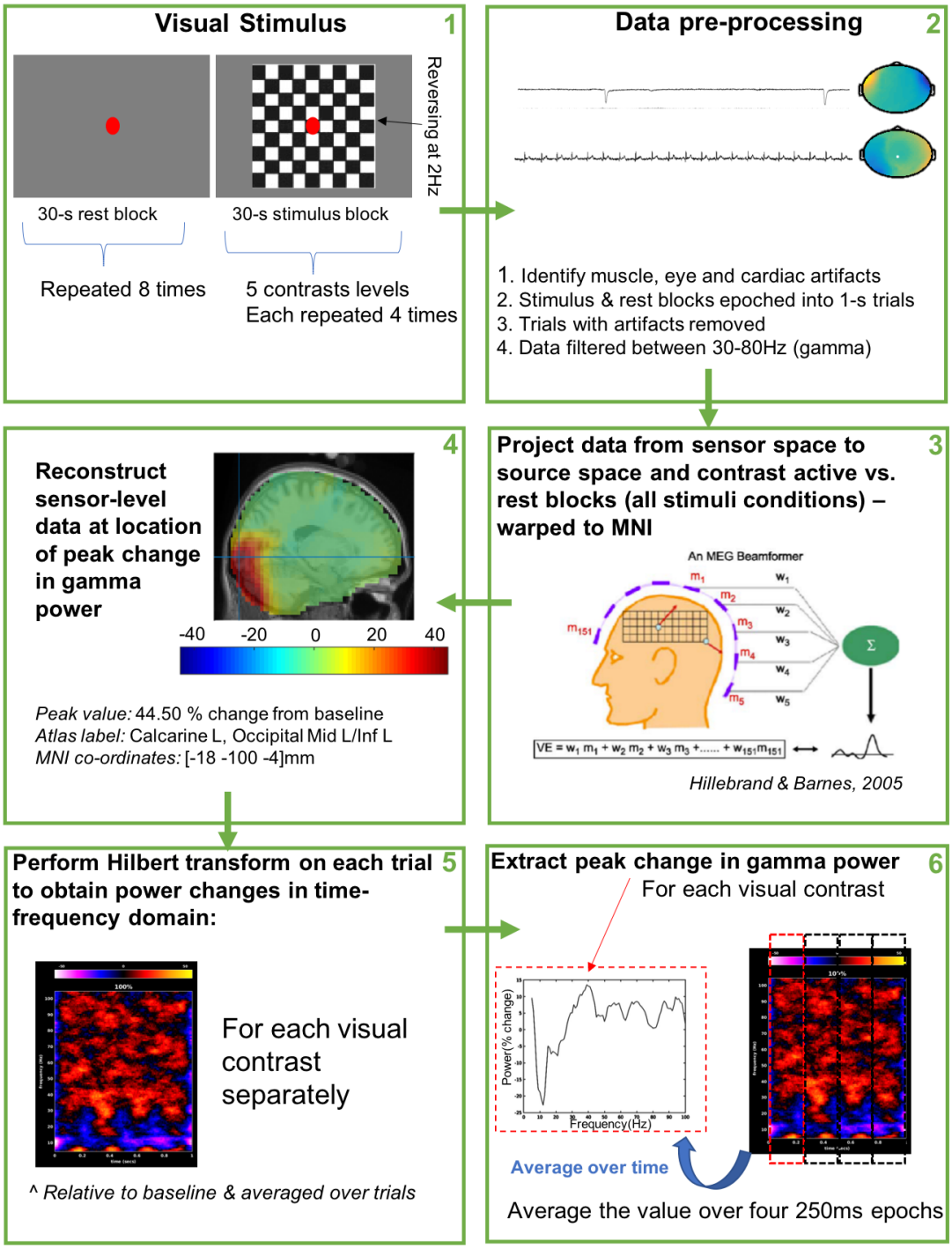

Figure 4-1. Summary of the analysis steps used in order to characterise the peak gamma power response, for each participant.

To assess potential alterations in transmission to the visual cortex, latencies of VEFs were characterised, for the left and right eyes separately, and across all five contrast conditions together. The trials were first re-epoched around the time of reversal (0 s), with the baseline period defined as -0.04 to 0 s, and the stimulus period as 0 to 0.21 s. The data were then low-pass filtered at 15 Hz and baseline corrected. The VEFs were first investigated at the sensor level (mirroring methods used clinically for VEPs) by

averaging over trials for five posterior occipital sensors. The VEFs were subsequently also characterized in source space (more comparable with the analysis of the gamma power changes) by multiplying the pre-processed sensor level data with the beamformer weights for the location found to be the peak gamma response to the checkerboard stimuli. For both types of analysis, the latency of the peak amplitude between 0 and 0.21 s was then extracted for each participant.

MRI data analysis

Lesion filling. Lesion filling was carried out with the FSL function *lesion_filling*, following the protocol by Battaglini, Jenkinson, & De Stefano (2012), to improve registration, segmentation and volumetric measures of brain tissue. In brief, a lesion mask was manually created by drawing around any visible lesions on the patient's T1-weighted image. At least one lesion was visible for 11 out of the 14 patients. For these 11 patients, the lesion mask, their T1-weighted image, and a WM mask (FAST segmentation) was used in order to "fill" the lesion area in the T1-weighted image with intensities that are similar to those in the non-lesioned neighbourhood (WM only).

Tissue volumes. Brain tissue volume, normalised for subject head size, was estimated with SIENAX in FSL (Smith, De Stefano, Jenkinson, & Matthews, 2001; Smith et al., 2002). For patients with visible lesions, their T1-weighted images with filled lesions where inputted. Brain and skull images were extracted from the single whole-head input data. The brain image was then affine-registered to MNI152 space, using the skull image to determine the registration scaling, and to obtain the volumetric scaling factor. Next, tissue-type segmentation with PVE was carried out in order to calculate total volume of brain tissue (and volume of GM and WM separately), normalised for head size using the volumetric scaling factor.

Regional GM tissue volumes from the visual cortex were calculated for each subject. These visual ROIs were defined functionally, based on significant group activation to the visual checkerboard stimulus (explained below). The group visual ROI for the left and right eye stimulation were transformed from standard space to T1 subject space and multiplied with the GM partial volume estimate (PVE) image to give visual GM ROIs for each subject. Estimates of volume within these ROI were then normalised with the volumetric scaling factor outputted from the SIENAX analysis.

BOLD and CBF response to the visual checkerboard stimulus. The BOLD signal was isolated by surround averaging the second echo to remove the tag-control signal.

Registration of functional data to individual T1 structural data (linear, 6 degrees of freedom - DOF) and then to MNI standard space (linear, 12 DOF) was carried out using FSL FLIRT. Motion correction of time series data was performed using MCFLIRT, non-brain removal using BET spatial smoothing using a Gaussian kernel of FWHM 5mm, and a high-pass temporal filter applied with a cut off of 90s. Using FEAT, perfusion time courses were modelled from the first echo data with the inclusion of regressors explicitly describing the tag-control signal differences. Five stimulus conditions, and an average across the conditions, were specified as six output contrasts relative to the rest conditions.

A higher-level analysis was performed with FEAT using a mixed effects model (FLAME 1+2) to model the effect of group membership. Z statistic images were thresholded using clusters determined by Z>2.3 and a (corrected) cluster significance threshold of p = 0.05. A group region of interest (ROI) was generated from the output of this group analyses. The group ROI was determined as common significant voxels in the BOLD and CBF thresholded z-statistic images (for the contrast averaged across conditions and groups). After binarising this group ROI and transforming to subject space for each participant, a percentage signal increase in BOLD and percentage increase in CBF was calculated for each participant within that region. This higher-level analysis and group ROI creation was done separately for the left and right eye acquisitions. The final BOLD and CBF values were then averaged across eyes for each participant.

Baseline perfusion. As patients with MS are reported to be hypoperfused at rest a measure of resting CBF in ml/per/100g per min was quantified to establish if there were any differences in baseline perfusion. Baseline perfusion was estimated following a protocol described by (Warnert et al., 2014), using in-house scripts that used AFNI software (Analysis of Functional NeuroImages) and FSL-BASIL (Chappell, Groves, Whitcher, & Woolrich, 2009). In brief, ASL scans were first motion corrected using AFNI. All TIs (from both scans) were merged into one 4D dataset which included a single mean difference image per TI, averaged over the 16 volumes. The M_0 image was registered to this perfusion series and a mask of the lateral ventricles was created, and this was used in the subsequent model to calculate the equilibrium magnetization of blood (M_0). A two-compartment kinetic model was fitted to the multi-TI data to calculate baseline perfusion, in native space, in ml/100g/min along with mean arrival time (Chappell et al., 2010). Individual subject GM masks (from partial-volume tissue-segmentation, see *Tissue Volumes* above) were transformed to native space in order to estimate the baseline blood flow over GM. The standard-space ROI used in the checkerboard analysis was also transformed to native space, and the baseline

perfusion in this region was used to convert fractional estimates of task-induced change in blood flow to changes in absolute blood flow units.

Characterising Neurovascular Coupling

We characterised NVC by fitting a linear model that reflected the relationship between the electrophysiological response and the haemodynamic response to the visual checkerboard stimulus. Three coupling models were fitted for each subject: the relationship between gamma oscillations and the relative BOLD signal, the relative CBF signal, and the quantified CBF signal. We used BOLD signal changes, dependent on both metabolism and flow, as this has been the focus of most previous studies relating MEG and fMRI signals. We also quantified this CBF signal change in ml/100g/min, due to evidence showing baseline CBF can affect BOLD and CBF responses to stimulus (e.g. Cohen, Ugurbil, & Kim, 2002), and that absolute changes in CBF may more closely represent the neuronal response to a stimulus (Whittaker, Driver, Bright, & Murphy, 2016).

For each subject, there were 10 data points: one point for each visual contrast and for each eye. We chose not to average across eyes in order to retain useful variance in the responses between eyes, therefore helping us to better model the relationship between MEG and fMRI signals. The gradient of the line, extracted for each participant, was taken to be our coupling measure, indicating the strength of the relationship between these signals.

Statistical analysis of group differences and stimulus responses

Statistical analysis was carried out using IBM SPSS Statistics (Version 20) and R software packages (R Core Team, 2017). Independent t-tests assessed differences between MS patients and controls on age, behavioural measures, tissue volumes and baseline signals. Mann-Whitney U-tests were used to assess differences between MS patients and controls on the visual acuity scores, for each contrast level tested. Mixed ANOVAs were used to assess the effect of group membership and eye on the latency of the peak (of the VEFs), and the effect of group membership and contrast level on peak gamma power, BOLD and CBF metrics. For the NVC measure, gradients and intercepts were extracted from the linear model that was fitted separately for each person, and Mann-Whitney U-tests were used to test the differences in medians between MS patients and controls.

For the Mann-Whitney U-tests, an exact sampling distribution was used for *U*. For each comparison, the shape of the distribution was similar between groups, as assessed by visual inspection, so medians were compared. GG in the results refers to the Greenhouse-Geisser correction used when the assumption of homogeneity of variances is violated. In these statistical analyses, all hypothesis testing was two-tailed. The family wise error rate was controlled for dependent tests with the Holm-Bonferroni correction, a popular variant of the Bonferroni correction that is less conservative (Holm, 1979).

4.3 RESULTS

Demographics and Clinical Profile

The demographic and clinical characteristics of the 14 patients and 10 healthy controls are reported in Table 4-1. One patient did not complete the T25-FW. Patients were significantly slower than controls when completing the 9-HPT task and showed a trend towards being significantly slower in the T25-FW task.

	Patients (14)	**Controls (10)**	**P-value**
Age	43.46 ± 3.50	42.40 ± 3.73	0.69
Sex (M/F)	5/9	1/9	0.34
Disease Duration (Years)	7.31 ± 2.06	-	-
EDSS (Median, Range)	3.0, 0 - 4.5	-	-
History of Optic Neuritis	6/14	-	-
9-HPT (seconds)	25.65 ± 0.82	22.41 ± 0.95	0.02
T25-FW (seconds)	13.08 ± 1.58	9.63 ± 0.19	0.05
PASAT-3s (no. correct responses)	46.54 ± 2.57	48.10 ± 3.37	0.71
PASAT-2s (no. correct responses)	31.92 ± 1.86	36.20 ± 2.95	0.21
Normalised Brain Volume (mm^3) (lesion-filled images for patients)	1,492,761.57 ± 26644.57	1,523,284.20 ± 25006.90	0.43

Table 4-1. Demographic and clinical characteristics. Values are Mean ± SEM. 9-HPT is a mean of two trails for each hand. T25-FW is a mean of two trials. P-values from two-tailed unpaired t-tests (except for Fisher's Exact Test used to test sex differences).

Visual acuity and VEFs

One patient was not included in the right eye group analysis due to blindness of the right eye. The log(MAR) values were extremely non-normal in their distribution across eyes and groups, and different cells of the design (group vs. eye vs. contrast level) had different variances. Therefore, as the group difference was the focus, separate Mann-Whitney U tests were used to test the group difference in the visual acuity at each contrast level, and the p values were corrected for multiple comparisons with the Holm-Bonferroni correction. Group differences were assessed at each contrast (100%, 25%, 10%, 5%, 2.5%, 1.25%, 0.6%) and for each eye (left, right). There were no significant group differences between MS patients and controls in visual acuity scores (Table 4-2). We investigated the effect of group (controls, patient) and eye (left, right) on the latency of the peak amplitudes of the VEFs, for the sensor and source space analyses. The data were normally distributed, with no outliers. Results reported here are Mean $\pm$ Standard Error of the Mean(SEM), expressed in milliseconds. For latencies calculated in sensor space, MS patients (146 ± 9) and controls (147 ± 10) did not have significantly different latencies ($F(1,21) = 0.001$, $p = 0.98$), and the left eye (156 ± 9) and the right eye (137 ± 8) also did not differ ($F(1,21) = 3.04$, $p = 0.10$), for both groups. The results were similar for latencies calculated in source space: there was no main effect of group (MS patients: 137 ± 5, controls: 142 ± 6, $F(1,21) = 0.38$, $p = 0.55$) and no main effect of eye (left: 145 ± 6, right: 134 ± 6, $F(1,21) = 1.83$, $p = 0.19$). There was no significant interaction between group and eye for the latencies calculated in sensor space, ($F(1,21) = 0.001$, $p = 0.98$), or source space ($F(1,21) = 0.16$, $p = 0.70$).

Eye	Visual Contrast (%)	MEDIAN		Mann-Whitney U	P value	Significant if less than:
		Controls	Patients			
Left	**100**	0.10	0.00	52.5	0.63	0.016
	25	0.10	0.10	62	0.92	0.05
	10	0.20	0.20	69	0.58	0.01
	5	0.40	0.49	72.5	0.38	0.006
	2.50	0.85	1.00	80	0.20	0.004
	1.25	1.65	2.00	73	0.42	0.006
	0.60	2.00	2.00	69	0.58	0.01
Right	**100**	0.00	0.05	79.5	0.20	0.004
	25	0.10	0.10	79	0.23	0.005
	10	0.20	0.25	71	0.50	0.007
	5	0.40	0.49	75	0.35	0.005
	2.50	0.80	1.30	82.5	0.14	0.004
	1.25	2.00	2.00	71	0.47	0.007
	0.60	2.00	2.00	66	0.72	0.025

Table 4-2. Median log(MAR) visual acuity scores, for each contrast level and eye. Higher scores indicate greater visual acuity loss. Mann-Whitney U-tests, with holm-bonferroni correction (last row shows the threshold at which the p-value is significant.

MEG and fMRI responses to reversing checkerboard stimuli

There were no significant differences in GM volume, baseline CBF or baseline gamma power between MS patients and controls, across the whole brain and within the regions of interest used to characterise the visual response to the checkerboard stimulus (Table 4-3).

	Group	N	Mean	Std. Dev	P value
GM Volume (Total) *(mm^3)*	Controls	10	788328.70	55506.80	0.29 [a]
	Patients	14	755677.88	66346.84	
GM Volume (L) *(mm^3)*	Controls	10	5514.29	673.20	1.00 [c]
	Patients	14	5515.19	768.02	
GM Volume (R) *(mm^3)*	Controls	10	4154.44	530.05	0.90 [b]
	Patients	14	4184.46	585.56	
Baseline CBF GM *ml/100g/min*	Controls	10	36.91	10.17	0.90 [c]
	Patients	13	37.34	6.32	
Baseline CBF GM (L ROI) *ml/100g/min*	Controls	9	57.73	21.18	0.45 [a]
	Patients	13	51.96	15.16	
Baseline CBF GM (R ROI) *ml/100g/min*	Controls	9	57.30	21.00	0.48 [b]
	Patients	13	51.70	16.81	
Baseline Gamma (L ROI) **10 $^{-14}$ Tesla*	Controls	10	6.10	0.83	0.10 [b]
	Patients	13	7.07	1.63	
Baseline Gamma (R ROI) **10 $^{-14}$ Tesla*	Controls	10	6.80	1.19	0.94 [c]
	Patients	13	6.80	1.29	

L refers to left and **R** refers to right: the ROIs refer to the location used to extract the stimulus response to the checkerboard. Gamma power is a mean of the power at each frequency between 30-80 Hz, averaged over the 30-s rest block.

Table 4-3. Tissue volumes, and baseline signals compared between groups. P-values for GM Volume (3), Baseline CBF (3) and Baseline Gamma Power (2) were corrected separately with Holm-Bonferroni: a is significant at p<0.017, b at p<0.05, c at p<0.025.

Spatial comparison of MEG and fMRI results

One control's fMRI data was not useable due to a corrupted image file. Figure 4-2 shows the location of the ROI used in the BOLD and CBF analyses, for all participants, overlaid onto the primary visual cortex. Included in Figure 4-2 are the locations of the peak gamma responses for each patient and control, where the time-frequency analysis was performed. Figure 4-3 explores the whole-brain MEG source localisation plots for

each group. Figure 4-4 shows the whole-brain CBF activity for each group, and Figure 4-5 the whole-brain BOLD activity. Patients showed significantly higher CBF activity in a small cluster located in the intracalcarine and supracalcarine cortex, as well as the cuneus. Patients showed significantly higher BOLD activity in lingual gyrus, intracalcarine cortex, pre-cuneus and cuneus. These were localised using the Harvard-Oxford Cortical Structural Atlas.

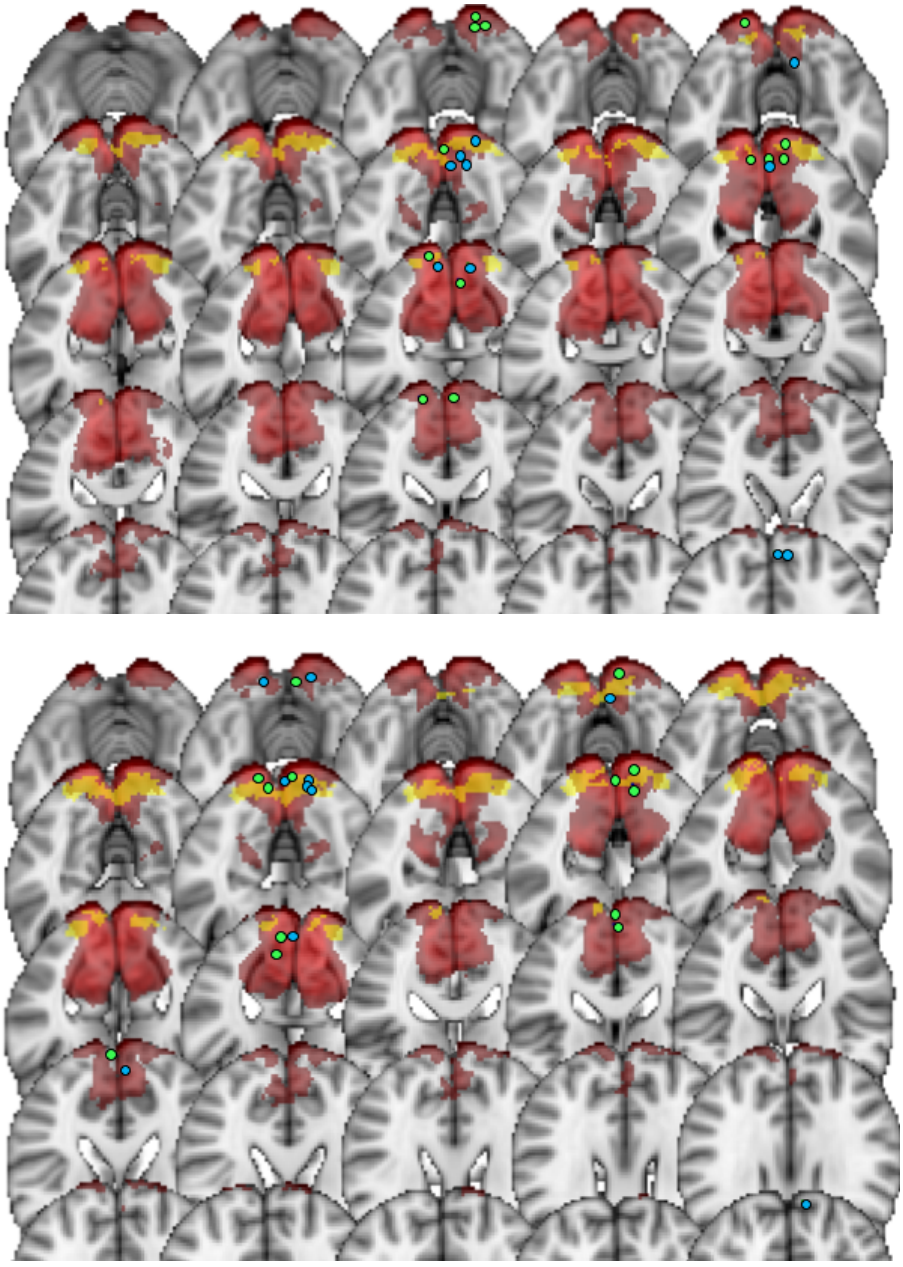

Figure 4-2. BOLD and CBF responses extracted over a group ROI (yellow), overlaid onto V1 (red). Top plot = left eye, bottom plot = right. Dots indicate location of the peak gamma response (% change) for each individual (blue = 10 controls, green = 13 patients).

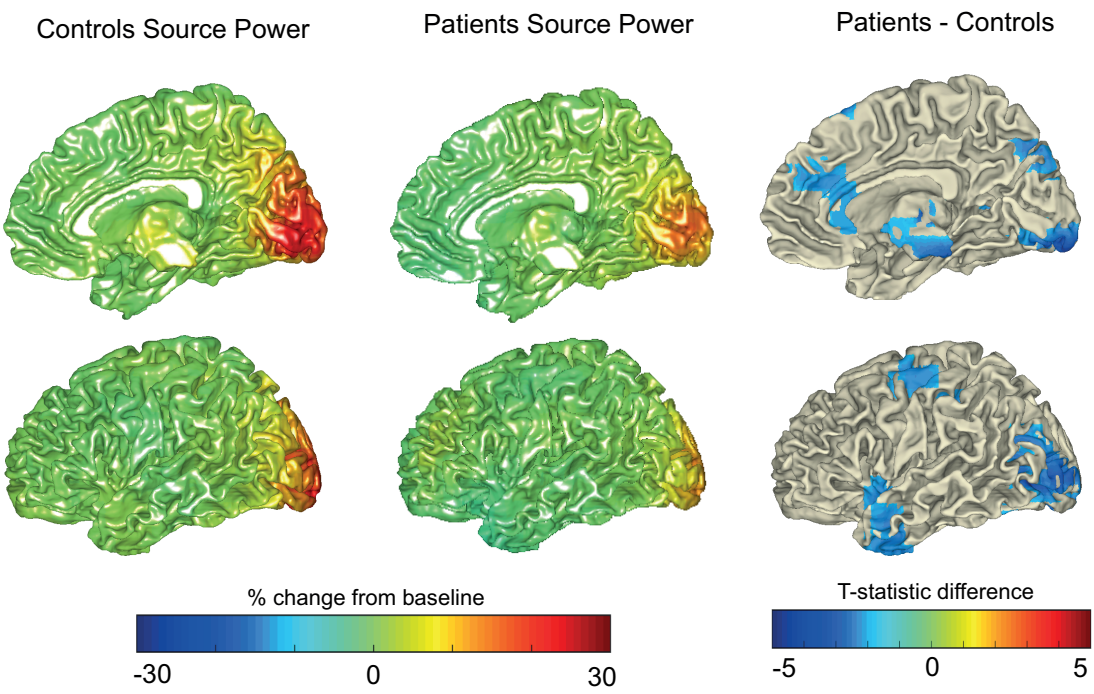

Figure 4-3. Beamformer contrast images (30-80 Hz), projected onto a template brain. Negative t-stats indicate lower amplitude for patients compared to controls. T-values are plotted here at the uncorrected level. Data averaged over both eyes.

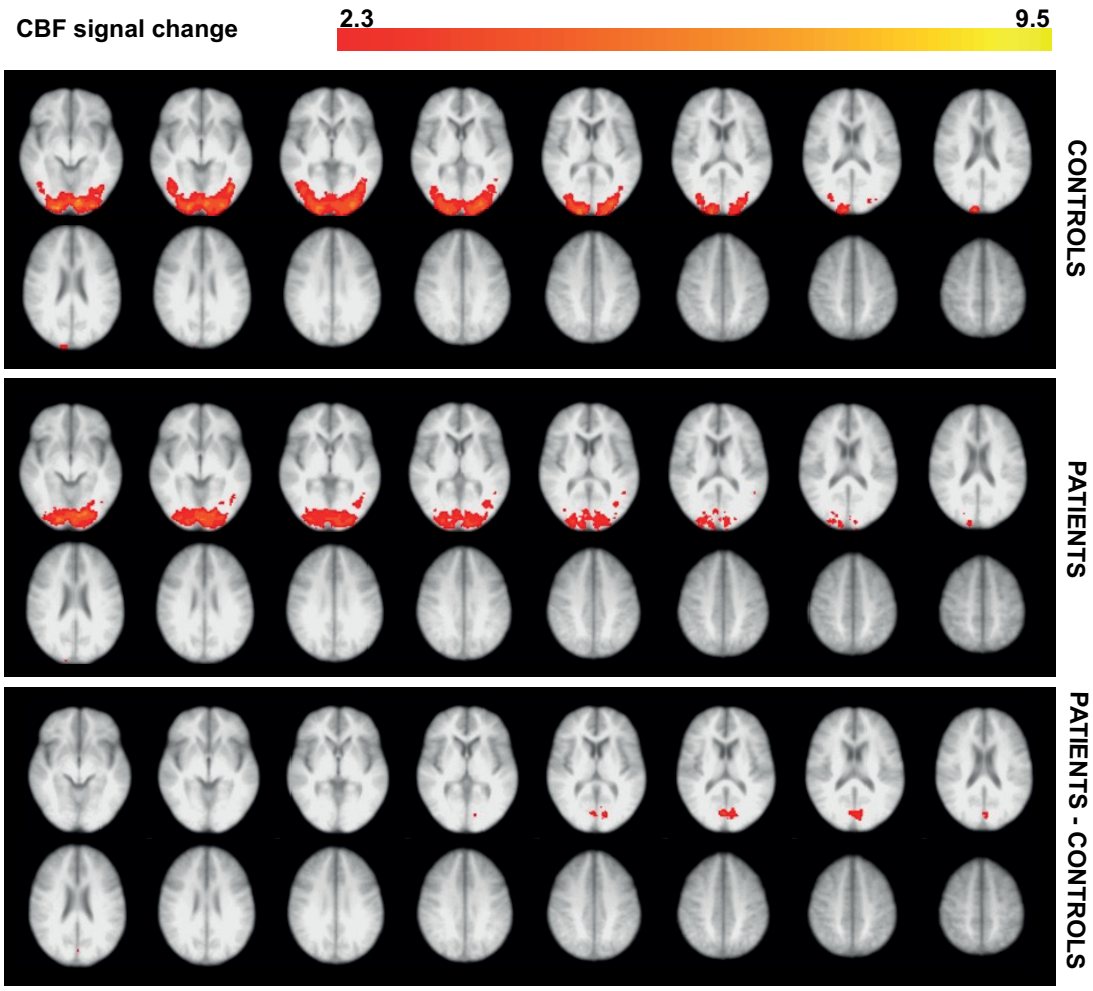

Figure 4-4. Significant CBF voxels at the group level in response to the checkerboard. Data is averaged over both eyes. Significant activity shown is the average activity across all visual contrasts. Voxel clusters thresholded at Z>2.3 and p<0.05. Right side of the image corresponds to the left side of the brain. No voxels showing greater activity for the control group compared to the patients.

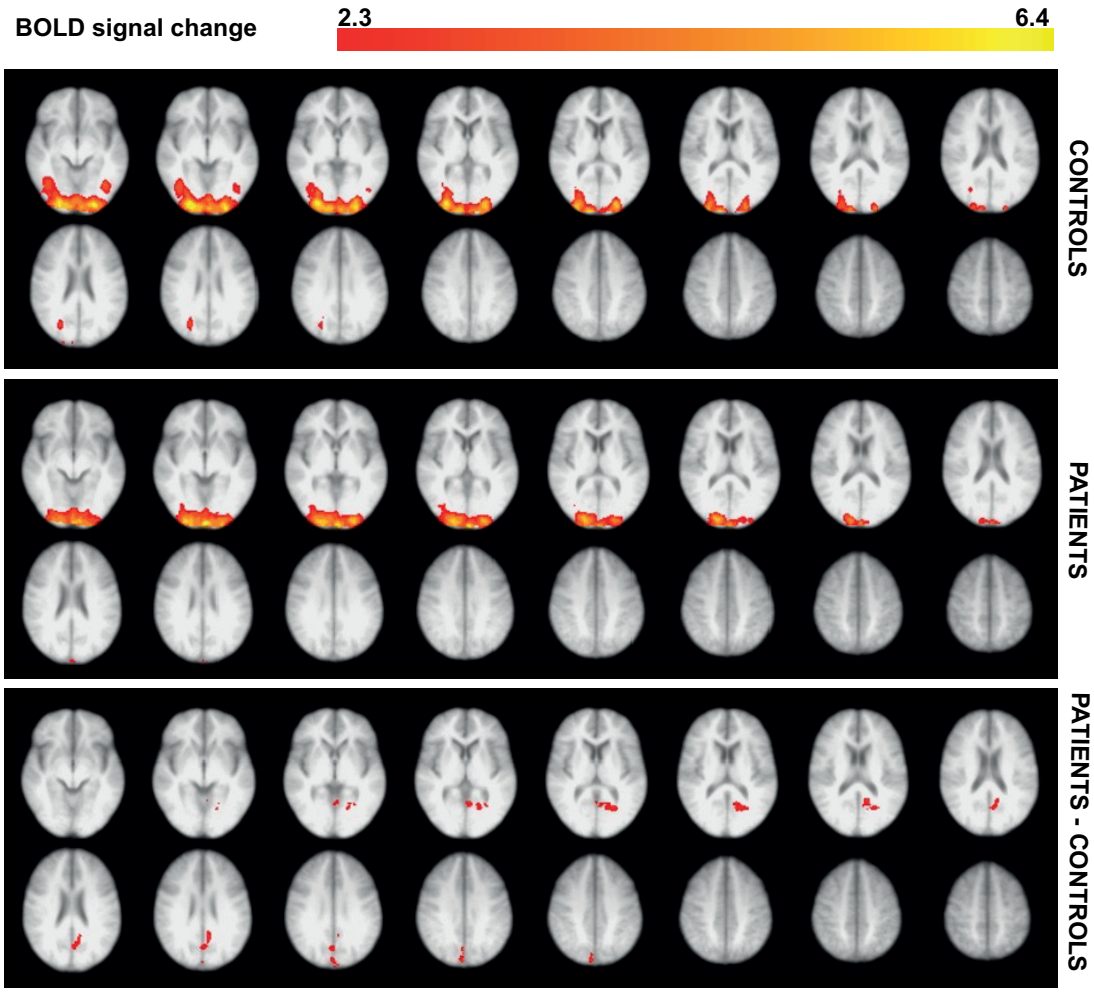

Figure 4-5. Significant BOLD voxels at the group level in response to the checkerboard. Data is averaged over both eyes. Significant activity shown is the average activity across all visual contrasts. Voxel clusters thresholded at Z>2.3 and p<0.05. Right side of the image corresponds to the left side of the brain. No voxels showing greater activity for the control group compared to the patients

Effect of group and stimuli contrast on BOLD, CBF and gamma power change

Given the absence of significant differences in the visual acuity scores and latency of the peak amplitudes between groups, the effect of group and stimuli contrast was statistically tested on data averaged across the two eyes. Figure 4-6 displays the effect of group and stimuli contrast on BOLD, CBF and peak gamma power signal changes.

BOLD, CBF quantified and CBF percent signals increased significantly as stimuli contrast increased: *F (1.75,33.17) = 46.59, p < 0.001 GG; F (4,76) = 35.41, p<0.001*; *F (4,76) = 35.63, p<0.001,* respectively. MS patients had significantly lower signal responses, compare with controls, for BOLD and CBF quantified signals, but this was not significant for CBF percent: *F (1,19) = 7.97, p = 0.01*; *F (1,19) = 6.62, p = 0.02*; *F (1,19) = 2.76, p = 0.11*, respectively. All pairwise comparisons between contrast levels were significant. There was no significant interaction between the effect of contrast and group on BOLD changes (*F (1.75, 33.17) = 0.86, p = 0.42, GG*) CBF quantified changes (*F (4, 76) = 1.25, p = 0.30)*, or CBF percent changes (*F (4, 76) = 0.70, p = 0.59*).

For the MEG results, there was a significant interaction between the effect of contrast and group on the peak gamma power changes (*F (1.50,31.54) = 7.87, p = 0.01, GG*). Therefore, simple main effects were investigated. There was no significant group difference at the 6.25% or 12.5% contrast levels (*F (1,21) = 1.13, p = 0.30*; *F (1,21) = 1.99, p = 0.17*, respectively), but MS patients showed significantly lower peak gamma power changes at 25%, 50%, and 100% (*F (1,21) = 6.28, p = 0.02*; *F (1,21) = 12.13, p < 0.01*; *F (1,21) = 10.71, p < 0.01,* respectively). Peak gamma power signals increased significantly as stimuli contrast increased, for both the control group (*F (1.59,14.29) = 46.03, p<0.001, GG*) and the patient group (*F (1.12, 15.99) = 22.46, p < 0.001*, *GG*). All pairwise comparisons between contrast levels were significant, except between 6.25% and 12.5%, and 12.5% and 25% in the patient group.

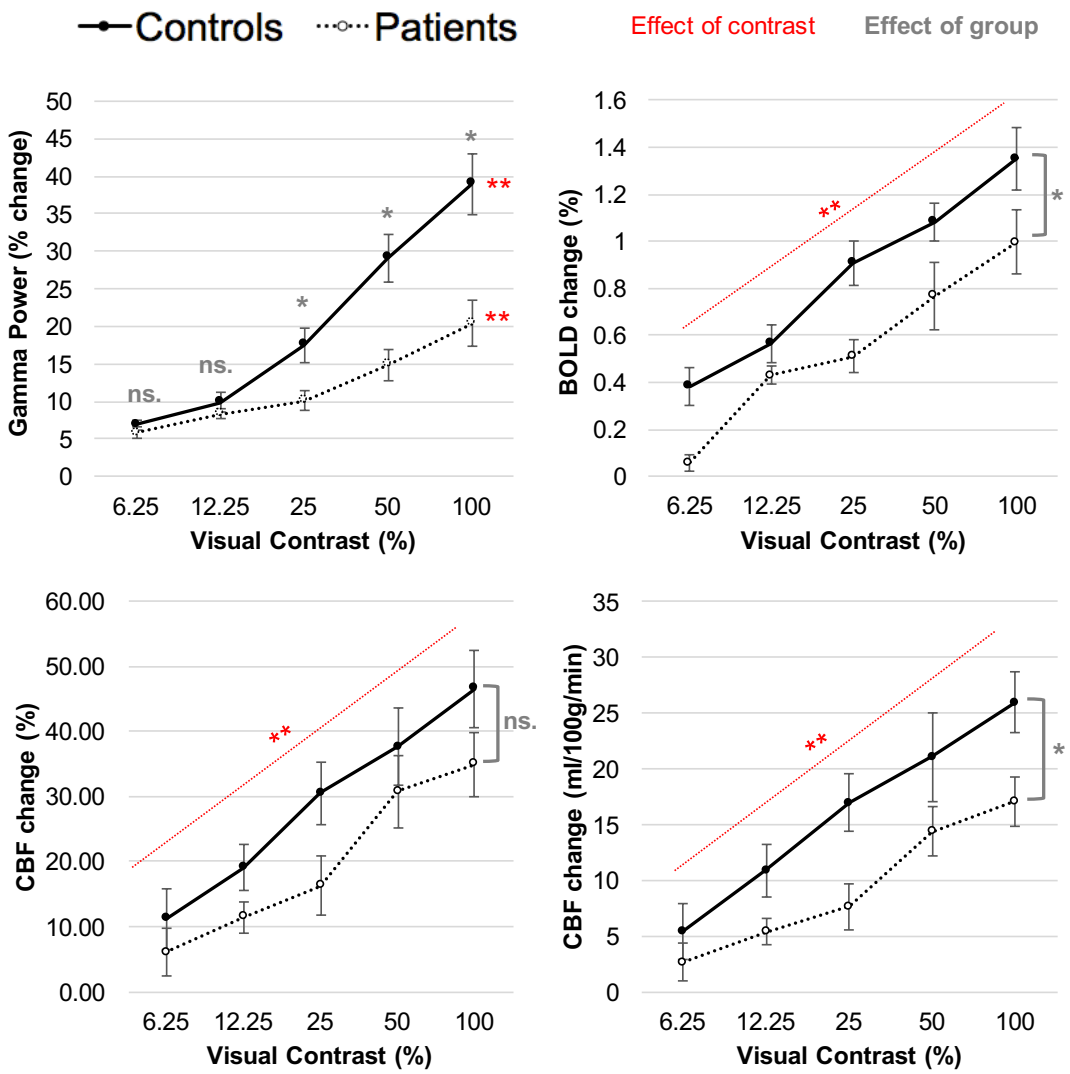

For BOLD, CBF and CBF quantified the effect of group was not significantly different across contrast level, so the * p-value labels refer to the main effect. For Gamma, there was an interaction between group and contrast level so the * p values refer to the simple main effects.

*Figure 4-6. Effect of group and visual contrast on peak gamma power, BOLD, CBF (percentage change) and CBF quantified (ml/100g/min change). Values are Mean ± SEM. *p<0.05, **p<0.001. Pairwise comparisons significant at p<0.05, with Holm-Bonferroni correction.*

Neurovascular coupling in MS patients and controls

The relationship between peak gamma power and BOLD and CBF signals was compared between groups. Figure 4-7 visually displays these coupling relationships, and Table 4-4 shows the statistical testing between groups.

Figure 4-7A displays the coupling relationships using the median values across each group. At this group averaged level, there is a good fit between the MEG and fMRI signals. The MS patients appear to have higher gradients on average (i.e. for the same peak gamma power change, higher BOLD and CBF change), as well as lower intercepts on average. Figure 4-7B shows what the coupling relationship looks like for every participant separately, showing that the patient group displays more variability in the coupling between peak gamma power and BOLD change compared to the controls. CBF coupling results for each participant (not shown) showed similar trends.

To statistically test these coupling differences, the median gradients and intercepts were extracted for each person and compared between groups. In general, higher gradients and lower intercepts are seen in the patient group, but no significant differences are found between groups (Table 4-4**).**

Outcome measure		**MEDIAN**		**Mann-Whitney U**	**P value**	**Significant if less than:**
		Controls	Patients			
Gradient	**BOLD**	0.03	0.04	66	0.42	0.050
	CBF	1.03	1.30	65	0.46	0.050
	CBF(q)	0.67	0.58	58	0.81	0.050
Intercept	**BOLD**	0.31	0.04	24	0.03	0.025
	CBF	5.08	1.97	38	0.28	0.025
	CBF(q)	3.91	1.16	35	0.19	0.025

Table 4-4. Median gradients and intercepts compared between groups, using peak gamma power to predict BOLD and CBF. q refers to quantified. Mann-Whitney U-tests performed; p values corrected with Holm-Bonferroni, for two dependent tests (gradient and intercepts).

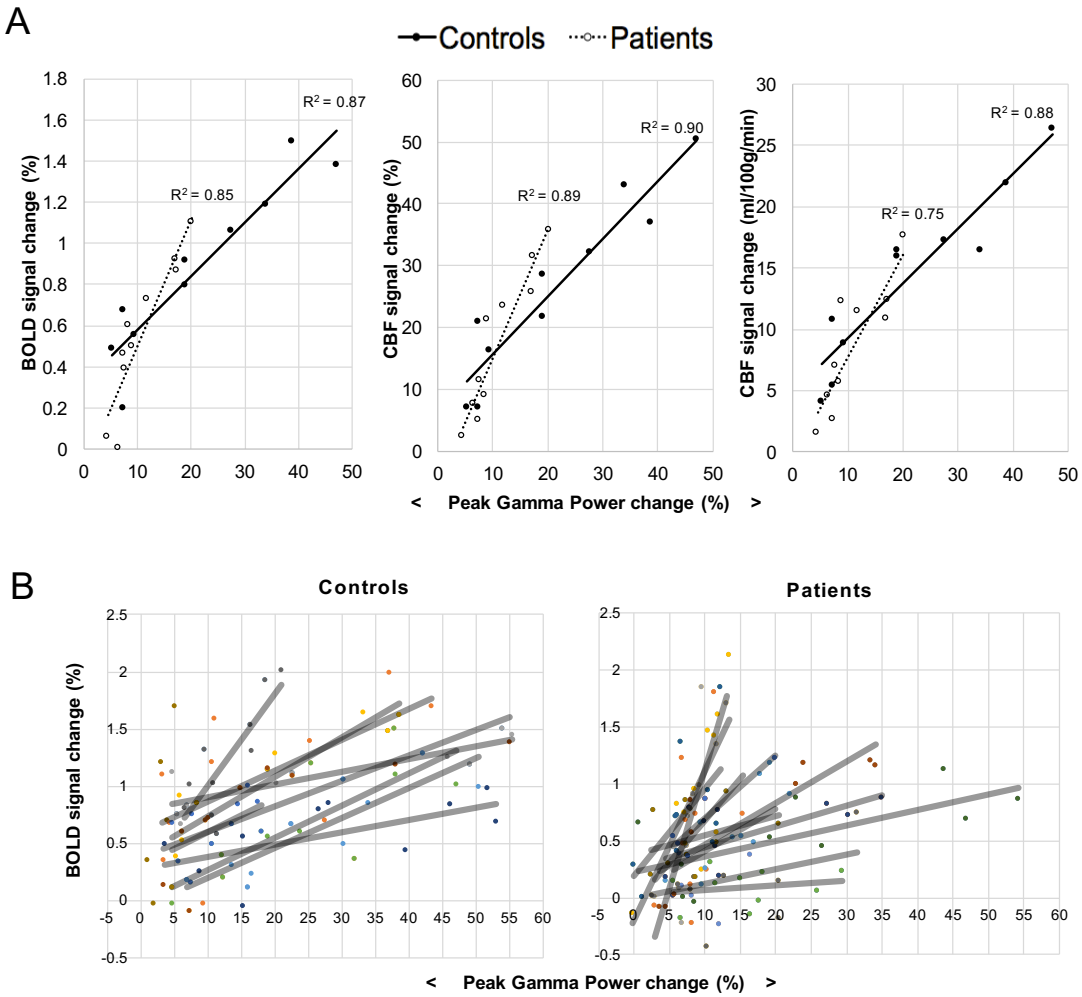

Figure 4-7. (A) relationship between gamma power and BOLD/CBF change in response to the checkerboard, using group median values. Each point represents a different contrast level for each eye. (B) BOLD relationship shown for each control (n=9) and patient (n=12). Colours represent each participant and the black line shows the linear fit.

4.4 DISCUSSION

We investigated the neuronal and haemodynamic responses to a reversing checkerboard visual stimulus in relapsing-remitting MS, observing smaller peak gamma power changes and BOLD and CBF responses. While the range of electrophysiological and haemodynamic responses were altered in MS, we found no significant group difference in the coupling relationship between these responses, indicating that NVC may remain intact in MS. Whilst the lack of significant differences between groups may be due to the limited statistical power of this study, due to relatively small samples sizes, it may also reflect the complexity and heterogeneity of MS as a disease, and NVC as a biological process.

Source localisation of gamma oscillations, BOLD and CBF

The group ROI used to extract the BOLD and CBF signals for all participants was located clearly in the primary visual cortex (Figure 4-4). For characterising the gamma response, we searched for the peak gamma power change within the calcarine sulcus and two adjacent regions: the cuneus and lingual gyrus. This was because previous studies suggest visual gamma, in response to this type of stimulus, to be located in the primary visual cortex. This method also ensured that the area was comparable to the fMRI source whilst allowing for some error in MEG signal localisation. Although we took a ROI approach to characterising the peak gamma, CBF and BOLD responses, we also visualised these responses across the whole brain. At the whole-brain group-averaged level, we saw a reduction in gamma power responses in visual areas for the MS patients (Figure 4-3). A reduction was also seen in sub-cortical and temporal regions; this possibly indicates activity differences more extensively along visual processing pathways, yet this was not further explored. For the CBF and BOLD group-average plots, a similar pattern of activity in the early visual cortex was seen for both groups (Figure 4-4 and Figure 4-5). There were voxels within the intra/supra-calcarine cortex and cuneus (for CBF) and the lingual gyrus, intracalcarine cortex, and cuneus (for BOLD) showing significantly greater activity in the MS group compared to the controls. A possible explanation of this result is compensatory functional reorganization of the cortex in MS patients (Tomassini et al., 2012; Werring et al., 2000).

Reduction of peak visual gamma, BOLD and CBF responses in MS

Here we used the oscillatory activity in the gamma band (30-80 Hz) to characterise the neuronal response. Broadly, the gamma rhythm is theorised to reflect the balance

between excitatory and inhibitory signalling; networks of fast-spiking, parvalbumin-expressing, GABAergic interneurons act on pyramidal cells to bring about synchronous inhibitory post synaptic potentials (Bartos, Vida, & Jonas, 2007; Buzsáki & Wang, 2012; Cardin et al., 2009). A large body of research shows an increase in gamma power when functional networks are engaged, widely across the brain and for many different processes e.g. (Jensen, Kaiser, & Lachaux, 2007; Jia & Kohn, 2011; Nyhus & Curran, 2010). Specifically, gamma oscillations are thought to have a functional role in attention, perception and mediation of information transfer across different cortical areas (Fries, 2009).

Disruptions in gamma oscillations have been reported in many brain disorders (Uhlhaas & Singer, 2006). In MS, task-induced changes have remained largely unexplored until recently (Arpin et al., 2017; Barratt et al., 2017b). Barret et al (2017) reported significantly reduced visual gamma amplitudes in a similar MS population, the only other study, to our knowledge, that has investigated task-induced gamma oscillatory changes in MS. There is evidence that parvalbumin-expressing GABAergic interneurons, thought to contribute to gamma oscillations, are reduced in normal appearing GM of the motor cortex in MS (Clements, McDonough, & Freeman, 2008), and that secondary progressive MS patients have significantly lower GABA levels in the hippocampus and sensorimotor cortex (Cawley et al., 2015).

GABA concentration has also been related to visual gamma oscillations and BOLD signals in healthy participants in the visual cortex (Magazzini et al., 2016; Muthukumaraswamy & Singh, 2009). Therefore, a possible interpretation of our results is that these gamma power reductions in the visual cortex of MS patients could be an indicator of early GM dysfunction, mediated by GABAergic changes. However, more conclusive empirical evidence is needed to fully understand the role of gamma oscillations in neural communication, and their relationship with GABA, therefore making any interpretation of their alteration in MS a tentative one at this stage. Furthermore, we did not see a significant reduction in whole brain or visual GM volumes in the MS group when compared to the healthy control group. A lack of volumetric differences may simply result from the small sample size, but a contributing factor may also be ongoing inflammation as these patients were treatment naïve. The contribution of inflammation to an increase in brain volume (and thus to an apparent normalisation despite MS pathology) has been indirectly demonstrated by showing that the onset of DMT leads to the occurrence of brain volume reduction, a phenomenon called “pseudo-atrophy” (Gasperini et al., 2002; Vidal-Jordana et al., 2016; Zivadinov et al., 2008).

Although they presented with preserved visual acuity and latency of VEFs, the MS patients showed significant haemodynamic alterations, in the form of reduced BOLD and CBF responses to the visual checkerboard, in the primary visual cortex. In the context of largely preserved NVC, the reduced haemodynamic response is consistent with the reduced electrophysiological response. Changes in the BOLD response to visuomotor tasks have been previously demonstrated, showing that inflammation and WM structural damage play a role in altering haemodynamic responses in MS (Hubbard et al., 2016; Tomassini et al., 2016). Our alterations in BOLD and CBF responses support these findings, as well as altered responses to visual stimuli at different contrasts (Faro et al., 2002). Uzuner & Uzuner (2016), also using a 2Hz reversing checkerboard stimulus, found blood flow velocities in the posterior cerebral arteries to be higher in a large MS patient group in the state of relapse. Although a different measure, this is in contrast to the reduced blood flow responses we reported in this MS group, but highlights the potential impact of testing MS participants at different states of the disease.

No significant alteration of neurovascular coupling in MS

The relationship between the peak gamma power change and the BOLD/CBF response (using the variance given by the visual contrast manipulation) was our empirical measure of NVC. While this is intuitive, assuming that the blood flow response only reflects a coupling with gamma oscillatory activity is simplistic. The amplitude of gamma oscillations can be modulated by the phase of slower oscillations, termed cross-frequency phase-amplitude coupling (Buzsáki & Wang, 2012), and an increase in gamma power is often accompanied by a decrease in power of lower frequencies. BOLD and gamma oscillations are also known to be decoupled in some circumstances. For example, in the visual cortex, gamma amplitudes are altered with changes in the spatial frequency and colour of the stimuli, but BOLD signals are not (Muthukumaraswamy & Singh, 2008, 2009; Swettenham et al., 2013). Despite these limitations, and although the temporal relationship of MEG and fMRI signals is complex, they are generally thought to originate from the same electrophysiological source and have reasonable spatial overlap. Gamma oscillations have high test-retest reliability, with stable features within the same participants for at least 4 weeks (Muthukumaraswamy, Singh, Swettenham, & Jones, 2010; Tan, Gross, & Uhlhaas, 2016), which is important considering the practical limitation of doing the MEG and fMRI scanning sessions separately.

In this study, we could not demonstrate significant differences in NVC between the MS

patients and controls. While this may be related to the power of the study, it may also reflect the complexity of the biology underlying the relationship between neuronal activity and the haemodynamic response, which in MS is affected by the inflammatory *milieu*. Indeed, the response of blood vessels to neuronal activity is not only mediated by reactivity of the smooth muscle cells, but also by neuronal and glial signalling, involving many chemical mediators. Increased levels of both vasodilators (e.g., NO, (Smith & Lassmann, 2002) and vasoconstrictors (e.g., ET-1, D'haeseleer et al., 2013) have been reported in MS, due to the proliferation of glial cells to damaged areas, which could interfere with NVC pathways in contrasting ways. In line with the hypothesis that inflammation affects NVC, there is the evidence that the MS group appeared to display more variance in their coupling relationships, suggesting a greater inter-individual variability.

While not significantly different from healthy volunteers, the analysis of the NVC showed a trend for the MS group to have lower intercepts and higher gradients, when predicting the BOLD and CBF changes from the peak gamma power changes. An increased blood flow response, for same gamma power change, may seem counterintuitive considering the reports of blood vessels being less reactive in MS (Marshall et al., 2014, 2016). However, an increased blood flow response could reflect the need to deliver more oxygen or nutrients to tissue, if there is inefficiency in their use to support a given level of electrophysiological activity.

Conclusion

We found evidence for reduced neuronal and haemodynamic responses in the early visual cortex in MS in response to visual stimulation, in the absence of substantial functional impairments to visual acuity or delayed VEFs, or baseline CBF. Despite altered neuronal and vascular responses, NVC appears to be preserved in MS, at least within the range of damage and disability studied here.

5 Quantifying blood flow and oxygen utilisation at rest, in Multiple Sclerosis, using dual-calibrated fMRI

5.1 INTRODUCTION

In MS, the directionality of damage is not clear; the classic theory is a dysregulation of the immune system leading to tissue injury, but some have proposed that cytodegeneration happens first, which promotes an autoimmune and inflammatory response (Stys et al., 2012). As covered in Chapter 3.2, there is evidence that individuals with MS present with clear vascular and metabolic impairments, within normal-appearing GM and WM, and within lesioned tissue. The extent of these vascular and metabolic impairments, and how and when they contribute to the disease progression, is still not fully known. The consistently reported finding of hypoperfusion in MS has many biological interpretations. It could simply be due to a reduced demand because of neurodegeneration, or due to the vasculature not responding adequately to demand because of a reduction in reactivity of blood vessels. Further to this, tissue hypoxia could occur due to restricted CBF or restricted diffusion of oxygen into the tissue, possibly mediated by the proposed mitochondrial dysfunction in MS. These disease mechanisms could happen in parallel, and also include compensatory mechanisms. It is therefore important to develop non-invasive methods of separating out these physiological signals, to inform about the state of the vasculature, and metabolic activity, in MS. This chapter extends the work of Chapter 4, studying a larger sample, and characterising multiple quantitative physiological measurements related to oxygen utilisation, as opposed to the relative BOLD signal in response to a visual stimulus which has restrictions to its interpretation.

This chapter presents a dual-calibrated fMRI method, the background to which was explained in Chapter 2.3.4. This refers to a modulation of blood flow, blood volume, and venous blood oxygenation using both hypercapnic and hyperoxic gas challenges during MRI. In this chapter, measurement and physiological modelling allows quantitative estimates of CBF, OEF, $CMRO_2$, CVR, and Effective Oxygen Diffusivity of the capillary network (D_c) at rest. Dual-calibrated fMRI modelling has, until now, not been used to estimate D_c, which, alongside CBF, determines the direct transport of oxygen into the neural tissue (Hayashi et al., 2003; Hyder, Shulman, & Rothman, 1998; Vafaee & Gjedde, 2000a). In the model we apply here (Germuska et al., 2019) , the exchange of oxygen between the capillaries and the tissue (D_c) is modelled from the observations of CBF and OEF. Despite D_c largely reflecting capillary density (Gjedde, Poulsen, & Ostergaard, 1999), it also been shown to change according to metabolic demand

(Hayashi et al., 2003; Fahmeed Hyder et al., 1998) therefore potentially playing an important role in NVC mechanisms.

Dual-calibrated fMRI techniques are still being actively developed and there are only a few examples in the literature of applications of this method to patient populations, for example in Alzheimer's Disease (Lajoie et al., 2017) and internal carotid artery occlusion (De Vis et al., 2015). Lajoie et al (2017) report decreases in CBF and $CMRO_2$, particularly in parietal and temporal regions, in the Alzheimer's group. A small number of PET studies have estimated regional quantitative oxygen metabolism in MS, showing reductions in $CMRO_2$ and CBF in both WM and GM, with correlations with atrophy, cognition, vision, EDSS and number of relapses (Brooks et al., 1984; Lycke et al., 1993; Sun et al., 1998). One MRI study has characterised global venous oxygen saturation and $CMRO_2$ at rest in an MS population (Ge et al., 2012) finding increased venous oxygen saturation and decreased $CMRO_2$, which significantly correlated with EDSS and lesion load. Calibrated-fMRI has also been used in MS to show reduced task-induced regional changes in relative $CMRO_2$ (Hubbard, Araujo, et al., 2017; Hubbard, Turner, et al., 2017). However, this chapter presents the first study using a dual-calibrated fMRI method in a MS population, to non-invasively quantify blood flow and oxygen utilisation at rest, across the whole GM. Based on the previous literature, we predicted a reduced CBF and CVR in the MS group. We also expected to see reduced $CMRO_2$ in the MS group and a relationship between $CMRO_2$ and disease burden.

5.2 METHODS

Participants

26 patients and 25 age and gender matched controls were recruited. In total, complete calibrated-fMRI datasets were collected for 22 patients and 22 controls, due to 3 in each group either having gas screening contraindications or data acquisition errors. Figure 5-1 gives an overview of the patient recruitment process. Extensive screening questionnaires were carried out for patients and controls to ensure no MRI contraindications, and to ensure that it was safe for them to experience the respiratory gas modulations. None of the participants were current, or previous, smokers. The list of inclusion and exclusion criteria can found in Supplementary Figure 5-1. Written consent was obtained according to the protocol approved by Research Ethics Committee, Wales, UK. All participants received £10 per hour for taking part.

Patients had a diagnosis of relapsing-remitting MS (*Polman et al., 2011*) and were recruited at the University Hospital Wales, Cardiff. Patients had been medication stable and relapse-free for at least 3 months. One participant used a unilateral walking aid.

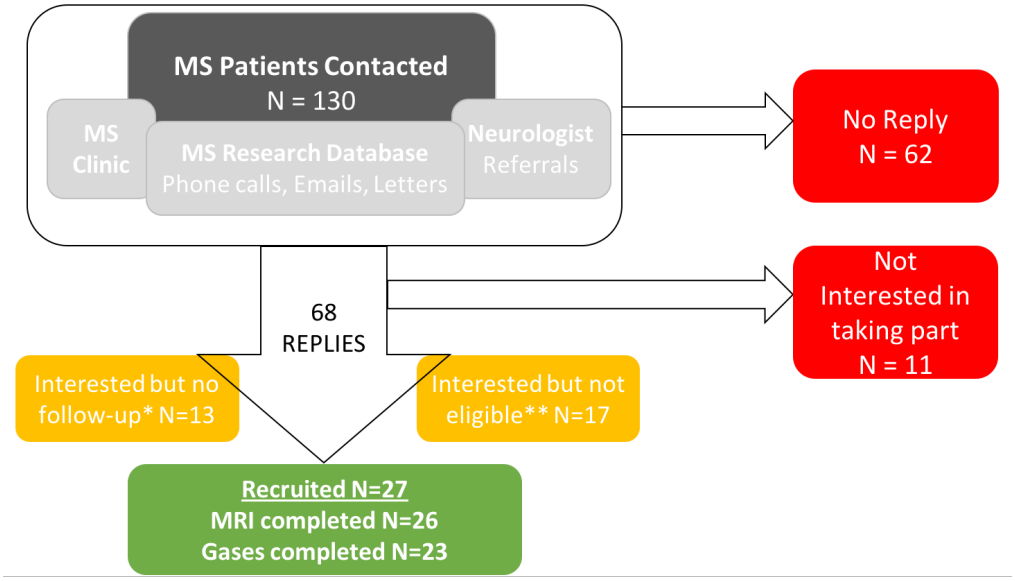

*Figure 5-1. MS patient recruitment overview, showing numbers at each recruitment stage. This took place over approximately 14 months, alongside recruiting and testing 25 matched controls. Patients were approached in person within MS clinics or through neurologist referrals, but mostly contacted directly via phone, email or letter with contact details obtained from the MS research database. Out of the 27 patients recruited and booked in for a testing session, one was not able to be scanned due MRI contraindications that became apparent on the day of testing. 3 patients were scanned but without the gas-paradigm due to gas contraindications, discomfort, or technical problems. *No follow-up refers to when the patient initially replied expressing interest but did not reply to further contact. **Patients were not eligible to take part due to not meeting eligibility criteria, normally MRI or gas-paradigm contraindications.*

Data Collection

The same controls and patients were used in Chapter 5 (this chapter), Chapter 6 and Chapter 9; an overview of this data collection is displayed in Supplementary Figure 5-2. Patients and controls all completed questionnaires and behavioural testing, a haemoglobin (finger prick) blood sample, and an MRI session (explained in detail below). Before the MRI scanning, the participant's tolerance of hypercapnic periods and breathing through a face-mask was tested outside the MRI scanner, and the researchers ensured the participant was comfortable and happy to continue before proceeding to the MRI scanning.

Questionnaires and behavioural testing. All participants completed a socio-demographic and lifestyle questionnaire. This included age, height, weight, alcohol

consumption (if yes: 'how many units per week?'), caffeine intake (if yes: 'Do you drink more than 3 cups of coffee, tea and cola drinks combined per day?'), and years of education (from start of school onwards). Tests from the MS Functional Composite (*Cutter et al., 1999*) were carried out on all participants: 9-HPT for arm/hand function, the T25-FW for leg function/ambulation, and the PASAT 2 and 3 seconds as a measure of cognitive function. The Symbol Digit Modalities Test (SDMT) was also used to assess cognitive function (*Benedict et al., 2017*). Visual acuity was assessed, in each eye separately, with a SLOAN letter chart (*Precision Vision*) at 100% contrast and scored in two ways: (1) the smallest letter size (in M-units) where 3 out of 5 letters were correctly read, and (2) a cumulative score of total letters read correctly, out of 60. Participants were tested with corrected-vision; matched to the correction that they had during the MRI scans.

For patients only, disability and disease impact was assessed with the self-reported Multiple Sclerosis Impact Scale (MSIS-29) (*Hobart, Lamping, Fitzpatrick, Riazi, & Thompson, 2001*) and the Fatigue Scale for Motor and Cognitive Functions (FSMC) (*Penner et al., 2009*). Clinical records and a short interview on disease history and impact gave information on: disease onset, EDSS (*Kurtzke, 1983*), relapse history and impact of MS on occupation.

Haemoglobin blood concentration. A blood sample was drawn via a finger pick with a 1.8mm lancet and analysed with the HemoCue® Hb 301+ system as per the manufacturer's guidelines (*Hemo Ängelholm, Sweden*). This gave a reading of systemic haemoglobin concentration, in grams per litre. This was done within one hour of the start of the MRI scan. A measure of haemoglobin represents the oxygen carrying capacity of blood and is used in the modelling of the dual-calibrated fMRI data.

MRI Scanning. Data were acquired on Siemens Prisma 3T MRI scanner (*Siemens Healthineers, Erlangen, Germany*), using a 32-channel head coil. All of the scans described below were acquired during one scanning session. A magnetization-prepared rapid acquisition with gradient echo (MPRAGE), T1-weighted scan was acquired for registration and brain segmentation purposes (1mm isotropic resolution, 200 slices, TR/TE = 2100/3.24ms). A 3D T2-weighted Fluid Attenuated Inversion Recovery (FLAIR) image (1mm isotropic resolution, 256 slices, slice thickness = 1mm, TR/TE = 5000/388ms) and T2/Proton Density dual-echo image (41 slices, slice thickness = 3mm, 0.8 x 0.8 x 3.9 mm, TR/TE1/TE2= 4050/11/90ms) were acquired for lesion identification.

Whilst participants were at rest, a dual-calibrated fMRI scan including interleaved periods of hypercapnia, hyperoxia and medical air were delivered through a facemask worn by the participant, following the protocol previously described by (Germuska et al., 2016; Merola, Germuska, Murphy, & Wise, 2018). This gas delivery circuit is shown in Supplementary Figure 5-3. Three periods of hypercapnia were given, interleaved with two periods of hyperoxia (see Figure 5-3.A). During the hypercapnic blocks, 5% CO_2 in air was given. During the hyperoxic blocks 50% O_2 in air was given, with short period of 100% O_2 and 10% O_2 delivered to accelerate the transitions to the hyperoxic state and back to baseline. Participant's heart rate and oxygen saturation were monitored with a pulse oximeter constantly throughout the scanning session. $P_{ET}CO_2$ and $P_{ET}O_2$ (partial pressure of end-tidal carbon dioxide or oxygen) were sampled from the facemask, using a rapidly responding gas analyser (AEI Technologies, Pittsburgh, PA, USA). An example breathing trace is shown in Figure 5-3.B.

During this gas protocol, a pCASL acquisition was run, using pre-saturation and background suppression (Okell, Chappell, Kelly, & Jezzard, 2013), with a dual-excitation (DEXI) readout (Schmithorst et al., 2014). The labelling duration and PLD were both 1.5s, GRAPPA acceleration (factor of 3) was used with TE1=10ms and TE2=30ms. An effective TR (the total TR including labelling and both readouts) of 4.4 seconds was used to acquire 16 slices, in-plane resolution 3.4 x 3.4 mm and slice thickness 7mm with a 20% slice gap. A diagram of this sequence is shown in Figure 5-2. Before this scan, an M_0 image was acquired for ASL quantification with TR of 6 seconds, TE=10ms.

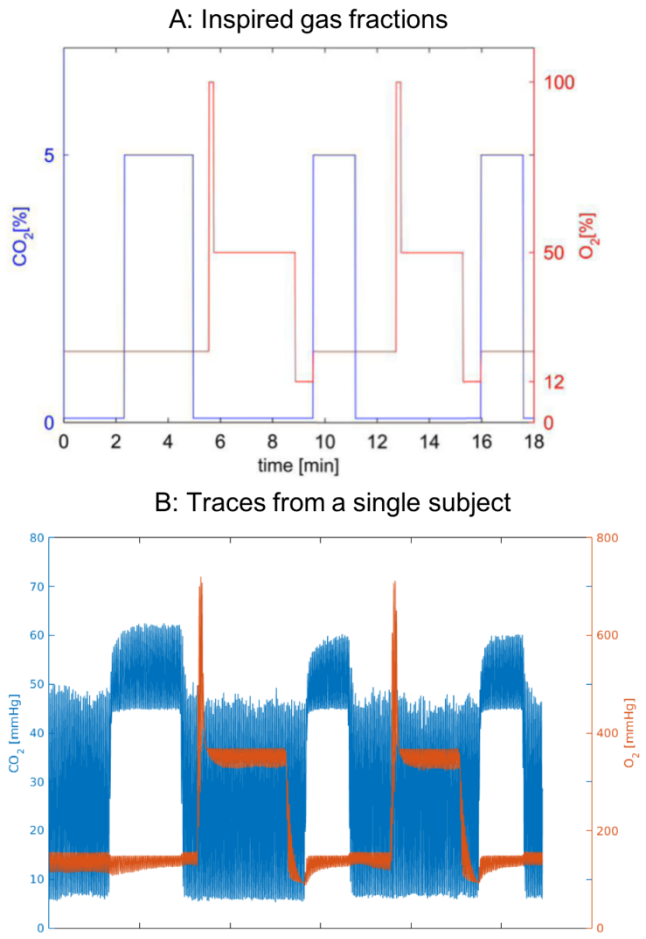

Figure 5-3. Inspired gas fractions used during the respiratory protocol, and (B) Example trace of one subject. The design is 18 minutes in total and consisted of three blocks of hypercapnia (fixed inspired fractions of 5% CO_2 in air), interleaved with two periods of hyperoxia (fixed inspired fractions of 50% O_2 in air). A short period (14 seconds) of 100% O_2 is delivered before each hyperoxic block, to aid the fast transition from baseline to stable hyperoxia. A short period of hypoxic gas mixture (10% O_2, 90% N_2) was delivered to ensure fast transition back to baseline. These periods were not included in the modelling. Oxygen saturation levels were constantly monitored with a pulse oximeter, and the hypoxic gas delivery did not induce arterial hypoxia due its short duration and because it follows a longer hyperoxic block.

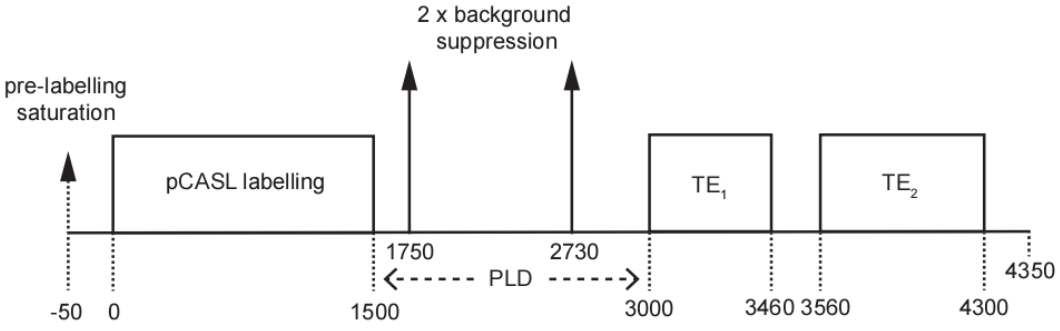

Figure 5-2. Pulse sequence timing diagram for the DEXI-pCASL acquisition. Sequence timings are in milliseconds (ms) to the nearest 5ms. This figure is produced by Michael Germuska and used here with permission.

Data Analysis

Normalised Whole Brain Volume. Whole brain tissue volume, normalized for subject head size, was estimated with SIENAX (Smith, De Stefano, Jenkinson, & Matthews, 2001; Smith et al., 2002) in FSL. Brain and skull images were extracted from the single whole-head input data (T1-weighted image, lesion-filled for the patients). The brain image was then affine-registered to MNI152 space using the skull image to determine the registration scaling, and to obtain the volumetric scaling factor. Three-class segmentation was carried out and whole brain volumes, normalized for head size, were calculated using the volumetric scaling factor.

Lesion Volumes, Lesion Filling and GM mask. Figure 5-4 describes the protocol followed to calculate lesion volumes, and improve the accuracy of the segmentation (Battaglini et al., 2012; Gelineau-Morel et al., 2012). First, the T2, PD, and T2-FLAIR images were brain extracted. The T2-FLAIR image was transformed to the same space as T2-PD image (linear, 6 DOF). Using *JIM* (Version 6.0) lesions were drawn around manually using the contour ROI tool, without 3D propagation. All three image contrasts were used to locate the lesions, and if in doubt a lesion was not drawn around. This lesion map was exported as a NIFTI file, with a pixel area threshold of 50% threshold, and a lesion volume was calculated for each patient.

For the lesion filling of the T1 image, the PD image was registered to the T1 image, and the lesion map was binarised and transformed to T1-space. The lesion map was thresholded at 0.4, to approximately preserve the size of the original lesion map but also allow a small amount of inflation so that that the lesion map better overlapped the lesions on the T1-image, in case of registration errors. The lesion map was then binarised. The function *lesion_filling* (Battaglini et al., 2012) was used; this fills the lesion area with intensities similar to those in the non-lesion neighbourhood (restricted to WM only – a WM PVE map was created with FAST previous to this). Using the lesion-filled T1-image, FSL-FAST was run again to produce a new PVE of GM.

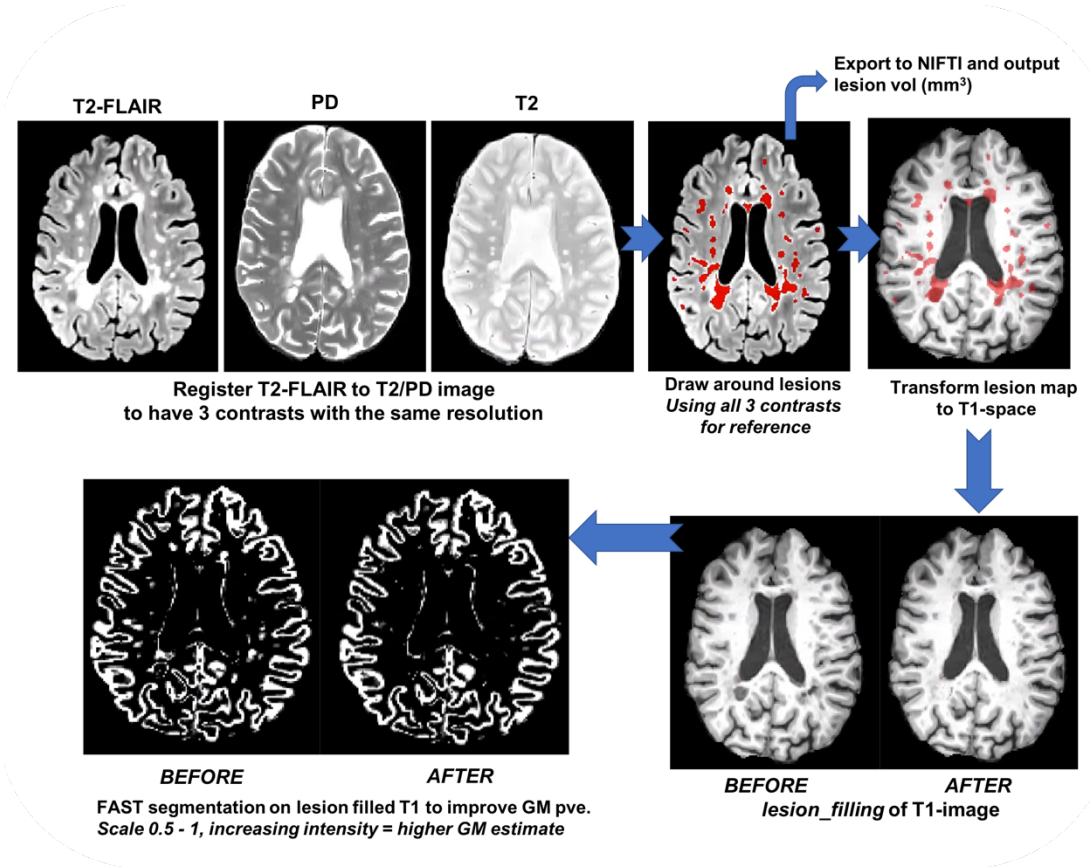

Figure 5-4. Summary of the pipeline used to calculate lesion volumes, and perform lesion filling, on each patient's T1-weighted image, to improve tissue segmentation.

Dual-calibrated fMRI pre-processing. Motion correction was performed with FSL-MCFLIRT and spatial smoothing (FWHM=4.5mm) of the BOLD data (surround average of echo 2) was performed with SUSAN (Smith & Brady, 1997). ASL data (surround subtraction of echo 1) and the M_0 acquisitions were spatially smoothed using a 3D Gaussian kernel (FWHM 4.5mm). Functional DEXI data was registered to the structural T1-weighted image using FSL's *epi-reg* tool, which also creates and outputs GM, WM and CSF PVE through FAST segmentation of the T1-weighted image. Using the inverse of this matrix, the T1-image and the GM-PVE image were transformed to DEXI space. The GM-PVE image was thresholded at 0.5 and binarised and used as a GM mask for the parameter estimates. The GM-PVE was also used for regularisation of the D_c estimates (non-lesion filled for the patients), explained below.

Dual-calibrated fMRI modelling. Code for the pre-processing of physiological traces was written by Michael Germuska (Germuska, 2018b), alongside the code for physiological modelling of the dual-calibrated fMRI data (Germuska, 2018a). The model development was not the focus of this chapter but the application of this model to the patient-control comparison. For details, see (Germuska et al., 2016) and (Germuska et al., 2019).

In brief, a compartmental model of oxygen exchange is used to model the relationship between CBF, D_c and OEF. Quantification of resting OEF and CBF (and therefore $CMRO_2$) is calculated using a dual-calibrated fMRI method (Bulte et al., 2012; Gauthier et al., 2012; Wise et al., 2013), within a forward modelling framework (Germuska et al., 2016). A simplified calibration model is used (Merola et al., 2016), assuming isometabolic alteration of flow during hypercapnia, and isometabolic alterations of venous oxygenation during hyperoxia. End-tidal traces were aligned with the DEXI data via a cross-correlation between $PaCO_2$ (partial pressure of CO_2) and the mean GM ASL signal. Measured haemoglobin concentration helped inform the relationship between baseline CBF and D_c to OEF in the fitting. A non-linear least squares minimisation routine was used to optimise voxel-wise estimates of baseline D_c, OEF, CBF and CVR. Regularisation was applied to D_c and OEF to reduce instability in fitting a non-linear model to the data and reduce sensitivity to noise variation across voxels and participants. The regularisation parameter for OEF was assumed to be uniform, with a nominal baseline OEF of 0.4. As D_c nominally scales with CBV, GM-PVE were used to impose spatial variation on the D_c regularisation, with a PVE of 1 corresponding to a nominal diffusivity of 0.12 ml/100g/mmHg/min. See Figure 5-5 for a brief overview of how the data collected is used in this modelling framework.

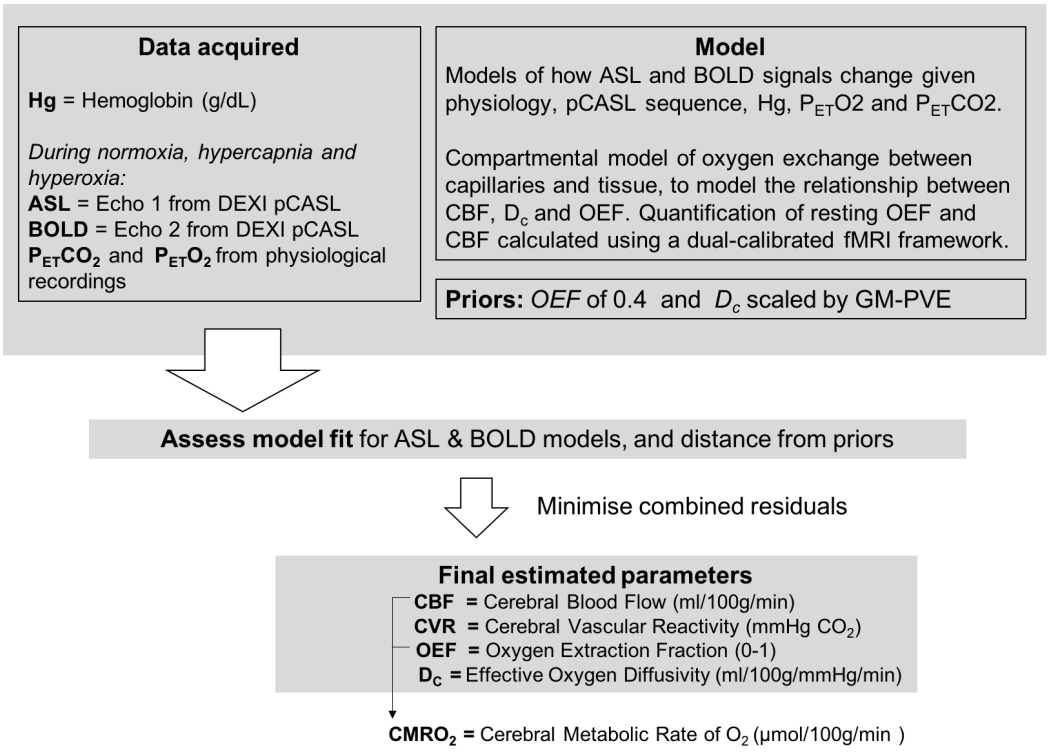

Figure 5-5. Diagram explaining how the different data acquired during DEXI-pCASL scan (and the Hg measurement) is modelled to estimate the multiple physiological parameters that are compared between patients and controls.

GM voxel-wise comparison. A GM voxel-wise comparison between groups was carried out by another researcher in the lab and therefore the results are included in this chapter, in order to aid the interpretation of the average GM parameter results. With FSL-FLIRT, two transformation matrices were created and combined into one: a registration from the individual's functional DEXI space to their T1-anatomical space, and from T1-anatomical space to MNI (2mm) template space. All parameter maps, including the GM-mask, were then transformed to MNI-space. In MNI space, each parameter map was masked with their MNI GM-mask. After merging all participants into one 4D file, FSL's *randomise* function was used to perform nonparametric t-tests to test the difference between patients and controls, for each parameter. Two t-statistic contrasts were produced (Patients > Controls, and Controls > Patients), thresholded at $p<0.05$, with Threshold-Free Cluster Enhancement correction.

Statistics

Group-comparisons. For each participant a map of CBF, $CMRO_2$, OEF, CVR and D_c was outputted in native space, from the physiological modelling. An average value (median) across voxels in the GM mask was outputted for each parameter. In SPSS, independent sample t-tests were used to test differences between patients and controls for each parameter. When the assumption of normality was violated (tested with Kolmogorov-Smirnov test) Man-Whitney U tests were performed (with an exact sampling distribution for *U*). When distributions of scores were similar for patients and controls, determined by visual inspection, medians were compared. For comparison of categorical variables, between groups, Pearson's Chi-square tests were run. Outliers were defined as being 3xSD above or below the mean, or 3xIQR above or below the lower or upper quartile, respectively. All p-values reported are two-tailed. Group means and standard errors are presented in brackets as Mean ± SEM, and errors bars display ± SEM unless stated otherwise.

Patient regressions. In SPSS, Multiple linear regressions were performed to investigate what disease characteristics could predict the variability of CBF and $CMRO_2$ GM averages. Unless stated in the results, the assumptions of multiple linear regression were met: normality of residuals, predictor variables linearly related to the outcome variable, homoscedasticity (residuals are equal for all values of the outcome variable), multicollinearity (high correlations between predictor variables), and no significant outliers or highly influential points. For outliers, standardized and studentized deleted residuals were examined, and outliers were classed as ± 3. Cook's distance was

calculated, with a typical cut-off of greater that 1 being used to indicate highly influential points.

5.3 RESULTS

For the group comparisons, 2 controls and 1 patient were left out of the analysis due to bad quality data. These three participants did not return to a stable $P_{ET}CO_2$ baseline during the periods of medical air delivery; this was judged to be a deviation of greater than 5mmHg with reference to the first baseline block. This was alongside lower quality physiological and imaging data in general for these participants, due to noticeable motion artifacts. This left 20 controls and 22 patients. Patient disease characteristics are displayed in Table 5-1 and demographics and behavioural tests scores for both groups are displayed in Table 5-2. An example of all the parameter maps is shown for one control and one patient in Figure 5-6.

		Patients	Min – Max (Outliers)
	Lesion Vol (mm^3)[b]	7253.64 (7392.75)	2062 – 35963 (P1 =35963; P2 = 33850).
	Disability: EDSS [a]	2.23 ± 1.38	0 - 6
Disease History	Months since onset [a]	95.54 ± 59.37	20 - 253
	Months since relapse [a]	33.95 ± 20.25	5 - 78
Self-report Disease Impact	FSMC-Motor	25.73 ± 11.31	10 - 45
	FSMC-Cognitive	24.59 ± 9.91	10 - 43
	MSIS-29-P [b]	31 (21.5)	20 - 76
	MSIS-29-C [a]	16.91 ± 6.57	9 - 32
	Job change? Y/N	4/18	/

Table 5-1. Patient disease characteristics. a refers to Mean ± SD. Some data were not normally distributed and therefore b refers to Medians (IQR). FSMC (total scores for each domain); MSIS-29 (total scores for each domain), and Job change refers to whether their job had changed due to MS

		Patients	Controls	Test Statistic	P
Dems & Lifestyle	Gender (M/F)	5 / 17	6 / 14	$\chi(1) = 0.29$	0.592
	Age (Yrs) [a]	35.45 ± 7.15	34.15 ± 5.69	$t(40) = -0.65$	0.519
	Education (Yrs) [b]	18 (2)	18 (5)	$U = 148$	0.182
	BMI [a]	26.81 ± 4.95	24.67 ± 4.02	$t(40) = -1.53$	0.133
	Caffeine >3 Y/N	11 / 11	5 / 15	$\chi(1) = 2.78$	0.096
	Alcohol (Units/wk) [b]	2 (2.5)	2 (3.75)	$U = 148$	0.362
Visual	Visual Acuity-L [b]	45 (9.5)	48 (7)	$U = 162$	0.223
	Visual Acuity-R [b]	44 (8)	47 (8)	$U = 134$	0.045
Motor	T25-FW (sec) [a]	4.66 ± 0.63	3.98 ± 0.63	$t(39) = -3.50$	0.001
	9HPT-dom (sec) [a]	19.76 ± 2.53	20.18 ± 2.28	$t(38) = 0.594$	0.556
	9HPT-ndom(sec) [a]	22.86 ± 2.56	21.25 ± 2.97	$t(40) = -1.891$	0.066
Cognitive	PASAT3 (/60) [a]	50 (21)	54 (16)	$U = 187$	0.398
	PASAT-2 (/60) [a]	34.90 ± 12.16	35.9 ± 12.21	$t(39) = 0.80$	0.795
	SDMT [a]	59.90 ± 7.14	62.40 ± 9.75	$t(40) = 0.95$	0.348
	Brain Vol (mm^3) [a]	1508183 ± 76523	15488667 ± 59496	$t(40) = 1.91$	0.063
Outliers (C = Control, P = Patient) Alcohol (C1 = 24 units, C1 = 18 units, P1 = 15), Visual Acuity-L (C1 = 8 score), Visual Acuity-R (P1 = 0), T25-FW (P1 =11.03), 9HPT-dom (P1 = 30.53, P2 = 38.07).					

Table 5-2. Demographics and behavioural data compared between groups. a refers to Mean ± SD, alongside Independent Sample T-tests, and b refers to Medians (IQR), alongside Mann-Whitney U Tests. For the categorical variables, Pearson's Chi-square tests were run. [BMI = Body Mass Index; Caffeine >3 = drink more than 3 caffeinated drinks per day; Visual Acuity is based on the cumulative score across all letter sizes; dom = dominant hand, ndom = non-dominant hand; Brain Vol = whole brain volume normalised for skull size.

Model fit

For each patient and each control, the average of the residuals and the SD of residuals across voxels was calculated, to broadly estimate how well the model fit for each participant. Median residual estimates for patients (0.64) and controls (0.63) were not significantly different, $U = 252$, $z = 0.81$, $p = 0.420$. Median residual SD estimates were higher in patients (0.30) compared to controls (0.26), suggesting more variance in the model fit *across voxels* for the patient group, however this was not a significant difference, $U = 294$, $z = 1.86$, $p = 0.062$.

Model outcome parameters

The following data refer to Means ± SEM and are displayed in Figure 5-7. For GM CBF averages, patients (46.64 ± 1.29 ml/100g/min) displayed significantly lower values than controls (51.53 ± 1.44 ml/100g/min), $t(40) = 2.53$, $p = 0.015$. For GM $CMRO_2$ averages, patients (131.55 ± 4.81 µmol/100g/min) also showed significantly lower values compared to controls (145.51 ± 4.28 µmol/100g/min), $t(40) = 2.15$, $p = 0.038$. There were no significant differences between patients and controls for GM OEF (Patients: 0.41 ± 0.14, Controls: 0.40 ± 0.14, $t(40) = -0.493$, $p = 0.625$), GM CVR (Patients: 2.27 ± 0.14 %CBF change/mmHg CO_2, Controls: 2.51 ± 0.15 %CBF change/mmHg CO_2, $t(40) = 1.17$, $p = 0.249$) or GM D_c (Patients: 0.081 ± 0.004 ml/100g/mmHg/min, Controls: 0.087 ± 0.003 ml/100g/mmHg/min, $t(40) = 1.211$, $p = 0.233$). GM volume (the area used to extract these average values) was significantly lower in patients (489273.31 ± 13881.48 mm^3), compared to controls (528354 ± 13622.62 mm^3), $t(40) = 2.00$, $p = 0.05$. The hemoglobin measurement, used in the modelling of capillary oxygen content, was not significantly different between patients (135.7 ± 3.29 g/L) and controls (136.5 ± 2.83 g/L), $t(39) = 0.19$, $p = 0.849$.

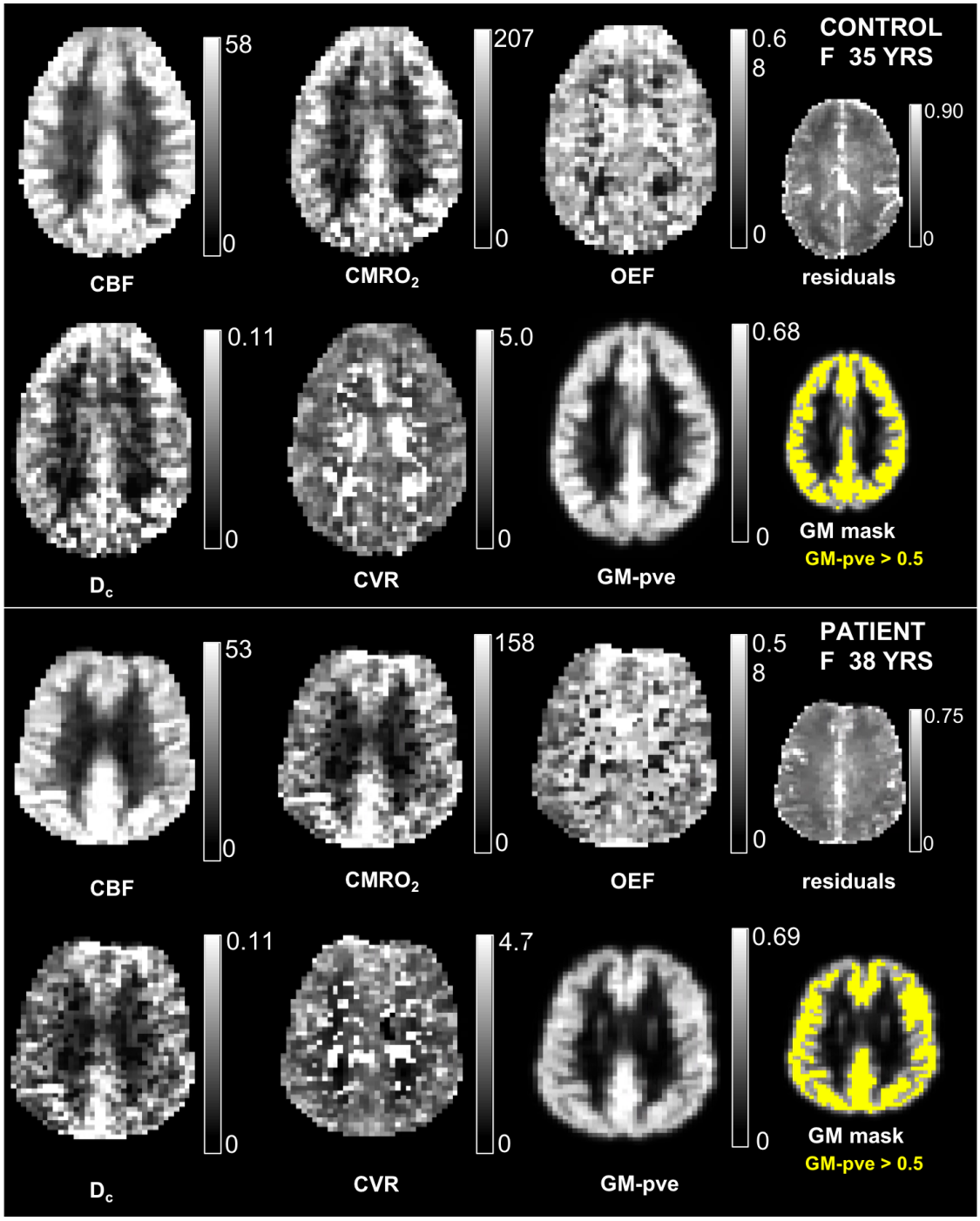

Figure 5-6. Example baseline parameter maps for one control (top) and one patient (bottom), showing CBF (ml/100g/min), $CMR0_2$ (μmol/ml/min), OEF, D_c (ml/100g/mmHg/min), CVR (%CBF change/mmHg CO_2), GM-PVE (probability estimate) in individual subject space, the GM mask (binarised) which is the GM-pve thresholded at 0.5, and the residuals of the model fit.

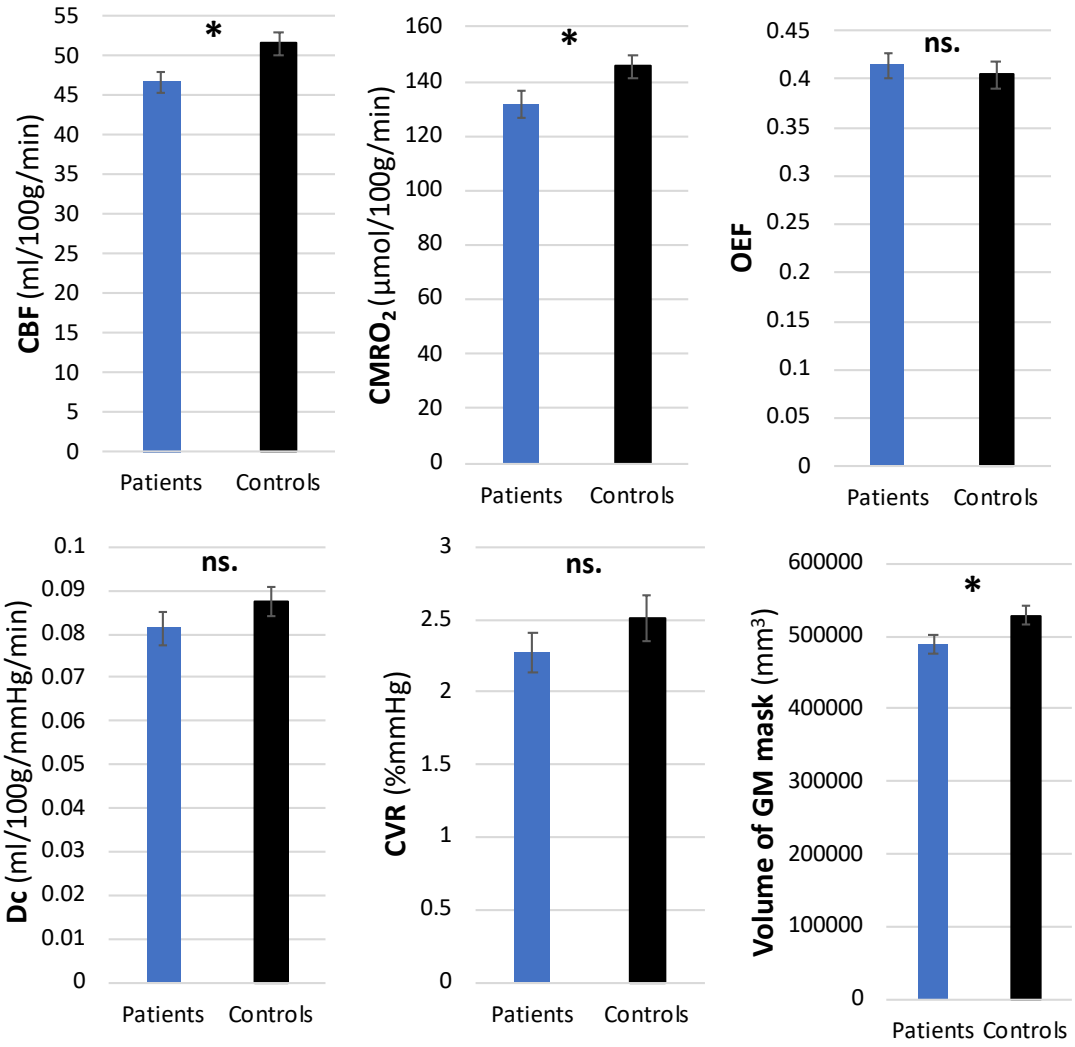

*Figure 5-7. Comparing patient (n=22) and control (n=20) group means for CBF (ml/100g/min), CMR0$_2$ (µmol/ml/min), OEF, D$_c$ (ml/100g/mmHg/min), CVR (%CBF change/mmHg CO$_2$) and volume of the GM mask (mm3) used to extract average (median) parameter values for each participant. Differences between means are tested with independent t-tests. *p≤0.05, ns = p>0.05. Errors bars display ± SEM.*

Are partial volume estimates different in the patient group, and how does this affect the GM averages?

If patients have different partial volume characteristics than controls this has the potential to introduce bias in our parameter estimates from GM. Studies have reported a relationship between lesion load and GM volume estimation, when segmentation involves modelling intensity distributions of different classes of tissue (Battaglini et al., 2012; Popescu et al., 2016). By performing the tissue segmentation of lesion-filled T1 images we hoped to mitigate this effect, however some biases may still remain. To investigate this, a mean across voxels in the unbinarised GM PVE image, thresholded at 0.5, was calculated for each participant. This gives an estimate of the amount of GM in each voxel, on average, after thresholding. This GM PVE voxel-average for patients

(Group median = 0.61) and controls (Group median = 0.62) were not significantly different, U = 160.52, z = -1.157, p = 0.116. Furthermore, we compared all parameters after thresholding the GM PVE at 0.75, a more conservative value. The results were unchanged compared to the 0.5 thresholded results, except for no significant difference in volume of the GM mask (when thresholding at 0.75). Only CBF and $CMRO_2$ were significant different between groups, as before. The mean difference between patients and controls actually increased with the threshold of 0.75. For CBF, the mean difference between groups for the 0.5 threshold was 4.89 (t(40) = 2.53, p = 0.015), and for the 0.75 threshold it was 6.411 (t(40) = 2.66, p = 0.011). For $CMRO_2$, the mean difference between groups for the 0.5 threshold was 13.96 (t(40) = 2.15, p = 0.038), and for the 0.75 threshold it was 16.55 (t(40) = 2.26, p = 0.029).

What disease characteristic can explain the reduced CBF and $CMRO_2$ in patients?

As CBF and $CMRO_2$ were significantly different between groups, we investigated what patient disease characteristics could predict variability in these scores. As the CBF and $CMRO_2$ are averages across the whole GM, we did not include behavioural data specific to one functional system (e.g. SDMT for cognition, or 25FW for motor function). As an indication of recent and general disease impact, across functional systems, we used the MSIS-19 and FSMC questionnaire data, in physical and cognitive domains. Higher scores indicated higher impact of cognitive and physical symptoms on everyday life. As a general indictor of whole brain disease activity, we included lesion volume and GM volume (used to extract the CBF and $CMRO_2$ averages).

Scores from the four questionnaire subsections all strongly correlated with each other: MSIS-19 physical and cognitive (r = 0.73, p <0.001), FSMC cognitive and FSMC physical (r = 0.88, p <0.001), MSIS-19 physical and FSMC physical (r = 0.75, p <0.001), MSIS-19 cognitive and FSMC cognitive (r = 0.80, p <0.001), MSIS-19 cognitive and FSMC physical (r = 0.84, p <0.001), MSIS-19 physical and FSMC cognitive (r = 0.57, p <0.01). Therefore a 'total disease impact' scores was included in the model instead, which was simply the sum of each questionnaire domain. Therefore, the models to predict CBF and $CMRO_2$ included these predictors: total disease impact, GM volume, and lesion volume.

For predicting CBF, the overall model was significant, with an R^2 of 35.7% and an adjusted R^2 of 25.0% (F (3, 18) = 3.33, p = 0.043). Lesion volume significantly contributed to this model (β = -0.64, p = 0.008), but GM volume (β = -0.17, p = 0.483)

and composite disease impact score (β = 0.036, p = 0.827) did not. CBF decreased by 0.000432 ml/100g/min for every 1mm^3 increase in lesion volume. For the $CMRO_2$ regression, one patient had studentized deleted residual of -3.25, and also a cook's distance of 1.1, suggesting it has a large effect on the regression. Therefore, this patient was removed from the regression. The overall model was significant, with an R^2 of 37.3% and an adjusted R^2 of 26.3% (F (3, 17) = 3.37, p = 0.043. GM volume significantly contributed to the model (β = 0.62, p = 0.038), but lesion volume (β = -0.13, p = 0.596) and composite disease impact score (β = -0.447, p = 0.116) did not. $CMRO_2$ increased by 0.0002 µmol/100g/min for every 1mm^3 increase in GM volume. The relationship between CBF, $CMRO_2$, GM volume and lesion volume are displayed in Figure 5-8. To establish whether the relationship between GM volume and $CMRO_2$ was specific to patients, this was also explored in the controls. No significant relationship between GM volume and CBF or GM volume and $CMRO_2$ was seen for the controls (Supplementary Figure 5-4).

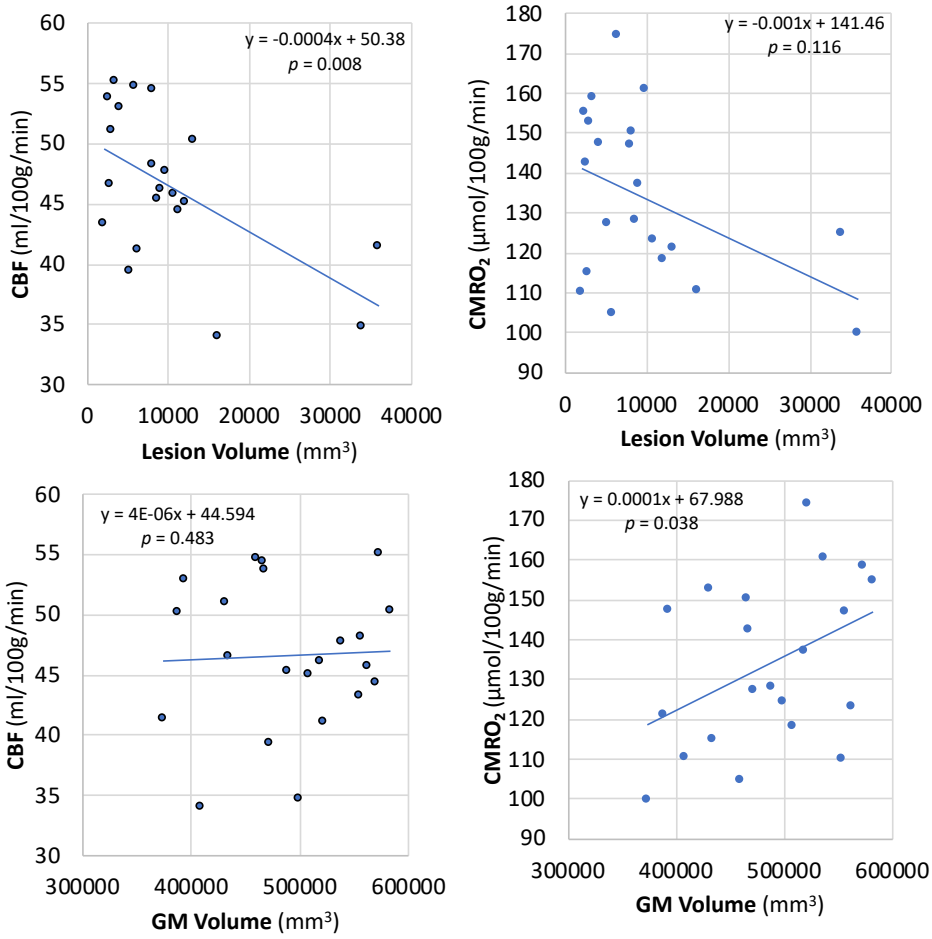

Figure 5-8. The relationship between lesion volume and GM CBF (top left), lesion volume and GM $CMRO_2$ (top right), GM volume and CBF (bottom left) and GM volume and $CMRO_2$ (bottom right). These results are for the patient group only. Lesion volume was the only significant predictor of CBF, and GM volume the only significant predictor of $CMRO_2$. The p-values refer to the significance of the beta coefficients in the multiple regression model.

Voxel-wise differences between groups

Four small significant clusters, showing higher values for controls compared to patients, were found for both the CBF and for $CMRO_2$ voxel-wise comparisons (Figure 5-9). No significant voxel-wise differences were found for CVR, OEF or D_c. The following p-values refer to the maximum corrected p-value in that cluster, with the corresponding MNI coordinates [x,y,z]. The brain regions refer to the peak location, referencing the Harvard-Oxford Cortical Structural Atlas in FSL. The peak locations of common significant clusters for both CBF and $CMRO_2$ were located in the Subcallosal Cortex (CBF: p-value = 0.024, 54 voxels; $CMRO_2$: p-value = 0.025, 27 voxels, both located at [45 73 40]), and medial/orbital frontal regions (CBF: p-value = 0.047, [50 77 24], 14 voxels; $CMRO_2$: p-value = 0.037, [49 79 23], 39 voxels). For CBF, the peak location of the other two significant clusters were located in the occipital pole (p-value = 0.031, [44 16 41], 41 voxels), and the para-hippocampal gyrus (p-value = 0.046, [55 42 28], 6 voxels). For $CMRO_2$, it was the nucleus accumbens (p-value = 0.033, [40 70 34], 39 voxels) and the paracingulate gyrus (p-value = 0.048, [51 85 42], 2 voxels).

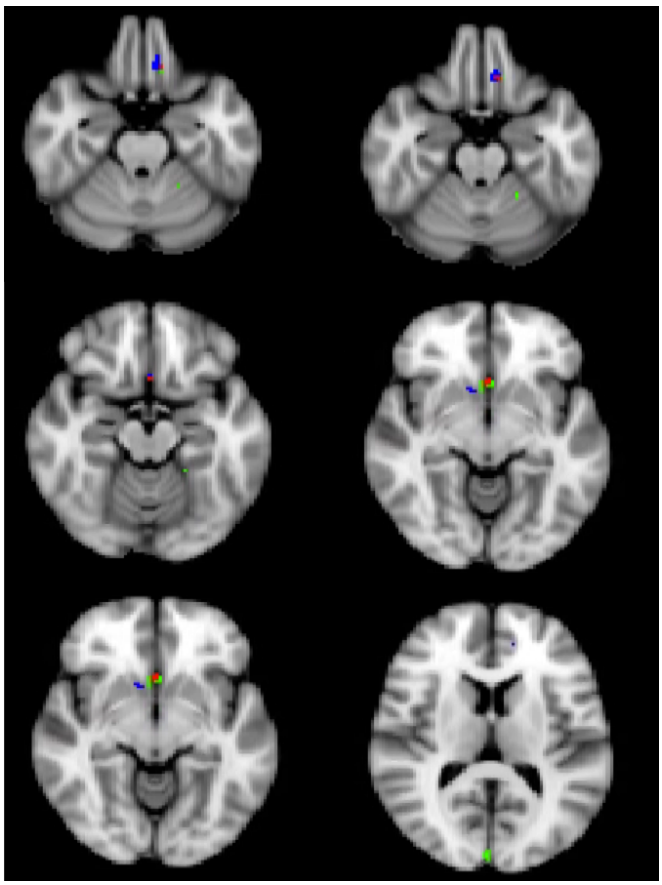

Figure 5-9. Clusters of voxels showing significantly higher CBF and $CMRO_2$ in the control group compared to the patient group. Red displays voxels with significantly higher CBF and $CMRO_2$, green displays voxels with significantly higher CBF only and blue displays voxels with significantly higher $CMRO_2$ only.

5.4 DISCUSSION

This chapter presents the first application of a dual-calibrated fMRI protocol in a MS population, allowing simultaneous baseline quantification of many important physiological parameters reflecting vascular and metabolic function. The patients and controls were age and gender matched and did not differ on years of education, BMI and self-reported caffeine and alcohol intake. Behaviourally, patients showed significant impairments in visual acuity (right eye only) and the 25-foot walk, suggesting impaired mobility and leg function in this group. For the GM parameter averages, CBF and $CMRO_2$ were significantly lower in patients, but no significant differences were seen for CVR, OEF or D_c. In the patient group, self-reported disease impact did not significantly predict CBF or $CMRO_2$, however lesion volume did significantly predict variability in CBF, and GM volume predicted variability in $CMRO_2$. Consistent with the GM-average analysis, the voxel-wise analysis only showed significant group differences for CBF and $CMRO_2$ signals, in a few small clusters. Firstly, the GM parameter comparisons will be discussed, followed by modelling limitations and lastly practical considerations.

A reduction in CBF and $CMRO_2$, over the GM, is consistent with previous literature in MS, as summarised in Chapter 3.2. In the introduction of this chapter, some potential mechanisms were proposed: a reduced CBF reflecting a reduced metabolic demand due to neurodegeneration; a reduced CBF due to an impaired CVR which could lead to hypoxic tissue; a restricted CBF or alterations in the diffusion of oxygen into the tissue also leading to hypoxia. As we only report reductions in CBF and $CMRO_2$, but no differences in OEF, CVR or D_c, this suggests that the reduced $CMRO_2$ and CBF most likely reflect a reduced demand from the tissue, with little evidence for a hypoxic state. The lack of difference in oxygen diffusivity supports this interpretation, considering there is evidence suggesting diffusivity can increase with increasing demand (Hayashi et al., 2003; Hyder et al., 1998).

Two previous studies reported widespread CVR decreases in MS (Marshall et al., 2014, 2016), in contrast to our results. These studies used a pCASL sequence, as done here, so their units of measurement for CVR were the same (%CBF change/mmHg CO_2). The cause of this discrepancy is not clear, and they report similar disease durations and EDSS scores for their patients. In the calculation of their CBF-CVR maps they implemented GM partial volume correction, and their GM tissue mask was defined at 70%. We defined ours at 50%, however also showed no significant differences in CVR when exploring the results with a threshold of 75%. In contrast, a study by a different

lab used transcranial doppler imaging with a BH task, and report no CVR differences in MS across three time points (Uzuner et al., 2007). Therefore, more research is needed to understand how relevant CVR deficits are to MS pathology. Nevertheless, in this MS group, normal CVR suggests that the blood vessels were dilating appropriately when stimulated. There are very few studies applying dual-calibrated fMRI to study a patient population. One of them is by Lajoie et al (2017); they carried out a dual-calibrated study in Alzheimer's Disease (AD) and had similar aims: to assess the extent of vascular and metabolic impairments in AD, as well as to assess the feasibility and practicality of these types of methods. They highlight some key methodological challenges to overcome (choice of post-labelling delay, presence of susceptibly artefacts, and challenges administering hypercapnia to elderly participants). Nevertheless, they report similar results to us: decreased CBF and $CMRO_2$ in GM parietal, precuneus and temporal regions in AD patients, with no differences in OEF, CVR and M values in their ROI analysis. However, they do find some reductions in OEF and M in their voxel-wise analysis, in a small parietal-precuneus cluster. They state that these results tend to rule out chronic global cerebral ischemia at this stage of AD.

The reasons for the lower CBF and $CMRO_2$ GM signals in MS is not fully clear. The volumes of the GM mask, used to extract these parameter averages, were significantly lower in patients compared to controls, suggesting GM atrophy in this patient group. However, as the parameter estimates are averages over each voxel in the *remaining* GM, the CBF and $CMRO_2$ reductions cannot simply be attributed to a lower GM volume. However, the density of GM in each voxel (the PVE) could still have been different in the patient group (Battaglini et al., 2012; Popescu et al., 2016), biasing the overall averages. We report no significant group differences in the average PVE across voxels, above 0.5, and no difference in the parameter comparisons when thresholding at 0.75. This suggests that partial volume effects of the GM mask did not contribute significantly to the group differences report. However, the regression analyses showed a positive association between GM volume and $CMRO_2$ GM averages, in the patient group only. This suggests GM atrophy may reflect some disease activity that is also affecting the metabolism of oxygen specifically, as there was no significant relationship between CBF and GM volume. A significant relationship between lesion volume and GM CBF averages was reported, showing patients with higher lesion volume to have lower CBF values. Similar relationships have been reported previously, including negative correlations between T2-lesion load and global GM CBF (Amann et al., 2012) and GM CVR (Marshall et al., 2014, 2016). Lesion volume was not significantly related to GM $CMRO_2$ averages but the trend appeared very similar. In fact, Ge et al (2012) report a significant negative correlation between their whole-brain $CMRO_2$ measure and lesion

load. These findings are interesting, as the majority of these lesions were not identified within GM, meaning the level of WM damage relates to the level of GM CBF impairment. It could be assumed that a higher WM lesion load simply reflects a higher GM lesion load; GM lesions that are likely present in this MS group based on previous literature (Klaver, De Vries, Schenk, & Geurts, 2013a) but not measured in our study. However, it is not clear from the literature whether this assumption can be made: some literature reports no correlations between WM and GM damage (Bö, Geurts, van der Valk, Polman, & Barkhof, 2007), whereas others show that they are related (Mühlau et al., 2013). The GM masks for the patients likely included both healthy and damaged GM; we cannot separate these with the data collected. For future studies, it would be valuable to include other scans more sensitive to GM damage, to report alongside these GM physiological measurements, for example double inversion recovery FLAIR sequences to characterise GM lesions (Abidi, Faeghi, Mardanshahi, & Mortazavi, 2017) and techniques using quantitative mapping of MR parameters to characterise myelination within GM (Lutti, Dick, Sereno, & Weiskopf, 2014).

The voxel-wise analysis showed multiple small clusters that had significant decreases in the patient group, for CBF and $CMRO_2$ only. Both CBF and $CMRO_2$ were decreased in the subcallosal cortex and medial frontal regions, just CBF in the occipital pole and the para-hippocampal gyrus, and just $CMRO_2$ in the nucleus accumbens and the paracingulate gyrus. Considering the wide-spread nature of the damage reported in MS we did not have any clear predictions of certain regions showing vascular or metabolic differences at the group level, and it must be noted that these clusters are very small. However, it is interesting that some of the regions we report are areas where new lesions appear more frequently. For example Calabrese et al (2015) tracked the distribution and evolution of GM lesions over 5 years and showed new lesions appeared more frequently in the hippocampus, parahippocampal gyri, insula, cingulate cortex, superior frontal gyrus and cerebellum. The corpus callosum, subcortical regions and visual pathways are also common regions (Ge, 2006), which are close to the regions we observe these voxel-wise differences. We can therefore speculate that these differences in GM CBF and $CMRO_2$ are driven by existing or developing lesions in these areas, however this link has not been directly tested.

Patients reported lower GM volumes on average, lower $CMRO_2$ signals on average, and GM volumes positively correlated with $CMRO_2$ signals. Therefore, this is consistent with the idea that $CMRO_2$ is modelling tissue oxygen demand and that this demand is decreasing as GM volume decreases. It is difficult to say whether this relates simply to GM atrophy, or if there is a more generalised metabolic dysfunction in the GM of MS,

as has been proposed (Paling et al., 2011). Nevertheless, it adds to the evidence for a clear GM dysfunction in MS, mediated by metabolic and vascular impairments.

Model Assumptions

In order to estimate all these physiological parameters, there are many assumptions made about the underlying biology. It is important to consider whether the same assumptions would hold for a patient group, and also consider assumptions specific to this model. Future research should investigate these model assumptions to maximise the applicability of this method to an MS population, and disease populations in general.

We did not measure CBV but estimate the CBV changes within our model by assuming a power law relationship with CBF changes. This CBF-CBV coupling constant is based on animal data which was later confirmed with human data (Chen & Pike, 2010). However, this coupling relationship has not been explicitly studied in disease, and it may be that the assumptions are not valid for an MS population. The coupling may spatially vary with the variation in GM or WM tissue integrity. Indeed, DSC MRI studies have typically reported CBV reductions in an MS group (Aviv et al., 2012; Inglese et al., 2007, 2008; Papadaki et al., 2012; Vitorino et al., 2017), although often in the deep GM. In this literature, CBF and CBV reductions, in the same participants, have been reported in different regions (Vitorino et al., 2017), and significant regional changes in GM CBV have been reported without changes in GM CBF, after controlling for confounds (Aviv et al., 2012). The modelling of the dual-calibrated data (Germuska et al., 2019) included priors to stabilise the fitting process, as has been done previously (Germuska et al., 2016; Wise et al., 2013). This was in the form of a non-linear least squares fit, with regularisation. This regularisation procedure gives the model additional information, to help prevent overfitting, and therefore minimise the effect of random noise on the model fit. Germuska et al (2019) carried out digital phantom simulations to optimise the amount of regularisation, which was applied to the OEF and D_c parameters only. For OEF, an expected value of 0.4 was set for all voxels, and D_c was assumed to be linearly related to the voxel-wise GM PVE. The noise variance was estimated for each voxel separately, therefore this regularisation technique was spatially adaptive. Considering the use of this OEF prior, it is possible that the lack of difference between patients and controls for OEF could be driven by underfitting or overfitting of the data, if this is not an appropriate assumption to make about the MS physiology in general. If there was a true difference in OEF in the MS group that is not being measured, this would also affect the $CMRO_2$ group comparisons. As mentioned in the introduction, Ge et al (2012) report decreased global OEF and decreased global $CMRO_2$ using the T2-relaxation-

under-spin-tagging (TRUST) sequence. Another study (Fan et al., 2015) showed a 3.4% difference in OEF between MS patients and controls, using a phase-based MRI method at 7T. This is a very different method than our dual-calibrated approach: selected veins parallel to the magnetic field were modelled as long cylinders to quantify the susceptibility difference between the vessel and the tissue, in order to model OEF. However, it gives some evidence there may be OEF difference in MS. In contrast to this, MR susceptometry-based oximetry data (Jain, Langham, & Wehrli, 2010) we collected on a subset of the same participants (14 controls and 18 patients), in the same session as the dual-calibrated data, showed no differences in OEF between groups (Supplementary Table 5-1). These results are whole-brain measurements, with no priors informing the estimates of CBF, $CMRO_2$ and OEF. Lastly, parameter maps looked physiological plausible, and there were no significant differences in model fit (as characterised by the average and SD of residuals over voxels) between patients and controls.

Practical considerations and applications

We did not find any relationships between the composite disease impact scores (cognitive and physical general disease impact and experience of fatigue) and CBF or $CMRO_2$. The four sub-scores from the two questionnaires strongly correlated with each other, so it was important not to include them in the model as separate predictor variables. Absence of correlation between perfusion abnormalities in MS and clinical measures of disability is a common finding in the literature (Lapointe et al., 2018). The dual-calibrated study in Alzheimer's patient's (Lajoie et al., 2017) also reported no significant correlations between the physiological parameters and cognitive assessments. Larger samples and further investigation is needed to understand the clinical relevance of vascular and metabolic impairments we report. However, as can be seen in Figure 5-1 recruitment for this type of study is challenging considering the long list of eligibility criteria, and the commitment required from each participant. Furthermore, two researchers are required to be both MRI trained and trained to administer gases, and in this study an anaesthetist was also present to ensure participant safety, and to respond in the case of an adverse reaction to the gas delivery. However, compared to the dual-calibrated Alzheimer's study by Lajoie et al (2017) we did not have as many issues with patient drop-out. Lajoie et al (2017) go from n=64 patients recruited to n=34 datasets due to: 10 dropping out during the hypercapnia testing, 4 due to equipment malfunction, 6 due to the presence of mask leakage and 5 during the gas inhalation. Although we report some similar issues (Figure 5-1) we had a lower drop-out rate. One likely contributing factor to this is the age of our participants:

the average age our MS sample was 35 years, and for their Alzheimer's cohort it was 77 years. Furthermore, individuals with MS are often familiar with the MRI environment considering it is used within the diagnostic and treatment monitoring process. Therefore, application of these methods to an MS population is likely to be practical feasible.

Finally, these vascular and metabolic impairments may differ at different stages of MS. In this sample, the MS patients were of the RRMS type, they had no changes in medication for at least 3 months, and no relapse in the last 3 months. In actively inflamed WM tissue, there are reports of higher CBF and CBV, not lower (Ge et al., 2005; Haselhorst et al., 2000; Ingrisch et al., 2012; Wuerfel et al., 2004). These CBF and CBV increases presumably reflect a higher metabolic demand, but this had not been tested directly. For chronic WM lesions, looking T1-hypointense, there is evidence for a reduction in CBF (Haselhorst et al., 2000; L. Li et al., 2014). One study reports lower CBF and CBV in cortical lesions, in RRMS patients, compared to normal appearing GM (Peruzzo et al., 2013), however, a small subset show increased CBF and CBV, suggestive of acute inflammation.

Conclusions

This chapter displayed the first application of a dual-calibrated fMRI method in an MS population, showing evidence for reduced blood flow and oxygen metabolism across the GM, in the absence of changes in reactivity of blood vessels, OEF and effective oxygen diffusivity. As $CMRO_2$ was positively correlated with total GM volume, and GM volume was reduced in these patients, this may suggest there is a reduced demand for oxygen in the GM. The development of these methods are ongoing, but these results demonstrate the feasibility of measuring and estimating many important physiological parameters relevant to MS pathology.

5.5 SUPPLEMENTARY

ELIGIBILITY CRITERIA
[Patient only]

Inclusion

- Aged between 18 and 45 years
- Speak fluent English
- ***Diagnosis of MS*** (no other neurological/psychiatric conditions)
- ***Medications and rehab stable for at least 3 months***

Exclusion

- MRI contraindications
- Current smoker
- History of diabetes, blood-borne disease, haemophilia, rest angina, asthma (in past 2 years), shortness of breath at rest, regular dizziness, epilepsy, head trauma
- Pregnant or have given birth in the last 6 weeks
- Been involved in any drug trials in the last 4 weeks
- History of drug dependency or have taken any illicit drugs in the last 4 weeks
- ***Have experienced a relapse in the 3 months prior to taking part***
- ***Have been prescribed steroid drugs in the 3 months prior to taking part***

  Information on any medications the participant was currently taking (prescribed and unprescribed) was asked about to ensure that they did not interfere with breathing, and therefore interact with the gas protocol. An anaesthetist reviewed all reported medications before proceeding with the practise gas protocol.

Supplementary Figure 5-1. Eligibility criteria for controls and patients, for the dual-calibrated fMRI study.

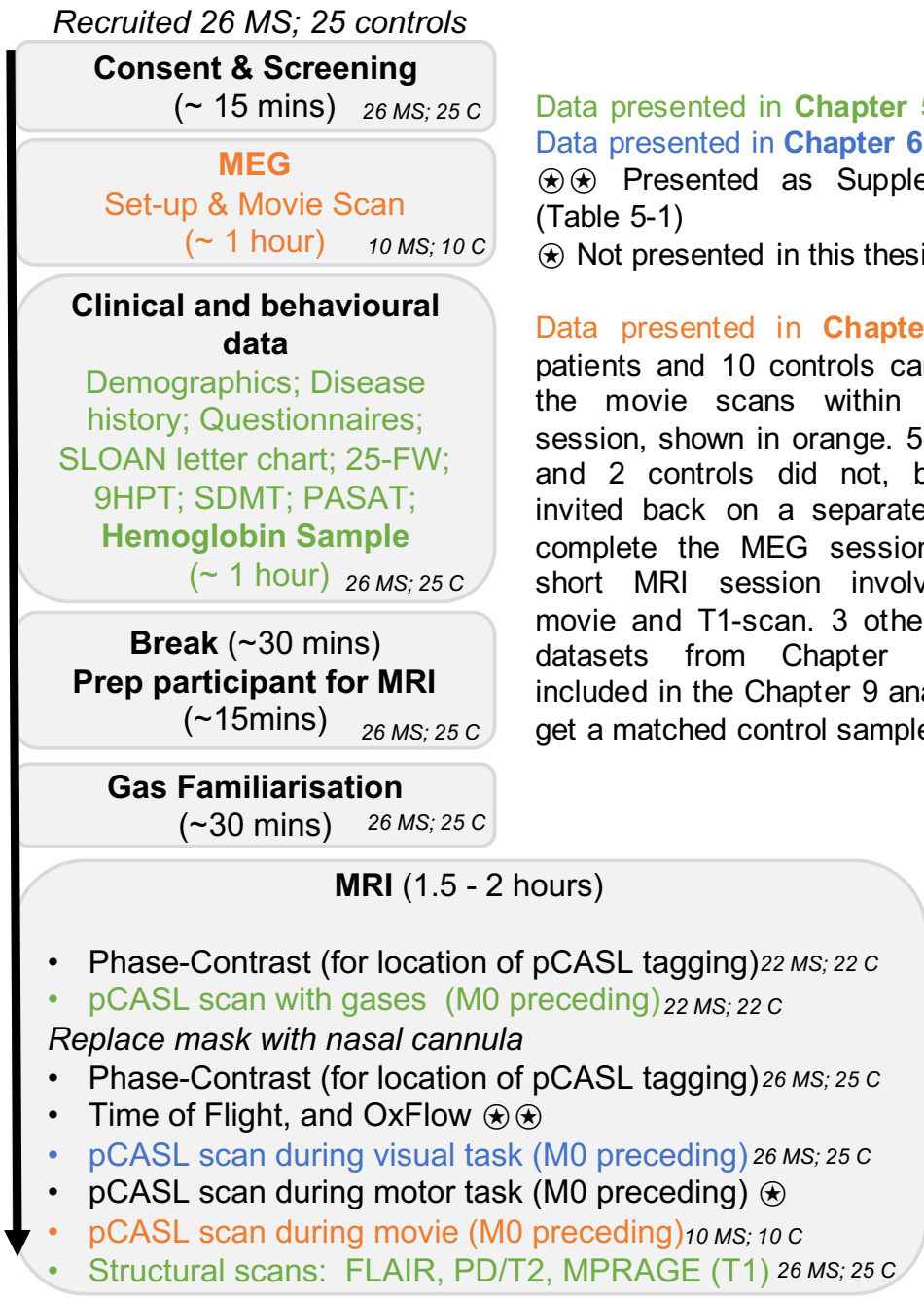

Data presented in **Chapter 5 and 6.**
Data presented in **Chapter 6.**
⍟⍟ Presented as Supplementary (Table 5-1)
⍟ Not presented in this thesis

Data presented in **Chapter 9.** 10 patients and 10 controls carried out the movie scans within the full session, shown in orange. 5 patients and 2 controls did not, but were invited back on a separate day to complete the MEG session and a short MRI session involving the movie and T1-scan. 3 other control datasets from Chapter 7 were included in the Chapter 9 analysis, to get a matched control sample of 15.

Supplementary Figure 5.2. A typical testing session for one participant, showing which data contributed to Chapters 5, 6 and 9.

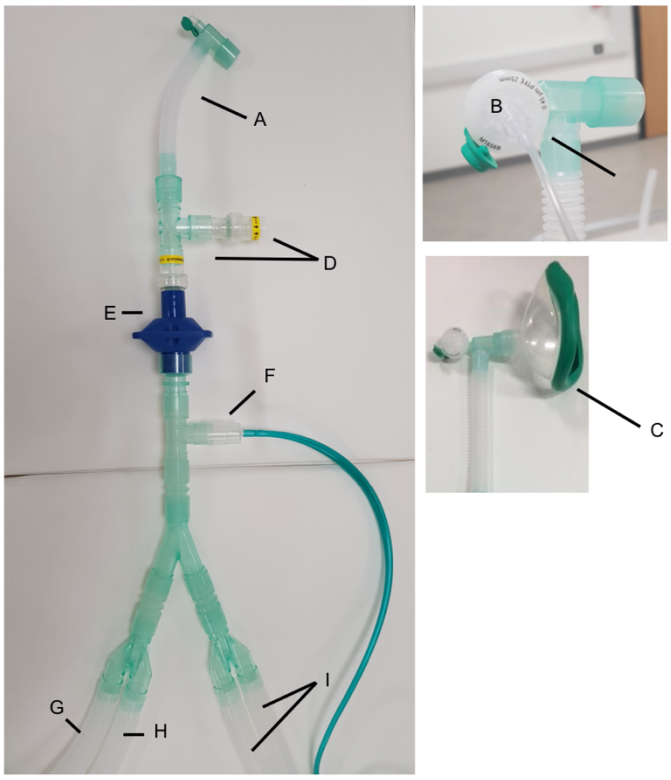

A: Flexible catheter mount
B: Small round filter for catheter mount, with sampling line attached, to measure the end-tidal gases.
C: Participant's face mask attached to [B]
D: One-way valves to prevent rebreathing of expired gases
E: Blue bacterial filter
F: Oxygen analyser outlet connecting to the the oxygen analyser in the MR control room. Alarm sounds if the inspired oxygen is too low.
G: Emergency oxygen connection. Corrugated tubing connects to a short green tube and the emergency oxygen cylinder (100% O_2) in the control room. This set up is critical to ensure that in an emergency O_2 can very quickly be supplied to a participant.
H: Main gas supply from the mixing chamber. The mixing chamber (in the MR control room) is connected to a mass flow-controller where MATLAB software control the gas mixtures at each stage of the experiment. Gases from this mixing chamber are passed through a humidifier chamber (more comfortable for the participant to breathe) before flowing through corrugated tubing (typically 24 lengths), reaching the circuit, and being delivered to the participant through the face-mask.
I: Corrugated tubing (3 lengths) not connected to anything. Therefore, in an event of a failure of the gas delivery system, participants will breathe in normal room air.
Parts not labelled are typically T or Y shaped connectors.

Supplementary Figure 5-3. Gas delivery circuit set-up for the calibrated fMRI study.

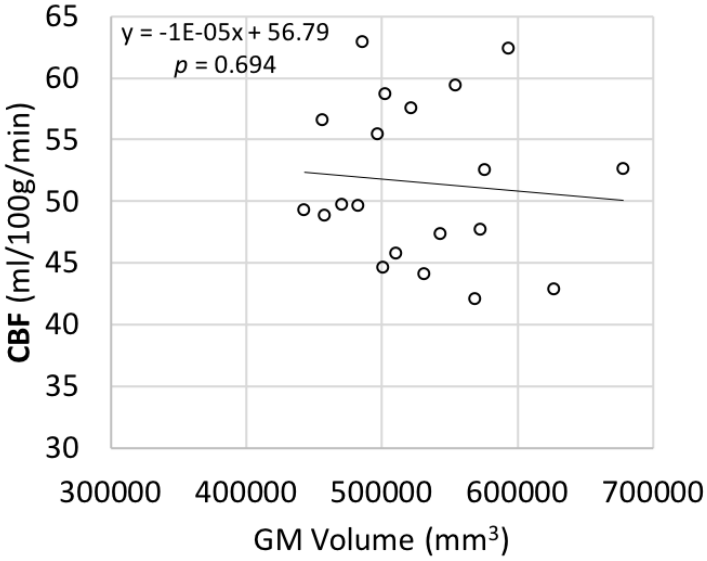

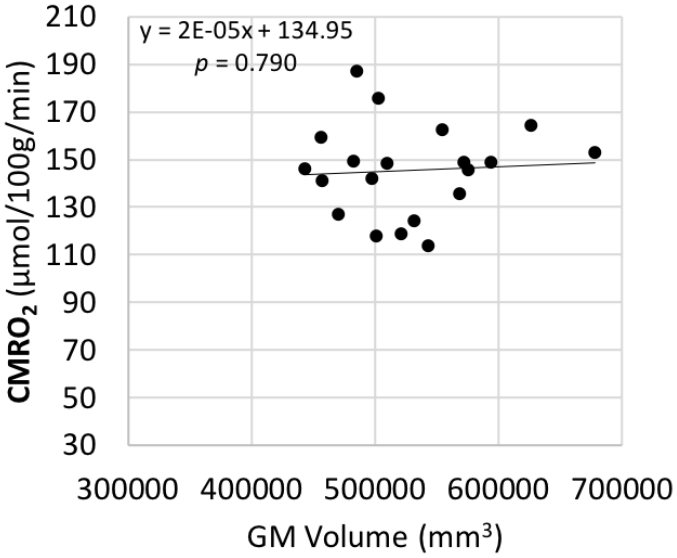

Supplementary Figure 5.4. Relationship between GM volume and CBF (top), and between GM volume and CMRO2 (bottom), for the control group only. p values refer to testing the beta coefficients against zero (uncorrected).

	Patients (n=18)	Controls (n=14)	P-value (2-tailed)
CBF	49.22 ± 8.93	51.95 ± 6.46	0.343
OEF	0.25 ± 0.08	0.24 ± 0.07	0.591
$CMRO_2$	107.14 ± 35.12	106.10 ± 20.27	0.922

Supplementary Table 5-1. Results from an OxFlow sequence in a sub-set of the same participants presented in this chapter. OxFlow calculates SvO_2 in the superior sagittal sinus (SSS) through susceptometry-based oximetry. Scan duration of 1.17 minutes. A time of flight sequence is also acquired to localised the SSS, and a phase-contrast scan to localise the neck vessels.

6 Blood flow and oxygen metabolism changes in Multiple Sclerosis, during visual stimulation, using calibrated-fMRI

6.1 INTRODUCTION

Chapter 5 provided evidence for reduced CBF and $CMRO_2$ in MS, when the brain is at rest. It is also important to understand how blood flow and oxygen usage change when there is a change in demand (i.e. in response to a functional task) as this may be more directly related to functional impairments and therefore disease impact. By measuring $CMRO_2$ signals, we are getting closer to measuring the metabolic demand of neural activity (Buxton, 2010; Du et al., 2008; Hyder, 2010). If this metabolic demand is altered in MS, it may indicate neural or metabolic dysfunction or atrophy in these areas. Furthermore, if we characterise the coupling between CBF and $CMRO_2$ signals to the same task or stimulus, this will inform whether the vascular system is responding appropriately to the level of demand. If it isn't, this may be a factor contributing to longer term damage in the MS brain.

There is evidence to suggest that investigating the visual system may help probe MS pathology both when functional impairments are present and when they are not. A common initial presentation of MS is optic neuritis, an acute visual impairment characterised by a reduction in visual acuity and connectivity in visual pathways (Polman et al., 2011; Toosy et al., 2014). However, abnormalities of visual pathways, in the absence of optic neuritis and visual symptoms, have also been reported in MS (Alshowaeir et al., 2014; Graham & Klistorner, 2017; Sisto et al., 2005), mostly attributed to post-chiasmal damage along the visual WM pathways, but could also be related to the more widespread vascular and metabolic alterations (discussed in Chapter 3.2). Only one research group have previously investigated task-induced $CMRO_2$ in an MS population (Hubbard, Araujo, et al., 2017; Hubbard, Turner, et al., 2017). They demonstrated significant lower CBF and $CMRO_2$ visual evoked changes in MS patients compared to controls, and report that the $CMRO_2$ change was one of the top measures to accurately classify MS status (Hubbard, Araujo, et al., 2017).

For these reasons, and due to the visual fMRI recordings being easy to implement in patient groups, we investigated BOLD, CBF and $CMRO_2$ changes to a visual-checkerboard stimulus in MS. Based on the findings by Hubbard et al, on the lower baseline CBF and $CMRO_2$ signals we report in Chapter 5, and on the reductions in BOLD and CBF to a visual stimulus in Chapter 4, we hypothesised reduced visual

BOLD, CBF and $CMRO_2$ responses in the MS group, and correlations with disability. Unlike the previous work, this chapter also considers the effect of baseline CBF and $CMRO_2$ on the task-induced visual BOLD, CBF and $CMRO_2$ changes.

6.2 METHOD

Participants

The same controls and patients were used in Chapter 5, Chapter 6 (this chapter) and Chapter 9; an overview of this data collection is displayed in Supplementary Figure 5-2. 26 patients and 23 controls completed the visual checkerboard task after the dual-calibrated acquisition. Of these, 22 patients and 20 controls had corresponding dual-calibrated fMRI data, allowing us to model the $CMRO_2$ response.

Data Collection

Data collected from questionnaires and behavioural testing is explained in Chapter 5. For the imaging, the same DEXI pCASL acquisition, as explained in Chapter 5, was acquired during a visual task. The visual stimulus consisted of a reversing checkerboard (total size 8x8 degrees of visual angle, checks 3 cycles per degree, 100% contrast, checkerboard polarity reversing every 250ms). The design included a 30 second rest block followed by a 30 second stimulus block, repeated 8 times, then ending on rest block (total time 8.5 minutes). Participants were asked to focus on a red fixation square in the centre of the image, present during rest blocks and stimulus blocks.

Data Analysis

Pre-processing. The first and second echo from the visual DEXI-pCASL data were motion corrected (McFLIRT) and brain extracted (BET). Spatial smoothing was carried out with a Gaussian kernel of FWHM 4.3mm, with a high-pass temporal filter applied with a cut off of 90s. Registration of CBF data (first echo) and BOLD data (surround average of second echo) to individual T1-structural data (linear, 6 DOF) and then to MNI standard space (linear, 12 DOF) was carried out using FSL FLIRT. Using FSL-FEAT, perfusion time courses were modelled from the first echo data, and BOLD time courses from the second echo data (in a separate FEAT design), with the inclusion of regressors explicitly describing the tag-control signal differences. A higher-level analysis was performed with FEAT using a mixed effects model (FLAME 1+2) to model the effect of the checkerboard stimulus across all participants (regardless of group),

and to model any 'Control-Patient' or 'Patient-Control' significant differences. Z statistic images were thresholded using clusters determined by Z>2.3 and a (corrected) cluster significance threshold of p = 0.05 (Worsley, 2001). Diagrams of the FEAT models can be seen in Supplementary Figure 6.1.

BOLD, CBF, M and $CMRO_2$ over group ROIs. For each subject, BOLD and CBF signals (and therefore the modelling of $CMRO_2$) were characterised as change from baseline, averaged over two ROIs. The first ROI consisted of common significant voxels between the BOLD group contrast and the CBF group contrast (average contrast across patients and controls). The second ROI consisted of common significant voxels between the BOLD 'Control-Patient' contrast and the CBF 'Control-Patient' contrast. There were no significant voxels in the 'Patient-Control' contrast for BOLD or CBF. These two ROIs, in MNI space, where transformed to subject space, binarised, and a mean BOLD and CBF percentage signal change to the visual stimulus was calculated over each ROI.

In order to model $CMRO_2$ we need an estimate of the calibration factor *M* over the same ROI, to input into:

$$\frac{CMRO2}{CMRO2_0} = \left(\frac{CBF}{CBF_0}\right)^{1-\frac{\alpha}{\beta}} \cdot \left(1 - \frac{\frac{\Delta BOLD}{BOLD_0}}{M}\right)^{\frac{1}{\beta}}$$

This equation, based on (Davis et al., 1998), was introduced and explained as Equation 2-7 in Chapter 2. In Chapter 5, the baseline data was quantified using a simplified BOLD model (Merola et al., 2016), so for consistency the standard calibration model (Davis, Kwong, Weisskoff, & Rosen, 1998) was modified to:

$$\frac{CMRO2}{CMRO2_0} = \left(\frac{CBF}{CBF_0}\right)^{1-\theta} \cdot \left(1 - \frac{\frac{\Delta BOLD}{BOLD_0}}{TE \cdot \kappa \cdot [\mathrm{dHb}]_0}\right) \qquad \text{(Equation 6-1)}$$

TE is the echo time of the acquisition, κ is a composite calibration parameter that represents the combination of the venous weighted blood volume and water diffusion effects, *[dHb]* is the de-oxyhemoglobin concentration and is equal to Hemoglobin x (1-S_vO_2) and θ (assigned a value of 0.06, previously represented by both α and β) is an empirical parameter combining contributions from venous blood volume changes and extra-vascular water diffusion effects.

Therefore, maps of *M* (specifically: $TE \cdot \kappa \cdot [\mathrm{dHb}]_0$) where made from the baseline (resting) pCASL data in Chapter 5 for each participant. Example M-maps, for 2 patients and 2 controls, are showed in Figure 6-1. The group visual ROIs (in MNI space) were transformed to T1-space, then to the subject's M-map space, to obtain an average *M* over this region, as with BOLD and CBF response to the visual stimulus. Then the relative $CMRO_2$ response to the stimulus was modelled as per Equation 6-1. Baseline CBF and $CMRO_2$ were also averaged over these ROIs, in order to include in the statistical modelling. The coupling between CBF and $CMRO_2$ to the visual response was calculated (CBF/ $CMRO_2$) and represented by the parameter *n.*

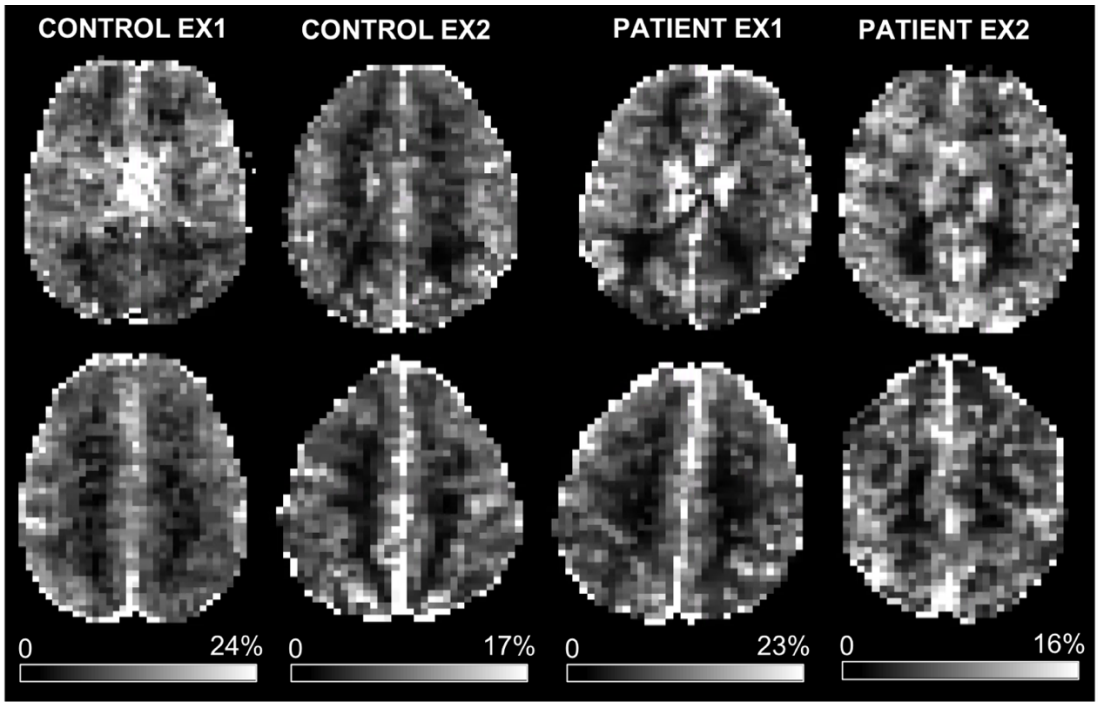

Figure 6-1. Maps of the M parameter ($TE \cdot \kappa \cdot [dHb]_0$) outputted from the dual-calibrated fMRI modelling in Chapter 5. Examples are shown for two controls and two patients.

Statistics

To test the difference between groups for the *M* and *n* parameters independent sample t-tests were carried out. If assumptions of normality were violated, Mann Whitney U tests were carried out to test medians. In the *difference ROI* (explained below), variance in BOLD, CBF and $CMRO_2$ visual responses were predicted with group membership, visual acuity and baseline CBF/$CMRO_2$ over the same ROI, using multiple linear regressions. In the patient group only, a linear multiple regression was performed to predict the patient's CBF and $CMRO_2$ visual responses in the *difference ROI* using the composite disease impact score and lesion volume. All assumptions were met unless

other otherwise stated Outliers were defined as being 3xSD above or below the mean, or 3xIQR above or below the lower or upper quartile, respectively.

6.3 RESULTS

BOLD and CBF responses to the visual stimulus

Figure 6-2 (A-C) display the BOLD and CBF results from the group FEAT analysis. Four significant clusters were found for the BOLD response to the visual stimulus: an occipital cluster (Z-MAX = 8.6, [26,-96,4]), a right precentral gyrus/middle frontal gyrus cluster (Z-MAX = 4.82, [-46 0 30]), a left precentral gyrus cluster (Z-MAX =4.33, [52,-6,50]), and a frontal pole cluster (Z-MAX =4.06, [-20, 62, 24]). Significant voxels, in response to the stimulus, common to BOLD and CBF (across both groups) were found in the posterior occipital cortex (occipital pole) and lateral occipital cortex, and this is referred to as the '*Group ROI'* from now on. This region was the only significant cluster in the CBF group analysis. A small region (localised centrally, overlapping with the occipital pole and posterior areas of lingual gyrus, central voxel: [2,-90,-12]) was found to have significantly greater activity for controls than patients, in both BOLD and CBF contrasts, and this is referred to as the '*Difference ROI'* from now on.

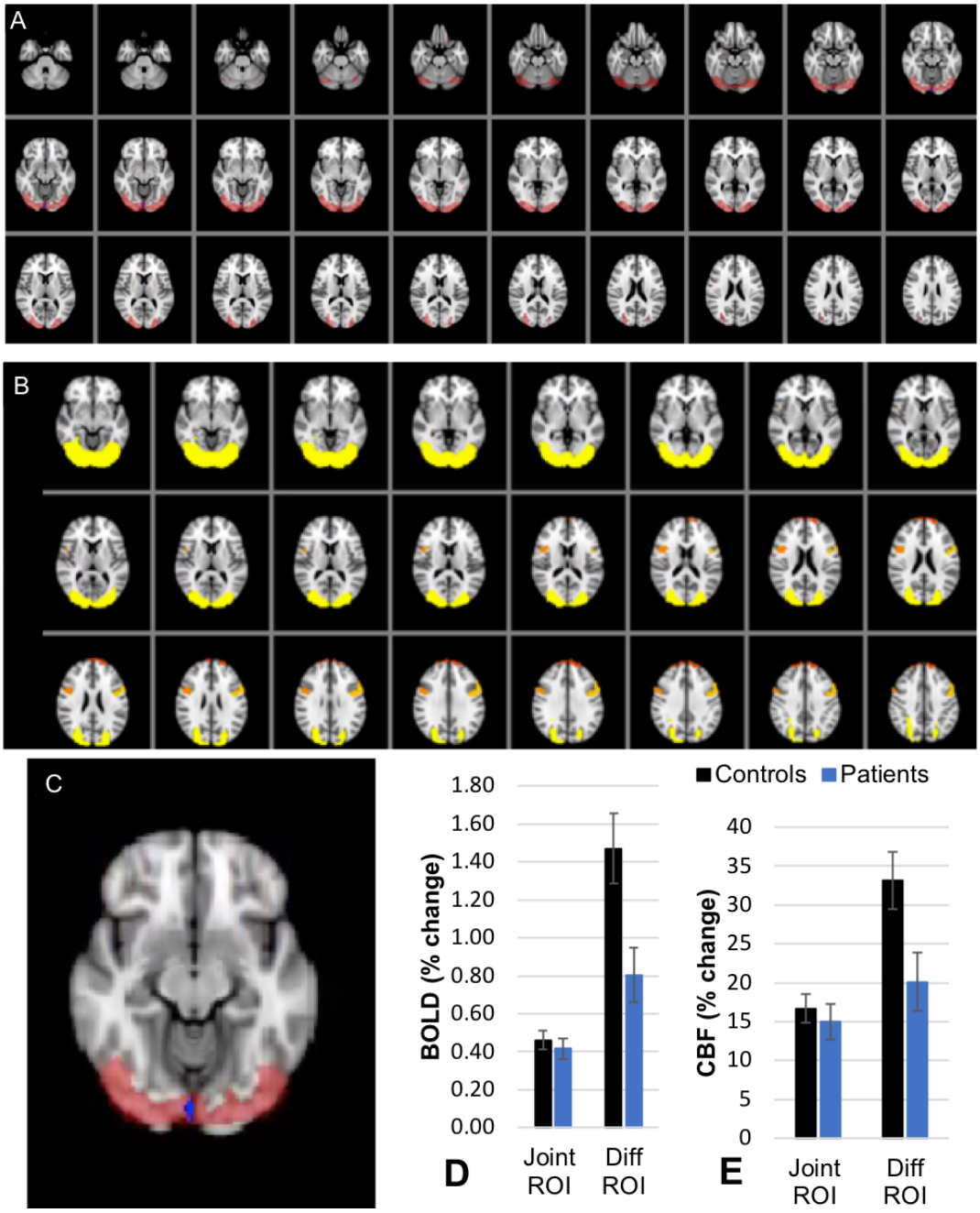

Figure 6-2. ***A & C****: Red displays significant voxels in response to visual stimulus, common to BOLD and CBF (based on Z>2.3 thresholded clusters, p=0.05), across both groups. The small blue region displays voxels with significantly greater activity for controls compared to patients, common to BOLD and CBF.* ***B:*** *Significant clusters in the BOLD analysis, across groups. Yellow shows an occipital cluster, light orange a right precentral gyrus/middle frontal gyrus cluster, dark orange a left precentral gyrus cluster and red a frontal pole cluster. There were no further significant voxels in the CBF analyses, than the one common to BOLD shown in Figure A.* ***D and E****: Comparing percentage change BOLD and CBF signals between patient and controls, averaged over the Joint ROI (red, A & C) and the Difference ROI (blue, A & C) to display the magnitude of the signal changes, on average.*

Modelling the $CMRO_2$ response to the visual stimulus

Group averages for the visual BOLD, CBF and $CMRO_2$ responses for both ROIs are displayed in Table 6-1. The *Difference ROI* (Figure 6-2C) was only made up of 39 voxels and therefore averaging M over this ROI for each subject separately, in order to model $CMRO_2$, was unreliable. Many participants, in both groups, had very physiologically unrealistic M value estimates over this ROI. For example, the minimum *M* value was 6%, the maximum was 62% and the mean ± SD was 15% ± 12, presumably because there were not enough voxels to average out noise. Therefore, the subsequent $CMRO_2$ modelling in the *Difference ROI* was based on *M* values averaged over the *Group ROI* (Figure 6-2A) for each subject. For *M* values in the *Group ROI*, one patient was an extreme outlier (with a z-score of 3.87 and an average *M* value of 20.03%) so was left out of the subsequent $CMRO_2$ group comparison. The remaining 20 controls (7.57% ± 0.31) and 21 patients (8.01% ± 0.30) did not have significantly different M values, ($t(39) = 1.01$, $p = 0.315$). The $CMRO_2$ responses from the *Group ROI* were not significantly different between patients and controls, $t(38) = 0.125$, $p = 0.901$. Statistical comparisons are not reported for the *Difference ROI* here, as group comparisons are carried out within a regression model later in the results, alongside other predictor variables.

	BOLD (% change)		**CBF (% change)**		**$CMRO_2$ (% change)**	
	Group ROI	*Diff ROI*	*Group ROI*	*Diff ROI*	*Group ROI*	*Diff ROI*
Controls Mean	0.46	1.33	15.79	33.76	7.63	5.05
Patients Mean	0.46	0.87	16.39	21.98	7.44	5.66
Controls SD	0.23	0.57	7.93	15.71	4.51	9.97
Patients SD	0.24	0.64	9.71	16.56	4.91	8.72

Table 6-1. BOLD, CBF and $CMRO_2$ visual response, expressed as percentage change from baseline, for each ROI. Extreme outliers were removed from these means: one patient for Group ROI $CMRO_2$ and one control for Diff ROI BOLD.

Is Flow-Metabolism coupling altered in patients?

The coupling between task-induced change in CBF and $CMRO_2$ was compared between patients and controls in each ROI, and this is shown in Table 6-2. A coupling of around *n=2* is consistent with previous work, however there were no significant differences between patients and controls. In the *Group ROI*, there was a trend for patients to have lower *n* values on average (*p*=0.07).

	Group ROI		***Difference ROI***	
	n *(Mean ± SD)*	***p-value***	***n*** *(Median, IQR)*	***p-value***
Controls	2.07 ± 0.38	0.07	1.50, *3.73*	0.35
Patients	1.82 ± 0.49		2.56, *6.48*	

Table 6-2. Comparison of the coupling parameter n (CBF/CMRO2) between patients and controls, to the visual stimulus. For the group ROI comparison, two patients and one control where removed as they were extreme outliers. For the difference ROI, one patient was removed as they were an extreme outlier. The n values for the difference ROI were not normally distributed for both groups, so a non-parametric test of medians was run.

What factors can explain the differences between patients and controls?

We investigated factors that may explain the BOLD, CBF and $CMRO_2$ differences between patients and controls in the region where there was significantly reduced activity (*Difference ROI).* As this regression analysis is based on average signals in the region where the group FEAT analysis showed significant group differences, we expect group membership to make a significant contribution to this model. Including this variable also allows us to consider interactions between group and other predictor variables. Visual acuity in the right eye (shown in Chapter 5) was significantly worse for the patient group, therefore visual acuity (averaged across both eyes, as the stimulus was shown bilaterally) was included as a predictor. Visual acuity was included, instead of history of optic neuritis, as this data existed for both patients and controls and was reflective of the patient's visual function on the same day of scanning. Ten patients had no history of optic neuritis, five patients reported one previous episode, four patients reported two and one patient reported three episodes. As baseline CBF and $CMRO_2$ differences were demonstrated in Chapter 5 their effect on the visual stimulus response was also modelled. The relationship between baseline signals and group membership with visual stimuli responses is displayed in Figure 6-3.

For predicting visual CBF responses, the overall model was significant, R^2 of 29.3% (F (3, 36) = 4.98, p = 0.005. Baseline CBF (β = -0.362, p = 0.021) and group membership (β = 0.552, p = 0.001) significantly contributed to the model predicting visual CBF. Visual acuity did not make a significant contribution to the model (β = -0.193, p = 0.186). Including an interaction term in the model between baseline CBF and group membership did not make a significant contribution to the model (p = 0.902). For predicting visual BOLD responses, the overall model was significant R^2 of 29.3% (F (3, 36) = 4.98, p = 0.005). Baseline $CMRO_2$ (β = -0.377, p = 0.012) and group membership (β = 0.387, p = 0.011) significantly contributed to the model predicating visual BOLD, but visual acuity did not (p = 0.962). Including an interaction term in the model between baseline $CMRO_2$ and group membership did not make a significant contribution to the model (p = 0.342). For predicting visual $CMRO_2$ responses, the overall model was not significant, R^2 of 12.0% (F (3, 36) = 1.63, p = 0.199). Baseline $CMRO_2$ (β = 0.146, p = 0.361), group membership (β = 0.021, p = 0.898), or visual acuity (β = -0.297, p = 0.074), did not display beta coefficients significantly different to zero.

What factors can explain variability in the patient group?

As Hubbard et al (2017) showed a relationship between visual $CMRO_2$ and disease impact scores (fatigue) and WM damage, we examined whether the composite disease impact score and lesion volume could predict BOLD, CBF or $CMRO_2$ visual responses in the patient group only, in this *Difference ROI*. Lesion volume and disease impact did not significant predict BOLD (R^2 of 8.3% (F (2, 18) = 0.81, p = 0.459), CBF (R^2 of 8.1% (F (2, 18) = 0.79, p = 0.468), or $CMRO_2$ (R^2 of 8.1% (F (2, 18) = 0.79, p = 0.468) visual responses in the patient group.

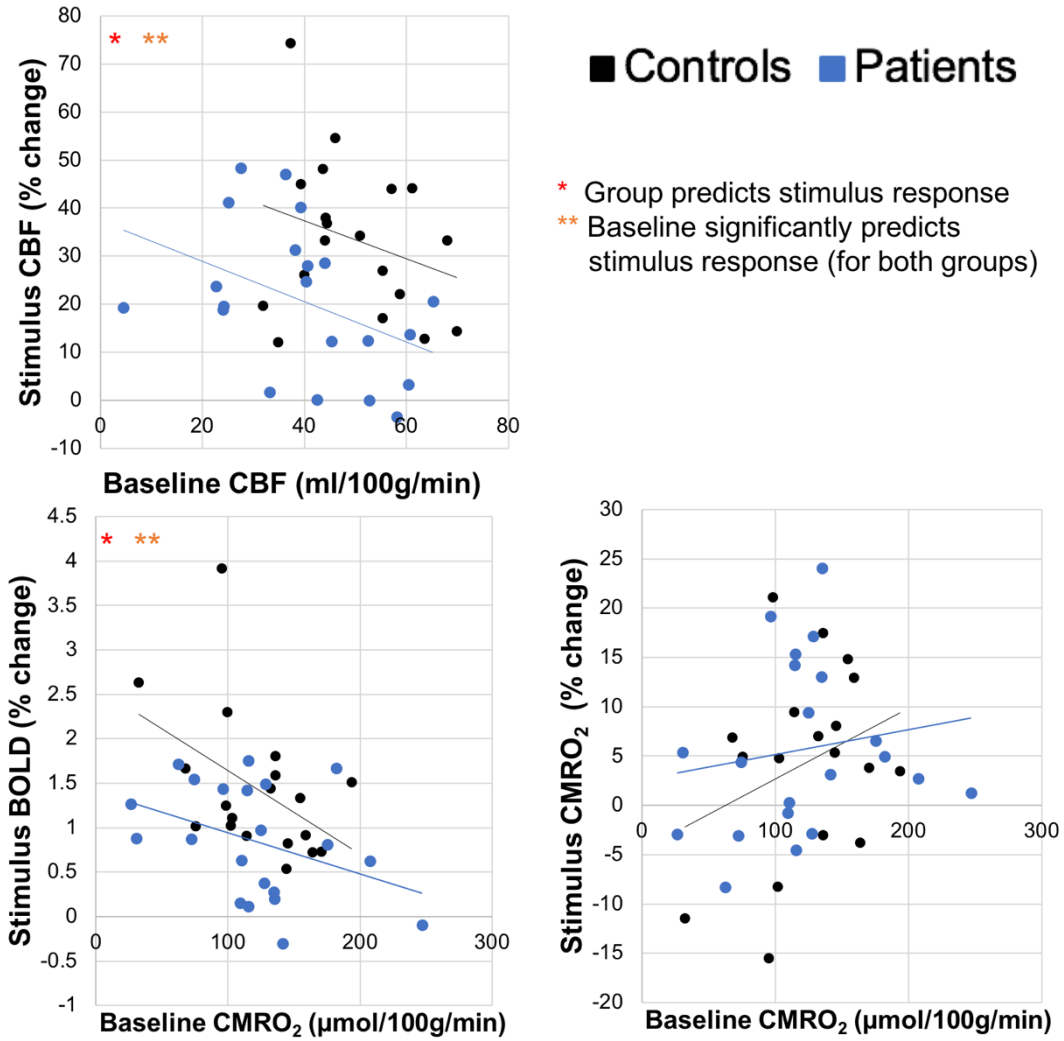

Figure 6-3. Top: relationship between baseline CBF (ml/100g/min) and visual stimulus CBF (percentage change). Middle: relationship between baseline $CMRO_2$ (µmol/100g/min) and visual stimulus BOLD (percentage change). Bottom: relationship between baseline $CMRO_2$ (µmol/100g/min) and visual stimulus $CMRO_2$ (percentage change). Patients are shown in blue and controls in black. Signals are modelled in the Difference ROI from the group FEAT analysis

6.4 DISCUSSION

As has been done previously in calibrated-fMRI studies, here we characterised the relative $CMRO_2$ response to a visual stimulus, based on a simplified BOLD model (Merola et al., 2016), combined with the standard calibration model (Davis, Kwong, Weisskoff, & Rosen, 1998). We created the calibration factor *M* using sequence parameters and parameter outputs from the dual-calibrated modelling in Chapter 5, in order to model the relative $CMRO_2$ response. As we had quantified baseline CBF and $CMRO_2$ responses in the same participants, from Chapter 5, we considered the effect of these signals in the same brain region when looking at stimulus responses. In response to the visual stimulus, a small region in the visual cortex showed significantly lower CBF and BOLD stimulus responses in the patient group compared to the controls. However, no significant differences were found between patients and controls for visual $CMRO_2$ responses, and disease characteristics did not predict BOLD, CBF or $CMRO_2$ responses in the patient group. There were no significant differences for flow-metabolism coupling between groups. For both patients and controls, we found that baseline CBF and $CMRO_2$ values significantly predicted stimulus CBF and stimulus BOLD responses, respectively.

Changes in the BOLD response to visuomotor tasks have been previously demonstrated, showing that inflammation and WM structural damage play a role in altering haemodynamic responses in MS (Hubbard et al., 2016; Tomassini et al., 2016). Consistent with this, we found a significantly reduced BOLD and CBF response in the visual cortex of MS patients, although this could not be predicted by their visual acuity scores. It was surprising to not find more wide-spread differences in BOLD, CBF or $CMRO_2$ signals in the patient group, except for this small ROI in occipital pole/posterior lingual gyrus, considering previous literature, and our results presented in Chapter 4. In Chapter 4, we do not report $CMRO_2$ responses to a visual stimulus, but do show clear BOLD, CBF and gamma power reductions in the MS group. In fact, the biggest difference in gamma power change (directly reflecting neural activity) was seen at 100% visual contrast. This is not consistent with the lack of differences we report here with the visual checkerboard also at 100% contrast. In Chapter 4, the patients and controls were older on average (around 43 years), compared to the cohort presented in this chapter, and were treatment naive. This may have meant they had higher levels of inflammation, which is one explanation for greater impairments reported. In Chapter 4, the visual stimulus was shown to each eye separately; considering optic neuritis and visual abnormalities are common in MS, this may have given more sensitivity to

measure abnormalities. In this study, we chose to display to both eyes together due to time constraints but also to better reflect natural visual processing.

Visual $CMRO_2$ responses and the coupling between $CMRO_2$ and CBF (Blockley, Griffeth, Simon, & Buxton, 2013) were in expected ranges. Despite the *M* values being calculated from the dual-calibrated fMRI data in Chapter 5, they are in good agreement with the values from studies using only hypercapnia to calibrated the BOLD signals, which is more typical. We reported an average of 7.57% for controls and 8.01% for patients, which is in good agreement with previous single and dual calibrated studies (Driver, Wise, & Murphy, 2017; Gauthier & Hoge, 2013; Wise et al., 2013). Ideally, a voxel-wise approach to characterising $CMRO_2$ would be taken, allowing for more spatial sensitivity to functional changes. However, here we took an ROI approach, considering the level of noise in the *M* maps, which was particularly noticeable when trying to average *M* values over the small *Difference ROI.* In order to model $CMRO_2$ changes in this area, an average *M* value from the larger *Group ROI* was used, unfortunately reducing the spatial specificity of the *M* estimate.

Consistent with our results, Hubbard, Araujo, et al (2017) also report no differences between patients and controls for coupling between CBF and $CMRO_2$ to a visual stimulus. They also report no changes in visual BOLD responses. Their study had a specific focus on the predictive ability of visual evoked $CMRO_2$ responses in classifying MS status; alongside this they report large reductions in visual CBF responses (~45% reduced CBF response) and $CMRO_2$ response (~8% reduction) in their MS cohort, contrary to our results. Differences in characteristics of their MS cohort may be one factor to explain this. For example, their sample of 10 patients and 13 controls were much older on average (around 50 years) compared to our sample of 22 patients and 20 controls (around 35 years). Their patient group therefore had a longer average disease duration (119 months) compared to ours (95 months), and less time had passed since their last relapse, on average. It is therefore possible that these patients had more GM dysfunction due to more disease progression (Klaver et al., 2013a). Their visual task was different and more complex than the one used here; they controlled the participant's attention by changing the luminance of the fixation and requiring a button press response, they altered the orientation to avoid neural adaptation, and they had a flicker rate of 8Hz. Although fMRI studies typically report a peak response at 8Hz (Li, Chen, & Chen, 2011; Sun et al., 2014) thereby potentially giving the greatest signal-to-noise estimate, we wanted to keep our reversal rate (4Hz) consistent with what was used in Chapter 4, which was chosen in order to compare with MEG responses. Furthermore, as this chapter aimed to characterise $CMRO_2$ to a visual stimulus, there

is some evidence that the electrophysiological response, and the $CMRO_2$ response in accordance, peaks at 4Hz and not at 8Hz (see data in 11. Appendix 1).

In this chapter, we report no significant relationship between visual BOLD, CBF or $CMRO_2$ and disease impact scores (fatigue) and WM damage (lesion volume), in the patient group. This in contrary to the study by Hubbard, Turner, et al (2017), a different study to the one discussed earlier, which reported positive correlations between visual $CMRO_2$ responses and neurological disability and fatigue scores, in a study involving MS patients only. The direction of this relationship appears contrary to the results of the reduced $CMRO_2$ response in patients, compared to controls, reported in their other work. Further to this, they report that radial diffusivity of the occipital tract to be significantly positively correlated with visual $CMRO_2$ and negatively correlated with visual BOLD. The mechanisms for this are not clear, but they discuss neurovascular uncoupling in MS as a potential explanation for these different relationships. It is clear that more research needs to be done to characterise task-induced $CMRO_2$ changes in MS, particularly if they can show such different relationships with structural damage compared with BOLD signals.

In this chapter, baseline CBF (ml/100g/min) predicted CBF visual stimulus responses (%), and baseline $CMRO_2$ (μmol/100g/min) predicted BOLD visual stimulus responses (%), in the same brain region. These relationships were not significantly different for patients and controls, although it is interesting to note that one of the regions showing significantly lower CBF values in the voxel-wise analysis of Chapter 5 appears to be in a very similar location to the *Difference ROI* reported here, so it is likely this may have had some effect on the functional patient control differences reported here. Here we report that the lower the baseline CBF or $CMRO_2$ a participant has the higher their relative stimulus response. This has been reported previously in many fMRI studies (Hyder, Rothman, & Shulman, 2002; Kannurpatti, Biswal, & Hudetz, 2003; Pasley, Inglis, & Freeman, 2007; Shulman, Rothman, & Hyder, 2007). This suggests, if the CBF and $CMRO_2$ is lower at baseline, it will need to increase proportionately more to match the CBF and $CMRO_2$ changes due to neural activity. These findings show the importance of characterising the baseline state, in patient and healthy populations, for proper interpretation of relative stimulus changes.

Conclusions

We report differences in BOLD and CBF responses in MS, in a small region of visual cortex, not explained by changes in visual acuity. We do not report visual $CMRO_2$

changes, or differences in the coupling between CBF and $CMRO_2$ in the patient group, suggesting the vascular system is responding adequately to the level of demand. Although visual abnormalities are common in MS, MS is not specifically a disease of the visual system and there is great variability across participants in the type of symptoms and their severity. The signals and parameters modelled here, specifically CBF and $CMRO_2$, are physiologically specific and interpretable, yet they are noisy and sometimes spatially insensitive. With continual improvement of these methods, baseline and task-induced $CMRO_2$ changes will be able to be characterised more robustly on a voxel-wise basis.

6.5 SUPPLEMENTARY

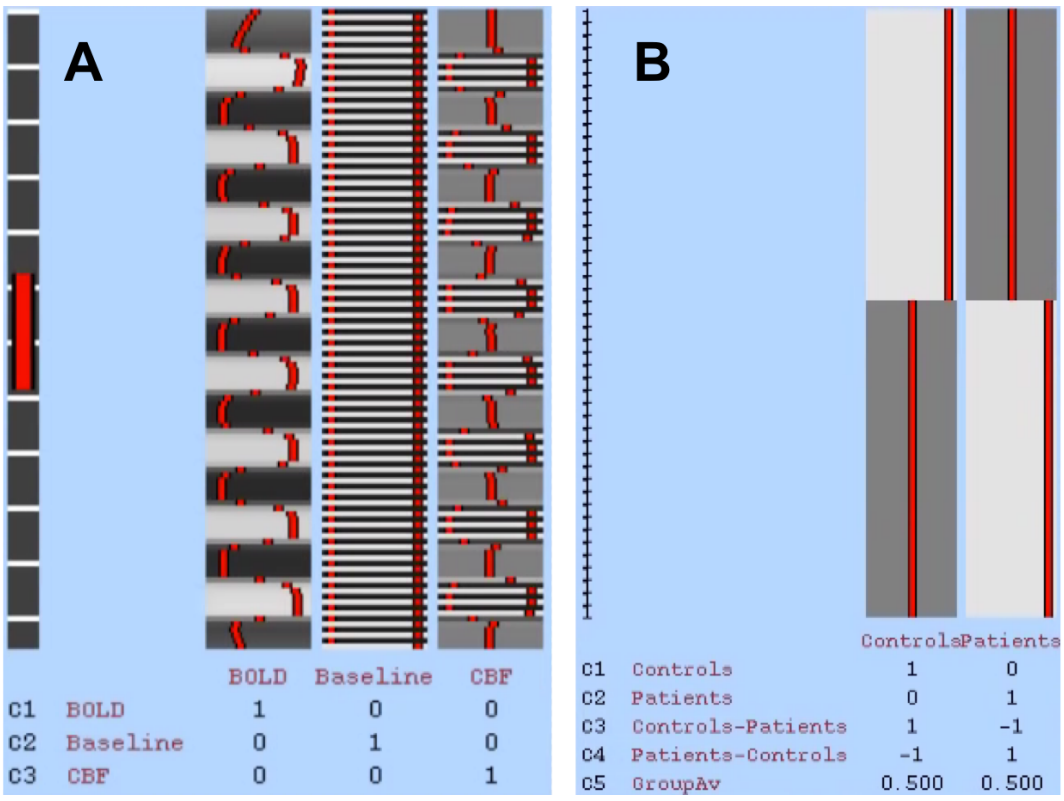

Supplementary Figure 6.1. (A) Diagram of the FEAT model used to estimate the BOLD and CBF responses to the visual stimulus for echo 1 and echo 2, for each participant, using FEAT's Full Perfusion Modelling. (B) Diagram of the higher-level FEAT analysis to model the effect of the visual stimulus across all participants (Group Av) as well as differences between groups (Controls – Patients and Patients – Controls).

7 Coupling between brain oscillations, CBF, and BOLD signals during naturalistic movie viewing

7.1 INTRODUCTION

In Chapter 1.2.3, we covered the importance of understanding NVC in the healthy brain, as it is the physiological basis of many commonly used neuroimaging techniques, including fMRI. Coupling between neural activity, blood flow, and oxygen usage is also thought to be altered in different disease pathologies. Therefore, to accelerate our understanding of this in health and disease, we need to develop non-invasive ways of investigating these coupling mechanisms, with practically feasible methods applicable to patient populations.

In Chapter 4 we measured the electrophysiological response (with MEG) and the hemodynamic responses (with fMRI), and the coupling between them, in response to a visual checkerboard stimulus. This type of stimuli, artificial and with highly-controlled visual features, is what is typically used in E/MEG and fMRI studies. This approach often limits the analysis to a few localised regions, and specific oscillatory frequencies, and is not particularly representative of normal visual experiences. Furthermore, participants can often struggle to attend to the high-contrast full-field stimulus types, typically chosen to elicit maximal signal responses.

In this current chapter, we again compare brain oscillations with CBF and BOLD responses, but with a naturalistic movie viewing paradigm. Previous literature has shown that passive-viewing of movie clips allows activity to be characterised across multiple brain areas, and multiple oscillatory frequency bands, giving reliable inter-subject correlations and intra-subject correlations (between two repetitions of the same clip). This has been shown extensively with BOLD-fMRI (e.g. Bartels & Zeki, 2004, 2005; Hasson, Nir, Levy, Fuhrmann, & Malach, 2004; Jääskeläinen et al., 2008; Lahnakoski et al., 2014; Nummenmaa et al., 2012), as well as with EEG and MEG (Chang et al., 2015; Dmochowski, Sajda, Dias, Parra, & Rousselet, 2012; Ki, Kelly, & Parra, 2016; Lankinen, Saari, Hari, & Koskinen, 2014). Very few papers have characterised CBF responses to movie viewing (Griffeth, Simon, & Buxton, 2015; Rao, Wang, Tang, Pan, & Detre, 2007). Rao et al (2007) revealed both CBF and BOLD increases and decreases to a movie stimulus, with CBF showing activation patterns across more areas.

Only a few studies have compared both MEG and BOLD-fMRI signals to a movie stimulus (Betti et al., 2013; Kaisu Lankinen et al., 2018; Whittingstall, Bartels, Singh, Kwon, & Logothetis, 2010). MEG and BOLD signals often show similar spatial topographies, yet their relationship becomes more complex when comparing across different oscillatory frequency bands. The strongest and most consistent relationships between MEG and fMRI are reported in occipital areas, most likely due to the visual stimuli used.

In this study, we aimed to characterise inter-subject correlations (ISCs) to a naturalistic movie clip for MEG, BOLD and CBF signals, as well as the coupling between them to represent an empirical measure of NVC. To the best of our knowledge, this has not been done previously in the same study. We re-sampled the MEG and fMRI data to the same spatial and temporal scales, to investigate voxel-wise relationships between brain oscillatory amplitude envelopes across a wide-range of frequency bands (1 – 145Hz), alongside BOLD and CBF weighted signals, using a pseudo continuous ASL (pCASL) acquisition. As CBF images typically have poorer signal-to-noise ratios than BOLD, one aim was simply to see if the MEG-BOLD coupling relationships that have been reported previously, and that we investigated, can also be seen for MEG-CBF relationships, and if there are any differences, spatially and temporally.

We predict that this design will give temporal similarity across participants in each modality, and across modalities, allowing us to evaluate its utility as a way to investigate NVC in a healthy population. We predict we will replicate previous findings of how oscillatory frequencies correlate with BOLD signals and extend this by investigating coupling with CBF signals. We characterise the ISCs and the cross-modality coupling correlations in a voxel-wise analysis, therefore also investigating spatial variation in NVC relationships across different brain regions.

7.2 METHODS

Participants

19 healthy volunteers participated in this study, and 17 were used in the final analysis. All participants had normal or corrected-to-normal vision and had no history of neurological or psychiatric disorder. All participants gave written informed consent prior to participation and received £10 per hour for taking part. The study was approved by the Cardiff University School of Psychology ethics committee.

Design and Procedure

All participants had a MRI scan and a MEG scan (see diagram below). Both scanning sessions included passive viewing of the same movie clip from the James Bond film 'Skyfall' (approximately the first 19 minutes 38 seconds). A subset of these participants also had a BH scan during the MRI session, and this data is analysed in Chapter 8.

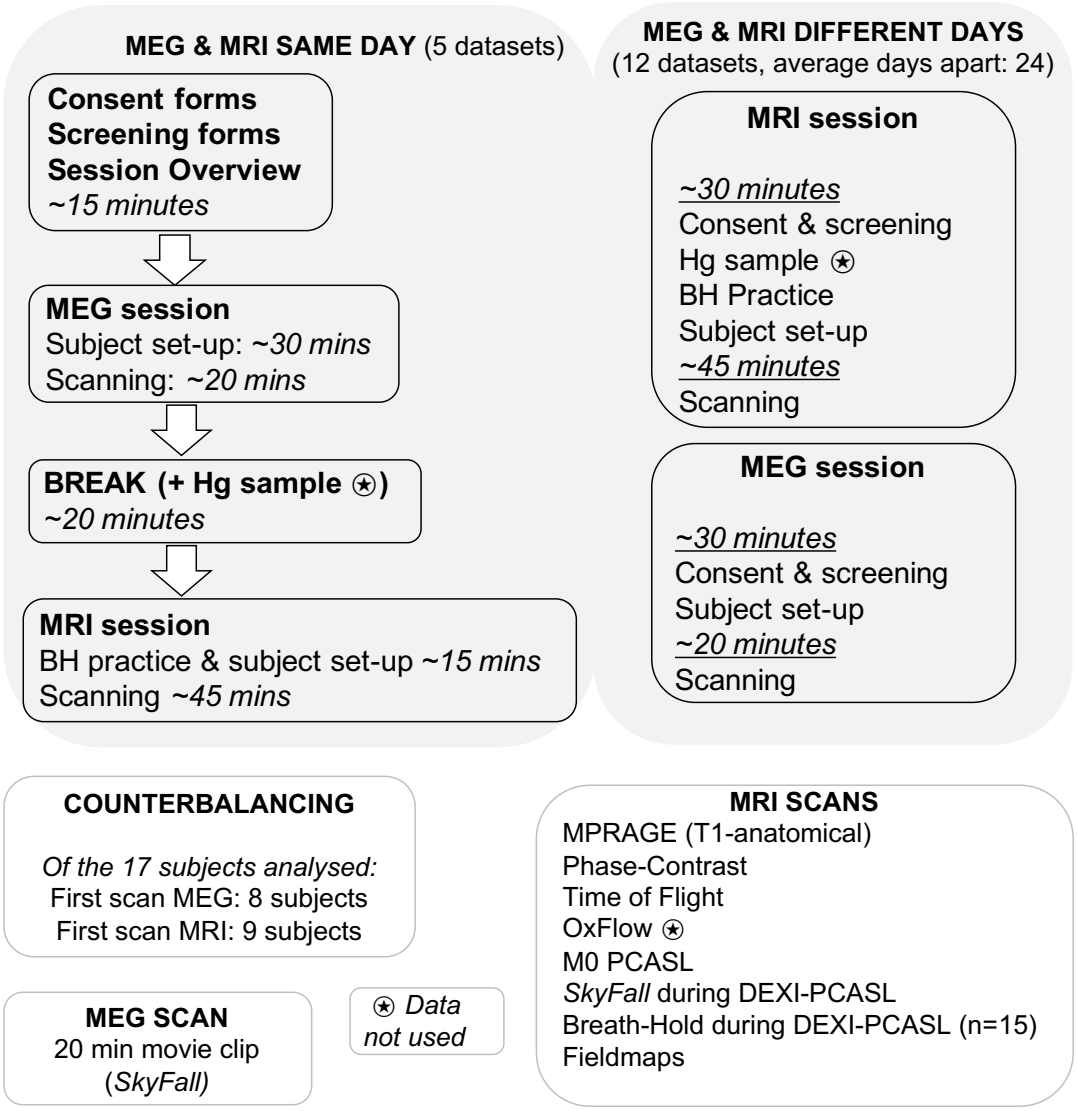

Figure 7-1 gives an overview of the data collection and analysis pipeline, which is then explained in detail in the next section.

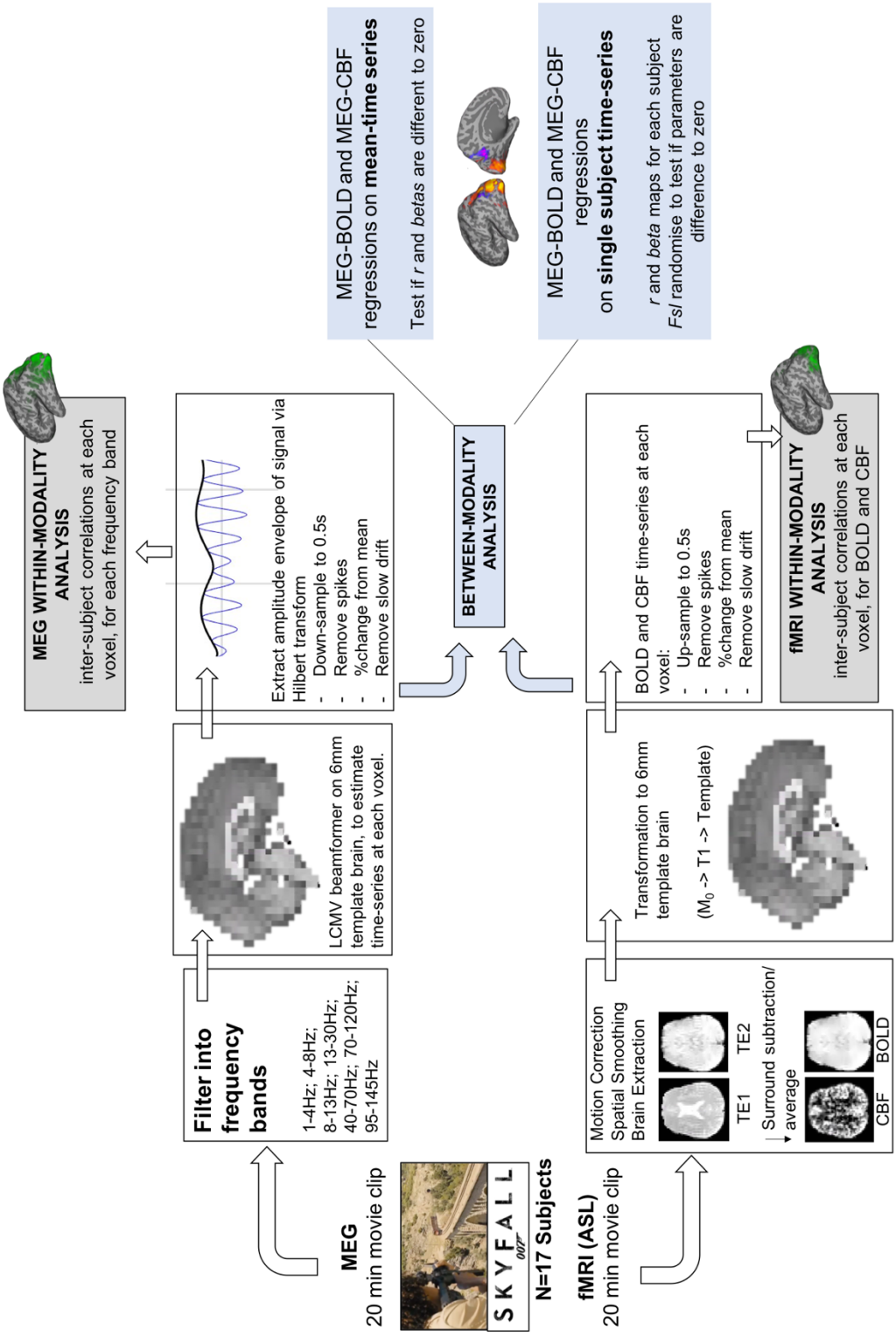

Figure 7-1. Diagram showing the analysis pipeline used to analyse the MEG and fMRI data, to produce the within-modality and between-modality results.

MRI acquisition and pre-processing

Data were acquired on Siemens Prisma 3T MRI scanner (*Siemens Healthineers, Erlangen, Germany*), using a 32-channel head coil. A magnetization-prepared rapid acquisition with gradient echo (MPRAGE) T1-weighted scan was acquired for co-registration and source localisation purposes (matrix 165 x 203 x 197, $1mm^3$ resolution, TR/TE = 2100/3.24ms). During the movie, a pCASL acquisition was run, as explained in Chapter 5. A DEXI readout gives BOLD and CBF weighted signals. An effective TR of 4.4. seconds was used to acquire 16 slices, in-plane resolution 3.4 x 3.4 mm and slice thickness 7mm with a 20% slice gap. Before this scan, an M_0 image was acquired.

Motion correction was performed with the FSL-McFLIRT function and spatial smoothing (FWHM=4.5mm) of the BOLD data (surround average of TE_2) was performed with SUSAN (Smith & Brady, 1997). CBF data (surround subtraction of TE_1) and the M_0 acquisitions were spatially smoothed using a 3D Gaussian kernel (FWHM 4.5mm). The first and last volume of the BOLD and CBF time-series were removed. Registrations were carried out with FSL-FLIRT. The BOLD and CBF data were both registered to the M_0 image. The M_0 image was registered to the brain extracted T1 image and this T1 image was registered to MNI-2mm standard space. The data were then down-sampled to 6mm, to match the spatial resolution of the MEG beamformers. BOLD and CBF time-series at each voxel were up-sampled to 0.5 seconds (with MATLAB's *interp1* function), in order to compare with MEG time-series. Spikes were removed using a median replacement filter, time-series were changed to percentage change from mean in each voxel, and a high-pass filter at >0.01Hz was applied to remove drift. At this stage a mean time-series was calculated, across participants, at each voxel, termed the *Group BOLD time-series* and the *Group CBF time-series.* Each participant's data was also separately computed and saved, to give a *Subject BOLD times-series* and *Subject CBF time-series.*

MEG acquisition and pre-processing

Whole-head MEG recordings were collected using a 275-channel CTF Omega system, sampled at 600Hz and analysed as synthetic third-order gradiometers. The continuous MEG recording was synchronised to the start of the movie clip, which ran for 19 minutes and 39 seconds. We used continuous head localisation of electromagnetic fiducial coils; these were placed at fixed distances from three anatomical landmarks (1cm anterior to left and right tragus, 1cm superior to nasion). Fiduciary locations were later manually marked on the anatomical MRI for co-registration (with Fieldtrip toolbox in MATLAB),

based on this 1cm distance, as well as verified with photographs. Offline, the data were divided into 2-second epochs and visually inspected for major artefacts. Head location at each time point was changed to the average head location across the recording. Two out of the nineteen participants were removed due to excessive eye and motion artefacts.

The data were filtered into these frequency bands: delta (1-4Hz), theta (4-8Hz), alpha (8-13Hz), beta (13-30Hz), low gamma (40-70Hz) and a range of 50Hz-wide overlapping 'high gamma' bands (70-120Hz, 95-145Hz). We also filtered the data into two frequency bands (120-170Hz, 145-195Hz) above the anti-alias filter cut-off (150Hz for this MEG acquisition). This filtered data were source-localised using an LCMV beamformer (Van Veen et al., 1997) which provides estimates of the virtual-sensor time-series at each voxel in the brain. These time-series were re-constructed on a 6mm grid in standard MNI-template space (using the 2mm MNI template brain down-sampled to 6mm), within cortical areas only. The time-series at each voxel was converted to an amplitude envelope using the analytic function, via the Hilbert Transform. The amplitude envelopes were down-sampled to 0.5 seconds to match the up-sampled fMRI data. Spikes were removed using a median replacement filter, time-series were changed to percentage change from mean in each voxel, and a high-pass filter at >0.01Hz was applied to remove drift. At this stage a mean time-series was calculated, across participants, at each voxel. This mean time-series was convolved with a canonical hemodynamic response function (HRF) from SPM to delay and disperse the oscillatory power in order to match to the BOLD and CBF responses. This will be termed the *Group MEG time-series* for each frequency band. Each participant's data separately, after high-pass filtering, was also convolved with the HRF, to give a *Subject MEG time-series* for each frequency band.

Within-modality analysis: inter-subject correlations (ISCs)

For each type of analysis (*BOLD*, *CBF*, *MEG* at each frequency band), we correlated the time-series between each pair of participants, transformed the *r* values using Fisher's Z transform and then averaged all pairwise coefficients to give a mean inter-subject correlation (ISC) for each voxel. This is a model free analysis to indicate where there are changes in activity common across the group. To test if these correlation coefficients were significantly different from zero, we performed a one sample-test at each voxel. This was statistically tested with randomisation testing (10,000 permutations, alpha = 0.05). The absolute maximum t-statistic at each randomisation

stage was used to define the null distribution, and the absolute t-score was tested against this null distribution (Nichols & Holmes, 2001).

Between-modality analysis: MEG-fMRI coupling

First, at each voxel, we performed a linear regression analysis with MATLAB's *fitlm* function, using the *Group MEG time-series* (for each frequency band) to predict the *Group BOLD time-series* or the *Group CBF time-series,* separately, and computed maps of correlation coefficients and beta values for each fMRI to MEG regression. *R* values and not R^2 values were outputted and tested, in order to represent the shared variance between the MEG and fMRI signals whilst still preserving the sign of the relationship. Beta coefficients represent the relationship in meaningful units. These maps were thresholded to $p<0.05$ (with false discovery rate (FDR) correction to account for multiple comparisons), and also masked to areas that had significant ISCs in either the BOLD or MEG data, for that specific frequency band. For example, for the BOLD and 1-4Hz correlation analysis results, we plot FDR-thresholded voxels only in areas that had significant MEG 1-4Hz ISCs *or* significant BOLD ISCs, for ease of interpretation. Voxel-wise correlation coefficients for the *Group-BOLD* and *Group CBF time-series* where also produced, to aid with interpretation of results.

At each voxel we had 7 correlation coefficients and 7 beta values, for the BOLD and CBF regressions. We performed a principle component analysis (MATLAB's default *pca* function, centered) on the correlation coefficients and beta values, to explore the dominant tuning function across the brain. We examine the principal component explaining the most variance and display how this function loads spatially across different areas of the brain.

This analysis explained above is performed only on mean time-series data, across participants. Therefore, to consider between-subject variance in coupling, we also performed a linear regression analysis for each subject separately, regressing the *Subject MEG time-series* in each frequency band at each voxel location onto the *Subject BOLD times-series* and the *Subject CBF time-series.* To test whether the correlation coefficients (Fisher transformed) or beta values were significantly different from zero for each voxel, we used FSL's *randomise* function to perform a nonparametric one-sample t-test at each voxel (5000 permutations), FWER-corrected p-values at $p<0.05$ and TFCE (Threshold-Free Cluster Enhancement). Due to our relative small sample size, we used variance smoothing of 12mm, to increase power to detect effects (Nichols & Holmes, 2001; Singh, Barnes, & Hillebrand, 2003).

A different study carried out at CUBRIC also showed the same movie clip in MEG and fMRI (BOLD-weighted sequence only), showing very similar results. With the researcher's approval, their data was combined with some of the data from this study, where appropriate, in order to investigate whether significant effects would be seen with more statistical power. Their data were processed in the same way, and correlation maps between MEG (at each frequency band) and BOLD for each participant (n=16) was combined with the ones from this study (n=17). For this data, a BOLD-EPI sequence was run (TR = 2 seconds, TE = 30ms, voxel resolution = $2mm^3$).

7.3 RESULTS

There were 17 participants included in the final analysis, as two were removed for poor data quality (excessive head motion and motion artefacts throughout the MEG or fMRI recording). The 17 participants were aged 28.29 ± 1.64 (Mean ± SEM), and 4 were male. There were 14 who had watched the movie before and 5 who had not.

Within-modality analysis: ISCs for MEG, BOLD and CBF signals

To uncover activity related to the movie, consistent across participants, we calculated ISCs at each voxel. Figure 7-2 shows significant ISCs for the BOLD and CBF analyses, and Figure 7-3 shows significant ISCs for the MEG analyses for each frequency band. Using the whole movie clip or using the first half of the movie clip gave extremely similar results, both in the spatial coverage of significant ISCs and the magnitude of correlations. Supplementary Figure 7-1 shows cross-correlations of two frequency bands above the anti-alias filter cut-off for the MEG acquisition (120 – 170Hz, 145 – 195Hz), which still show feasible ISCs locations and magnitudes. With a sampling frequency of 600Hz, the anti-alias filter in the MEG starts at 150Hz but falls off quite slowly, so this is why plausible signals may still be seen just above this cut-off.

We examined what anatomical areas the ISCs where located in by looking at their overlap with the AAL atlas (Tzourio-Mazoyer et al., 2002). Common areas with significant ISCs in BOLD, CBF, and all MEG frequency bands (both left and right unless stated) were seen across inferior, superior and middle occipital regions, including calcarine sulci, cuneus, lingua gyri, and fusiform gyri, and superior/middle/inferior temporal gyri. Except for CBF, significant ISCs were also found in the angular gyrus (anterior parietal). Except in the 40-70Hz frequency band, significant ISCs were seen for BOLD, CBF and MEG seen in the pre-cuneus (part of the superior parietal lobe).

Significant ISCs in frontal regions (superior, middle, medial or inferior frontal) were seen for 4-8Hz, 8-13Hz, 13-30Hz and 40 – 70Hz only.

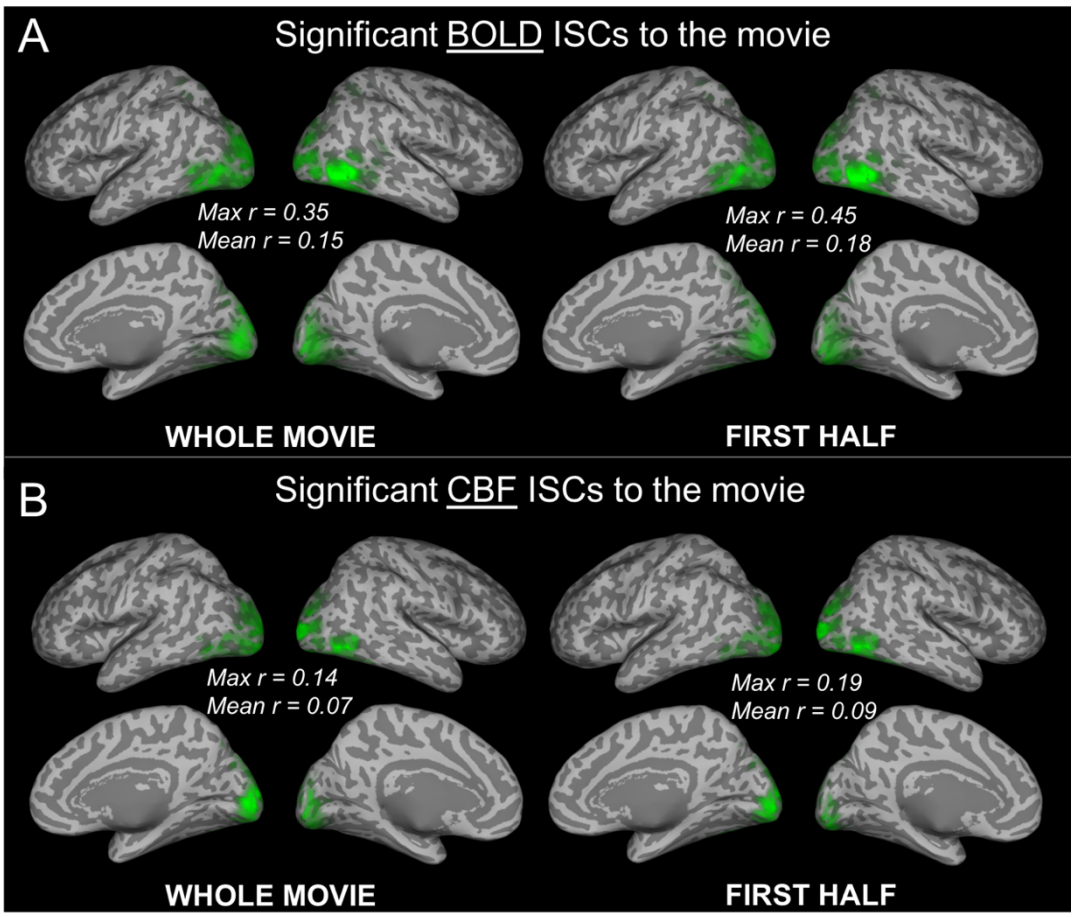

Figure 7-2. Significant BOLD and CBF inter-subject correlations (ISCs) showing movie-activated areas, using all the data (Whole Movie) and just half the data (First Half). Correlation values corrected to p<0.05, with randomisation testing. Correlations are displayed on an inflated MNI template brain. Mean correlation over voxels (Mean r*) and maximum correlation over voxels (Max* r*) are reported.*

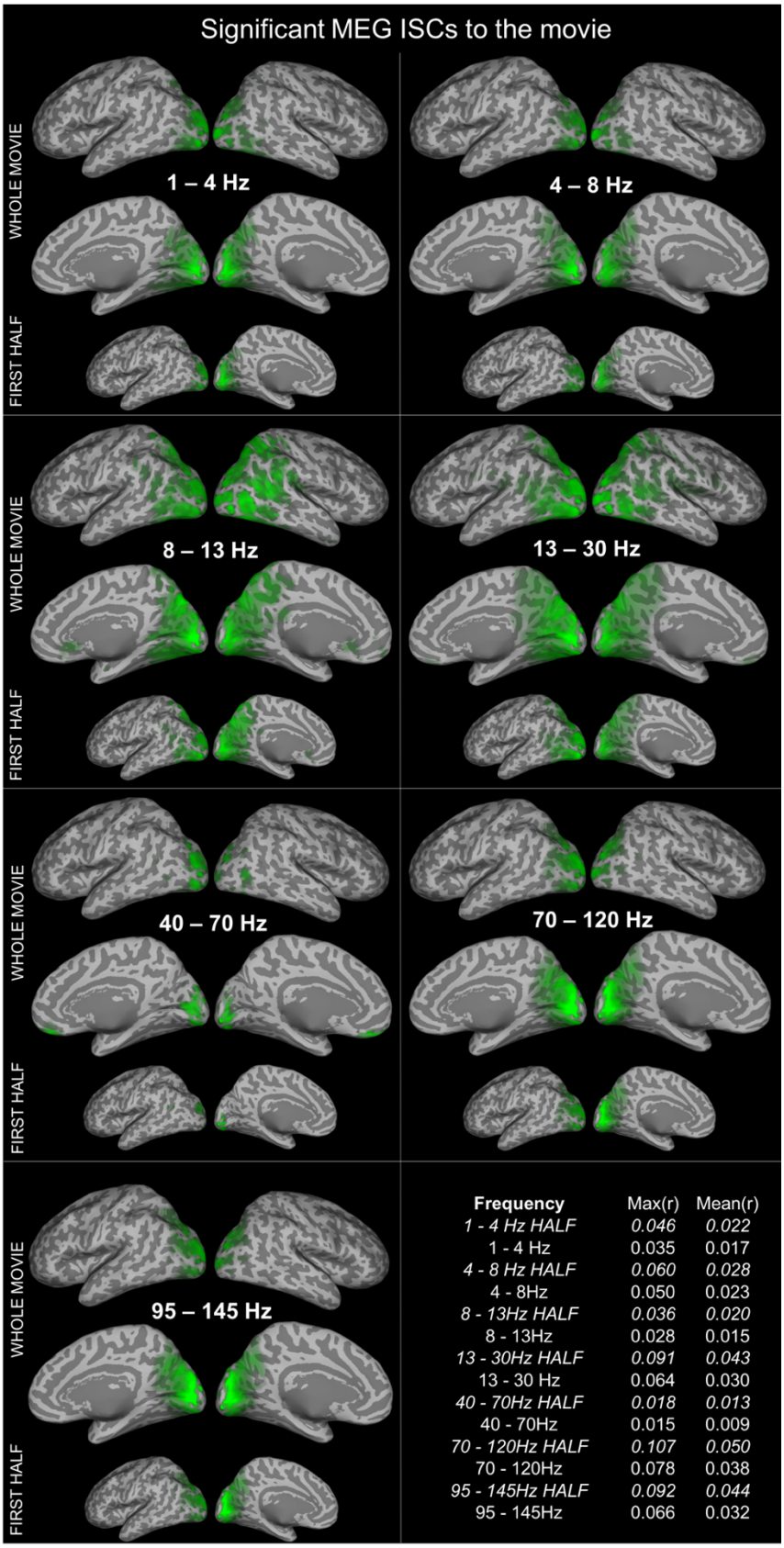

Frequency	Max(r)	Mean(r)
1 - 4 Hz HALF	*0.046*	*0.022*
1 - 4 Hz	0.035	0.017
4 - 8 Hz HALF	*0.060*	*0.028*
4 - 8Hz	0.050	0.023
8 - 13Hz HALF	*0.036*	*0.020*
8 - 13Hz	0.028	0.015
13 - 30Hz HALF	*0.091*	*0.043*
13 - 30 Hz	0.064	0.030
40 - 70Hz HALF	*0.018*	*0.013*
40 - 70Hz	0.015	0.009
70 - 120Hz HALF	*0.107*	*0.050*
70 - 120Hz	0.078	0.038
95 - 145Hz HALF	*0.092*	*0.044*
95 - 145Hz	0.066	0.032

Figure 7-3. Significant MEG inter-subject correlations (ISCs) showing movie-activated areas, using all the data (Whole Movie) and just half the data (First Half). Correlation values corrected to p<0.05, with randomisation testing. Correlations are displayed on an inflated MNI template brain. Mean correlation over voxels (Mean r*) and maximum correlation over voxels (Max* r*) are reported.*

Between-modality analysis: MEG-BOLD and MEG-CBF coupling

Figure 7-4 displays the relationship between the *Group MEG time-series* and the *Group BOLD/CBF times-series,* for 1-30Hz, and Figure 7-5 displays this for 40-145Hz. For both BOLD and CBF, significant positive and negative correlations are seen between all frequency bands, except 40-70Hz which only displays positive. In fact, activity in 40-70Hz frequency band displays the largest correlation for both BOLD and CBF signals and appears to be one of the MEG coupling relationships that is most similar for BOLD and CBF.

Many areas where BOLD displays positive correlations CBF displays negative correlations, and vice versa, for example this can be seen clearly in the coupling with 8-13Hz, 13-30Hz and 70 – 120Hz. There appears to be more negative correlations with BOLD signals, than CBF. Areas near the cuneus and the pre-cuneus appear to have opposing correlation directions i.e. when one has a positive correlation between MEG and BOLD, the other has a negative. However, the correlation between BOLD and CBF across the brain appears to be predominately positive (Supplementary Figure 7-2).

We explored these relationships further by running a PCA to determine the dominant tuning function across the brain, and this can be seen in Figure 7-6. The first PCA component explained 45% of the variance in the BOLD-MEG PCA and 32% in the CBF-MEG PCA. Here we see that some areas of the brain load positively and some negatively onto this first component, indicating different NVC characteristics for different areas. Very similar trends were found for PCA analysis run on the beta coefficients (data not shown).

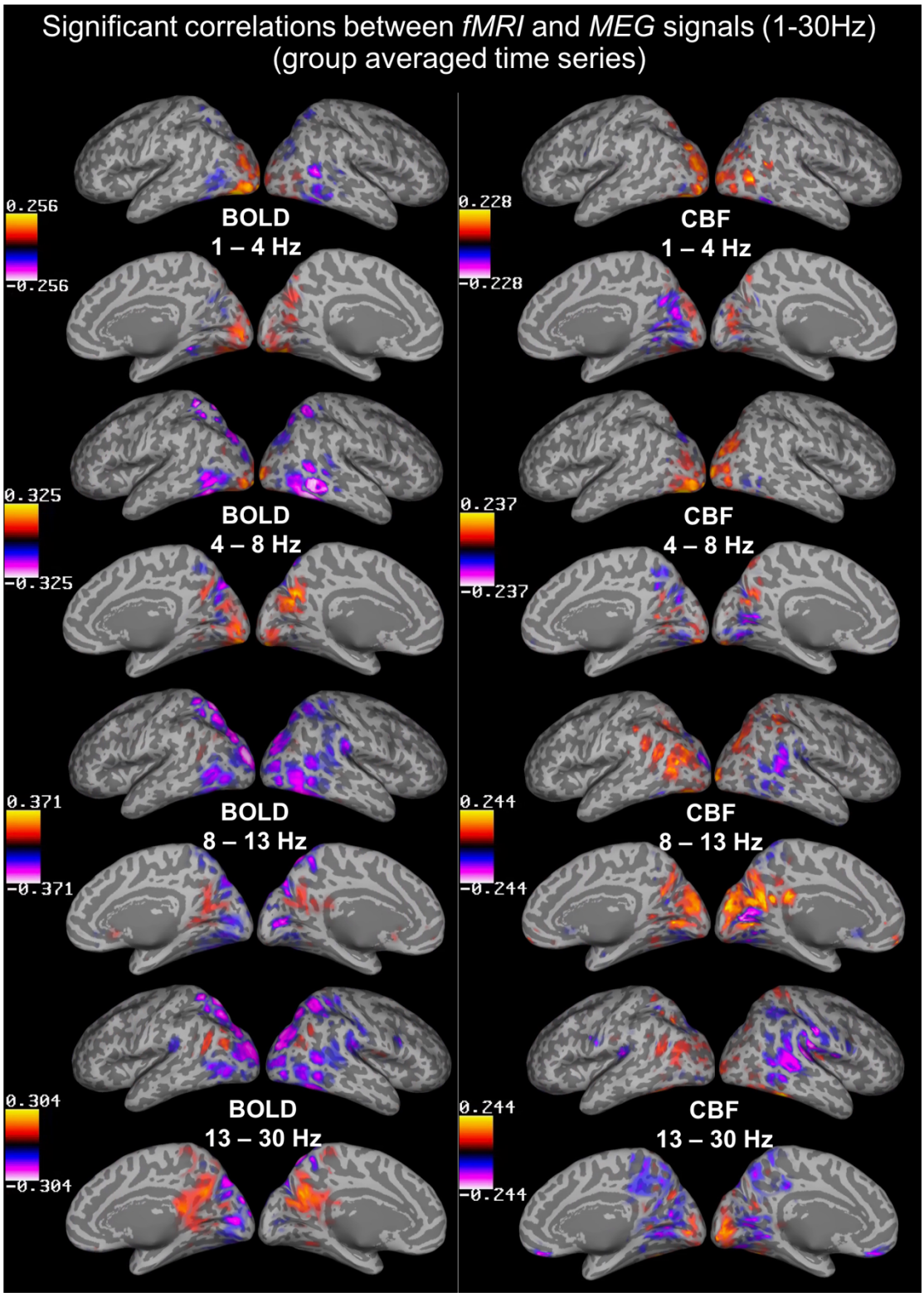

Figure 7-4. Correlation coefficients between Group BOLD time-series and Group CBF time-series with Group MEG time-series, for frequencies 1-30Hz, thresholded to p<0.05 (FDR corrected), as well as masked to voxels that had significant BOLD ISCs or significant MEG ISCs, in that frequency band. Black – Red – Yellow display increasing positive correlations, and Black – Blue – Pink increasing negative correlations. Correlations are displayed on an inflated MNI template brain.

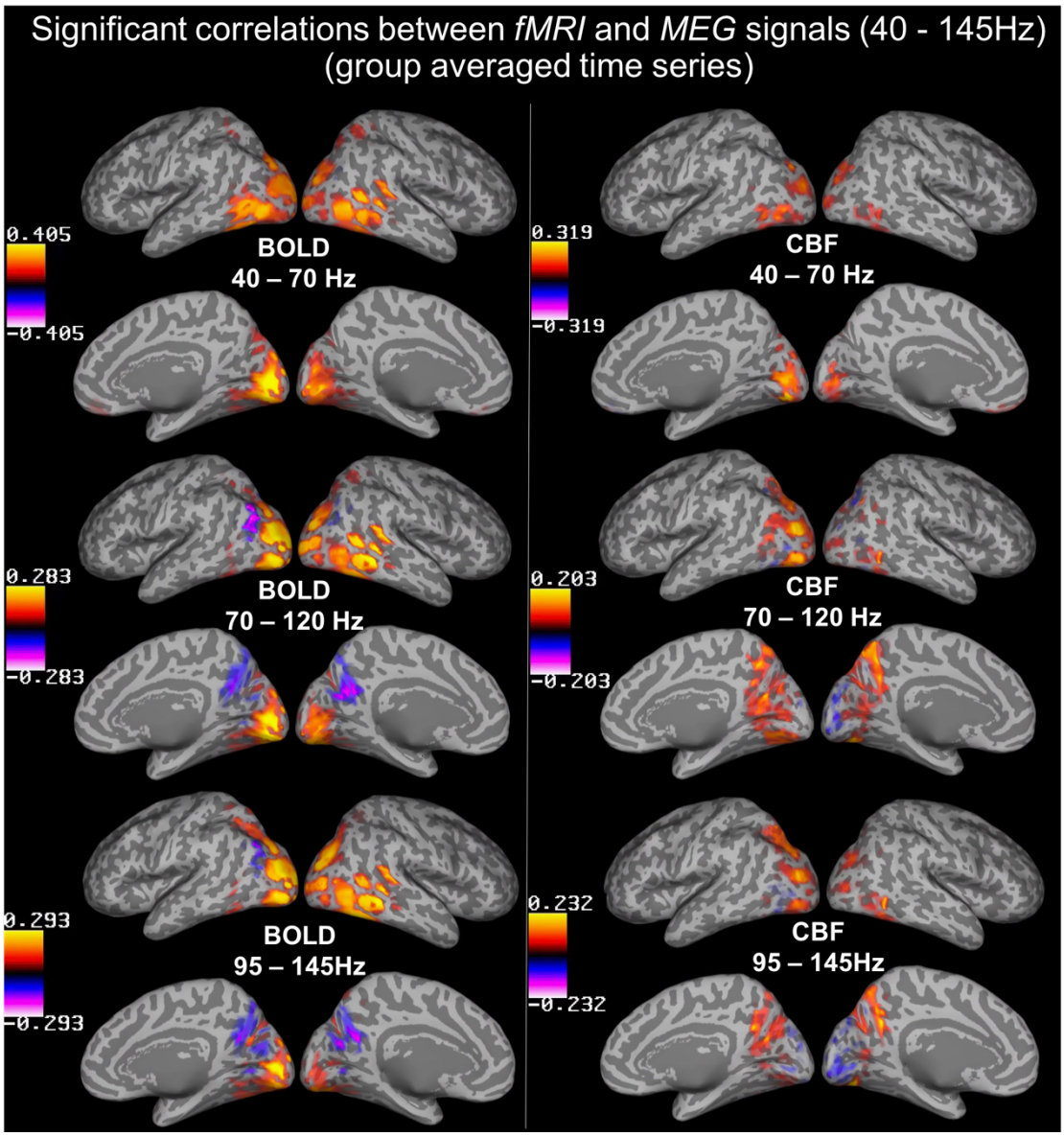

Figure 7-5. Correlation coefficients between Group BOLD time-series and Group CBF time-series with Group MEG time-series, for frequencies 40-145Hz, thresholded to p<0.05 (FDR corrected), as well as masked to voxels that had significant BOLD ISCs or significant MEG ISCs, in that frequency band. Black – Red – Yellow display increasing positive correlations, and Black – Blue – Pink increasing negative correlations. Correlations are displayed on an inflated MNI template brain.

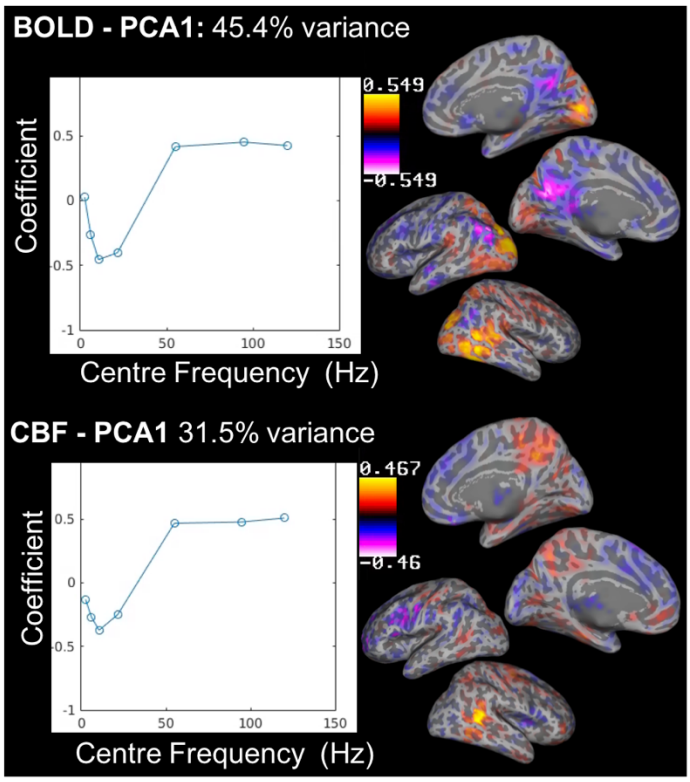

Figure 7-6. Principle Component (PC) Analysis to investigate how MEG-BOLD and MEG-CBF relationships change across frequency bands and in different brain areas. The plots show the dominant tuning function (the PC explaining the most variance), and the inflated MNI template brains show how each voxel loads onto this PC.

So far, the MEG-fMRI relationships have been presented based on the group mean time-series data. We also characterised the coupling for each individual first, then tested whether correlation coefficients or beta coefficients were significantly different to zero, across the group of participants, for each voxel. Figure 7-7 (top) displays the MEG-BOLD or MEG-CBF pairings that had significant correlations. All correlation coefficients are much lower in magnitude, compared to the group time-series analysis explained above. Significant correlations were found between BOLD and MEG signals in the 4-8Hz, 40-70Hz, and 70-120Hz frequency bands, in visual areas, specifically the cuneus. Only in the 70 – 120Hz band was there significant correlations between CBF, and this was in the middle/superior frontal gyrus. There were no significant voxel-wise beta coefficients, except for BOLD and 40-70Hz, again located near the cuneus (data not shown). Supplementary Figure 7-3 displays the unthresholded t-statistics (testing if beta coefficients are different to zero) for each voxel in the MEG-BOLD coupling, and Supplementary Figure 7-4 for the MEG-CBF coupling, which suggested similar trends to the mean time-series results (Figure 7-4 and Figure 7-5). Suspecting the lack of statistically significant voxels to be due to low statistical power, we combined our BOLD-MEG correlations maps (17 participants) with some from a different cohort (16

participants) and tested again whether correlation coefficients significantly different to zero. These results are shown in Figure 7-7 (bottom). More significant voxels, in the directions we would expect, are seen: negative correlations between BOLD and alpha (8-13Hz) and beta (13 – 30Hz), and positive correlations between BOLD and theta (3-8Hz) and BOLD and gamma (40Hz+).

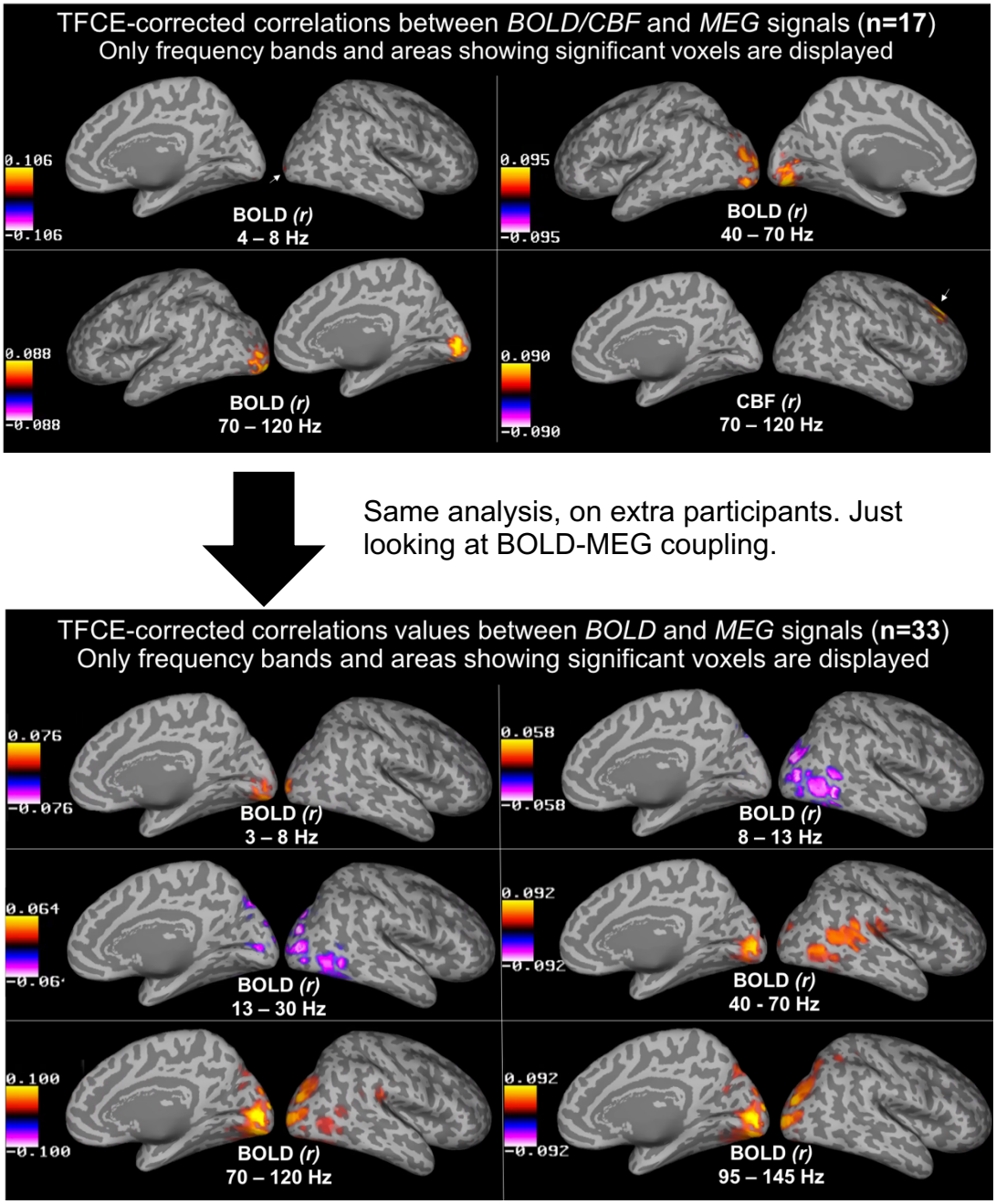

Figure 7-7. Top: Significant correlation coefficients, for MEG-fMRI coupling. Only shown for coupling relationships that had significant voxels. Bottom: Significant correlation coefficients, for MEG-BOLD coupling only, for a combined analysis of this dataset (n=17) and data from a different cohort (n=16). There was also a small region in superior occipital areas that showed significant coupling between 1-4Hz and BOLD. This data was calculated by first calculating correlation coefficients at each voxel for each subject, then using FSL's randomise function to perform a nonparametric one-sample t-test at each voxel, FWER p<0.05 corrected, TFCE and 12mm of variance smoothing.

7.4 DISCUSSION

Passive viewing of a simple movie stimulus, easy to implement with MEG and fMRI acquisitions, allowed us to characterise frequency-dependent NVC, across many brain areas. Compared to resting-state paradigms, getting each participant to view the same movie clip imposed some common temporal structure on the MEG and fMRI responses, allowing group average MEG and fMRI time-series to be correlated. Below, a brief discussion of the within modality analysis is given, before moving on to a more detailed discussion of the between-modality analysis, the main purpose of this chapter.

Within modality analysis: MEG, BOLD and CBF activity

Significant common activity across participants was seen for MEG (across multiple frequency bands up to 145Hz), BOLD and CBF, across occipital, parietal, temporal and frontal regions, but most consistently in visual areas. These results are similar to the single modality movie literature, but looking at MEG, BOLD and CBF movie responses in a single combined study has not been previously reported. When using half the data, the ISCs were almost unchanged, suggesting a shorter movie clip is sufficient to characterise significant ISCs. Showing an isolated movie clip, with no sound or sub-titles, likely gave varied levels of emotional engagement, and narrative recognition, from subject to subject, therefore frontal attentional networks are less likely to be consistently activated. Indeed, significant frontal activity, common across participants, was not seen in BOLD or CBF movie responses, and only seen for some MEG frequencies. Responding to shapes, colour, movement, faces and scenes is likely to be more consistent across participants, reflected in the more consistent significant activity we report in visual and perceptual regions across BOLD, CBF and MEG. This movie clip displayed emotional engaging and high arousal content, and there is evidence that these factors increase BOLD ISCs to movie stimuli (Ki et al., 2016; Nummenmaa et al., 2012). Using audio or sub-titles would increase the emotional engagement and attention further, and potentially give more significant ISCs in wider brain areas, however achieving similar audio delivery in MEG and fMRI environments is very challenging.

The magnitude of the significant MEG ISCs were very small ($r < 0.1$), and smaller than BOLD and CBF ISCs. A recent study by Lankinen et al (2018) report very similar ISCs for MEG and for BOLD, and suggest some potential reasons for this difference. They suggest spatial inaccuracies going from sensor to source space, but also the fact that

MEG time-series have richer temporal information so differences between participants may have a greater effect. Fewer ISCs, and ISCs with smaller magnitudes, were seen for the CBF analysis, compared with the BOLD, most likely due to poorer SNR for CBF signals.

Between modality analysis: Coupling between MEG, BOLD and CBF

Consistent with previous non-invasive (e.g. Zumer, Brookes, Stevenson, Francis, & Morris, 2010) and invasive (e.g. Mukamel et al., 2005) human literature, our results in Figure 7-7 (bottom, larger sample), show a frequency-dependent NVC relationship, with negative correlations with BOLD at lower frequencies (alpha, 8-13Hz, beta 13-30Hz) and positive correlations with BOLD at higher frequencies. In fact, EEG and MEG paradigms using visual stimuli typically report an increase in gamma oscillatory power at the same time as a decrease in alpha (e.g. Muthukumaraswamy & Singh, 2013; Swettenham, Muthukumaraswamy, & Singh, 2009). Looking at BOLD and CBF coupling with MEG, with the smaller sample (Figure 7-7*,* top), only positive correlations showed significant activity, for BOLD (4-8Hz, 40-70Hz, 70-120Hz) in visual areas, and for CBF (70-120Hz only) in the middle/superior frontal gyrus. This was presumably due to the smaller sample size, as the T-statistic maps (Supplementary Figure 7-3 and 7-4) showed similar trends. This frontal activity in CBF stood out, as it was not seen in BOLD or the other analysis approaches; although it could be noise or eye artefacts, it could also be meaningful activity of the frontal eye fields, which play a key role in saccadic eye movements for the purpose of directing attention (Schall, 2009). This would make sense in the context of the free-viewing of the movie clip.

For the results in Figure 7-7, each MEG frequency band is dominated by either a positive or negative relationship with BOLD or CBF, unlike the mean time-series analysis which showed both positive and negative relationships with BOLD and CBF in a *single* frequency band. This is summarised in the PCA analysis (Figure 7-6); the dominant relationship between frequency and BOLD/CBF was very consistent with what has been reported previously (Mukamel et al., 2005; Zumer et al., 2010). This function loads positively onto some brain areas, and negatively onto others, suggesting opposite NVC for different regions. Regional differences in NVC have been reported before (Bentley, Li, Snyder, Raichle, & Snyder, 2016; Devonshire et al., 2012; Huo, Smith, & Drew, 2014), but we are not aware of any other studies reporting inverted NVC relationships in different brain areas, using the relationship between MEG/EEG and fMRI. Many of the inverted relationships where seen most clearly in the pre-cuneus, a key area in the default mode network (Utevsky, Smith, & Huettel, 2014), a network of

regions that decreases in connectivity during tasks and increases during rest. Therefore, these findings could have interesting and important implications for the interpretation of activity in the default mode network; a decrease in BOLD-connectivity may not directly reflect decreased activity in neural activation, as these regions may be functionally coupled together in different ways than assumed.

Hermes, Nguyen, & Winawer (2017) make the distinction between *synchronization* of neural responses, compared with changing levels of neural activity due to metabolic demand, and propose this as an explanation for discrepancies between measured electrophysiological and BOLD responses, and for different positive and negative relationships seen for different frequencies. However, a confound in the interpretation of these positive and negative relationships arises from the fact that MEG beamformers are sensitive to source leakage. For instance, a strong oscillatory source may have a weak tail of activation that 'leaks' to an adjacent brain region which, under certain conditions, could arise as a spurious correlation with fMRI signals that do not have the same spatial errors.

Not only did the relationship between neural oscillatory frequency and fMRI vary across brain areas, but these relationships often appeared opposite for BOLD and CBF. This opposite relationship can be seen quite clearly in the BOLD and CBF PCA loadings in areas near the cuneus and pre-cuneus, and particularly in coupling with 13-30Hz in Figure 7-4 and with 70-120Hz in Figure 7-5. However, there were positive correlations between BOLD and CBF signals in these areas (Supplementary Figure 7-2), making this divergence of BOLD and CBF coupling with neural activity hard to interpret. In some areas, it is possible that BOLD and CBF are explaining different parts of the MEG signal; considering it is a rich temporal signal with both amplitude and phase changes reflecting functional activity, this could be plausible. Another factor to consider, is that BOLD is a complex signal with known vascular contamination. For instance, mislocalisation between neural activity and BOLD signal changes can occur due to large velocity changes in draining veins (Fukuda, Poplawsky, & Kim, 2016). However, performing the analysis at 6mm spatial resolution should have mitigated this effect to some degree.

Animal work has shown similar regional discrepancies between neural, BOLD and CBF signals, for example one study showed that increases in hemodynamic, neuronal, and metabolic activity were associated with positive BOLD signals in the cortex, but with negative BOLD signals in hippocampus, during seizure activity in rats (Schridde et al., 2008). Although we did not characterise our MEG signals in sub-cortical areas (due to depth insensitivity) this is still evidence for regional differences in the coupling between

these signals. Another study with anesthetized macaques showed evidence that the cortical layers may have different NVC behaviours, and that CBF and CBV relate to positive and negative BOLD changes differently in response to a visual stimulus (Goense, Merkle, & Logothetis, 2012). However, there is not a lot of research charactering these differences in humans due to the invasive nature of measuring these signals simultaneously.

The CBF response, despite having lower SNR, is a more meaningful and interpretable signal, directly reflecting blood flow to an amount of tissue. However, the CBF signal still only tells us about the delivery of blood to the tissue, and not about neural metabolism. The BOLD response cannot be taken as a direct reflection of underlying metabolic changes, as it relies on CBF, CBV, $CMRO_2$ changes, as well as the baseline tissue state. Furthermore, there is evidence that coupling between CBF and $CMRO_2$ (Ances et al., 2008), and variations in capillary vascularisation (Ekstrom, 2010) vary across brain regions. Both factors would affect the resultant BOLD response, causing it to not be a true reflection of neural activity. Therefore, it is important to develop non-invasive ways of measuring both CBF and $CMRO_2$ signals and investigate how they relate to different types of neural activity, in different brain regions. The relationship between MEG and $CMRO_2$ signals has not been characterised previously, and this is the focus of Chapter 8, displaying some exploratory relationships between MEG and $CMRO_2$ signals to the movie stimulus.

Methodological considerations and limitations

It is a possible that these inverted coupling behaviours, and the differences between BOLD and CBF, have not been reported previously due to the stimuli type normally used. Using highly controlled visual stimuli (e.g. checkerboards, gratings) typically focuses the analysis on the low gamma-band (similar to our 40-70Hz range). The 40-70Hz band was actually the only frequency band that showed only positive correlations with BOLD and was the most similar in the BOLD and CBF coupling. It also showed some of highest correlations with BOLD and CBF, in both types of analyses.

Although these inverse NVC patterns, and discrepancies between BOLD and CBF, where seen across multiple frequency bands, it is important to note that this was only found for the mean time-series analysis. This was not seen when fitting the model for each participant first, then testing for statistical differences, the more typical approach taken for neuroimaging data. A larger sample would be needed to adequately characterise both fixed effects (parameters constant across individuals, our mean time-

series correlations/regressions) and random effects (parameters can vary across individuals, our subject time-series correlations/regressions). Considering random effects in the modelling becomes more important if you want to test differences between two populations.

An assumption made in this analysis, is that the neural response to the movie stimuli was the same in MEG and fMRI. They are unlikely to be identical, considering they are measured at different times, but still share a lot of similarity. Counterbalancing the order of MEG and fMRI movie presentation, as done in this study, is therefore an important factor considering reports of how ISCs can change on repeated viewing (e.g. Chang et al., 2015), but this only controls order differences at the group level.

When characterising the MEG and fMRI coupling relationship on the group mean time-series data, the data were masked to significant BOLD or MEG ISCs regions, to look at coupling only in places where there was a significant response to the movie. However, Lankinen et al (2018) showed that the regions with the most consistent MEG activity across participants may not be the same as regions that are most correlated with fMRI. Also, they critique the use of the typical univariate voxel-wise correlation approach to characterise responses to a continuous naturalistic stimulus and propose instead a spatial filtering approach which they use to demonstrate more significant coupling relationships.

Conclusions

Passive viewing of a simple movie stimuli in MEG and fMRI allowed us to measure neural oscillations in multiple frequency bands, BOLD signals and CBF signals, non-invasively in the same participants. This demonstrated complex patterns of coupling between neural activity and vascular and metabolic responses. NVC is dependent on both oscillatory frequency and brain region and appears different for BOLD and CBF signals.

7.5 SUPPLEMENTARY

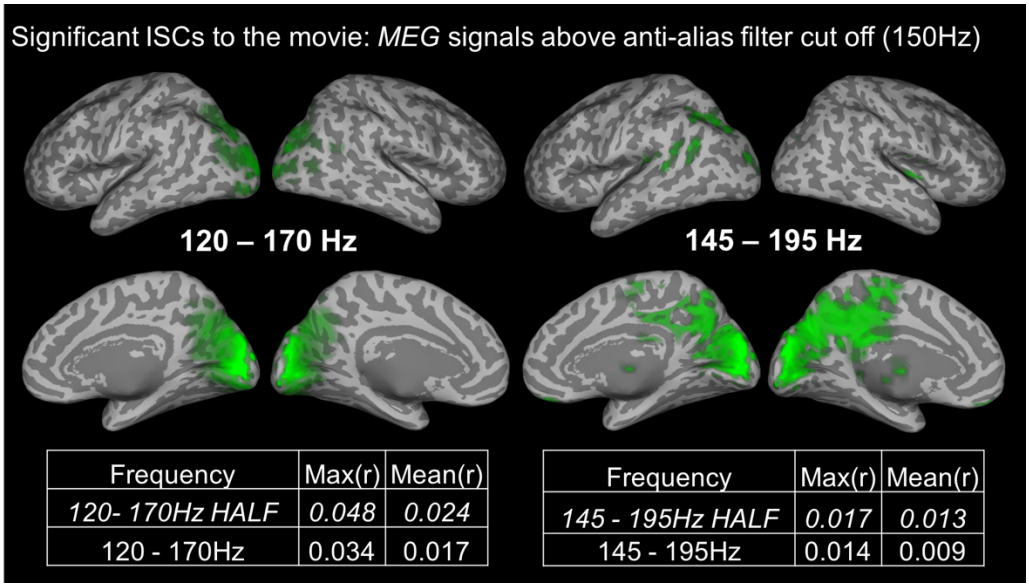

Frequency	Max(r)	Mean(r)
120- 170Hz HALF	*0.048*	*0.024*
120 - 170Hz	0.034	0.017

Frequency	Max(r)	Mean(r)
145 - 195Hz HALF	*0.017*	*0.013*
145 - 195Hz	0.014	0.009

Supplementary Figure 7-1. Significant inter-subject correlations (ISCs) showing movie-activated areas, for the two MEG frequency bands above the anti-alias filter cut-off of 150Hz. Correlation values corrected to p<0.05, with randomisation testing. Correlations are displayed on an inflated MNI template brain. Mean correlation over voxels (Mean r) and maximum correlation over voxels (Max r) are reported.

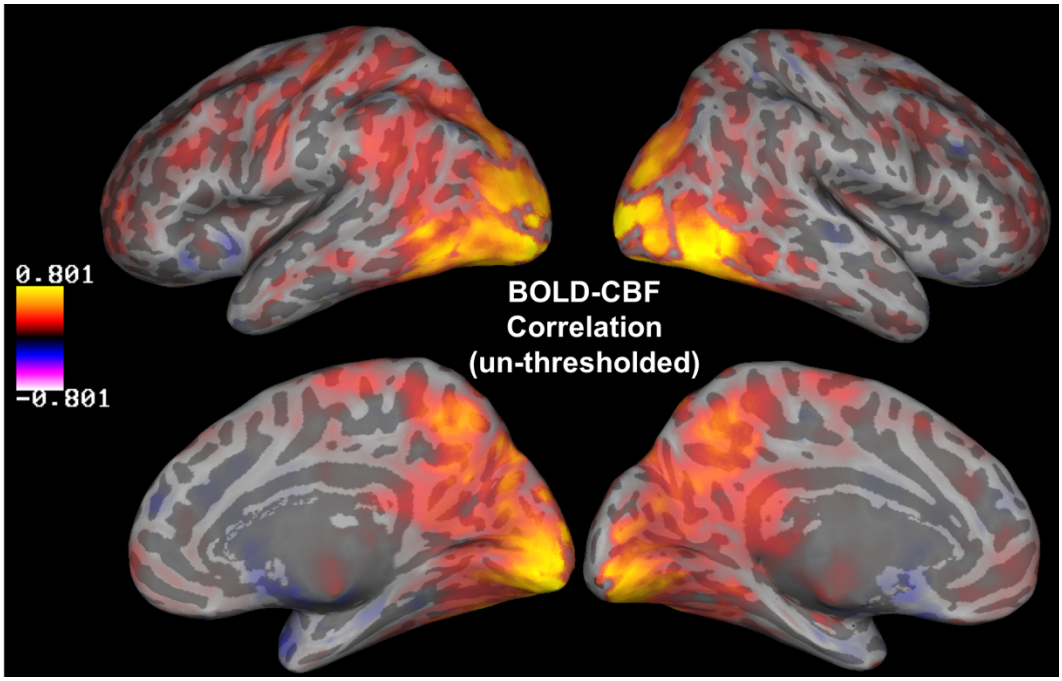

Supplementary Figure 7-2. Correlation coefficients between Group BOLD time-series and Group CBF time-series, unthresholded. Black – Red – Yellow display increasing positive correlations, and Black – Blue – Pink increasing negative correlations. Correlations are displayed on an inflated MNI template brain.

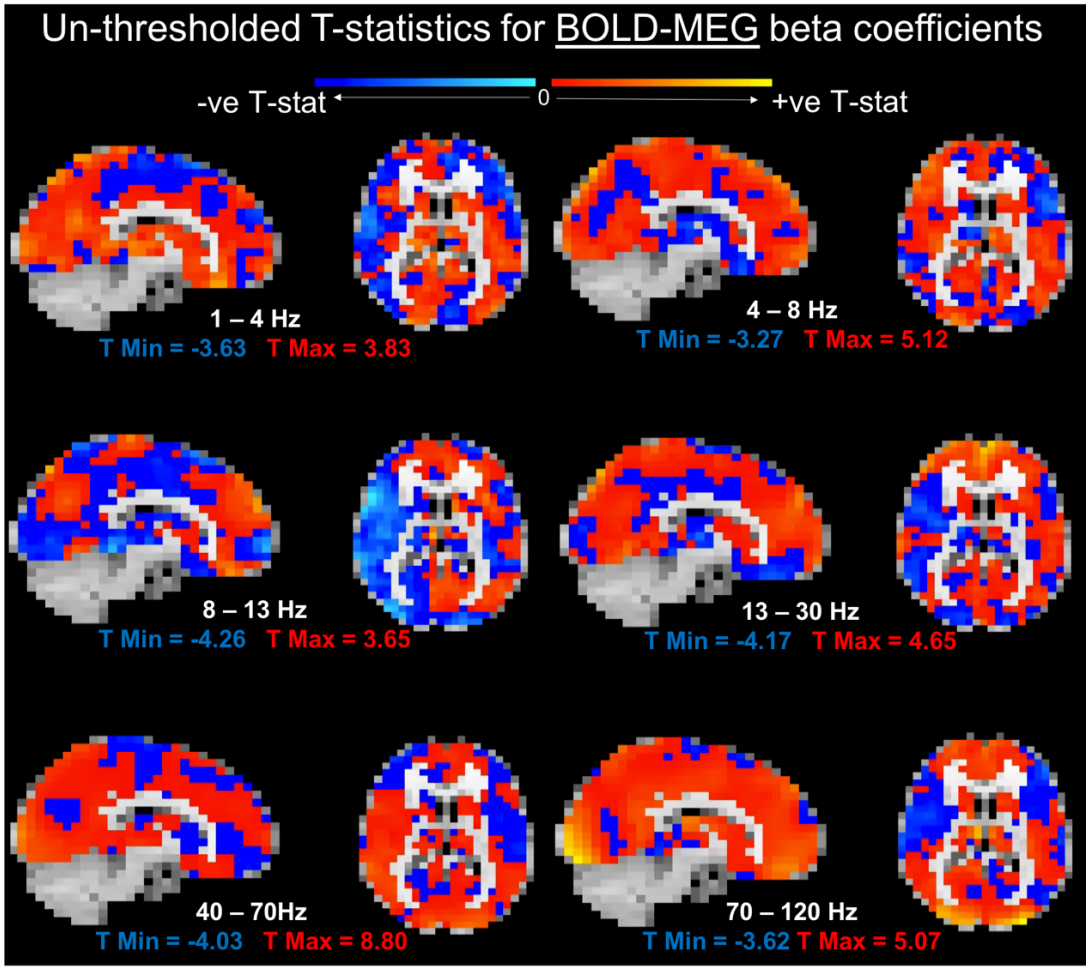

Supplementary Figure 7-3. Unthresholded T-statistics for each voxel, testing if the beta coefficients are different to zero for MEG-BOLD coupling. Light blue to dark blue represents increasing negative T-statistics (beta-coefficients less than zero) and red to yellow increasing positive T-statistics (beta-coefficients greater than zero). The subject average beta coefficients, across voxels, ranged from -0.0012 to 0.0013 for BOLD 1-4Hz regression, from -0.0011 to 0.0019 for the BOLD 4-8Hz regression, from -0.0016 to 0.0020 for BOLD 8-13Hz,from -0.0032 to 0.0031 for BOLD 13-30Hz, from -0.0032 to 0.0055 for BOLD 40-70Hz and from -0.0027 to 0.0055 for BOLD 70-120Hz.

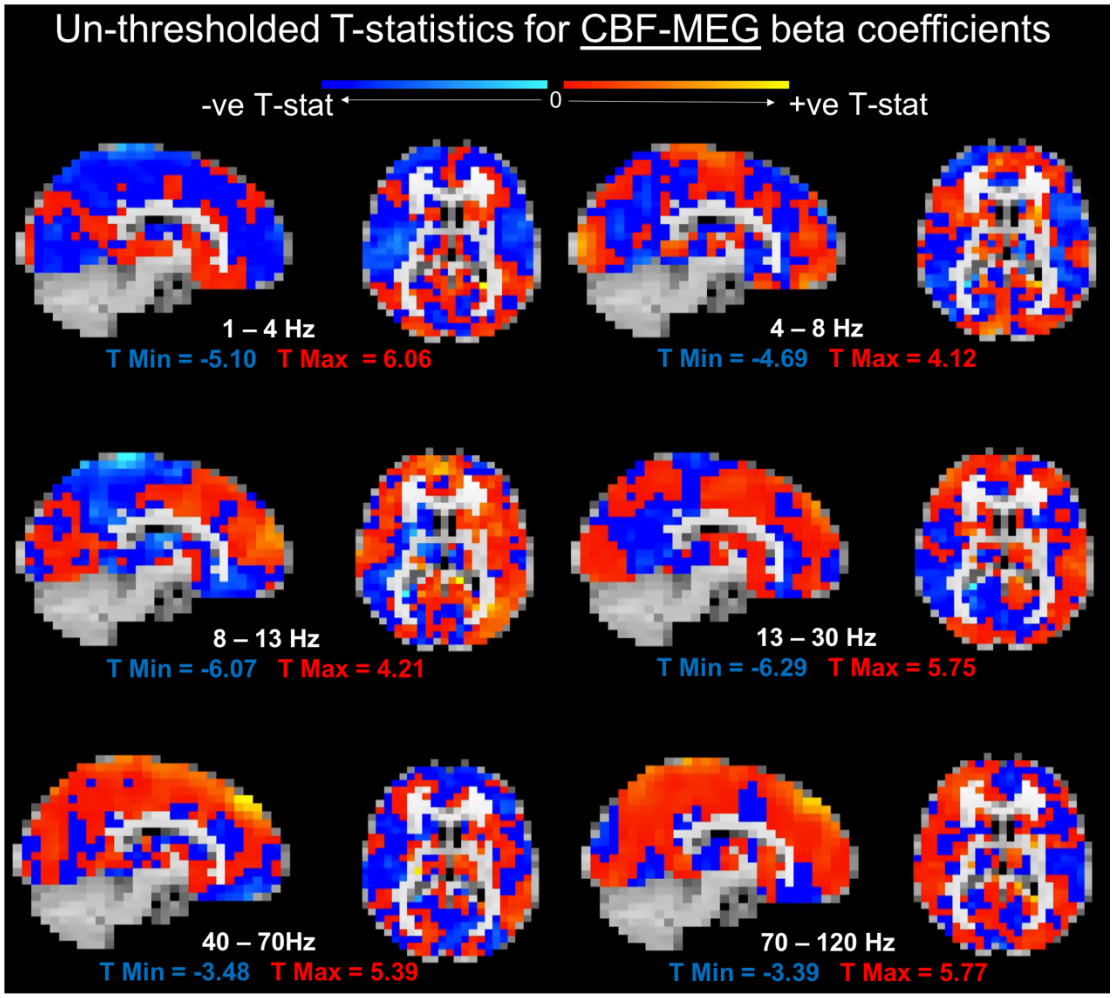

Supplementary Figure 7-4. Unthresholded T-statistics for each voxel, testing if the beta coefficients are different to zero for MEG-CBF coupling. Light blue to dark blue represents increasing negative T-statistics (beta-coefficients less than zero) and red to yellow increasing positive T-statistics (beta-coefficients greater than zero). The subject average beta coefficients, across voxels, ranged from -0.0012 to 0.0013 for CBF 1-4Hz regression, from -0.0011 to 0.0019 for the CBF 4-8Hz regression, from -0.0016 to 0.0020 for CBF 8-13Hz,from -0.0032 to 0.0031 for CBF 13-30Hz, from -0.0032 to 0.0055 for CBF 40-70Hz and from -0.0027 to 0.0055 for CBF 70-120Hz.

8 Using a breath-hold design to estimate the calibration factor *M*: can we model $CMRO_2$ to a movie-stimulus?

8.1 INTRODUCTION

Following on from Chapter 7, this chapter aimed to characterise relative change in the $CMRO_2$ to the movie stimulus. As covered in Chapter 1.2.1, oxidative metabolism of glucose is the predominant mechanism through which the energy demands of neural activity are met. Compared with CBF and BOLD signals, $CMRO_2$ is thought to be more closely coupled to neural activity (Du et al., 2008; Hyder, 2010). As demonstrated in Chapter 6, we can 'calibrate' our BOLD and CBF signals with hypercapnic stimuli, allowing us to estimate the *M* parameter. Estimating the *M* parameter in the same scanning session as measuring BOLD and CBF signals to the movie stimulus can allow us to model $CMRO_2$ to the movie stimulus. Here we present an alternative way of estimating the *M* parameter by modelling the relationship between BOLD and CBF signals to hypercapnia, induced by a breath-hold (BH) design. Although there have been many studies using a BH task to characterise Cerebrovascular Reactivity (CVR), very few have gone on to estimate *M* (One example: Kastrup, Krüger, Glover, & Moseley, 1999). The majority of studies use increases in inspired CO_2 gas fractions to estimate *M* (Blockley et al., 2013). Using a BH task is easy to implement and needs less equipment but requires more subject compliance to achieve good data.

A previous study characterised the $CMRO_2$ responses to a naturalistic movie stimuli (Griffeth et al., 2015). Their focus was to compare flow-metabolism coupling between different stimulus types, and they report no significance difference in flow-metabolism coupling to a movie stimulus and to a flickering checkerboard stimulus. Their movie clips were shown for ~6 minutes, and interspersed with rest blocks, therefore quite a different design to our continuous 20-minute recording. Here, we also characterise CBF- $CMRO_2$ coupling to the movie stimulus.

In this chapter, we report an exploratory, region of interest, analysis where we model the relationship between MEG and $CMRO_2$ signals. In Chapter 7, we reported divergent coupling relationships between MEG and BOLD and MEG and CBF, therefore being able to characterise MEG-$CMRO_2$ coupling may bring insight into why these differences occur. More generally, it is important to understand how $CMRO_2$ signals modelled with fMRI paradigms correlate with neural oscillations, considering $CMRO_2$ is thought to more closely reflect the ATP consumption needed to restore ionic gradients after neural

signalling (Buxton, 2010). If most energy is replenished by the oxidative metabolism of glucose (Buxton, 2009; Du et al., 2008), we would expect $CMRO_2$ to be a good index of neural activity, and therefore correlate with the neural oscillations measured with MEG. To the best of our knowledge, the relationship between MEG signals and $CMRO_2$ has not been explored previously.

8.2 METHODS

Participants and Design

15 out of the 19 participants described in Chapter 7 performed a BH task in the same MRI session as the movie-watching. 14 out of these 15 participants also had movie data from MEG. The BH task took 8 minutes and 44 seconds and is described in Figure 8-1.

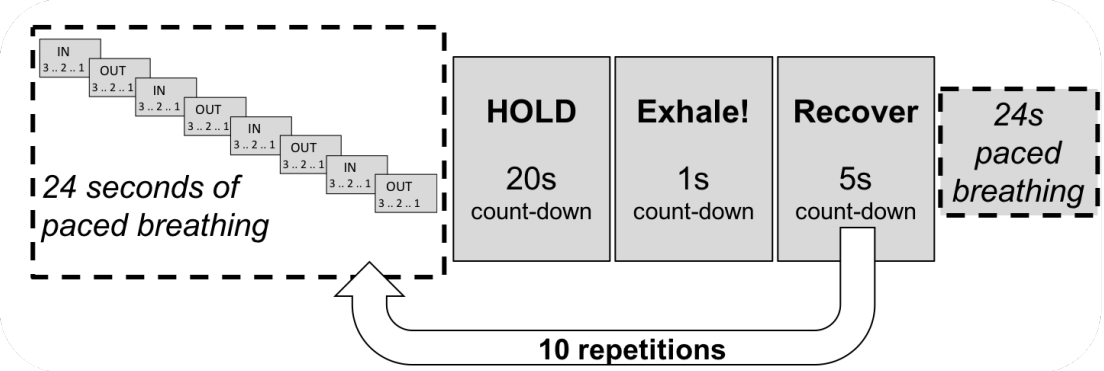

Figure 8-1. The timings for the BH task. Participants practiced this task outside of the scanner first, until they fully understood the instructions and were comfortable to proceed. Before the task started in the scanner an instruction screen appeared saying "The breath-hold task is about to start. Follow the instructions on the screen, and please remember to breathe through your nose." The task started with 24 seconds of paced breathing, where a screen alternated from 'Breath In' to 'Breath Out' with 3 second count downs in both. This was followed by a 'Hold' instruction where participants knew to not breathe through their nose or mouth for 20 seconds. After the breath-hold an 'Exhale!' was given to measure the change in end-tidal CO_2. Lastly, a 'Recover' was shown, where participants could breathe how they wished for 5 seconds. This cycle repeated 10 times before ending on one last 24 seconds paced breathing section.

Task Compliance

As the main purpose of the BH analysis was to estimate regional *M* values, the O_2 and CO_2 traces recorded through-out the experiment were not used in the modelling. The modelling of the *M* parameter was simply based on the fact that BOLD and CBF signals are changing in the response to the same CO_2 increase due to the BH manipulation.

However, the physiological traces were inspected to ensure sufficient quality, and compliance with the BH task. Two participants were left out of the analysis due poor compliance with the BH task (Figure 8-2). This left 12 participants, all of which had at least 8 clear BH segments in their physiological traces. Examples of acceptable and good traces from two participants are shown in Figure 8-2.

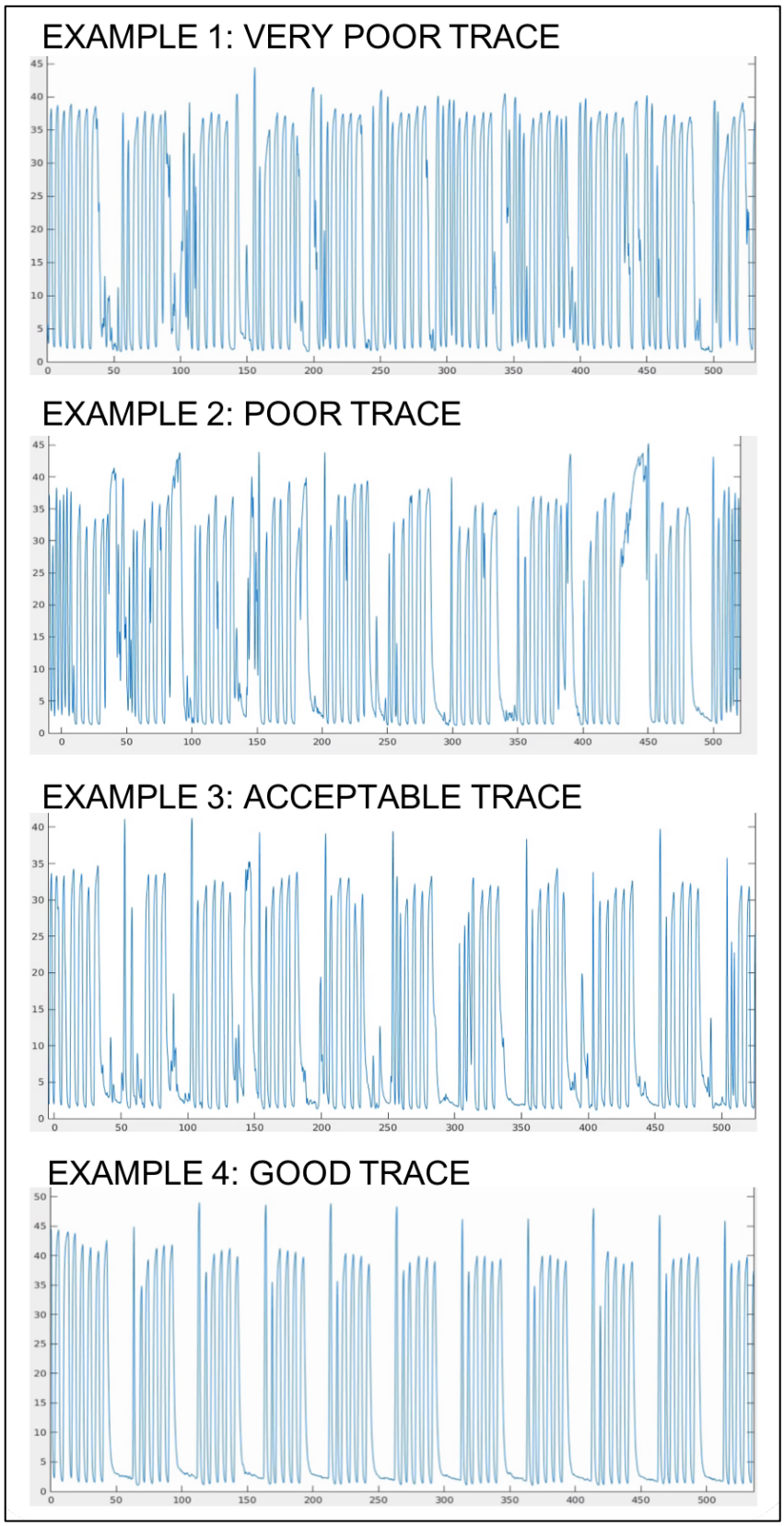

Figure 8-2. Example BH traces from 4 participants. X-axis is time and y-axis are CO_2 in mmHg. In example 1, it is very hard to notice any breath-holds. In example 2, the breath-holds are noticeable but still inconsistent, and there are many spikes of exhalations. In example 3, there are also spikes of exhalation in the breath-hold segments however the end-tidal increases are clearer and there are more prolonged breath-hold segments. In example 4, you can see 10 clear breath-holds ending in 10 clear end-tidal increases.

MRI acquisition and Data Analysis

During the BH task, the sequence used was the same pCASL acquisition that was run during the movie stimuli (described in detail in Chapter 5), with a total of 119 volumes.

Data Pre-processing

BH data was pre-processed in the same way as the pCASL movie data, explained in Chapter 7. In brief, motion correction with FSL-McFLIRT, spatial smoothing (FWHM=4.5mm) for the BH-BOLD data with SUSAN, and for the BH-CBF data with a 3D Gaussian kernel (FWHM 4.5mm). Surround subtraction and surround averaging was performed on the BH-CBF and BH-BOLD data, respectively. The BH-BOLD and BH-CBF data were both registered to the M_0 image that was acquired before the movie. The BH-BOLD and BH-CBF data were transformed to M_0 image, then to the T1 image and to the MNI-2mm image, using the movie-data transformation matrices made already. The BH-BOLD and BH-CBF data were then down-sampled to 6mm, in order to estimate M values in same space as the fMRI and MEG movie analysis.

In this MNI-6mm space, *M* was only estimated in voxels that had significant movie-BOLD ISCs (Figure 7-2A). We split the significant movie-BOLD ISC image into anatomical areas using the AAL atlas (Tzourio-Mazoyer et al., 2002). We chose this ROI method instead of doing a voxel-wise analysis (as in Chapter 7) to: (1) constrain the *M* estimates to areas where the movie was activated as these are the areas where movie-$CMRO_2$ will go on to be modelled (assuming movie-BOLD activation to be spatially similar to movie-CBF activation but with more voxels reaching statistical significance), and (2) to average out noise. The AAL atlas regions where in MNI-2mm space so these where first down-sampled to 6mm in order to overlay onto the movie-BOLD ISC image. This gave 28 ROIs (see Table 8-1 for list). For each ROI, a mean over voxels was calculated for BH-BOLD and BH-CBF data, resulting in a representative time series (119 volumes) for that ROI.

Baselining the BOLD and CBF BH data

The equation used to model *M* (see page 136) based on the relationship between BOLD and CBF to an isometabolic stimulus, requires both BOLD and CBF signals to be expressed as change from baseline. As this experimental design did not include a long continuous baseline period at the beginning (limitations of which are covered in the discussion), we did not take a block-design approach to baselining the data. Instead we

defined an empirical baseline. In MATLAB, for BH-BOLD and BH-CBF times-series over each ROI, we calculated the 40th percentile of the time series (to approximately reflect the proportion of data points in the paced breathing periods) and took a mean over any data points less than the 40th percentile to be represent the baseline. We then transformed the BH-BOLD and BH-CBF time-series to change from this baseline (for every point we divided by this baseline value). Plotting this 40th percentile with the data, for each participant, seemed to give a reasonable estimate of where the baseline was (via visual inspection) and Figure 8-3 demonstrates this for one participant.

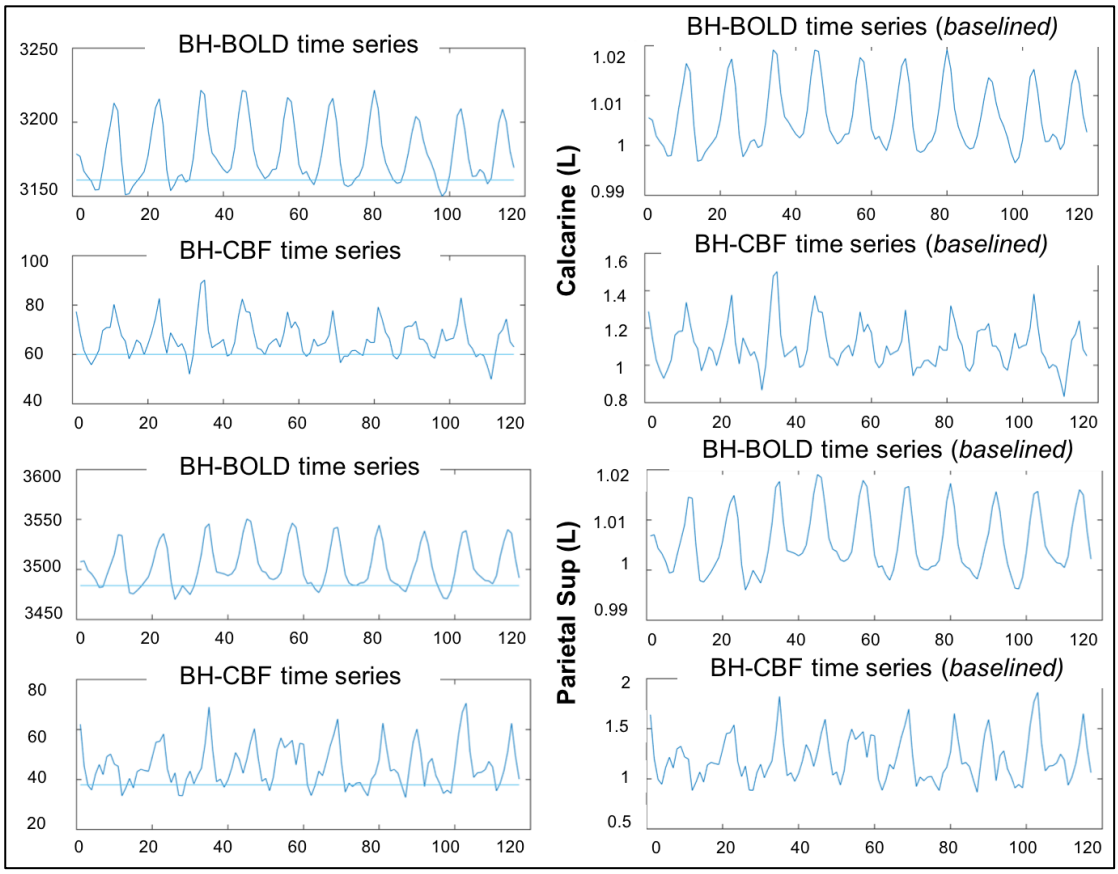

Figure 8-3. Average BOLD and CBF time-series for one participant, in response to the BH task, shown for two example ROIs (Calcarine Left – top, Superior Parietal Left – bottom). Note the 10 BHs that can be seen in these BOLD and CBF time series. Plots on the left side show data that is not relative to baseline, with the 40th percentile being plotted as the straight blue line. Average of the values below this 40th percentile where taken as 'baseline' and used to change the time-series into change from baseline (plots on the right).

Fitting for M

Assuming no change in $CMRO_2$ to hypercapnia or very mild hypoxia due to the BH, Equation 2-6 introduced in Chapter 2.3.3 (based on Davis, Kwong, Weisskoff, & Rosen (1998)) showed that:

$$\frac{\Delta BOLD}{BOLD_0} = M\left(1 - \left(\frac{CBF}{CBF_0}\right)^{\alpha-\beta}\right)$$

Using MATLAB's curve fitting function ('fit'), with non-linear least squares, the below curve was fitted to the inputted BH-BOLD (*B*) and BH-CBF data (*C*), to estimate the *M* parameter. A start point of 0.05, a lower point of 0 and an upper point of 2 was given to guide the fitting. An estimate for *M* alongside R^2 and the Root Mean Square Error (RMSE) were extracted for each fit.

$B = \boldsymbol{M}(1 - C^{-1.1})$, as setting α = 0.2 and β = 1.3, so $\alpha - \beta$ = -1.1

$CMRO_2$ movie time-series

Only in ROIs where the M parameter could be reasonably estimated (no complex values in the fitting, and $R_2 > 0.1$) was the $CMRO_2$ time-series to the movie estimated for each subject. The pre-processed BOLD and CBF movie data, explained in Chapter 7 were averaged over each voxel within the anatomical ROI to give a representative time-series. Therefore, in each ROI, there was an average *M* value, a BOLD movie time-series (relative to baseline) and CBF movie time-series (relative to baseline). Therefore, $CMRO_2$ (relative to baseline) could be estimated using the Equation 2-7 introduced in Chapter 2.3.3 (based on Davis, Kwong, Weisskoff, & Rosen (1998)):

$$\frac{CMRO2}{CMRO2_0} = \left(\frac{CBF}{CBF_0}\right)^{1-\frac{\alpha}{\beta}} \cdot \left(1 - \frac{\frac{\Delta BOLD}{BOLD_0}}{M}\right)^{1/\beta}$$

CBF-$CMRO_2$ and MEG-$CMRO_2$ coupling in each ROI

The relationship between CBF and $CMRO_2$ responses (n = $\Delta CBF/\Delta CMRO_2$) is an important physiological parameter that has been characterised widely in the calibrated-fMRI literature, so this was characterised over each ROI. In order to look at the relationship between MEG and $CMRO_2$ signals, a representative amplitude envelope in

each frequency band needed to be obtained over each ROI. Instead of averaging the MEG amplitude envelopes over each voxel in the ROI, the coefficient of variance (SD/Mean) was calculated for each voxel, to locate the voxel with the biggest variance in signal, scaled by the mean. This is important as the SNR of MEG source reconstructions are spatially non-uniform (for example, poorer SNR for sources deeper in the cortex), (Hillebrand & Barnes, 2002). Therefore, the SD/Mean approach gives voxel-wise scaling and is similar to typical BOLD-fMRI analysis where signal changes are often expressed in terms of the mean intensity. Therefore, the MEG time-courses (pre-processing explained in Chapter 7) that were correlated with CBF/BOLD/$CMRO_2$ were taken from one voxel within this ROI, that had the largest coefficient of variance.

Statistical Testing

For each participant, over each ROI, a linear model was fit using the MEG data (in each frequency band) to predict the $CMRO_2$ signals. For each fit, the beta coefficients were extracted for each participant. One sample t-tests tested whether these beta coefficients were significantly different to zero across the group.

As was done with MEG-fMRI coupling in Chapter 7, we also tested the coupling between MEG and $CMRO_2$ signals on the group mean-time series data. The MEG and $CMRO_2$ signals that were averaged over each ROI were then averaged across participants, before fitting the linear model to characterise if MEG data (in each frequency band) could predict the $CMRO_2$ signals.

8.3 RESULTS

M fitting

Table 8-1 shows the group average estimates of *M*, including the model fit parameters. These group averages are based on variable numbers of participants because of variability in the *M* fitting across ROIs. Figure 8-4 displays examples of the *M* fitting for five ROIs for one participant.

ROI	N subjects $R^2 > 0.1$	R^2 Mean	R^2 SD	RMSE mean	RMSE SD	**M mean**	**M SD**
Angular_R	4	0.324	0.150	0.004	0.001	**0.028**	**0.012**
Occipital_Inf_R	9	0.437	0.161	0.004	0.001	**0.030**	**0.010**
Occipital_Inf_L	9	0.512	0.160	0.003	0.001	**0.030**	**0.008**
Occipital_Mid_R	7	0.443	0.096	0.003	0.001	**0.029**	**0.005**
Occipital_Mid_L	9	0.528	0.152	0.003	0.001	**0.027**	**0.007**
Occipital_Sup_R	8	0.438	0.174	0.004	0.001	**0.031**	**0.007**
Occipital_Sup_L	8	0.416	0.167	0.004	0.001	**0.031**	**0.011**
Calcarine_R	9	0.501	0.147	0.004	0.001	**0.034**	**0.007**
Calcarine_L	11	0.412	0.172	0.006	0.001	**0.045**	**0.014**
Cuneus_R	8	0.377	0.189	0.005	0.001	**0.035**	**0.008**
Cuneus_L	6	0.376	0.144	0.005	0.001	**0.038**	**0.011**
Lingual_R	9	0.438	0.114	0.005	0.001	**0.042**	**0.011**
Lingual_L	11	0.408	0.184	0.005	0.001	**0.041**	**0.015**
Parietal_Inf_R	4	0.276	0.078	0.006	0.003	**0.035**	**0.012**
Parietal_Inf_L	2	0.196	0.027	0.005	0.001	**0.026**	**0.000**
Parietal_Sup_R	3	0.223	0.070	0.008	0.001	**0.042**	**0.009**
Parietal_Sup_L	3	0.257	0.091	0.005	0.000	**0.027**	**0.005**
Precuneus_L	3	0.421	0.128	0.004	0.000	**0.022**	**0.003**
Precuneus_R	4	0.280	0.070	0.007	0.001	**0.039**	**0.009**
Temporal_Inf_R	5	0.515	0.126	0.004	0.001	**0.036**	**0.010**
Temporal_Inf_L	8	0.370	0.188	0.005	0.001	**0.033**	**0.013**
Temporal_Mid_R	5	0.353	0.162	0.004	0.001	**0.031**	**0.004**
Temporal_Mid_L	6	0.394	0.177	0.004	0.001	**0.028**	**0.008**
Temporal_Sup_R	3	0.252	0.197	0.005	0.000	**0.032**	**0.011**
Fusiform_R	9	0.426	0.168	0.004	0.001	**0.031**	**0.009**
Fusiform_L	9	0.425	0.160	0.004	0.001	**0.030**	**0.011**
Postcentral_R	1	0.109	/	0.006	/	**0.027**	**/**
Postcentral_L	2	0.196	0.030	0.004	0.000	**0.024**	**0.001**
	Grand Mean	0.368	0.136	0.005	0.001	**0.032**	**0.008**

Table 8-1. Estimates of M, including fit parameters. Averages for each ROI are displayed, only for subjects that did not have complex values in the model fit (often due to negative CBF values) and had an R2 of greater than 0.1. RMSE = Root Mean Square Error.

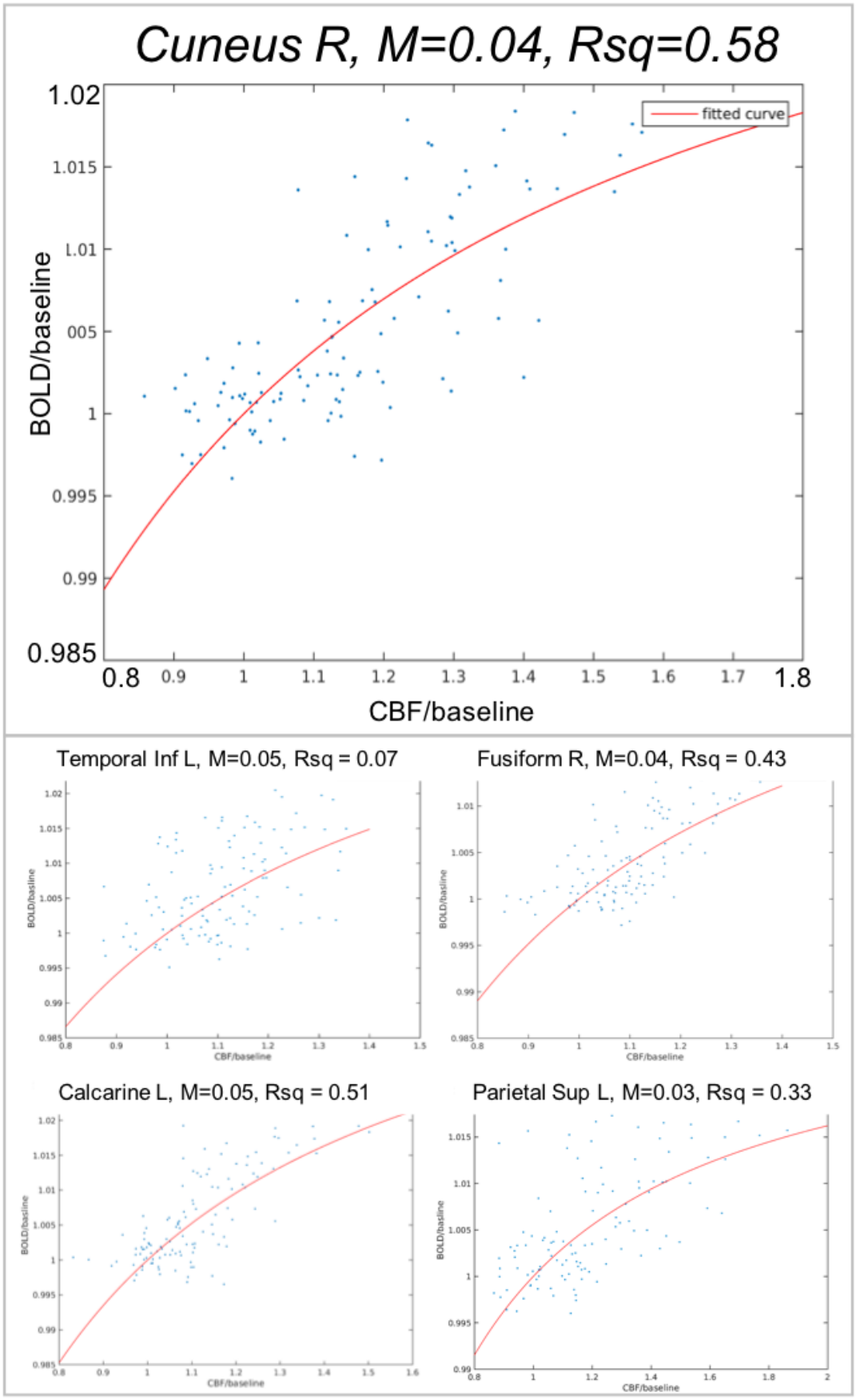

Figure 8-4. Examples of the M fitting for one participant, across 5 different ROIs.

CBF-$CMRO_2$ coupling to the movie stimulus

Table 8-2 shows the average *n* coupling values (*n* = $\Delta CBF/\Delta CMRO_2$) across participants for each ROI, and Figure 8-5 displays shows an example of this coupling for a single participant, across three example ROIs.

ROI	subjects	*n* Mean	*n* SD
Angular_R	4	2.78	1.83
Occipital_Inf_R	9	1.55	2.96
Occipital_Inf_L	9	2.41	1.33
Occipital_Mid_R	7	2.67	1.14
Occipital_Mid_L	9	3.14	2.58
Occipital_Sup_R	8	2.64	0.93
Occipital_Sup_L	8	3.40	2.38
Calcarine_R	9	2.24	0.68
Calcarine_L	11	1.92	0.43
Cuneus_R	8	2.23	0.67
Cuneus_L	6	2.02	0.50
Lingual_R	9	1.73	0.32
Lingual_L	11	1.74	0.47
Parietal_Inf_R	4	1.94	0.76
Parietal_Inf_L	2	2.97	0.80
Parietal_Sup_R	3	2.22	1.22
Parietal_Sup_L	3	2.70	1.20
Precuneus_L	3	3.34	1.83
Precuneus_R	4	1.95	0.68
Temporal_Inf_R	5	2.55	0.57
Temporal_Inf_L	8	2.13	0.74
Temporal_Mid_R	5	2.97	1.50
Temporal_Mid_L	6	2.25	0.69
Temporal_Sup_R	3	2.05	0.57
Fusiform_R	9	1.91	0.58
Fusiform_L	9	1.71	0.39
Postcentral_R	1	1.77	/
Postcentral_L	2	5.12	5.14

Table 8-2. Average n *parameter across participants, for each ROI, representing CBF-$CMRO_2$ coupling to the movie. The number of participants that $CMRO_2$ was estimated for varies across ROI and is shown in the 'subjects' column.*

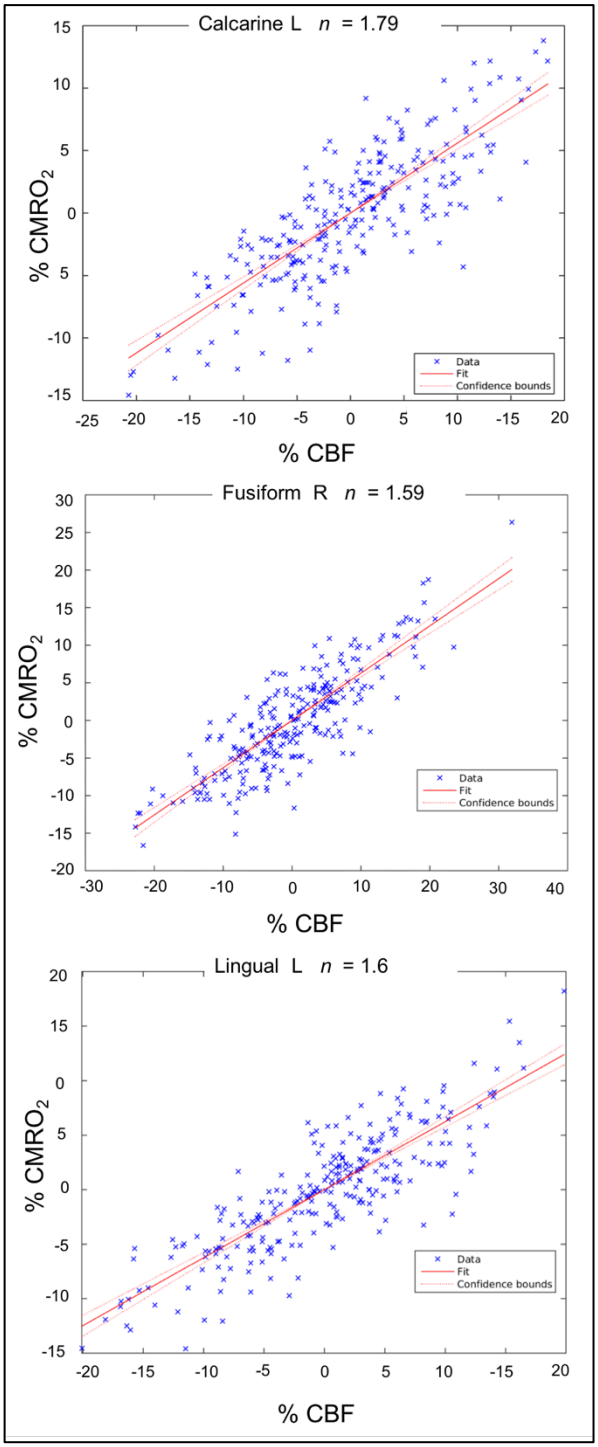

Figure 8-5. CBF-$CMRO_2$ coupling to the movie stimulus, for one participant, over three different ROIs.

Coupling between MEG and $CMRO_2$ movie signals

Figure 8-6 shows an example subject time-series for BOLD, CBF, $CMRO_2$ and MEG 1-4Hz activity extracted over the same ROI, to demonstrate the shape and magnitude of each signal change. The relationship between MEG and $CMRO_2$ signals to the movie was explored in six ROIs with some of the largest numbers of participants showing

acceptable *M* fitting in both hemispheres: Calcarine Left (n=10), Calcarine Right (n=8), Lingual Left (n=10), Lingual Right (n=8), Fusiform Left (n=8) and Fusiform Right (n=8). These values are one less than those displayed in Table 8-1 due to there being only 14 participants, out of the 15 participants with BH-data, also having MEG data.

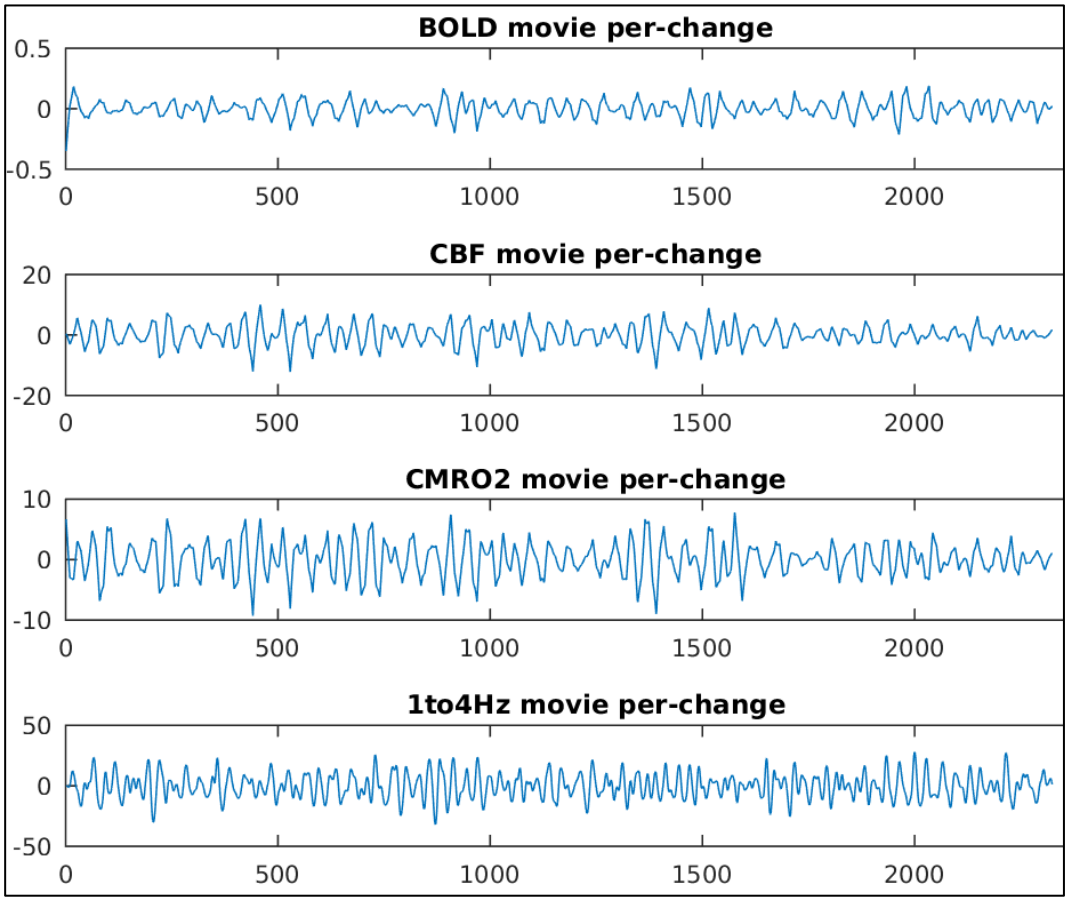

Figure 8-6. An example time-series for BOLD, CBF, $CMRO_2$ and MEG 1-4Hz activity extracted over the same ROI. This data is from one participant, just to demonstrate the shape and magnitude of each signal change. Per-change refers to signals expressed as percentage change from baseline.

MEG, in each frequency band separately, was used to predict $CMRO_2$ for each participant, in each ROI. Beta-coefficients were extracted for all participants. There were no beta coefficients significantly different to zero for any MEG-$CMRO_2$ relationships. Two relationships showed p-values less than 0.05 (1-4Hz and $CMRO_2$, 8-13Hz and $CMRO_2$ in Right Fusiform gyrus) however considering the many statistical tests performed this would not reach statistical significance after any multiple comparison correction. These beta-coefficients are shown in Table 8-3. We explored the relationships between $CMRO_2$ and MEG using the group mean-time series data, in these ROIs. Three model fits had p-values less than 0.05 (1-4Hz and $CMRO_2$, and 95-145Hz and $CMRO_2$ in the Right Fusiform gyrus, and 1-4Hz and $CMRO_2$ in the Right Calcarine Sulcus). Again, these do not survive corrections for multiple comparison.

These relationships are displayed in Supplementary Figures 8.1 - 8.3, alongside the MEG-BOLD and MEG-CBF coupling in the same ROI, for comparison.

Calcarine Left (n=10)

	1-4Hz	4-8Hz	8-13Hz	13-30Hz	40-70Hz	70-120Hz	95-145Hz
$CMRO_2$ AV	0.001	0.005	0.010	0.013	-0.019	-0.008	0.013
$CMRO_2$ SD	0.010	0.019	0.023	0.026	0.071	0.090	0.103

Calcarine Right (n=8)

	1-4Hz	4-8Hz	8-13Hz	13-30Hz	40-70Hz	70-120Hz	95-145Hz
$CMRO_2$ AV	0.006	0.007	0.004	0.005	-0.056	-0.033	0.005
$CMRO_2$ SD	0.014	0.017	0.021	0.037	0.075	0.080	0.062

Fusiform Left (n=8)

	1-4Hz	4-8Hz	8-13Hz	13-30Hz	40-70Hz	70-120Hz	95-145Hz
$CMRO_2$ AV	-0.003	0.007	0.008	0.012	-0.063	-0.020	0.022
$CMRO_2$ SD	0.019	0.015	0.023	0.033	0.112	0.050	0.087

Fusiform Right (n=8)

	1-4Hz	4-8Hz	8-13Hz	13-30Hz	40-70Hz	70-120Hz	95-145Hz
$CMRO_2$ AV	0.013	0.008	0.011	0.005	-0.041	-0.025	-0.007
$CMRO_2$ SD	0.012	0.020	0.011	0.037	0.078	0.099	0.105

Lingual Left (n=10)

	1-4Hz	4-8Hz	8-13Hz	13-30Hz	40-70Hz	70-120Hz	95-145Hz
$CMRO_2$ AV	-0.003	0.009	0.004	0.001	-0.019	0.006	0.008
$CMRO_2$ SD	0.019	0.022	0.026	0.030	0.080	0.082	0.092

Lingual Right (n=8)

	1-4Hz	4-8Hz	8-13Hz	13-30Hz	40-70Hz	70-120Hz	95-145Hz
$CMRO_2$ AV	0.001	0.009	0.006	0.010	-0.024	-0.005	0.000
$CMRO_2$ SD	0.017	0.023	0.016	0.035	0.077	0.083	0.064

Table 8-3. Averages (AV) and standard deviations (SD), across participants, of beta coefficients (unstandardised) from the model fit of MEG activity (in each specific frequency band) and $CMRO_2$ activity, over 6 ROIs that showed acceptable M fitting for either 10 participants (Calcarine Left, Lingual Left) or 8 participants (Calcarine Right, Lingual Right, Fusiform Left, Fusiform Right). The beta coefficients highlighted in grey were significant at $p<0.05$, uncorrected for multiple comparisons.

8.4 DISCUSSION

Breath-Hold Task to estimate M

In order to model $CMRO_2$ to the movie an estimate of *M* had to be obtained in the same brain region. *M* is a scaling parameter which represents the maximum BOLD signal change that would occur if all deoxyhaemoglobin was washed out of the venous blood vessels. In practice, smaller physiological changes are induced with hypercapnic stimuli, but it is enough to change the BOLD and CBF responses to get some estimate of the baseline tissue state, summarised by *M.* In this chapter, we fit for the *M* parameter using an accepted biophysical model linking BOLD and CBF changes. Although the model fit of *M* varied across participants, an adequate model fit was achieved in multiple brain regions, particularly in the visual cortex. It is important to highlight that in this study, we *fit* for the M parameter and only characterise $CMRO_2$ in ROIs where the fit was reasonable. Most studies that have estimated *M* from a hypercapnic stimulus have taken baselined BOLD and CBF signals, *averaged over time*, and inputted these point estimates into the equation for *M*. The average *M* values we report were around 3%. However higher values of at least 6% are more typically reported for these brain regions (e.g. Wise, Harris, Stone, & Murphy, 2013). As *M* does not only depend on physiological factors, but also on image acquisition parameters and data analysis choices, it can be difficult to make meaningful comparisons across studies. However, there are many factors that may have contributed to these lower *M* values, some of which are discussed below.

An assumption in the model fit for *M* is that the BH-paradigm induces isometabolic changes in BOLD and CBF. The assumed mechanism is an increase of PCO_2 causing blood vessels to dilate, resulting in increased CBF and resultant increased BOLD signals (Ainslie & Duffin, 2009), without any change in oxygen metabolism. However, this assumption has been challenged and there is evidence for metabolic changes induced by hypercapnia (Driver et al., 2017; Yablonskiy, 2011; Zappe, Uludağ, Oeltermann, Uğurbil, & Logothetis, 2008). There is recent work demonstrating how to measure and correct for the likely reduction of resting $CMRO_2$ during hypercapnia, and therefore increase the accuracy of the *M* value estimates, and therefore the modelled task-induced $CMRO_2$ changes (Driver et al., 2017), and this should be considered for future work. Unlike with a gas-delivery design, inspired oxygen is not being held constant, therefore there will also be small reductions in arterial PO_2 (Bulte, Drescher, & Jezzard, 2009), which will decrease the BOLD signal and cause an underestimation

of M. Although these changes in arterial PO_2 are likely to have a small effect over a short BH, this is a likely explanation for why we report lower *M* values with this design.

Another factor contributing to the lower *M* values we report here could be an underestimation of the CBF change in the BH paradigm. This underestimation in CBF could be due to the long TR in the ASL sequence used (4.4 seconds) due to a pseudo-continuous tagging design with dual excitation. The CBF changes are therefore effectively smoothed due a low sampling rate. This lower sampling rate is the same for the BOLD-weighted signal but for CBF it is worsened by the need to do tag-control subtraction in order to obtain the perfusion signal. The estimate of the baseline BOLD and CBF signals was challenging due to this low sampling rate, accompanied with a dynamically changing stimulus. For each block of paced-breathing, only 5 brain volumes were acquired. A clear improvement to this BH design would be to include a long baseline at the start and/or end, to more accurately estimate the baseline BOLD and CBF under normal breathing conditions, in each brain region. This BH task design is more appropriate for fMRI sequences with a shorter TR. Nevertheless, the relative values we got for BOLD and CBF response to the BH stimulus are in the ranges we would expect (see Figure 8-3), which shows BOLD changes of around 1-2% and CBF of around 20-60%). There was a large variability in the fitting of *M* for each participant, presumably due to different task compliance and data quality. There was also a difference in the fitting of M across brain regions. There is evidence that coupling between CBF and $CMRO_2$ (Ances et al., 2008), and variations in capillary vascularisation (Ekstrom, 2010) vary across brain regions. Fitting for *M* was best in the visual cortex; this could be explained by the fact the visual cortex has a higher density of capillaries (Buxton, 2009; Zheng, LaMantia, & Purves, 1991) and therefore this will result in higher CBV and higher *M* values.

Modelling $CMRO_2$ to the movie-stimulus

Modelling the $CMRO_2$ response with the standard calibrated-fMRI model (Davis et al., 1998) gave physiologically reasonable $CMRO_2$ changes (Buxton, 2009), see Figure 8-6 showing $CMRO_2$ increases and decreases to the movie stimuli of around 0-10%. Importantly, the CBF-$CMRO_2$ coupling (*n*) was close to 2 or 3 in 27 out of the 28 ROIs, very consistent with what has been reported previously (Blockley et al., 2013). Griffeth et al (2015) characterised *n* to a movie stimulus and found very similar values: their average *n* over the visual cortex was 2.47, and our grand average *n* over the 12 visual ROIs was 2.31. They did not measure *M* but assumed different values (as well as different values for the parameters α and β) when comparing between their conditions.

They assumed a much higher *M* when modelling $CMRO_2$ (11.6%), and actually show that when modelling the data with a lower M of 8.1% the difference between the increase in relative $CMRO_2$ from the movie compared to the 10% visual contrast condition was no longer statistically different. Our underestimation of *M*, already discussed above, could have led to an underestimation in $CMRO_2$, and contributed to the lack of significant correlations seen between MEG and $CMRO_2$ movie signals.

There were no reliable significant relationships between $CMRO_2$ and MEG signals. This was most likely due to sample size, and propagated noise. $CMRO_2$, being a derived parameter, is highly sensitive to the noise in the CBF timeseries, measured with ASL. Only datasets from 12 out of the 14 participants who had completed the BH task were good enough quality to analyse, and after this the fitting of *M* greatly varied over brain region, such that 10 was the maximum number of participants left to characterise MEG-$CMRO_2$ relationships over a specific ROI. Unfortunately, in areas showing different BOLD-MEG and BOLD-CBF coupling in Chapter 7 (for example, cuneus and pre-cuneus) *M* could not be well estimated, and therefore $CMRO_2$ time-series were not characterised over these regions. In the regions that suggested at a relationship between MEG and $CMRO_2$, these were mostly in neural oscillations at lower frequencies (1-4Hz and 8-13Hz) which is possibly driven by the 1/f power spectrum known to exist in the brain i.e. higher amplitudes at lower frequencies (Jia & Kohn, 2011). For the relationships shown in Supplementary Figures 8.1 - 8.3, based on the mean-time series data, all beta coefficients (relating MEG to BOLD, CBF and $CMRO_2$) were negative, which is not expected for delta and gamma frequencies, which we would predict positive correlations based on previous literature with BOLD-fMRI (Mukamel et al., 2005; Zumer et al., 2010).

Conclusions

This chapter demonstrated it is possible to use simple modelling of BOLD and CBF signals, elicited with a BH-design, to give reasonable estimates of *M* in different brain regions, although a slight underestimation compared to other literature. This allowed characterisation of CBF-$CMRO_2$ coupling across different brain regions. With an improved BH design, including better estimation of the baseline, these *M* values, and therefore the modelled $CMRO_2$ values, are likely to be more accurate. This research acts as a proof of principle that MEG and $CMRO_2$ signals can both be modelled in response to the same stimulus, however much larger samples and optimised modelling of the relationship between these signals, is needed to characterise this relationship robustly.

8.5 SUPPLEMENTARY

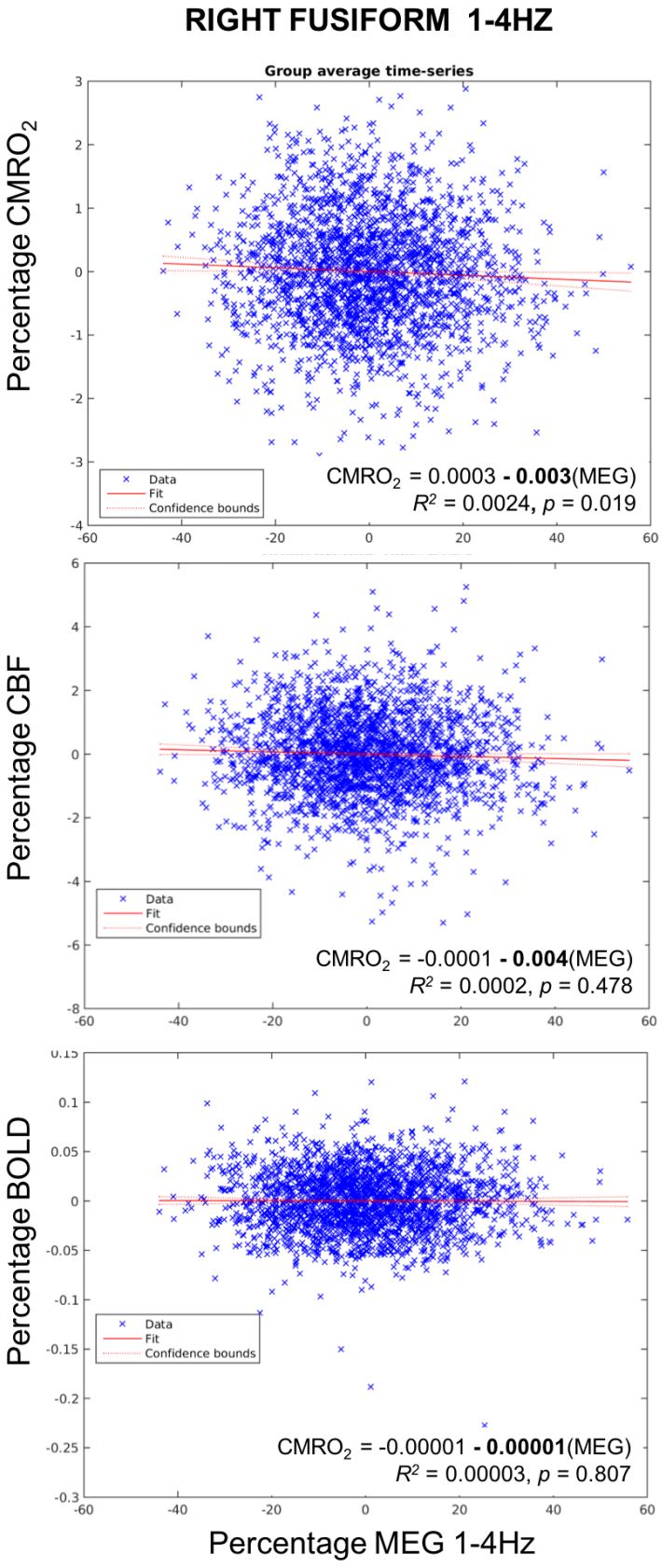

Supplementary Figure 8.1. The relationship between MEG (1-4Hz) and $CMRO_2$, CBF and BOLD signal changes in response to the movie stimuli, based on the mean-times data across participants, averaged over the right fusiform gyrus.

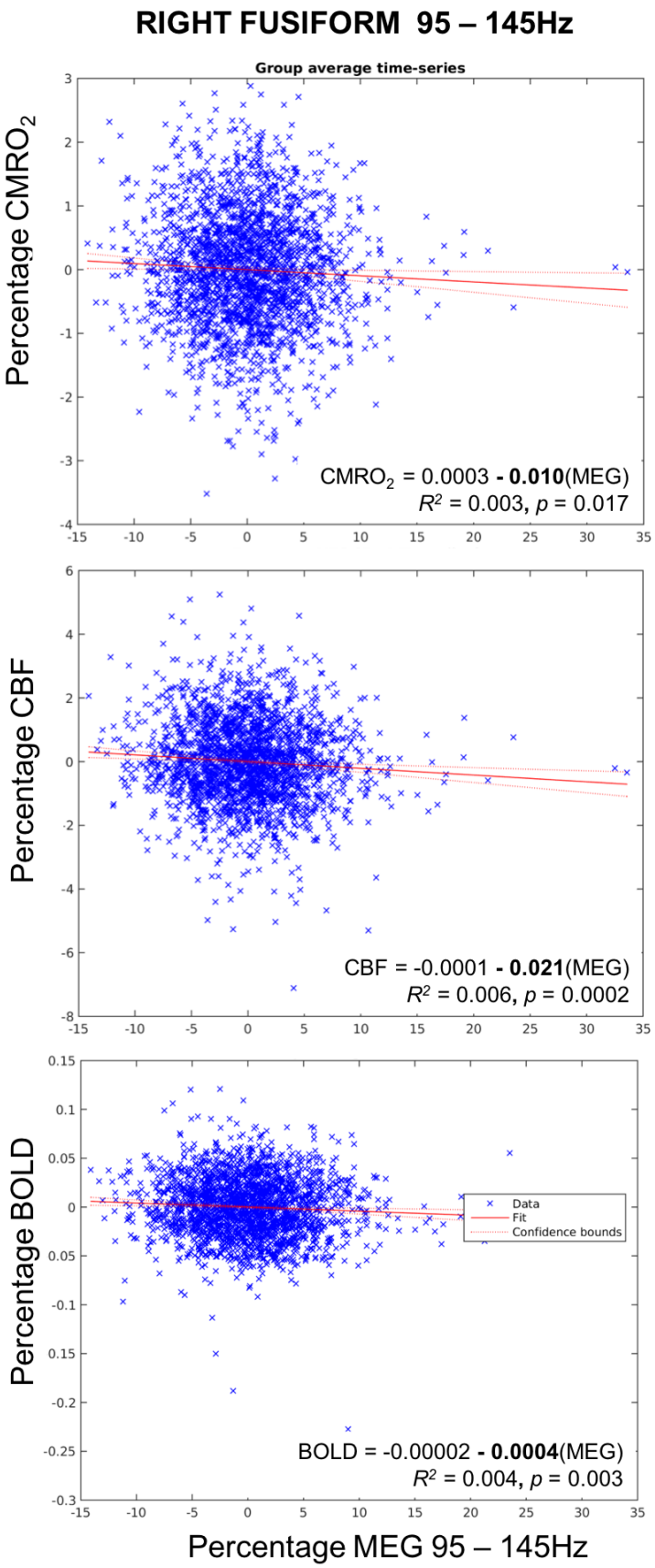

Supplementary Figure 8.2. The relationship between MEG (95 – 145Hz) and $CMRO_2$, CBF and BOLD signals changes in response to the movie stimuli, based on the mean-times data across participants, averaged over the right fusiform gyrus.

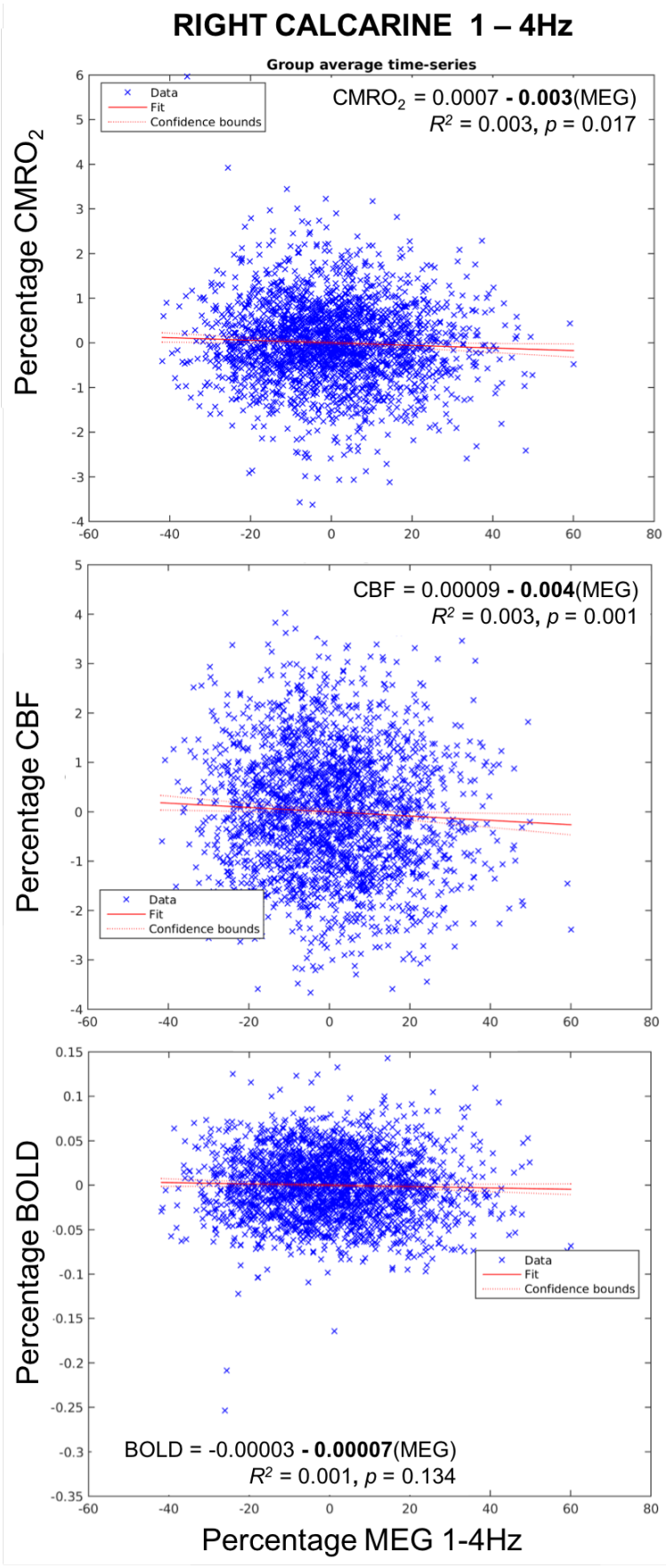

Supplementary Figure 8.3. The relationship between MEG (1 – 4Hz) and $CMRO_2$, CBF and BOLD signals changes in response to the movie stimuli, based on the mean-times data across participants, averaged over the right calcarine sulcus.

9 Coupling between brain oscillations, CBF, and BOLD signals during naturalistic movie viewing in Multiple Sclerosis

9.1 INTRODUCTION

As discussed in Chapter 7, the rationale of using a movie stimulus to investigate NVC was partly motivated by the aim to develop engaging and easy designs that can be used in patient populations during both MEG and fMRI. Another motivation of using such a design is that it is more representative of visual processing in natural real-world environments, and therefore may be more disease relevant (compared to highly controlled visual stimuli) as it simultaneously recruits more areas of the brain. Therefore, in this chapter, we applied the methods presented in Chapter 7 in order to investigate differences in NVC between the healthy and MS brain.

Although visual abnormalities are common in MS (Graham & Klistorner, 2017), MS is not specifically a disease of the visual system and there is great variability across participants in symptom severity. The movie stimulus used in Chapter 7 still predominantly recruits visual areas, however it recruits more of the occipital cortex than a visual checkerboard stimulus which is often more localised to primary visual areas. Furthermore, Chapter 7 also showed common movie activity, across participants, in temporal and parietal areas. Therefore, this design allows us to study NVC across more areas of the brain, which is important considering the wide spread damage in MS, and the fact that NVC is shown to vary across brain region (e.g. (Devonshire et al., 2012) and results from Chapter 7).

In Chapter 4, no significant differences in NVC to a visual stimulus were reported in MS, although the MS group did show lower amplitude changes for gamma oscillations, BOLD and CBF signals. Despite no significant NVC differences, the MS group displayed more variability in their coupling relationships. It may be the case that NVC is not uniformly altered in MS, despite the inflammatory environment affecting NVC signalling mechanisms (D'haeseleer et al., 2015; Lapointe et al., 2018; Paling et al., 2011; Spencer et al., 2018). Alternatively, the methods used may not have been sensitive enough to find differences between groups, considering they focused only on oscillations in the gamma frequency range in the early visual cortex.

The design presented in Chapter 7 allowed us to characterise neural oscillations from 1-145Hz. Different oscillatory frequencies are hypothesised to reflect activity across different scales of neural networks (Buzsáki & Draguhn, 2004) and in different cell

populations. Therefore, finding abnormalities in MS at specific oscillatory frequencies could give insight into possible disease mechanisms. This chapter presents the same methods used in Chapter 7, extending them to test differences between MS patients and healthy controls. The lack of baseline period in this continuous movie recording restricts the analysis approaches. Therefore, a simple aim of this chapter was to test the feasibility and utility of this type of design for studying NVC in MS. We also characterised the coupling between BOLD and CBF signals to the movie, as this may be informative about how blood flow and metabolism are coupled in MS. Based on previous work on neural, vascular and metabolic impairment in MS, we predicted the MS group would have more variable responses to the movie stimulus and altered NVC in some brain regions.

9.2 METHODS

Participants

15 MS patients with RRMS and 15 healthy controls are presented in this chapter. All of these patients and 12 of these controls were presented in Chapter 5, and three of these controls were from Chapter 7. Supplementary Figure 5-2 gives an overview of the data collection for the wider study. All participants gave written informed consent prior to participating in this part of the study and received £10 per hour for taking part. See Table 9-1 for participant details.

Design and Procedure

All participants had a MRI scan and a MEG scan. The order of these scans is given in Table 9-1. Both scanning sessions included passive viewing of the same movie clip from the James Bond film ‘Skyfall’ (approximately the first 19 minutes 38 seconds). For the MRI session, all participants also had a T1 structural scan.

Data Acquisition and Pre-Processing

MEG data and fMRI data were collected and pre-processed with the identical pipeline used in Chapter 7, for both patients and controls.

Within modality analysis: inter-subject correlations (ISCs)

The same within-modality analysis was run as was presented in Chapter 7, to get ISCs for BOLD, CBF and MEG in each frequency band. This was done for the control group and the patient group separately, simply to see where there was significant common activity to the movie stimulus in each group.

Cross-modality analysis: MEG-fMRI and CBF-BOLD coupling

The focus of this analysis was to understand if there are differences in NVC and CBF-BOLD relationships between patients and controls. Therefore, to take into account individual subject variability, MEG-BOLD, MEG-CBF and CBF-BOLD regressions were run for each subject separately, using MATLAB's *fitlm* function. For each participant, and for each voxel in the 6mm template brain, a *beta* coefficient and an *r* value were outputted (as explained in Chapter 7). FSL's *randomise* function was used to perform unpaired nonparametric t-tests at each voxel (5000 permutations) with FWER correction at $p<0.05$, and TFCE. T-statistic contrasts for Patients > Controls and Controls > Patient were examined.

9.3 RESULTS

Demographics for patients and controls are presented in Table 9-1, alongside disease characteristics for patients only. Patients and controls did not significantly differ in age, $t(28) = 1.24$, $p = 0.225$. Each group had the same number of male and female participants.

	Patients	**Controls**
Age (Mean ± SEM)	36.93 ± 1.60	34.13 ± 1.58
Gender (M/F)	3/12	3/12
First scan (MEG/fMRI)	15/0	10/5
Watched Movie (Y/N/DM)	10/3/2	11/4
Patients		
Months since onset (Mean ± SEM, min, max)	97 ± 15 (28, 213)	
Months since relapse (Mean ± SEM, min, max)	36 ± 4.4 (11, 64)	
EDSS (Mean ± SEM, min, max)	2.2 ± 0.3 (1, 4)	

Table 9-1. Demographic and clinical information for patients and controls. First scan = which scanner they watched the movie in first. DM = data missing. Onset refers to disease onset and relapse refers to patient's last clinically confirmed relapse.

Within modality results

To uncover activity related to the movie, ISCs were calculated at each voxel, for the control group and patient group separately. Figure 9-1 shows significant ISCs for the BOLD and CBF analyses, Figure 9-2 shows significant ISCs for the 1-30Hz MEG analyses, and Figure 9-3 shows significant ISCs for the 40Hz+ MEG analyses. The location of the significant ISCs are very similar to those reported in Chapter 7: across occipital, parietal and temporal cortical areas.

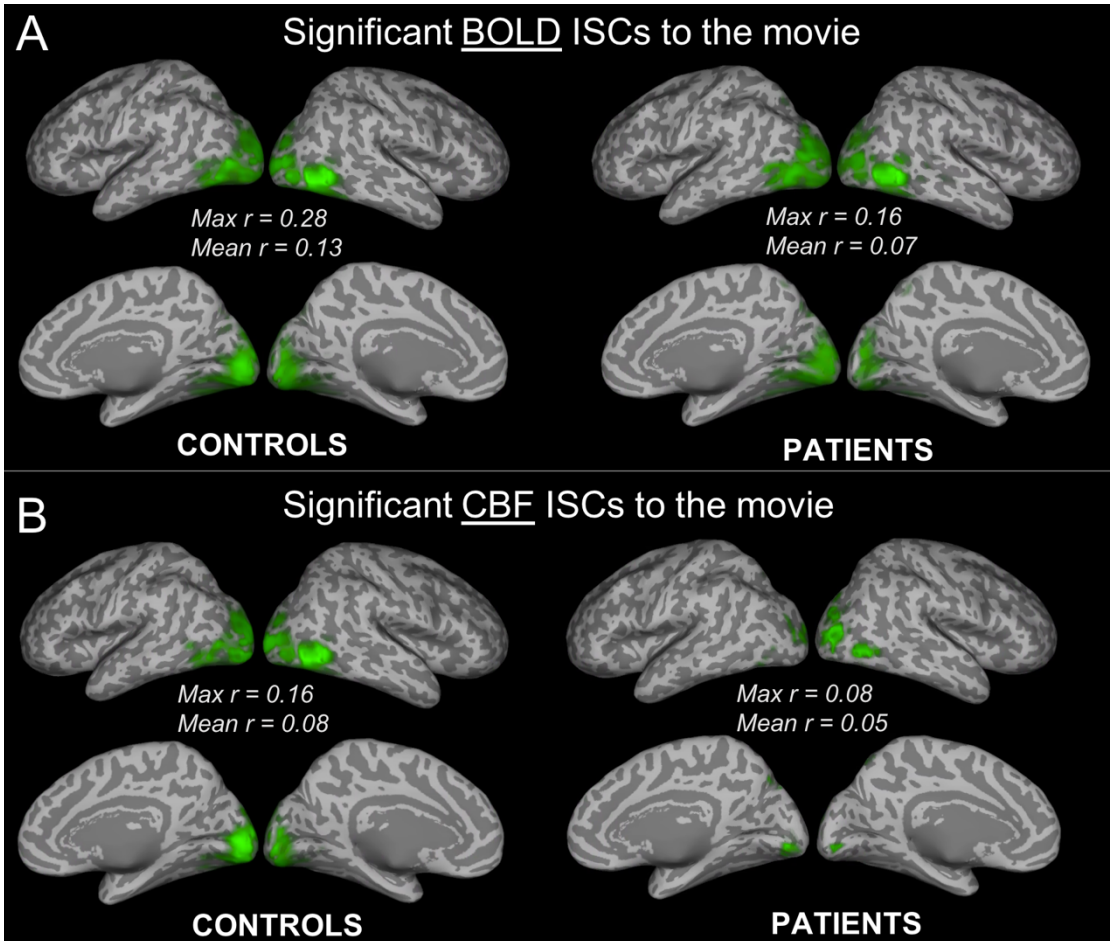

Figure 9-1. Significant BOLD and CBF inter-subject correlations (ISCs) showing movie-activated areas, for control and patient groups separately. Correlation values corrected to p<0.05, with randomisation testing. Correlations are displayed on an inflated MNI template brain. Mean correlation over voxels (Mean r) and maximum correlation over voxels (Max r) are reported.

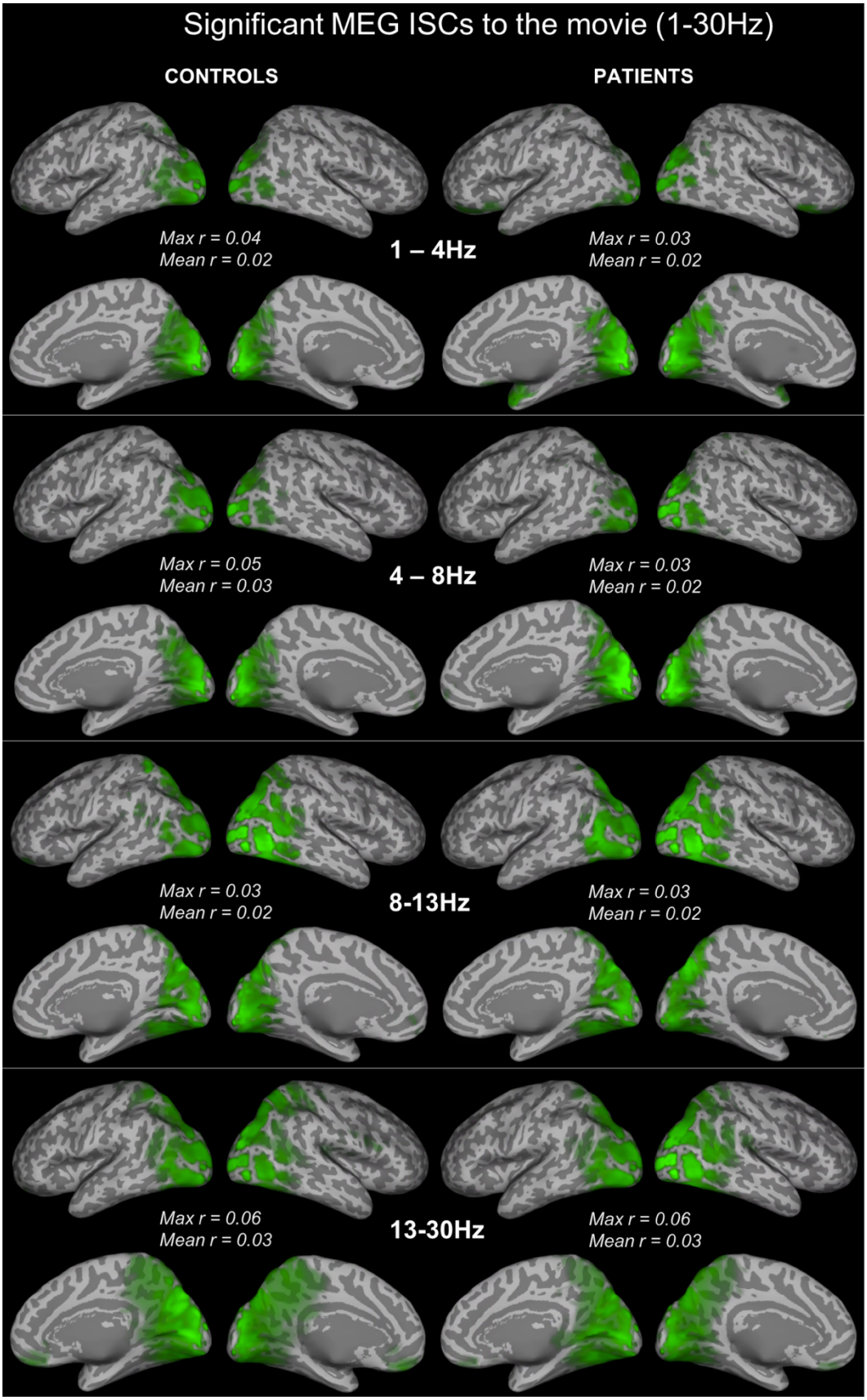

Figure 9-2. Significant MEG (1-30Hz) inter-subject correlations (ISCs) showing movie-activated areas, for control and patient groups separately. Correlation values corrected to p<0.05, with randomisation testing. Correlations are displayed on an inflated MNI template brain. Mean correlation over voxels (Mean r) and maximum correlation over voxels (Max r) are reported.

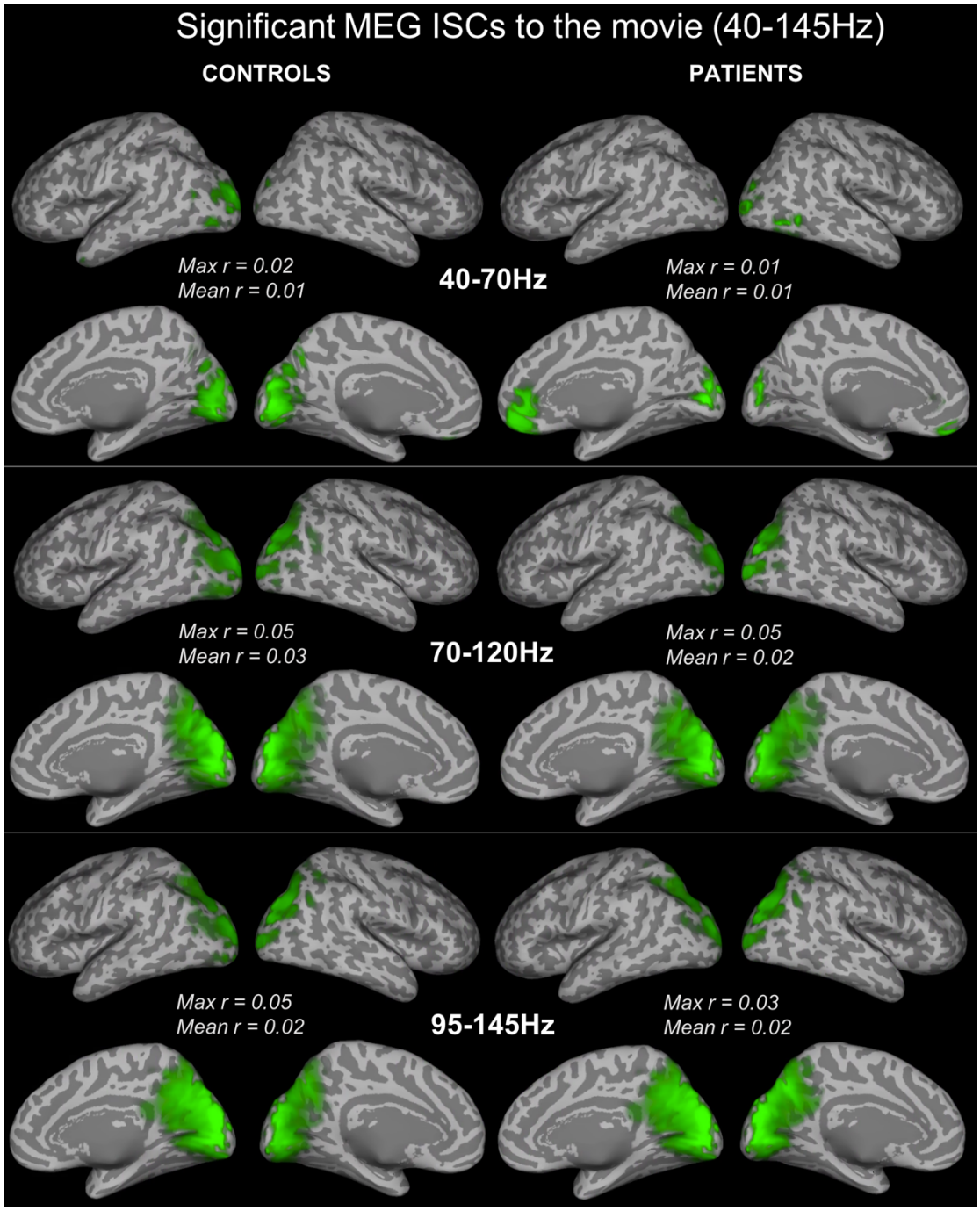

Figure 9-3. Significant MEG (40-145Hz) inter-subject correlations (ISCs) showing movie-activated areas, for control and patient groups separately. Correlation values corrected to p<0.05, with randomisation testing. Correlations are displayed on an inflated MNI template brain. Mean correlation over voxels (Mean r) and maximum correlation over voxels (Max r) are reported.

MEG-fMRI coupling

Maps of *beta* coefficients and *r* values for each MEG-BOLD and MEG-CBF relationship were created for each subject, and group differences were tested at each voxel. The only relationship showing significant differences between patients and controls was the 8-13Hz MEG and BOLD relationship. Significantly larger *r* values and significantly larger *beta* coefficients were reported in the patient group compared to the controls, see Figure 9-4. This figure displays the group mean *beta* or *r* values in areas where there were significant mean differences between the two groups. The sign of the relationship is different between groups, and not simply the magnitude of the relationship. For each group separately, a few small significant clusters of *r* or *beta* values were found to be significantly different to zero (similar to Chapter 7, data not plotted).

For each group, the *r* and *beta* maps for each subject were averaged and each relationship is displayed in Supplementary Figure 9-1 to demonstrate the unthresholded mean coupling relationships. These figures are not statistically thresholded but masked to areas that had significant ISCs for BOLD, CBF or that MEG within the frequency band of interest.

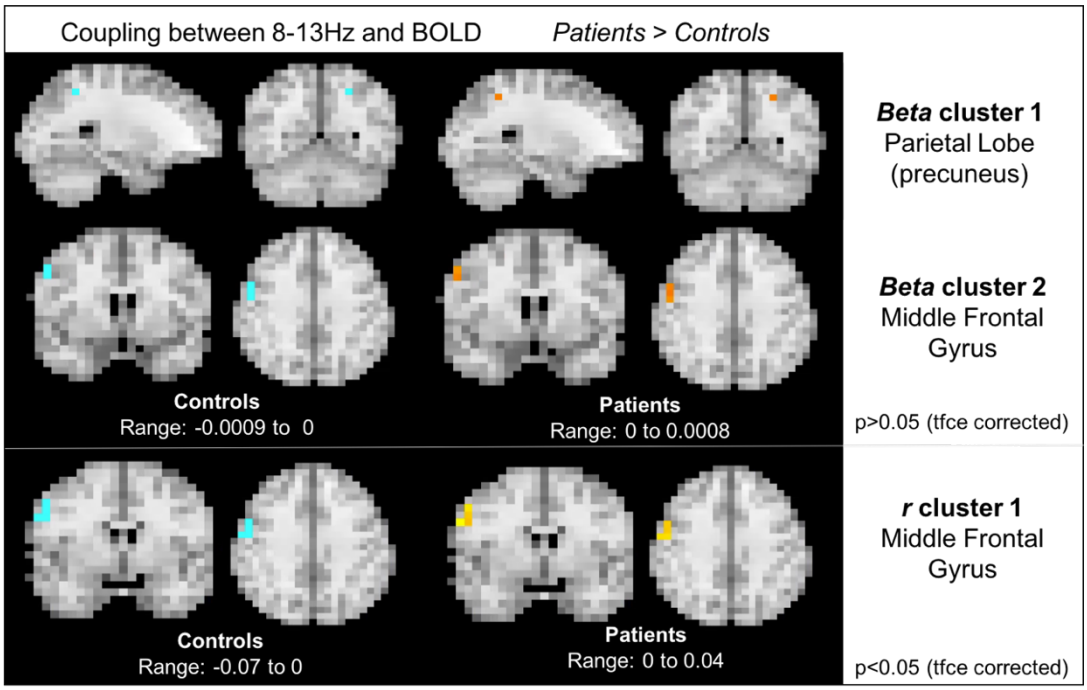

Figure 9-4. MEG-fMRI relationships that showed significantly different beta or r values between patients and controls. The values displayed are means across groups. Red/Orange/Yellow indicate positive values and Blue indicates negative values.

BOLD-CBF coupling

There were no *r* values or *beta* coefficients significantly different between patients and controls. However, for both groups, BOLD and CBF showed significant voxel-wise positive correlations to the movie stimulus in many areas across the brain. These significant correlations are displayed in Figure 9-5.

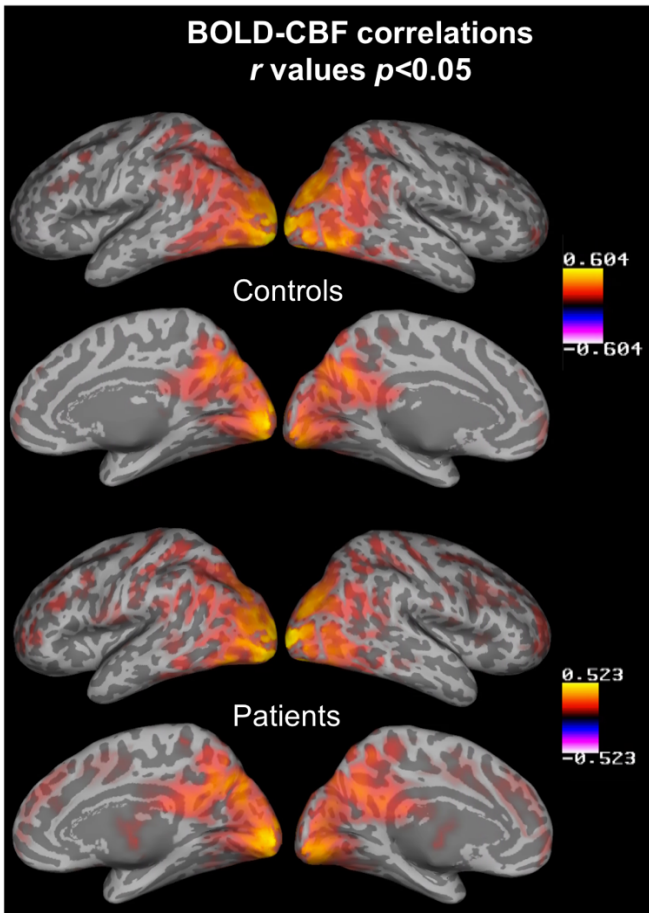

Figure 9-5. BOLD-CBF correlations to the movie stimulus, for patient and controls. Data displayed is thresholded at p<0.05 with tfce correction.

9.4 DISCUSSION

Responses to a continuous movie stimulus were compared between 15 MS patients and 15 controls, using MEG and fMRI. Results in a healthy population were explored in depth in Chapter 7, and therefore the focus of this chapter was to compare patients and controls in the context of NVC. Patients and controls were matched on age and gender, but there were differences in the order in which they watched the scan, with all patients watching the movie in the MEG first compared to only 10 out of the 15 controls. As habituation and memory effects have been demonstrated to affect the ISCs during movie watching (Chang et al., 2015; Dmochowski et al., 2012) this may have introduced bias in the group comparison.

For the within-modality results, significant ISCs were reported for both patients and controls across occipital, parietal and temporal cortical areas, consistent with what was found in Chapter 7. For all fMRI and MEG ISCs, the patient group displayed lower average and maximum correlations, suggesting the patients have more variable MEG, BOLD and CBF responses to the movie. This variability refers to how similar their responses are to one another. Some spatial differences in the distribution of the ISCs can also be seen. There are noticeably fewer significant ISCs for CBF in the patient group, compared to the controls, whereas the BOLD ISCs appear similar between groups. Patients display significant ISCs in the temporal cortex for 1-4Hz and in the frontal cortex for 40-70Hz, which was also seen in the control group in Chapter 7. As with Chapter 7, these ISCs are small, only explaining a very small fraction of shared variance between participants. A similar movie design has been used previously to study ISCs in a patient group; Hasson, Malach, & Heeger (2010) reported more variability in BOLD-fMRI activity for individuals with autism (lower ISCs), in response to 10 minute clip from a feature film. Although their questions were not centered around NVC, as they only report fMRI data, it demonstrates the application of this type of stimulus to studying disease related impairments.

For the MEG-fMRI coupling, we examined both *beta* coefficients to represent the strength of the relationship between MEG and fMRI signals in meaningful units, as well as *r* values to represent how much shared variance there is in the MEG and fMRI time-series. Despite some big visual differences in the mean correlation maps (in Supplementary Figure 9-1) there were only a few significant voxels found. This was between BOLD and 8-13Hz MEG responses showing patients to have significantly higher correlations and beta coefficients than controls. The sign of the relationship was in fact reversed for patients, showing a positive relationship instead of a negative.

Typically, negative correlations are reported between alpha (8-13Hz) frequencies and fMRI signals (Logothetis, 2002; Mukamel et al., 2005; Zumer et al., 2010). Therefore, this could reflect a reversed NVC pattern in patients, possibly reflecting an adaptation to damage. However, this is a tentative interpretation that needs further investigation. The results are hard to interpret with so few voxels making up the significant cluster. Also, considering this relationship is with BOLD and not CBF, this could point to a difference in CBF, $CMRO_2$, CBV or baseline tissue state and we cannot disentangle which with this data.

In Chapter 7, we did not statistically test CBF-BOLD relationships to the movie stimulus as done here. Here, we demonstrate that the movie stimulus elicits very strong positive correlations between BOLD and CBF signals, widely across the brain. Although no significant differences in the relationship between BOLD and CBF were reported in the patient group, this strong positive correlation in functionally relevant areas indicates the movie must be imposing a strong temporal structure on these two signal contrasts.

Considering Chapter 7 also reported an insensitivity to characterising NVC at the individual level, it is not surprising that few group differences were found between patients and controls. It is therefore difficult to establish whether this lack of differences are due to the limitations of the method, or no true difference in NVC in MS. A larger sample size is needed to address these questions, as Chapter 7 did demonstrate more significant coupling relationships between MEG and BOLD when expanding the dataset. A recent study comparing MEG and fMRI advocates the use of a spatial-filtering approach on the MEG data . This helped uncover consistent canonical variables which increased sensitivity to characterising coupling relationships (Lankinen et al., 2018), as opposed to this typical univariate voxel-wise approach. Therefore, different analysis strategies and larger sample sizes may make this design more applicable to investigating NVC in MS.

9.5 SUPPLEMENTARY

Supplementary Figure 1 (see next page). Correlation values between each MEG and fMRI relationship, displayed for each group. These maps are averages of each participant's correlation map and are not correlations based on the mean-time series. These images are not statistically thresholded but masked to areas that had significant ISCs for BOLD, CBF or the MEG frequency band of interest. Only views of the left hemisphere are shown; the right hemisphere showed similar trends.

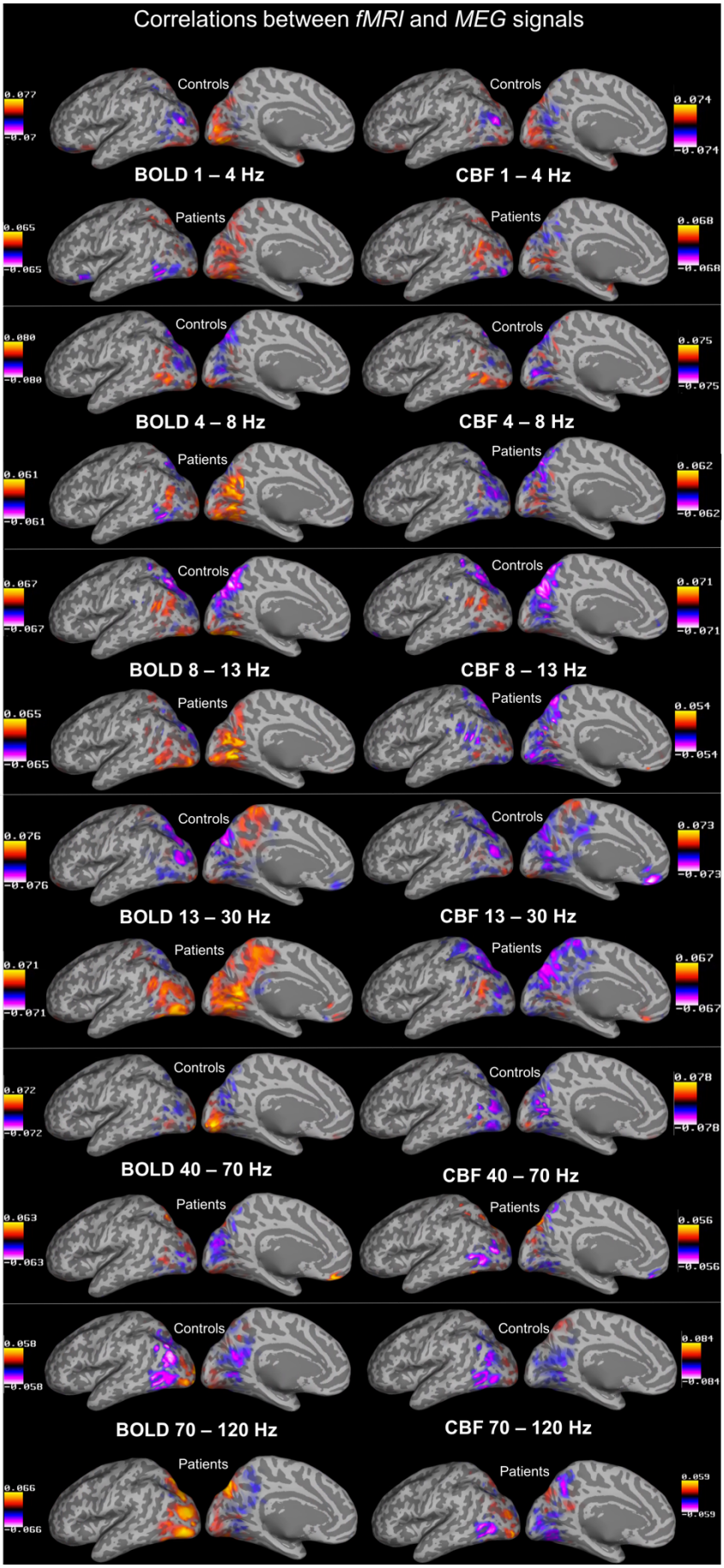
Correlations between *fMRI* and *MEG* signals
Controls
Controls
0.077
-0.07
0.074
-0.074
BOLD 1 – 4 Hz
CBF 1 – 4 Hz
Patients
Patients
0.065
-0.065
0.068
-0.068
Controls
Controls
0.080
-0.080
0.075
-0.075
BOLD 4 – 8 Hz
CBF 4 – 8 Hz
Patients
Patients
0.061
-0.061
0.062
-0.062
Controls
Controls
0.067
-0.067
0.071
-0.071
BOLD 8 – 13 Hz
CBF 8 – 13 Hz
Patients
Patients
0.065
-0.065
0.054
-0.054
Controls
Controls
0.076
-0.076
0.073
-0.073
BOLD 13 – 30 Hz
CBF 13 – 30 Hz
Patients
Patients
0.071
-0.071
0.067
-0.067
Controls
Controls
0.072
-0.072
0.078
-0.078
BOLD 40 – 70 Hz
CBF 40 – 70 Hz
Patients
Patients
0.063
-0.063
0.056
-0.056
Controls
Controls
0.058
-0.058
0.084
-0.084
BOLD 70 – 120 Hz
CBF 70 – 120 Hz
Patients
Patients
0.066
-0.066
0.059
-0.059

10 GENERAL DISCUSSION

One aim of this thesis was to develop different methods of investigating NVC in healthy and MS populations. A visual checkerboard design, with contrast manipulation, gave robust measurements of gamma oscillations, BOLD and CBF signals in the primary visual cortex, consistent with previous work. The amplitude of these signals was lower in the MS group, but there was no evidence to suggest NVC to this visual stimulus was impaired. As there is evidence showing NVC varies across brain regions, and neural oscillatory frequencies, it is important to consider that this visual checkerboard design only gives a narrow window into investigating these mechanisms. The movie design made some progress at addressing these limitations allowing characterisation of BOLD, CBF and neural oscillations from 1-145Hz across more brain regions. However, this design was not able to robustly characterise individual subject variability in NVC but only group averaged responses. With larger samples, and more refined analysis pipelines, the results presented show that this type of design has potential to provide useful information about NVC variability. This type of research provides insight into important biological processes and also can aid in the interpretation of how fMRI signals reflect changes in neural activity. More work is needed to investigate these mechanisms in the healthy brain before wider application to disease populations.

Another main aim of this thesis was to develop more quantifiable and interpretable measures of vascular and metabolic brain function, and this was demonstrated with the use of calibrated and dual-calibrated fMRI. The improvement of these methods and modelling strategies is an active area of research, but current application of these methods to patient populations still has practical value. Blood flow and oxygen metabolism signals were investigated in the brain at rest and in response to a stimulus. These signals are more physiologically interpretable than the BOLD-fMRI signal alone. At baseline, these blood flow and oxygen metabolism signals can also be estimated alongside oxygen extraction fraction, cerebrovascular reactivity and oxygen diffusivity, allowing clearer interpretations of patient-control differences. Our results demonstrated clear baseline vascular and metabolic impairment in MS, as well as some evidence for impaired stimulus responses. These methods are applicable to many patient populations that may have vascular and metabolic impairments contributing to the cause and/or progression of the disease.

In the next sections (10.1 and 10.2), a summary and interpretation of the main results is given (for healthy populations and MS), then a consideration of the strengths and

limitations of the methods. The interpretation of the results should be considered within the context of the validity of the methods used, which is discussed in Section 10.3.

10.1 Neurovascular coupling and metabolic function in healthy populations

Chapter 4 demonstrated that the change in BOLD and CBF signals were positively correlated with gamma oscillations and had good spatial overlap. This is consistent with a lot of previous work showing positive correlations between gamma amplitude and hemodynamic signals. In Chapter 7, the PCA results from the movie stimulus showed the characteristic tuning function that has been reported previously: in general, negative correlations between BOLD/CBF signals and low frequency oscillations and positive correlations at higher frequencies. Although these frequency-dependent relationships have been reported before, what is not clear from the literature is whether the same population of neurons is changing its oscillatory frequency patterns under conditions of stimulation, or different neural populations contribute to these frequency-dependent changes. A clear finding from Chapter 7, is that these frequency-dependent relationships vary across the brain, i.e. in some areas the low frequency-negative correlations and the high frequency-positive correlations were reported but in other areas this relationship appeared opposite. Furthermore, the direction of the coupling relationships appeared opposite for BOLD and CBF in some areas. This reminds us that (1) BOLD and CBF reflect different aspects of the NVC response with changes in $CMRO_2$ and CBV also contributing to BOLD signal changes and (2) interpretation of how BOLD and CBF responses reflect neural activity is complex and brain-region dependent.

There are many reasons why differences in BOLD and CBF responses to the same stimulus can be found, and many of these were discussed in Chapter 7. One reason not discussed in Chapter 7 is the consideration of how oxygen diffusivity can change in response to neural activity. There is evidence suggesting that CBF and $CMRO_2$ responses can be decoupled due to the $CMRO_2$ response reflecting a combination of the increased CBF *and* an increase of oxygen diffusion in the active region, because the oxygen diffusivity from the capillaries into the tissue can change locally in response to neural activity. These changes in oxygen diffusivity in response to a stimulus would therefore affect the $CMRO_2$ and BOLD measurement, but not CBF. Empirical evidence for this, and a short discussion, is given in Appendix 1 (Chapter 11). One potential mechanism for these changes in diffusivity is via pericyte control of *capillary* diameter (Hamilton et al., 2010), and not just at the level of arterioles and arteries as previously assumed.

In an attempt to investigate some of these mechanisms, the relationship between MEG and $CMRO_2$ signals in response to the movie stimulus was investigated in Chapter 8. Despite estimating reasonable *M* values across the brain and showing CBF-$CMRO_2$ coupling ratios in normal ranges, there no significant relationships between $CMRO_2$ and MEG signals. This is unlikely to reflect the underling physiologically but the insensitivity of the design and measurements.

10.2 Neurovascular coupling and metabolic function in Multiple Sclerosis

Chapter	Key Findings relating to MS
4	• No difference in baseline CBF, GM volumes, visual acuity and VEFs in MS <u>In response to a visual checkerboard stimulus (5 contrasts):</u> • *Decreased* amplitude of gamma oscillations, BOLD and CBF signals in MS over a visual ROI common to both groups • A small visual area showed *increased* BOLD and CBF responses in MS • No significant differences in NVC in the MS group but more variability
5	• Reduced baseline CBF and $CMRO_2$ in MS (quantified GM averages) • Reduced GM volumes in MS • No differences in baseline CVR, OEF or D_c in MS • Reductions in CBF and $CMRO_2$ in 2 small clusters: subcallosal cortex, medial/orbital frontal regions. Further CBF reductions in occipital pole, parahippocampal gyrus. Further $CMRO_2$ reductions in nucleus accumbens and paracingulate gyrus. • Self-report disease impact scores did not predict these reductions • Lesion volume predicted variability in CBF (negative relationship) • GM volume predicted variability in $CMRO_2$ (positive relationship)
6	<u>In response to a visual checkerboard stimulus (100% contrast):</u> • BOLD and CBF reductions were found in a small occipital cluster, in the MS group, not explained by visual acuity. • No differences in visual $CMRO_2$ responses in MS, and no differences in the coupling between CBF and $CMRO_2$. • In both controls and MS, baseline CBF and $CMRO_2$ values significantly predicted stimulus CBF and stimulus BOLD responses, respectively.

9	<u>In response to the movie stimulus:</u> • Reduced inter-subject correlations in the MS group for BOLD, CBF and all MEG frequency bands • MS group had significant differences in the 8-13Hz MEG to BOLD relationship only, showing a positive coupling relationship in the parietal lobe and middle frontal gyrus (whereas the controls displayed a negative). • No significant differences in the correlations between BOLD and CBF in the MS group

In general, the work presented in this thesis demonstrates clear vascular and metabolic impairment in MS. In terms of the brain at rest, CBF and $CMRO_2$ were significantly reduced, and so was total GM volume. Considering no differences were found in CVR, OEF or D_c, this suggests that the CBF is lower due to a lower metabolic demand. Furthermore, these CBF and $CMRO_2$ reductions were based on averages across each voxel in GM i.e. the CBF and $CMRO_2$ were lower per unit volume of the remaining GM. Therefore, the total brain oxygen consumption is likely to be even further reduced once the GM loss is also factored in. Consistent with this, in Chapter 4 a large decrease in gamma power amplitude was seen in MS, for example this decrease was close to 20%, for the visual checkerboard contrast of 100%. These gamma power reductions could be indicator of GM dysfunction in MS, mediated by GABAergic changes in interneuron populations (discussed in Chapter 4). The BOLD and CBF reductions seen in Chapter 4 are likely to be reflective of this decrease in neural activity. However, the baseline CBF and $CMRO_2$ signals from Chapter 5 correlated with different metrics of disease burden; they both appeared to have a similar negative relationship with lesion volume (although $CMRO_2$ not significantly), but only $CMRO_2$ positively correlated with GM volume. This suggests that explaining the CBF reduction simply as a reflection of a $CMRO_2$ reduction may not be sufficient (this is discussed in more detail in Chapter 5), and more research is needed to understand these relationships.

Unlike in Chapter 4, differences in BOLD, CBF or $CMRO_2$ to a visual checkerboard stimulus was not as pronounced in Chapter 6. There was a small visual area showing decreased BOLD and CBF responses in the MS group, but no changes in relative $CMRO_2$ and no changes in CBF-$CMRO_2$ coupling. This difference in findings was unexpected; one contributing factor could be that the patients in Chapter 4 were treatment naive, as opposed to the patients in Chapter 6 who were on DMTs. In the untreated group in Chapter 4, there was actually a small cluster in the visual cortex that showed increased BOLD and CBF responses compared to controls. This could be

interpreted as a compensatory mechanism, or it could be related to levels of inflammation being higher in this group. This relates to a broader point about testing these metabolic and vascular signals in MS: characterising the levels of inflammation and structural damage is very important for the interpretation of these results. Evidence reviewed in Chapter 3.2.1 showed that atrophy is likely to lead to a decreased CBF due to a lower metabolic demand, whereas increased CBF may be found due to active inflammation leading to higher metabolic demands. If both processes happen in parallel, averaging signals over course spatial scales could result in no differences. Therefore, developing non-invasive markers of levels of inflammation is crucial, ideally with regional information. Quantifying the level of GM atrophy is also important for the interpretation of these results, which is an ongoing challenge in the MS literature, particularly non-invasively (Amiri et al., 2018).

In Chapter 4 there were no significant differences in NVC, despite more variability in the patient group and a trend towards increased NVC in the visual cortex. In Chapter 9 there was also evidence showing the patient's MEG and fMRI responses were more variable. Differences in NVC relationships were found in two small clusters, only in one frequency band. Therefore, this data does not provide much evidence for alterations in NVC in MS. This may be due to the relatively small sample sizes, or it may be due limitations in the way NVC was studied (see Section 10.3.1 below). However, it could of course be due to no impairment of NVC in MS, at least within the range of damage and disability studied in this thesis. At the group level, this suggests that blood flow is generally responding appropriately to the level of neural activity in MS.

To understand the role of these metabolic and vascular impairments in disease progression, longitudinal studies are needed to track changes over time. Unfortunately, very few significant correlations between clinical disease measures were reported in this thesis, which is a pattern that has been noted on in previous studies (Lapointe et al., 2018). Therefore, there is still a lot of progress to be made in linking together changes between clinical and imaging metrics.

10.3 Strengths and limitations of methods

10.3.1 MEG-fMRI relationship as an empirical measure of NVC

An empirical measure of NVC was characterised, defined as the relationship between neural oscillations and BOLD/CBF signals. It is important to note that this is representative of the consequences of NVC, and not an investigation of the signalling

mechanisms themselves. The process of NVC is very complex; how the vascular cells, glial cells and neural cells all interact to produce a blood flow response in the right location at the right time is still not fully known (Cauli & Hamel, 2010; Chen, Kozberg, Bouchard, Shaik, & Hillman, 2014; Petzold & Murthy, 2011). From a modelling perspective, there is some evidence to suggest that NVC may be non-linear in some circumstances (Hoffmeyer, Enager, Thomsen, & Lauritzen, 2007; Sheth et al., 2004), and this should be considered for future studies. The majority of the research informing the work on NVC in humans comes from examining the relationship between neural activity and BOLD signals. As covered previously, there are many factors that can affect the variability in the BOLD signal, some of which are not related to neural activity. The CBF response is therefore more relevant, however, fewer studies have looked at the relationship between MEG or EEG signals and CBF, in the context of NVC.

NVC was investigated using two very different stimuli: a visual checkerboard within a block design and a clip from a movie within one continuous recording. Despite no significant differences between patients and controls, the gamma oscillations and fMRI signals displayed strong positive correlations in response to the checkerboard. Correlations of this magnitude were not seen with the movie paradigm, possibly due to it being a continuous recording. For the movie data, MEG and fMRI signals were correlated across time, whereas for the visual checkerboard the contrast manipulation was used to tune the amplitude of the MEG and fMRI responses in a similar way, and this manipulation was the basis of the NVC measure. For this low-level stimulus, the brain is likely to respond more similarly during MEG and fMRI, and more similarly across participants. For the more complex movie stimuli, there is likely to be more variation across people, and the neural responses may be slightly different on second viewing (Chang et al., 2015). Furthermore, it was challenging to characterise individual variability in NVC with this movie design; most of the significant results discussed are based on averaged time-series across individuals. However, despite these limitations with the movie paradigm, it has the advantage of inducing activity over multiple brain areas, in multiple oscillatory frequency bands, and is more reflective of naturalistic stimuli. Some potential strategies to improve the usefulness of this type of design for investigating NVC could be: (1) to use a resting state paradigm to help characterise the baseline noise profile of the MEG and fMRI signals (2) to implement a potentially more sensitive independent component analysis to characterise the responses to the movie and (3) look at the amplitude and phase coupling between the frequency bands and how this relates to the fMRI signals (explained below).

The assumption made in using the MEG-fMRI relationship as an empirical measure of NVC is that both the signals are sensitive to changes in the same type of neural activity. The empirical evidence that was summarised in the introductory chapters has led to the common view that both neural oscillations and BOLD/CBF signals closely reflect LFPs (of which PSPs mostly contribute) as opposed to multi-unit spiking activity (MUA). However, this has also been acknowledged to be an oversimplification, and it is likely that the BOLD, CBF and neural oscillatory signals reflect both LFPs and MUA (Ekstrom, 2010; Mukamel et al., 2005; Whittingstall & Logothetis, 2009). It is important to note that in some cases there is a strong correlation between spike rate, LFPs and BOLD, and in other cases they are decoupled (Ekstrom, 2010). More research is needed to understand the conditions that lead to this coupling or decoupling. A fairly recent idea proposed in the literature, with accompanying empirical evidence, is that high-frequency oscillatory activity (>100Hz) in LFPs reflect spiking activity (Scheffer-Teixeira, Belchior, Leão, Ribeiro, & Tort, 2013). With the movie paradigm, we characterised significant MEG correlations between subjects in frequencies up to 195Hz. It is intriguing that only in the highest frequency band (145-195Hz) we saw significant common activity in the thalamus (Supplementary Figure 1.1). Although this cannot be fully disentangled with this study, and was not the main aim, this provides promising new research avenues to explore if such a simple non-invasive design is sensitive to spiking activity.

Spatial sensitivity to neural activity is also an important factor to consider when comparing MEG and fMRI; activity of neurons in gyri that are perpendicular (radial orientation) to the cortical surface do not project outside the head and cannot be measured with MEG (Ahlfors et al., 2010), whereas fMRI signals would be sensitive to this activity. The main challenge with comparing MEG and fMRI signals to the same stimuli comes from their very different spatial and temporal resolutions. In order to carry out voxel-wise comparisons across the whole brain, we spatially down-sampled the fMRI to match the resolution of the MEG beamformers. Similarly, the fMRI time-series was temporally up-sampled and the MEG time-series was down-sampled. This results in pre-processing steps that are not optimum for each modality and may introduce bias in statistical testing as the DOF are altered. The need to perform the MEG and fMRI scans separately is a clear limitation in using their relationship to study NVC. Simultaneous EEG-fMRI is an alternative non-invasive methodology that can be applied to studying NVC. The decreased signal quality for both modalities makes the data acquisition and analysis challenging, however progress is being made to improve this (Huster, Debener, Eichele, & Herrmann, 2012).

Only the amplitude and frequency of neural oscillations were considered in this thesis. However, evidence suggests that the phase of the wave is also important for neural communication. A large area of research into neural oscillations is focused on characterising functional connectivity between brain regions, by looking at the how amplitude, frequency and phase correlate across regions (Bastos & Schoffelen, 2016). Coupling between phase and amplitude (Phase-Amplitude Coupling, PAC) also changes in response to a stimulus and is theorised to play a key role in neural communication. It is normally demonstrated by the phase of a low frequency oscillation modulating power of a higher frequency oscillation, i.e. when the slow wave is in one phase of its cycle the power in the fast wave increases, and when it's in the other phase the power decreases (Canolty & Knight, 2010). There is very little research studying how the PAC of neural oscillations is related to fMRI signals in humans, however one recent study did investigate this by simultaneously recording electrocorticography (ECoG) and fMRI data in the same participants whilst they performed a finger-tapping task (Murta et al., 2017). They reported the typical positive correlations between higher-frequency (>70Hz) oscillations and BOLD, and negative correlations between lower frequencies (4-30Hz) and BOLD. More importantly, they showed the PAC strength for alpha/gamma and for beta/gamma was negatively correlated with the BOLD amplitude in the contralateral hemisphere. Furthermore, they report that the PAC for beta/gamma explained variance in the BOLD amplitude that was not explained by amplitude changes in alpha, beta or gamma. The complexities of modelling the amplitude, frequency, phase *and* the couplings between them brings new challenges to relating fMRI signals to neural oscillations measured with EEG or MEG. However, it is clearly an important metric to consider in future studies investigating NVC and may partly explain why the amplitude of MEG signals in one frequency band are not strongly correlated with fMRI signals (as seen in Chapter 7).

10.3.2 Calibrated-fMRI to estimate oxygen metabolism

In Chapters 5, 6 and 8 we used calibrated-fMRI to model $CMRO_2$ at rest, and during stimulation. Chapter 5 was the first application of a dual-calibrated methodology in MS. Characterising multiple physiological parameters relating to cerebrovascular health (CBF, CBV, OEF, $CMRO_2$, D_c) brings a clearer picture of the vascular and metabolic impairments in MS, as interpretation of the changes in one parameter can be taken in the context of changes in others. The validity of the modelling assumptions in healthy populations are still being investigated and regularly updated, and caution must be taken when implementing these methods in patients groups, considering the biological assumptions may be less valid (Germuska & Wise, 2018). The most significant

assumption, common across all calibrated-fMRI implementations, is that the increasing inspired O_2 and CO_2 does not alter $CMRO_2$. Empirical data has shown that this is unlikely to be completely true (Yablonskiy, 2011; Zappe et al., 2008) and simulation data shows that if $CMRO_2$ changes during hypercapnia and hyperoxia this would strongly affect the estimates of baseline OEF (Merola et al., 2016). Much more research is needed to understand the magnitude of this effect, and how best to correct for it (Driver et al., 2017).

There are two main approaches to modulating end-tidal gases: fixed inspired fractions or targeted end-tidal changes. The methods presented in Chapter 5 used the former (fixed inspirations). In principle, targeting exact end-tidal changes in PCO_2 and PO_2 is better, as this allows for more controlled and repeatable modulation of $Cv0_2$ (in the case of $P_{ET}O_2$) and of CBF (in the case of $P_{ET}CO_2$), (Germuska & Wise, 2018). In practice, fixed inspirations are used more commonly due being less expensive and having a simpler equipment set-up.

A robust measurement of CBF is one of the main technical challenges in calibrated fMRI methodologies. All these models rely on an accurate quantified estimate of CBF, in order to model many other parameters. A limitation of all the ASL sequences used in this thesis (with the exception of the multi-TI ASL used in Chapter 4) is in assuming one value for how long the labelled blood takes to travel from the labelling site to the slice being imaged (TI for PASL sequences, and PLD for pCASL sequences). However, mean transit times have been shown to be altered in MS (see evidence in Chapter 3.2.1). One study showed that prolonged arrival times in MS, in both GM and WM, were associated with higher disability scores (Paling et al., 2013). If patients have altered arrival times, this could lead to a bias in CBF quantification.

Although fMRI gas studies are non-invasive, they can be complex from a data collection and analysis perspective. Furthermore, application of these methods in some populations (children, people with anxiety) may be challenging due the experience of breathing in raised CO_2. This is why other alternatives have been investigated to calibrate the fMRI signals. As discussed in Chapter 8, one of these is a BH design. This allows the participant to have more control and often a nasal cannula instead of a face-mask can be worn, making it a more comfortable procedure. This design requires a certain level of task compliance which can be variable across participants, although practising outside of the scanner can help improve this. However, unlike dual-calibrated fMRI, this BH modulation can still only give relative changes in $CMRO_2$, and not

baseline estimates. It also involves more physiological confounds due inspired O_2 decreasing during the BH (discussed in Chapter 8).

10.3.3 Statistical Power

Improvements in experimental design

Before considering the effect of sample size on statistical power, first let us consider improvements in the validity of the experimental designs. In relation to MEG-fMRI studies to investigate NVC, future studies should give more attention to controlling order effects (counterbalancing MEG/MRI session order), time-of-day effects (having each scan on a different day but at the same time) and measuring attentional levels to the stimulus. Considering the challenges that come with comparing MEG and fMRI signals at the same temporal and spatial scales, the experimental design needs to ensure that the subject's experience of the stimuli shown during MEG and fMRI is as similar as possible.

Some studies attempt to measure and/or control for lifestyle factors known to effect CBF (e.g. exercise, caffeine, nicotine), which have relevance for the validity of our methods characterising both resting and stimulus-induced CBF. Recruiting based on these factors must be done with caution because (1) a very long list of exclusion criteria may lead to recruiting a sample that is not representative of the population, and (2) instructing people to refrain from consuming their normal levels of caffeine on the day of the scan, for example, will lead to withdrawal effects which may also affect these measurements (Addicott et al., 2009). Nevertheless, these are important confounds to consider as these methods start to be applied to more questions and patient groups. Therefore, this type of data should be collected alongside the imaging data. Familiarisation sessions with hypercapnic gases, and practises with BH tasks, before the main MRI session is a valuable inclusion into a study design. This helps improve the quality of the data collected during the scan as well as ensuring safety.

All of these experimental controls should reduce subject variability due to confounding factors, making it more likely to detect an experimental effect if one is present.

Estimation of adequate sample size

In some of these chapters, particular Chapters 4 and 9 for patient-control comparisons, the sample sizes were particularly small. It is of course possible that the lack of

significant differences we report in NVC is partly or completely due to low statistical power. Improving the SNR of imaging techniques and minimising the confounding variables may help to reduce this variability, as well as increasing sample sizes. It is important to note that post-hoc power analyses, as a way to add some interpretation to a null result, are often criticised in the literature as not being meaningful or informative (Mumford, 2012), so they will not be covered here. Also, estimating sample sizes based on pilot data has been criticised in a recent paper due to inaccuracies in estimating the effect size, amongst other factors (Albers & Lakens, 2018). Pilot data are thought to be more useful in assessing feasibility of recruitment, methods and analysis than estimation of future effect sizes (Leon, Davis, & Kraemer, 2011). Power analyses for neuroimaging studies are even more challenging considering the multiple statistical comparisons performed for each voxel of the brain, or within ROIs (Mumford, 2012). Furthermore, the variability of the MEG and fMRI data will not be spatially uniform across the brain and statistical comparisons at each voxel are not truly independent of one another. It was often difficult to estimate appropriate sample sizes needed for the research studies in this thesis due to the fact that many of these methods are novel and in active development. However, the next paragraph describes some approaches that were used to assess this as well as some sample size recommendations for future studies.

For the data presented in Chapters 5 and 6, 26 MS patients and 25 controls were recruited. These numbers were broadly based on numbers in previous studies that showed CBF/CVR differences in MS using a pCASL sequence, for example: Marshall et al (2014) with 19 controls and patients, Marshall et al (2016) with 28 controls and patients, and Ota et al (2013) with 27 patients and 24 controls. In future, it would be advisable to collect 3-5 extra controls and MS patients than is needed based on sample size estimates (so ~30 in each group). This is because these (dual) calibrated-fMRI methods can often lead to data drop-out due to a participant not being eligible for the study, or the data quality being poor due to the gas challenge being novel and uncomfortable for some. When using the movie design to investigate NVC, data in Figure 7-7 attempted to address the question of sufficient sample size by combining data collection from the study with other researchers' data (common data only existed for MEG-BOLD coupling, not MEG-CBF). With a sample size of 33, significant positive or negative coupling relationships were seen across all frequency bands and in wider brain regions compared with the analysis including only 17 participants. Importantly, these coupling relationships were characterised at the individual level first, then statistically tested, taking into account individual variability. Therefore, similar studies in

the future should aim for at least a sample size of ~33 to characterise these NVC relationships, and even more if patient differences are to be compared.

10.4 Conclusions

Multi-modal neuroimaging studies, as presented in this thesis, can contribute to the knowledge of how neural, metabolic, and vascular responses interact. The non-invasive nature of MEG and MRI means they have wide applicability to studying young, old and disease populations, across multiple time points. In the context of studying MS, these methods have a lot of potential utility at investigating mechanisms that may contribute to disease progression. For future studies investigating vascular and metabolic changes in MS, longitudinal designs and more characterisation of GM damage would allow clearer interpretation of results. With any neuroimaging method, a good generative model is crucial; one that explains the biological underpinnings of the measured signals. More research is needed in this area, to help us model the signals we measure, and this will lead to greater applications in understanding the brain, in health and disease.

11 APPENDIX 1: Gamma Oscillations, BOLD, CBF and $CMRO_2$ signals in response to a moving annular grating stimulus

Study rationale: To investigate the relationship between different MEG and fMRI derived signals, including how they change with visual stimuli manipulation, in order to inform about NVC mechanisms.

Study design: 12 healthy volunteers (10F, 3M,18-28 years, right handed, normal or corrected to normal vision) performed a visual task during a MEG scan and during a pCASL fMRI scan. A T1-weighted structural scan was also obtained. *Approved by the School of Psychology Ethics Committee.*

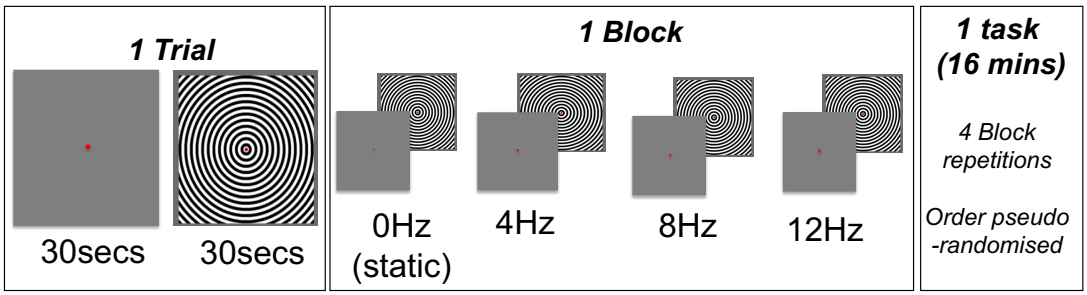

- Annular grating stimuli, full-field, 100% contrast, 3 cycles per degree
- Projector dimensions, screen refresh rate and degree of visual angle kept consistent between MEG and fMRI
- Stimuli drifted inwards towards the centre at 0,4,8 or 12Hz
- Participants told to fixate on red circle in centre and count colour changes from red -> green to maintain attention

MEG data collection and analysis: 275-channel CTF axial gradiometer system was used to obtain whole-head MEG recordings. To obtain the peak gamma response to the stimulus, the data was collected and analysed using very similar methods and pipelines as in Chapter 4. In brief, data was band-pass filtered between 40 and 90Hz. Source reconstruction with LCMV beamformer, contrasting active and stimuli periods. Across the four conditions, the location of the peak gamma amplitude was found. At this peak location, the source-level time-series were constructed by multiplying the sensor level data with the beamformer weights and constructing time-frequency information by calculating the amplitude envelope using the Hilbert transform. For each of the four conditions, the *Peak Gamma Amplitude* is the peak amplitude change, across the 30 seconds block, in this location. The *Frequency of Gamma Peak* was the specific frequency (constrained to 40-90Hz) of this peak amplitude.

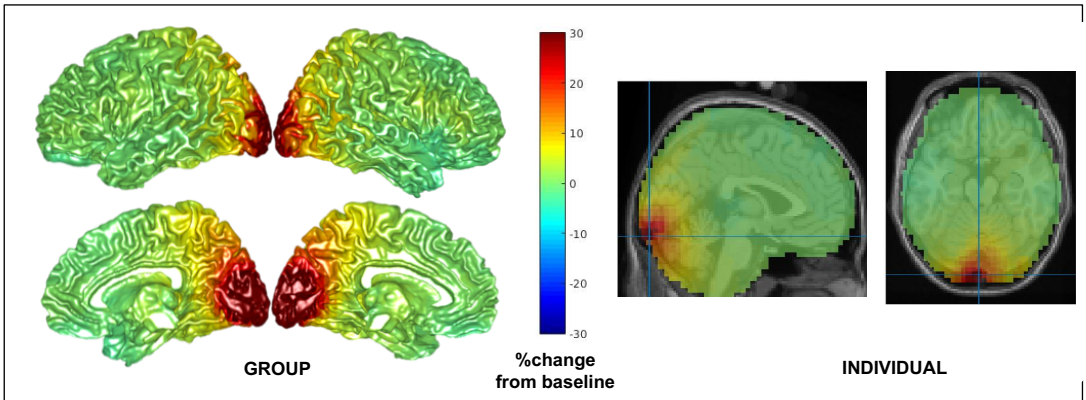

MEG Source Localisation. Gamma amplitude (40-90Hz) percentage change from baseline, shown as averages across the group in MNI space (left plot) and shown for one individual (right plot). The blue cross-hairs represent the peak gamma response for that individual. All participants had a peak gamma response in the primary visual cortex.

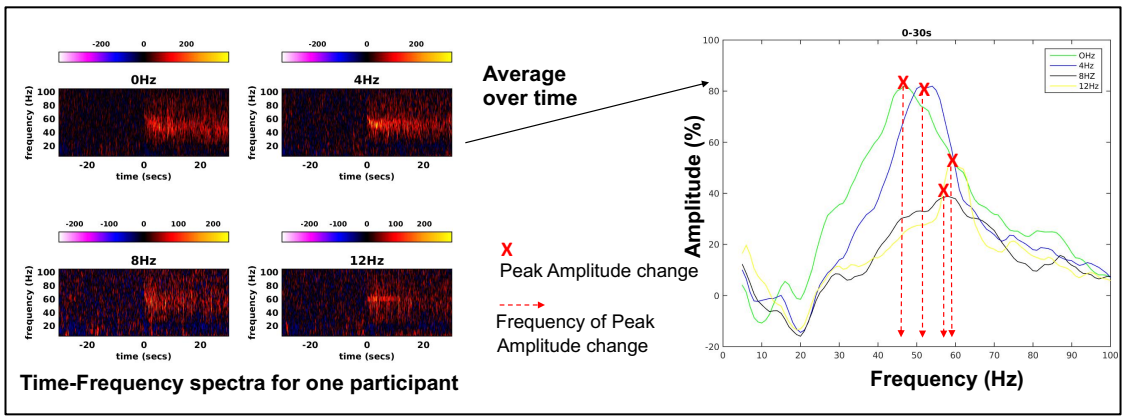

fMRI data collection and analysis: 3T GE MRI system, 8-channel receiver head coil, ran a PASL sequence, acquiring CBF and BOLD weighted images (TI1/TI2 = 700/1500ms, 20cm tag), with a dual GRE spiral readout (TR/TE1/TE2 = 2400/2.7/29ms, 64 x 64 x 14 (3x3x7mm,1.5mm gap). To obtain the BOLD and CBF responses to the stimulus, the data was collected and analysed using very similar methods and pipelines as explained in Chapter 4. In brief, BOLD time courses (surround average of the second echo) and ASL time courses (first echo) were modelled with FEAT's *Full Perfusion Signal* modelling, for each of the 4 conditions. A group ROI representing the significant activity to stimulus (across the four conditions, and common to both BOLD and CBF) was transformed from MNI to subject space and percentage change from baseline BOLD and CBF signals were extracted from this ROI. As explained in Chapters 8, the $CMRO_2$ response to the stimulus was modelled, based on the standard calibration model (Davis et al., 1998), assuming a value for *M* of 0.075, an alpha of 0.2 and a beta of 1.3, based on previous literature (Wise et al., 2013).

fMRI group Z-stat images

Corrected cluster significance threshold of p =0.05.

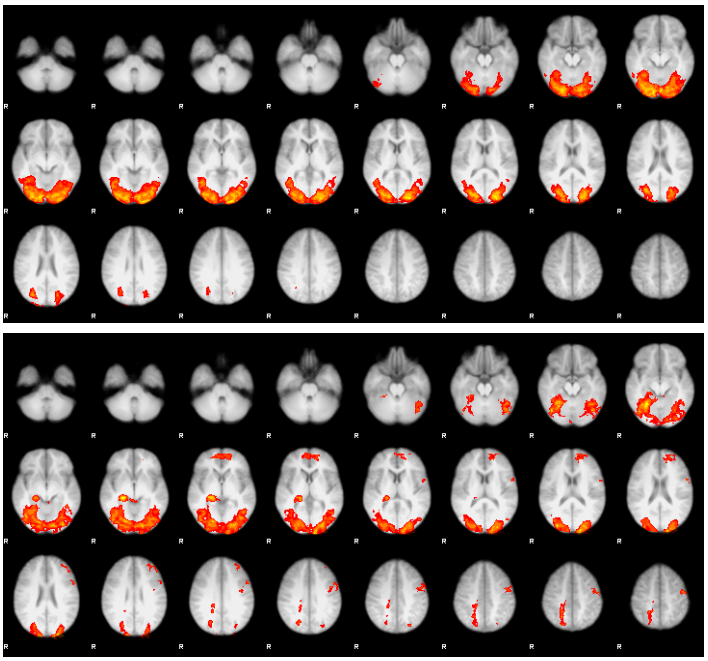

Example of a **subject ROI** containing voxels that were significant in the **CBF and BOLD** analyses, where the BOLD and CBF signals were extracted.

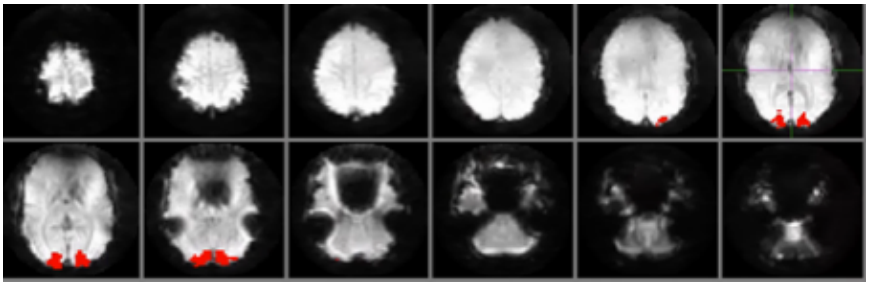

TEMPORAL FREQUENCY TUNING OF MEG AND FMRI SIGNALS

Two participants had MEG source localisation errors (due to eye artefacts and co-registration errors) leaving n=10 common MEG and fMRI datasets to compare (8F, 2M). For each parameter plotted below, the maximum percentage change from baseline was obtained, across the four stimuli conditions, for each participant. Each stimuli condition response was converted into a percentage of this maximum value, in order to compare the stimuli manipulation between all parameters, which have different magnitudes. The table shows unnormalised values for each parameter, averaged across the stimuli conditions ('Grand Mean') to give an indication of scale. Group means ± SEM are displayed.

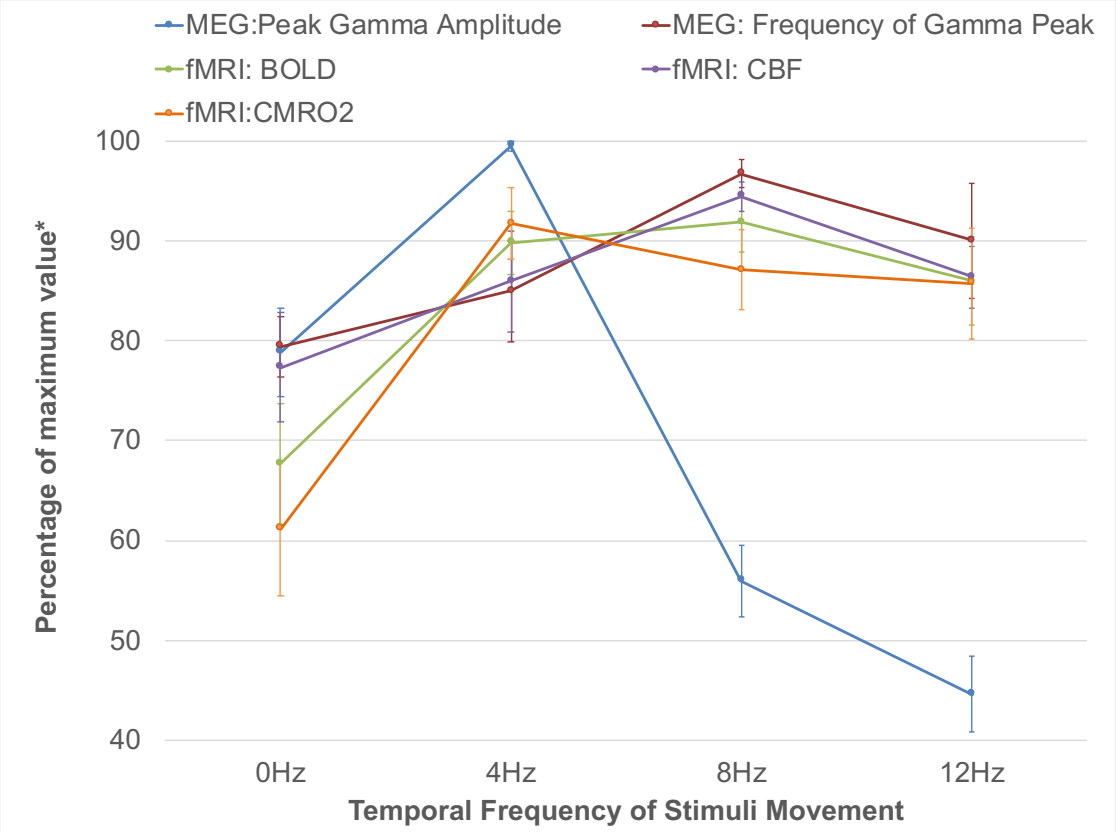

	PeakAmplitude (%)	FrequencyOfPeak (Hz)	CBF (%)	BOLD (%)	CMRO2 (%)
Grand Mean	69.68	53.03	30.70	1.06	11.33
SE	15.13	5.63	2.66	0.09	1.05

What do these results show?

- Peak amplitude of neural oscillations in the gamma band (40-90Hz), and the frequency of this peak, are tuned differently by this visual stimulus manipulation

- BOLD, CBF, and the frequency of the gamma peak all display peak responses at 8Hz of stimuli movement, whereas peak gamma amplitude and the modelled $CMRO_2$ response both peak at 4Hz

Why is this important?

- The biological mechanism that drives gamma oscillations is still not fully known, but there is evidence to suggest they are driven by a network of interconnected excitatory pyramidal cells and GABAergic inhibitory interneurons (Bartos et al., 2007). The balance of this excitation and inhibition is thought to play a role in setting the peak gamma oscillation *frequency* (Brunel & Wang, 2003). Increases in gamma *amplitude* may simply reflect a larger population of neurons firing in synchrony.

- These results very closely mirror those of a study using PET imaging (Vafaee & Gjedde, 2000b) that looked at CBF and $CMRO_2$ responses to similar visual grating, showing that CBF peaked at 8Hz and $CMRO_2$ peak at 4Hz of stimuli movement, as we have shown here. They modelled the oxygen diffusivity from capillaries into the active tissue and found that this followed the same pattern as $CMRO_2$, peaking at 4Hz. They explained this increase of oxygen consumption at 4Hz to be a combination of increased CBF and increased oxygen diffusion in the active region, and that oxygen diffusion can therefore change locally in response to neural activity. Another study testing visual responses at 0, 1, 4, 8, 16, 32, and 50Hz showed that $CMRO_2$ response peaked at 4Hz (Vafaee et al., 1999).

- This provides support that the $CMRO_2$ response may better reflect the energy demands of neural activity compared to both the BOLD and CBF response, and therefore developing methods of measuring $CMRO_2$ is important. There is other evidence to suggest that the CBF response is mediated by factors other than the demand of oxygen (Lin, Fox, Hardies, Duong, & Gao, 2010).However, the CBF response very closely follows the tuning pattern of the frequency of the gamma peak, suggesting instead that CBF and $CMRO_2$ may represent different information about neural activity. More generally, the fact that CBF and $CMRO_2$ responses to the same stimulus are different suggest that $CMRO_2$ responses may also be reflecting a more local regulation of blood flow, at the level of capillaries (Hamilton et al., 2010).

References

Aarli, J. A., Abramsky, O., Browne, P., Chandraratna, D., Angood, C., Tremlett, H., … Thompson, A. J. (2014). *Section Editors Global Perspectives ATLAS OF MULTIPLE SCLEROSIS 2013: A GROWING GLOBAL PROBLEM WITH WIDESPREAD INEQUITY*. Retrieved from http://www.msif.org/about-ms/publications-

Abbott, N. J., Rönnbäck, L., & Hansson, E. (2006). Astrocyte–endothelial interactions at the blood–brain barrier. *Nature Reviews Neuroscience*, *7*(1), 41–53. https://doi.org/10.1038/nrn1824

Abidi, Z., Faeghi, F., Mardanshahi, Z., & Mortazavi, H. (2017). Assessment of the diagnostic accuracy of double inversion recovery sequence compared with FLAIR and T2W_TSE in detection of cerebral multiple sclerosis lesions. *Electronic Physician*, *9*(4), 4162–4170. https://doi.org/10.19082/4162

Aboul-Enein, F., & Lassmann, H. (2005). Mitochondrial damage and histotoxic hypoxia: a pathway of tissue injury in inflammatory brain disease? *Acta Neuropathologica*, *109*(1), 49–55. https://doi.org/10.1007/s00401-004-0954-8

Addicott, M. A., Yang, L. L., Peiffer, A. M., Burnett, L. R., Burdette, J. H., Chen, M. Y., … Laurienti, P. J. (2009). The effect of daily caffeine use on cerebral blood flow: How much caffeine can we tolerate? *Human Brain Mapping*, *30*(10), 3102–3114. https://doi.org/10.1002/hbm.20732

Adhya, S., Johnson, G., Herbert, J., Jaggi, H., Babb, J. S., Grossman, R. I., & Inglese, M. (2006). Pattern of hemodynamic impairment in multiple sclerosis: Dynamic susceptibility contrast perfusion MR imaging at 3.0 T. *NeuroImage*, *33*(4), 1029–1035. https://doi.org/10.1016/J.NEUROIMAGE.2006.08.008

Ahlfors, S. P., Han, J., Belliveau, J. W., & Hämäläinen, M. S. (2010). Sensitivity of MEG and EEG to source orientation. *Brain Topography*, *23*(3), 227–32. https://doi.org/10.1007/s10548-010-0154-x

Ainslie, P. N., & Duffin, J. (2009). Integration of cerebrovascular CO 2 reactivity and chemoreflex control of breathing: mechanisms of regulation, measurement, and interpretation. *Am J Physiol Regul Integr Comp Physiol*, *296*, 1473–1495. https://doi.org/10.1152/ajpregu.91008.2008.-Cerebral

Albers, C., & Lakens, D. (2018). When power analyses based on pilot data are biased: Inaccurate effect size estimators and follow-up bias. *Journal of Experimental Social Psychology*, *74*, 187–195. https://doi.org/10.1016/J.JESP.2017.09.004

Alshowaeir, D., Yiannikas, C., Garrick, R., Parratt, J., Barnett, M. H., Graham, S. L., & Klistorner, A. (2014). Latency of Multifocal Visual Evoked Potentials in Nonoptic

Neuritis Eyes of Multiple Sclerosis Patients Associated With Optic Radiation Lesions. *Investigative Opthalmology & Visual Science*, *55*(6), 3758. https://doi.org/10.1167/iovs.14-14571

Alsop, D. C., Detre, J. A., Golay, X., Günther, M., Hendrikse, J., Hernandez-Garcia, L., … Zaharchuk, G. (2015). Recommended implementation of arterial spin-labeled perfusion MRI for clinical applications: A consensus of the ISMRM perfusion study group and the European consortium for ASL in dementia. *Magnetic Resonance in Medicine*, *73*(1), 102–116. https://doi.org/10.1002/mrm.25197

Amann, M., Achtnichts, L., Hirsch, J. G., Naegelin, Y., Gregori, J., Weier, K., … Gass, A. (2012). 3D GRASE arterial spin labelling reveals an inverse correlation of cortical perfusion with the white matter lesion volume in MS. *Multiple Sclerosis Journal*, *18*(11), 1570–1576. https://doi.org/10.1177/1352458512441984

Amiri, H., de Sitter, A., Bendfeldt, K., Battaglini, M., Gandini Wheeler-Kingshott, C. A. M., Calabrese, M., … Vrenken, H. (2018). Urgent challenges in quantification and interpretation of brain grey matter atrophy in individual MS patients using MRI. *NeuroImage: Clinical*, *19*, 466–475. https://doi.org/10.1016/J.NICL.2018.04.023

Ances, B. M., Leontiev, O., Perthen, J. E., Liang, C., Lansing, A. E., & Buxton, R. B. (2008). Regional differences in the coupling of cerebral blood flow and oxygen metabolism changes in response to activation: implications for BOLD-fMRI. *NeuroImage*, *39*(4), 1510–21. https://doi.org/10.1016/j.neuroimage.2007.11.015

Arpin, D. J., Heinrichs-Graham, E., Gehringer, J. E., Zabad, R., Wilson, T. W., & Kurz, M. J. (2017). Altered sensorimotor cortical oscillations in individuals with multiple sclerosis suggests a faulty internal model. *Human Brain Mapping*, *38*(8), 4009–4018. https://doi.org/10.1002/hbm.23644

Attwell, D., Buchan, A., Charpak, S., Lauritzen, M., MacVicar, B., & Newman, E. (2010). Glial and neuronal control of brain blood flow. *Nature*, *468*, 232–243. https://doi.org/10.1038/nature09613

Attwell, D., & Iadecola, C. (2002). The neural basis of functional brain imaging signals. *Trends in Neurosciences*, *25*(12), 621–625. https://doi.org/10.1016/S0166-2236(02)02264-6

Attwell, D., & Laughlin, S. B. (2001). *An Energy Budget for Signaling in the Grey Matter of the Brain*. Retrieved from http://journals.sagepub.com/doi/pdf/10.1097/00004647-200110000-00001

Aviv, R. I., Francis, P. L., Tenenbein, R., O'Connor, P., Zhang, L., Eilaghi, A., … Feinstein, A. (2012). Decreased frontal lobe gray matter perfusion in cognitively impaired patients with secondary-progressive multiple sclerosis detected by the

bookend technique. *AJNR. American Journal of Neuroradiology*, *33*(9), 1779–85. https://doi.org/10.3174/ajnr.A3060

Baranzini, S. E., & Oksenberg, J. R. (2017). The Genetics of Multiple Sclerosis: From 0 to 200 in 50 Years. *Trends in Genetics : TIG*, *33*(12), 960–970. https://doi.org/10.1016/j.tig.2017.09.004

Barkhof, F. (2002). The clinico-radiological paradox in multiple sclerosis revisited. *Current Opinion in Neurology*, *15*(3), 239–245. https://doi.org/10.1097/00019052-200206000-00003

Barratt, E. L., Tewarie, P. K., Clarke, M. A., Hall, E. L., Gowland, P. A., Morris, P. G., … Brookes, M. J. (2017a). Abnormal task driven neural oscillations in multiple sclerosis: A visuomotor MEG study. *Human Brain Mapping*. https://doi.org/10.1002/hbm.23531

Barratt, E. L., Tewarie, P. K., Clarke, M. A., Hall, E. L., Gowland, P. A., Morris, P. G., … Brookes, M. J. (2017b). Abnormal task driven neural oscillations in multiple sclerosis: A visuomotor MEG study. *Human Brain Mapping*, *38*(5), 2441–2453. https://doi.org/10.1002/hbm.23531

Bartels, A., & Zeki, S. (2004). Functional brain mapping during free viewing of natural scenes. *Human Brain Mapping*, *21*(2), 75–85. https://doi.org/10.1002/hbm.10153

Bartels, A., & Zeki, S. (2005). Brain dynamics during natural viewing conditions—A new guide for mapping connectivity in vivo. *NeuroImage*, *24*(2), 339–349. https://doi.org/10.1016/J.NEUROIMAGE.2004.08.044

Bartos, M., Vida, I., & Jonas, P. (2007). Synaptic mechanisms of synchronized gamma oscillations in inhibitory interneuron networks. *Nature Reviews Neuroscience*, *8*(1), 45–56. https://doi.org/10.1038/nrn2044

Bastos, A. M., & Schoffelen, J.-M. (2016). A Tutorial Review of Functional Connectivity Analysis Methods and Their Interpretational Pitfalls. *Frontiers in Systems Neuroscience*, *9*, 175. https://doi.org/10.3389/fnsys.2015.00175

Battaglini, M., Jenkinson, M., & De Stefano, N. (2012). Evaluating and reducing the impact of white matter lesions on brain volume measurements. *Human Brain Mapping*, *33*(9), 2062–2071. https://doi.org/10.1002/hbm.21344

Benedict, R. H. B., DeLuca, J., Phillips, G., LaRocca, N., Hudson, L. D., & Rudick, R. (2017). Validity of the symbol digit modalities test as a cognition performance outcome measure for multiple sclerosis. *Multiple Sclerosis Journal*. https://doi.org/10.1177/1352458517690821

Bentley, W. J., Li, J. M., Snyder, A. Z., Raichle, M. E., & Snyder, L. H. (2016). Oxygen Level and LFP in Task-Positive and Task-Negative Areas: Bridging BOLD fMRI and Electrophysiology. *Cerebral Cortex (New York, N.Y. : 1991)*, *26*(1), 346–57. https://doi.org/10.1093/cercor/bhu260

Bester, M., Forkert, N. D., Stellmann, J. P., Aly, L., Drabik, A., Young, K. L., … Siemonsen, S. (2015). Increased Perfusion in Normal Appearing White Matter in High Inflammatory Multiple Sclerosis Patients. https://doi.org/10.1371/journal.pone.0119356

Betti, V., Della Penna, S., de Pasquale, F., Mantini, D., Marzetti, L., Romani, G. L., & Corbetta, M. (2013). Natural Scenes Viewing Alters the Dynamics of Functional Connectivity in the Human Brain. *Neuron*, *79*(4), 782–797. https://doi.org/10.1016/J.NEURON.2013.06.022

Bitsch, A., Schuchardt, J., Bunkowski, S., Kuhlmann, T., & Brück, W. (2000). Acute axonal injury in multiple sclerosis. Correlation with demyelination and inflammation. *Brain : A Journal of Neurology*, *123 (Pt 6)*, 1174–83. Retrieved from http://www.ncbi.nlm.nih.gov/pubmed/10825356

Blockley, N. P., Griffeth, V. E. M., Simon, A. B., & Buxton, R. B. (2013). A review of calibrated blood oxygenation level-dependent (BOLD) methods for the measurement of task-induced changes in brain oxygen metabolism. *NMR in Biomedicine*, *26*(8), 987–1003. https://doi.org/10.1002/nbm.2847

Bö, L., Geurts, J. J. G., van der Valk, P., Polman, C., & Barkhof, F. (2007). Lack of Correlation Between Cortical Demyelination and White Matter Pathologic Changes in Multiple Sclerosis. *Archives of Neurology*, *64*(1), 76. https://doi.org/10.1001/archneur.64.1.76

Bø, L., Vedeler, C. A., Nyland, H. I., Trapp, B. D., & Mørk, S. J. (2003). Subpial demyelination in the cerebral cortex of multiple sclerosis patients. *Journal of Neuropathology and Experimental Neurology*, *62*(7), 723–32. Retrieved from http://www.ncbi.nlm.nih.gov/pubmed/12901699

Bø, L., Vedeler, C. A., Nyland, H., Trapp, B. D., & Mørk, S. J. (2003). Intracortical multiple sclerosis lesions are not associated with increased lymphocyte infiltration. *Multiple Sclerosis Journal*, *9*(4), 323–331. https://doi.org/10.1191/1352458503ms917oa

Brooks, D. J., Leenders, K. L., Head, G., Marshall, T. J., Legg, N. J., & Jones, T. (1984). Studies on regional cerebral oxygen utilisation and cognitive function in multiple sclerosis. *Neurosurgery, and Psychiatry*, *47*, 1182–1191. https://doi.org/10.1136/jnnp.47.11.1182

Brück, W., Kuhlmann, T., & Stadelmann, C. (2003). Remyelination in multiple sclerosis. *Journal of the Neurological Sciences*, *206*(2), 181–185. https://doi.org/10.1016/S0022-510X(02)00191-0

Brunel, N., & Wang, X.-J. (2003). What Determines the Frequency of Fast Network Oscillations With Irregular Neural Discharges? I. Synaptic Dynamics and Excitation-Inhibition Balance. *Journal of Neurophysiology*, *90*(1), 415–430.

https://doi.org/10.1152/jn.01095.2002

Bulte, D. P., Drescher, K., & Jezzard, P. (2009). Comparison of hypercapnia-based calibration techniques for measurement of cerebral oxygen metabolism with MRI. *Magnetic Resonance in Medicine*, *61*(2), 391–398. https://doi.org/10.1002/mrm.21862

Bulte, D. P., Kelly, M., Germuska, M., Xie, J., Chappell, M. A., Okell, T. W., … Jezzard, P. (2012). Quantitative measurement of cerebral physiology using respiratory-calibrated MRI. *NeuroImage*, *60*(1), 582–591. https://doi.org/10.1016/J.NEUROIMAGE.2011.12.017

Buxton, R. B. (2009). *Introduction to functional magnetic resonance imaging : principles and techniques*. Cambridge University Press.

Buxton, R. B. (2010). Interpreting oxygenation-based neuroimaging signals: the importance and the challenge of understanding brain oxygen metabolism. *Frontiers in Neuroenergetics*, *2*, 8. https://doi.org/10.3389/fnene.2010.00008

Buzsáki, G., Anastassiou, C. A., & Koch, C. (2012). The origin of extracellular fields and currents — EEG, ECoG, LFP and spikes. *Nature Reviews Neuroscience*, *13*(6), 407–420. https://doi.org/10.1038/nrn3241

Buzsáki, G., & Draguhn, A. (2004). Neuronal oscillations in cortical networks. *Science (New York, N.Y.)*, *304*(5679), 1926–9. https://doi.org/10.1126/science.1099745

Buzsáki, G., Logothetis, N., & Singer, W. (2013). Scaling brain size, keeping timing: Evolutionary preservation of brain rhythms. *Neuron*, *80*(3), 751–764. https://doi.org/10.1016/j.neuron.2013.10.002

Buzsáki, G., & Wang, X.-J. (2012). Mechanisms of Gamma Oscillations. *Annu Rev Neurosci*, *35*, 203–225. https://doi.org/10.1146/annurev-neuro-062111-150444

Calabrese, M., Reynolds, R., Magliozzi, R., Castellaro, M., Morra, A., Scalfari, A., … Monaco, S. (2015). Regional Distribution and Evolution of Gray Matter Damage in Different Populations of Multiple Sclerosis Patients. *PLOS ONE*, *10*(8), e0135428. https://doi.org/10.1371/journal.pone.0135428

Canolty, R. T., & Knight, R. T. (2010). The functional role of cross-frequency coupling. *Trends in Cognitive Sciences*, *14*(11), 506–15. https://doi.org/10.1016/j.tics.2010.09.001

Cardin, J. A., Carlén, M., Meletis, K., Knoblich, U., Zhang, F., Deisseroth, K., … Moore, C. I. (2009). Driving fast-spiking cells induces gamma rhythm and controls sensory responses. *Nature*, *459*(7247), 663–7. https://doi.org/10.1038/nature08002

Carhart-Harris, R. L., Muthukumaraswamy, S., Roseman, L., Kaelen, M., Droog, W., Murphy, K., … Nutt, D. J. (2016). Neural correlates of the LSD experience revealed by multimodal neuroimaging. *Proceedings of the National Academy of*

Sciences of the United States of America, *113*(17), 4853–8. https://doi.org/10.1073/pnas.1518377113

Cauli, B., & Hamel, E. (2010). Revisiting the role of neurons in neurovascular coupling. *Frontiers in Neuroenergetics*, *2*(June), 9. https://doi.org/10.3389/fnene.2010.00009

Cawley, N., Solanky, B. S., Muhlert, N., Tur, C., Edden, R. A. E., Wheeler-kingshott, C. A. M., … Ciccarelli, O. (2015). *Reduced gamma-aminobutyric acid concentration is associated with physical disability in progressive multiple sclerosis*. https://doi.org/10.1093/brain/awv209

Chang, W.-T., Jääskeläinen, I. P., Belliveau, J. W., Huang, S., Hung, A.-Y., Rossi, S., & Ahveninen, J. (2015). Combined MEG and EEG show reliable patterns of electromagnetic brain activity during natural viewing. *NeuroImage*, *114*, 49–56. https://doi.org/10.1016/j.neuroimage.2015.03.066

Chang, W. T., J????skel??inen, I. P., Belliveau, J. W., Huang, S., Hung, A. Y., Rossi, S., & Ahveninen, J. (2015). Combined MEG and EEG show reliable patterns of electromagnetic brain activity during natural viewing. *NeuroImage*, *114*, 49–56. https://doi.org/10.1016/j.neuroimage.2015.03.066

Chappell, M. A., Groves, A. R., Whitcher, B., & Woolrich, M. W. (2009). Variational Bayesian Inference for a Nonlinear Forward Model. *IEEE Transactions on Signal Processing*, *57*(1), 223–236. https://doi.org/10.1109/TSP.2008.2005752

Chappell, M. A., MacIntosh, B. J., Donahue, M. J., Günther, M., Jezzard, P., & Woolrich, M. W. (2010). Separation of macrovascular signal in multi-inversion time arterial spin labelling MRI. *Magnetic Resonance in Medicine*, *63*(5), 1357–1365. https://doi.org/10.1002/mrm.22320

Chard, D., & Trip, S. A. (2017). Resolving the clinico-radiological paradox in multiple sclerosis. *F1000Research*, *6*, 1828. https://doi.org/10.12688/f1000research.11932.1

Chavhan, G. B., Babyn, P. S., Thomas, B., Shroff, M. M., & Haacke, E. M. (2009). Principles, techniques, and applications of T2*-based MR imaging and its special applications. *Radiographics : A Review Publication of the Radiological Society of North America, Inc*, *29*(5), 1433–49. https://doi.org/10.1148/rg.295095034

Chen, B. R., Kozberg, M. G., Bouchard, M. B., Shaik, M. A., & Hillman, E. M. C. (2014). A critical role for the vascular endothelium in functional neurovascular coupling in the brain. *Journal of the American Heart Association*, *3*(3), e000787. https://doi.org/10.1161/JAHA.114.000787

Chen, J. J., & Pike, G. B. (2009). BOLD-specific cerebral blood volume and blood flow changes during neuronal activation in humans. *NMR in Biomedicine*, *22*(10), n/a-n/a. https://doi.org/10.1002/nbm.1411

Chen, J. J., & Pike, G. B. (2010). MRI measurement of the BOLD-specific flow–volume relationship during hypercapnia and hypocapnia in humans. *NeuroImage*, *53*(2), 383–391. https://doi.org/10.1016/J.NEUROIMAGE.2010.07.003

Cheyne, D. O., & Papanicolaou, A. C. (2015). *Magnetoencephalography and Magnetic Source Imaging*. (A. C. Papanicolaou, Ed.) (Vol. 1). Oxford University Press. https://doi.org/10.1093/oxfordhb/9780199764228.013.6

Christiansen, C. F., Christensen, S., Farkas, D. K., Miret, M., Sørensen, H. T., & Pedersen, L. (2010). Risk of arterial cardiovascular diseases in patients with multiple sclerosis: a population-based cohort study. *Neuroepidemiology*, *35*(4), 267–74. https://doi.org/10.1159/000320245

Clements, R. J., McDonough, J., & Freeman, E. J. (2008). Distribution of parvalbumin and calretinin immunoreactive interneurons in motor cortex from multiple sclerosis post-mortem tissue. *Experimental Brain Research*, *187*(3), 459–465. https://doi.org/10.1007/s00221-008-1317-9

Cohen, D. (1968). Magnetoencephalography: evidence of magnetic fields produced by alpha-rhythm currents. *Science (New York, N.Y.)*, *161*(3843), 784–6. Retrieved from http://www.ncbi.nlm.nih.gov/pubmed/5663803

Cohen, E. R., Ugurbil, K., & Kim, S.-G. (2002). Effect of Basal Conditions on the Magnitude and Dynamics of the Blood Oxygenation Level-Dependent fMRI Response. *Journal of Cerebral Blood Flow & Metabolism*, *22*(9), 1042–1053. https://doi.org/10.1097/00004647-200209000-00002

Cohen, M. X. (2017). Where Does EEG Come From and What Does It Mean? *Trends in Neurosciences*, *40*(4), 208–218. https://doi.org/10.1016/j.tins.2017.02.004

Cover, K. S., Vrenken, H., Geurts, J. J. G., van Oosten, B. W., Jelles, B., Polman, C. H., … van Dijk, B. W. (2006). Multiple sclerosis patients show a highly significant decrease in alpha band interhemispheric synchronization measured using MEG. *NeuroImage*, *29*(3), 783–788. https://doi.org/10.1016/J.NEUROIMAGE.2005.08.048

Crespy, L., Zaaraoui, W., Lemaire, M., Rico, A., Faivre, A., Reuter, F., … Audoin, B. (2011). Prevalence of grey matter pathology in early multiple sclerosis assessed by Magnetization transfer ratio imaging. *PLoS ONE*, *6*(9), e24969. https://doi.org/10.1371/journal.pone.0024969

Cutter, G. R., Baier, M. L., Rudick, R. A., Cookfair, D. L., Fischer, J. S., Petkau, J., … Willoughby, E. (1999). Development of a multiple sclerosis functional composite as a clinical trial outcome measure. *Brain : A Journal of Neurology*, *122 (Pt 5)*, 871–82. Retrieved from http://www.ncbi.nlm.nih.gov/pubmed/10355672

D'haeseleer, M., Beelen, R., Fierens, Y., Cambron, M., Vanbinst, A.-M., Verborgh, C.,

… De Keyser, J. (2013). Cerebral hypoperfusion in multiple sclerosis is reversible and mediated by endothelin-1. https://doi.org/10.1073/pnas.1222560110

D'haeseleer, M., Cambron, M., Vanopdenbosch, L., & De Keyser, J. (2011). Vascular aspects of multiple sclerosis. *The Lancet Neurology*, *10*(7), 657–666. https://doi.org/10.1016/S1474-4422(11)70105-3

D'haeseleer, M., Hostenbach, S., Peeters, I., Sankari, S. El, Nagels, G., De Keyser, J., & D'hooghe, M. B. (2015). Cerebral hypoperfusion: a new pathophysiologic concept in multiple sclerosis? *Journal of Cerebral Blood Flow and Metabolism : Official Journal of the International Society of Cerebral Blood Flow and Metabolism*, *35*(9), 1406–10. https://doi.org/10.1038/jcbfm.2015.131

David, O., Kilner, J. M., & Friston, K. J. (2006). Mechanisms of evoked and induced responses in MEG/EEG. *NeuroImage*, *31*(4), 1580–1591. https://doi.org/10.1016/j.neuroimage.2006.02.034

Davis, T. L., Kwong, K. K., Weisskoff, R. M., & Rosen, B. R. (1998). *Calibrated functional MRI: Mapping the dynamics of oxidative metabolism*. *Proceedings of the National Academy of Sciences* (Vol. 95). https://doi.org/10.1073/pnas.95.4.1834

Dawson, R. (2011). How Significant is a Boxplot Outlier? *Journal of Statistics Education*, *19*(2). https://doi.org/10.1080/10691898.2011.11889610

De Vis, J. B., Petersen, E. T., Bhogal, A., Hartkamp, N. S., Klijn, C. J., Kappelle, L., & Hendrikse, J. (2015). Calibrated MRI to Evaluate Cerebral Hemodynamics in Patients with an Internal Carotid Artery Occlusion. *Journal of Cerebral Blood Flow & Metabolism*, *35*(6), 1015–1023. https://doi.org/10.1038/jcbfm.2015.14

Debernard, L., Melzer, T. R., Van Stockum, S., Graham, C., Wheeler-Kingshott, C. A., Dalrymple-Alford, J. C., … Mason, D. F. (2014). Reduced grey matter perfusion without volume loss in early relapsing-remitting multiple sclerosis. *Journal of Neurology, Neurosurgery, and Psychiatry*, *85*(5), 544–51. https://doi.org/10.1136/jnnp-2013-305612

Demanuele, C., James, C. J., & Sonuga-Barke, E. J. (2007). Distinguishing low frequency oscillations within the 1/f spectral behaviour of electromagnetic brain signals. *Behavioral and Brain Functions*, *3*(1), 62. https://doi.org/10.1186/1744-9081-3-62

Dendrou, C. A., Fugger, L., & Friese, M. A. (2015). Immunopathology of multiple sclerosis. *Nature Reviews Immunology*, *15*(9), 545–558. https://doi.org/10.1038/nri3871

Devonshire, I. M., Papadakis, N. G., Port, M., Berwick, J., Kennerley, A. J., Mayhew, J. E. W., & Overton, P. G. (2012). Neurovascular coupling is brain region-

dependent. *NeuroImage*, *59*(3), 1997–2006. https://doi.org/10.1016/j.neuroimage.2011.09.050

Dienel, G. A. (2012). Brain lactate metabolism: the discoveries and the controversies. *Journal of Cerebral Blood Flow and Metabolism : Official Journal of the International Society of Cerebral Blood Flow and Metabolism*, *32*(7), 1107–38. https://doi.org/10.1038/jcbfm.2011.175

Dmochowski, J. P., Sajda, P., Dias, J., Parra, L. C., & Rousselet, G. A. (2012). HUMAN NEUROSCIENCE Correlated components of ongoing EEG point to emotionally laden attention-a possible marker of engagement? https://doi.org/10.3389/fnhum.2012.00112

Driver, I. D., Wise, R. G., & Murphy, K. (2017). Graded hypercapnia-calibrated BOLD: Beyond the Iso-metabolic hypercapnic assumption. *Frontiers in Neuroscience*, *11*(MAY), 276. https://doi.org/10.3389/fnins.2017.00276

Du, F., Zhu, X.-H., Zhang, Y., Friedman, M., Zhang, N., Ugurbil, K., & Chen, W. (2008). Tightly coupled brain activity and cerebral ATP metabolic rate. *Proceedings of the National Academy of Sciences of the United States of America*, *105*(17), 6409–14. https://doi.org/10.1073/pnas.0710766105

Duffin, J., Sobczyk, O., McKetton, L., Crawley, A., Poublanc, J., Venkatraghavan, L., … Fisher, J. A. (2018). Cerebrovascular Resistance: The Basis of Cerebrovascular Reactivity. *Frontiers in Neuroscience*, *12*, 409. https://doi.org/10.3389/fnins.2018.00409

Dunn, J.-O., Mythen, M., & Grocott, M. (2016). Physiology of oxygen transport. *BJA Education*, *16*(10), 341–348. https://doi.org/10.1093/bjaed/mkw012

Dury, R. J., Falah, Y., Gowland, P. A., Evangelou, N., Bright, M. G., & Francis, S. T. (2018). Ultra-high-field arterial spin labelling MRI for non-contrast assessment of cortical lesion perfusion in multiple sclerosis. *European Radiology*, 1–7. https://doi.org/10.1007/s00330-018-5707-5

Einevoll, G. T., Kayser, C., Logothetis, N. K., & Panzeri, S. (2013). Modelling and analysis of local field potentials for studying the function of cortical circuits. *Nature Reviews Neuroscience*, *14*(11), 770–785. https://doi.org/10.1038/nrn3599

Ekstrom, A. (2010). How and when the fMRI BOLD signal relates to underlying neural activity: the danger in dissociation. *Brain Research Reviews*, *62*(2), 233–44. https://doi.org/10.1016/j.brainresrev.2009.12.004

Fan, A. P., Govindarajan, S. T., Kinkel, R. P., Madigan, N. K., Nielsen, A. S., Benner, T., … Mainero, C. (2015). Quantitative oxygen extraction fraction from 7-Tesla MRI phase: reproducibility and application in multiple sclerosis. *Journal of Cerebral Blood Flow and Metabolism : Official Journal of the International Society of Cerebral Blood Flow and Metabolism*, *35*(1), 131–9.

https://doi.org/10.1038/jcbfm.2014.187

Faro, S. H., Mohamed, F. B., Tracy, J. I., Elfont, R. M., Pinus, A. B., Lublin, F. D., … Tsai, F. Y. (2002). *Quantitative functional MR imaging of the visual cortex at 1.5 T as a function of luminance contrast in healthy volunteers and patients with multiple sclerosis. AJNR. American journal of neuroradiology* (Vol. 23). Retrieved from http://www.ncbi.nlm.nih.gov/pubmed/11827876

Ferguson, B., Matyszak, M. K., Esiri, M. M., & Perry, V. H. (1997). Axonal damage in acute multiple sclerosis lesions. *Brain : A Journal of Neurology*, *120 (Pt 3)*, 393–9. Retrieved from http://www.ncbi.nlm.nih.gov/pubmed/9126051

Ferré, J.-C., Bannier, E., Raoult, H., Mineur, G., Carsin-Nicol, B., & Gauvrit, J.-Y. (2013). Arterial spin labeling (ASL) perfusion: Techniques and clinical use. *Diagnostic and Interventional Imaging*, *94*, 1211–1223. https://doi.org/10.1016/j.diii.2013.06.010

Franklin, R. J. M. (2002). Why does remyelination fail in multiple sclerosis? *Nature Reviews Neuroscience*, *3*(9), 705–714. https://doi.org/10.1038/nrn917

Franklin, R. J. M., & Goldman, S. A. (2015). Glia Disease and Repair-Remyelination. *Cold Spring Harbor Perspectives in Biology*, *7*(7), a020594. https://doi.org/10.1101/cshperspect.a020594

Fries, P. (2009). Neuronal Gamma-Band Synchronization as a Fundamental Process in Cortical Computation. *Annual Review of Neuroscience*, *32*(1), 209–224. https://doi.org/10.1146/annurev.neuro.051508.135603

Fukuda, M., Poplawsky, A. J., & Kim, S.-G. (2016). Submillimeter-resolution fMRI: Toward understanding local neural processing. *Progress in Brain Research*, *225*, 123–152. https://doi.org/10.1016/BS.PBR.2016.03.003

Gasperini, C., Paolillo, A., Giugni, E., Galgani, S., Bagnato, F., Mainero, C., … Pozzilli, C. (2002). MRI brain volume changes in relapsing-remitting multiple sclerosis patients treated with interferon beta-1a. *Multiple Sclerosis*, *8*(2), 119–123. https://doi.org/10.1191/1352458502ms788oa

Gauthier, C. J., Desjardins-Crépeau, L., Madjar, C., Bherer, L., & Hoge, R. D. (2012). Absolute quantification of resting oxygen metabolism and metabolic reactivity during functional activation using QUO2 MRI. *NeuroImage*, *63*(3), 1353–1363. https://doi.org/10.1016/J.NEUROIMAGE.2012.07.065

Gauthier, C. J., & Hoge, R. D. (2013). A generalized procedure for calibrated MRI incorporating hyperoxia and hypercapnia. *Human Brain Mapping*, *34*(5), 1053–1069. https://doi.org/10.1002/hbm.21495

Ge, Y. (2006). *Multiple sclerosis: the role of MR imaging*. *AJNR American journal of neuroradiology* (Vol. 27). https://doi.org/27/6/1165 [pii]

Ge, Y., Law, M., Johnson, G., Herbert, J., Babb, J. S., Mannon, L. J., & Grossman, R.

I. (2005). *Dynamic susceptibility contrast perfusion MR imaging of multiple sclerosis lesions: characterizing hemodynamic impairment and inflammatory activity. AJNR American journal of neuroradiology* (Vol. 26). https://doi.org/26/6/1539 [pii]

Ge, Y., Zhang, Z., Lu, H., Tang, L., Jaggi, H., Herbert, J., … Grossman, R. I. (2012). Characterizing brain oxygen metabolism in patients with multiple sclerosis with T2-relaxation-under-spin-tagging MRI. *Journal of Cerebral Blood Flow & Metabolism*, *32*(10), 403–412. https://doi.org/10.1038/jcbfm.2011.191

Gelineau-Morel, R., Tomassini, V., Jenkinson, M., Johansen-Berg, H., Matthews, P. M., & Palace, J. (2012). The effect of hypointense white matter lesions on automated gray matter segmentation in multiple sclerosis. *Human Brain Mapping*, *33*(12), 2802–14. https://doi.org/10.1002/hbm.21402

Germuska, M. (2018a). pMRI-CMRO2-diffusivity: First release. https://doi.org/10.5281/ZENODO.1285846

Germuska, M. (2018b). process-phys-traces: First release. https://doi.org/10.5281/ZENODO.1285863

Germuska, M., Chandler, H. L., Stickland, R. C., Foster, C., Fasano, F., Okell, T. W., … Wise, R. G. (2019). Dual-calibrated fMRI measurement of absolute cerebral metabolic rate of oxygen consumption and effective oxygen diffusivity. *NeuroImage*, *184*, 717–728. https://doi.org/10.1016/J.NEUROIMAGE.2018.09.035

Germuska, M., Merola, A., Murphy, K., Babic, A., Richmond, L., Khot, S., … Wise, R. G. (2016). A forward modelling approach for the estimation of oxygen extraction fraction by calibrated fMRI. *NeuroImage*, *139*, 313–323. https://doi.org/10.1016/J.NEUROIMAGE.2016.06.004

Germuska, M., & Wise, R. G. (2018). Calibrated fMRI for mapping absolute CMRO 2 : Practicalities and prospects. https://doi.org/10.1016/j.neuroimage.2018.03.068

Girouard, H., & Iadecola, C. (2006). Neurovascular coupling in the normal brain and in hypertension, stroke, and Alzheimer disease. *Journal of Applied Physiology (Bethesda, Md. : 1985)*, *100*(1), 328–335. https://doi.org/10.1152/japplphysiol.00966.2005

Gjedde, A., Poulsen, P. H., & Ostergaard, L. (1999). On the oxygenation of hemoglobin in the human brain. *Advances in Experimental Medicine and Biology*, *471*, 67–81. Retrieved from http://www.ncbi.nlm.nih.gov/pubmed/10659133

Glover, G. H. (2011). Overview of functional magnetic resonance imaging. *Neurosurgery Clinics of North America*, *22*(2), 133–9, vii. https://doi.org/10.1016/j.nec.2010.11.001

Goense, J., Merkle, H., & Logothetis, N. K. (2012). High-Resolution fMRI Reveals

Laminar Differences in Neurovascular Coupling between Positive and Negative BOLD Responses. *Neuron*, *76*(3), 629–639. https://doi.org/10.1016/J.NEURON.2012.09.019

Goodyear, B. G., & Menon, R. S. (1998). Effect of Luminance Contrast on BOLD fMRI Response in Human Primary Visual Areas. *Journal of Neurophysiology*, *79*(4), 2204–2207. https://doi.org/10.1152/jn.1998.79.4.2204

Graham, S. L., & Klistorner, A. (2017). Afferent visual pathways in multiple sclerosis: a review. *Clinical & Experimental Ophthalmology*, *45*(1), 62–72. https://doi.org/10.1111/ceo.12751

Griffeth, V. E. M., Simon, A. B., & Buxton, R. B. (2015). The coupling of cerebral blood flow and oxygen metabolism with brain activation is similar for simple and complex stimuli in human primary visual cortex. *NeuroImage*, *104*, 156–162. https://doi.org/10.1016/j.neuroimage.2014.10.003

Grubb RL Jr, Raichle ME, Eichling JO, T.-P. M. (1974). *The effects of changes in PaCO_2 on cerebral blood volume, blood flow, and vascular mean transit time*. *Stroke* (Vol. 5). https://doi.org/10.1161/01.STR.5.5.630

Guimarães, J., Sá, M. J., & Massano, J. (2012). Cognitive dysfunction in Multiple Sclerosis. https://doi.org/10.3389/fneur.2012.00074

Guo, A. C., Jewells, V. L., & Provenzale, J. M. (2001). Analysis of normal-appearing white Matter in multiple sclerosis: Comparison of diffusion tensor MR imaging and magnetization transfer imaging. *American Journal of Neuroradiology*, *22*(10), 1893–1900. https://doi.org/10.1148/radiol.2313030996

Hall, E. L., Robson, S. E., Morris, P. G., & Brookes, M. J. (2014). The relationship between MEG and fMRI. *NeuroImage*, *102*(P1), 80–91. https://doi.org/10.1016/j.neuroimage.2013.11.005

Hall, S. D., Holliday, I. E., Hillebrand, A., Singh, K. D., Furlong, P. L., Hadjipapas, A., & Barnes, G. R. (2005). The missing link: analogous human and primate cortical gamma oscillations. *NeuroImage*, *26*(1), 13–17. https://doi.org/10.1016/J.NEUROIMAGE.2005.01.009

Haller, S., Zaharchuk, G., Thomas, D. L., Lovblad, K.-O., Barkhof, F., & Golay, X. (2016). Arterial Spin Labeling Perfusion of the Brain: Emerging Clinical Applications. *Radiology*, *281*(2), 337–356. https://doi.org/10.1148/radiol.2016150789

Hamilton, N. B., Attwell, D., & Hall, C. N. (2010). Pericyte-mediated regulation of capillary diameter: a component of neurovascular coupling in health and disease. *Frontiers in Neuroenergetics*, *2*, 5. https://doi.org/10.3389/fnene.2010.00005

Hansen, P., Kringelbach, M., & Salmelin, R. (2010). *MEG: An Introduction to Methods*. Retrieved from https://brainmaster.com/software/pubs/brain/MEG - An

Intro.pdf

Haselhorst, R., Kappos, L., Bilecen, D., Scheffler, K., M□ri, D., Rad□, E. W., & Seelig, J. (2000). Dynamic susceptibility contrast MR imaging of plaque development in multiple sclerosis: Application of an extended blood-brain barrier leakage correction. *Journal of Magnetic Resonance Imaging*, *11*(5), 495–505. https://doi.org/10.1002/(SICI)1522-2586(200005)11:5<495::AID-JMRI5>3.0.CO;2-S

Hasson, U., Malach, R., & Heeger, D. J. (2010). Reliability of cortical activity during natural stimulation. *Trends Cogn Sci*, *14*(1), 40. https://doi.org/10.1016/j.tics.2009.10.011

Hasson, U., Nir, Y., Levy, I., Fuhrmann, G., & Malach, R. (2004). Intersubject Synchronization of Cortical Activity During Natural Vision. *Science*, *303*(5664), 1634–1640. https://doi.org/10.1126/science.1089506

Hayashi, T., Watabe, H., Kudomi, N., Min Kim, K., Enmi, J.-I., Hayashida, K., & Iida, H. (2003). A Theoretical Model of Oxygen Delivery and Metabolism for Physiologic Interpretation of Quantitative Cerebral Blood Flow and Metabolic Rate of Oxygen. https://doi.org/10.1097/01.WCB.0000090506.76664.00

Henrie, J. A., & Shapley, R. (2005). LFP Power Spectra in V1 Cortex: The Graded Effect of Stimulus Contrast. *Journal of Neurophysiology*, *94*(1), 479–490. https://doi.org/10.1152/jn.00919.2004

Hermes, D., Nguyen, M., & Winawer, J. (2017). Neuronal synchrony and the relation between the blood-oxygen-level dependent response and the local field potential. *PLOS Biology*, *15*(7), e2001461. https://doi.org/10.1371/journal.pbio.2001461

Hewson-Stoate, N., Jones, M., Martindale, J., Berwick, J., & Mayhew, J. (2005). Further nonlinearities in neurovascular coupling in rodent barrel cortex. *NeuroImage*, *24*(2), 565–574. https://doi.org/10.1016/J.NEUROIMAGE.2004.08.040

Hillebrand, A., & Barnes, G. R. (2002). A Quantitative Assessment of the Sensitivity of Whole-Head MEG to Activity in the Adult Human Cortex. *NeuroImage*, *16*(3), 638–650. https://doi.org/10.1006/NIMG.2002.1102

Hillebrand, A., & Barnes, G. R. (2005). Beamformer Analysis of MEG Data. In *International review of neurobiology* (Vol. 68, pp. 149–171). https://doi.org/10.1016/S0074-7742(05)68006-3

Hillebrand, A., Singh, K. D., Holliday, I. E., Furlong, P. L., & Barnes, G. R. (2005). A new approach to neuroimaging with magnetoencephalography. *Human Brain Mapping*, *25*(2), 199–211. https://doi.org/10.1002/hbm.20102

Hobart, J., Lamping, D., Fitzpatrick, R., Riazi, A., & Thompson, A. (2001). The Multiple Sclerosis Impact Scale (MSIS-29): A new patient-based outcome

measure. *Brain*, *124*(5), 962–973. https://doi.org/10.1093/brain/124.5.962

Hoffmeyer, H. W., Enager, P., Thomsen, K. J., & Lauritzen, M. J. (2007). Nonlinear neurovascular coupling in rat sensory cortex by activation of transcallosal fibers. *Journal of Cerebral Blood Flow & Metabolism*, *27*, 575–587. https://doi.org/10.1038/sj.jcbfm.9600372

Hoge, R. D., Atkinson, J., Gill, B., Crelier, G. R., Marrett, S., & Pike, G. B. (1999). Investigation of BOLD signal dependence on cerebral blood flow and oxygen consumption: The deoxyhemoglobin dilution model. *Magnetic Resonance in Medicine*, *42*(5), 849–863. https://doi.org/10.1002/(SICI)1522-2594(199911)42:5<849::AID-MRM4>3.0.CO;2-Z

Hojjat, S.-P., Vitorino, R., Cantrell, C. G., Feinstein, A., Zhang, L., Lee, L., … Aviv, R. I. (2016). Cortical perfusion alteration in normal appearing gray matter is most sensitive to disease progression in relapsing remitting Multiple Sclerosis HHS Public Access. *AJNR Am J Neuroradiol*, *37*(8), 1454–1461. https://doi.org/10.3174/ajnr.A4737

Holm, S. (1979). A Simple Sequentially Rejective Multiple Test Procedure. *Scandinavian Journal of Statistics*. WileyBoard of the Foundation of the Scandinavian Journal of Statistics. https://doi.org/10.2307/4615733

Hubbard, N. A., Araujo, Y. S., Caballero, C., Ouyang, M., Turner, M. P., Himes, L., … Rypma, B. (2017). Evaluation of Visual-Evoked Cerebral Metabolic Rate of Oxygen as a Diagnostic Marker in Multiple Sclerosis. *Brain Sci. Brain Sci*, *7*(7). https://doi.org/10.3390/brainsci7060064

Hubbard, N. A., Turner, M., Hutchison, J. L., Ouyang, A., Strain, J., Oasay, L., … Rypma, B. (2016). Multiple sclerosis-related white matter microstructural change alters the BOLD hemodynamic response. *Journal of Cerebral Blood Flow and Metabolism*, *36*(11), 1872–1884. https://doi.org/10.1177/0271678X15615133

Hubbard, N. A., Turner, M. P., Ouyang, M., Himes, L., Thomas, B. P., Hutchison, J. L., … Rypma, B. (2017). Calibrated imaging reveals altered grey matter metabolism related to white matter microstructure and symptom severity in multiple sclerosis. *Human Brain Mapping*, *38*(11), 5375–5390. https://doi.org/10.1002/hbm.23727

Huo, B.-X., Smith, J. B., & Drew, P. J. (2014). Neurovascular coupling and decoupling in the cortex during voluntary locomotion. *The Journal of Neuroscience : The Official Journal of the Society for Neuroscience*, *34*(33), 10975–81. https://doi.org/10.1523/JNEUROSCI.1369-14.2014

Huster, R. J., Debener, S., Eichele, T., & Herrmann, C. S. (2012). Methods for simultaneous EEG-fMRI: an introductory review. *The Journal of Neuroscience : The Official Journal of the Society for Neuroscience*, *32*(18), 6053–60.

https://doi.org/10.1523/JNEUROSCI.0447-12.2012

Hyder, D. S. F. (2010). Neurovascular and neurometabolic couplings in dynamic calibrated fMRI: transient oxidative neuroenergetics for block-design and event-related paradigms. *Frontiers in Neuroenergetics*, *2*. https://doi.org/10.3389/fnene.2010.00018

Hyder, F., Rothman, D. L., & Shulman, R. G. (2002). Total neuroenergetics support localized brain activity: Implications for the interpretation of fMRI. *Proceedings of the National Academy of Sciences*, *99*(16), 10771–10776. https://doi.org/10.1073/pnas.132272299

Hyder, F., Shulman, R. G., & Rothman, D. L. (1998). *A model for the regulation of cerebral oxygen delivery*. Retrieved from http://www.jap.org

Iadecola, C. (2017). The Neurovascular Unit Coming of Age: A Journey through Neurovascular Coupling in Health and Disease. https://doi.org/10.1016/j.neuron.2017.07.030

Iannetti, G. D., & Wise, R. G. (2007). BOLD functional MRI in disease and pharmacological studies: room for improvement? *Magnetic Resonance Imaging*, *25*(6), 978–988. https://doi.org/10.1016/j.mri.2007.03.018

Inglese, M., Adhya, S., Johnson, G., Babb, J. S., Miles, L., Jaggi, H., … Grossman, R. I. (2008). Perfusion Magnetic Resonance Imaging Correlates of Neuropsychological Impairment in Multiple Sclerosis. *Journal of Cerebral Blood Flow & Metabolism*, *28*(1), 164–171. https://doi.org/10.1038/sj.jcbfm.9600504

Inglese, M., Park, S.-J., Johnson, G., Babb, J. S., Miles, L., Jaggi, H., … Grossman, R. I. (2007). Deep Gray Matter Perfusion in Multiple Sclerosis. *Archives of Neurology*, *64*(2), 196. https://doi.org/10.1001/archneur.64.2.196

Ingrisch, M., Sourbron, S., Morhard, D., Ertl-Wagner, B., Kümpfel, T., Hohlfeld, R., … Glaser, C. (2012). Quantification of perfusion and permeability in multiple sclerosis: dynamic contrast-enhanced MRI in 3D at 3T. *Investigative Radiology*, *47*(4), 252–8. https://doi.org/10.1097/RLI.0b013e31823bfc97

Jääskeläinen, I. P., Koskentalo, K., Balk, M. H., Autti, T., Kauramäki, J., Pomren, C., & Sams, M. (2008). Inter-Subject Synchronization of Prefrontal Cortex Hemodynamic Activ-ity During Natural Viewing. *The Open Neuroimaging Journal*, *2*, 14–19. Retrieved from http://www.fmrib.ox.ac.uk/fsl/

Jain, V., Langham, M. C., & Wehrli, F. W. (2010). MRI estimation of global brain oxygen consumption rate. *Journal of Cerebral Blood Flow and Metabolism : Official Journal of the International Society of Cerebral Blood Flow and Metabolism*, *30*(9), 1598–607. https://doi.org/10.1038/jcbfm.2010.49

Jenkinson, M., Beckmann, C. F., Behrens, T. E. J., Woolrich, M. W., & Smith, S. M. (2012). FSL. *NeuroImage*, *62*(2), 782–790.

https://doi.org/10.1016/J.NEUROIMAGE.2011.09.015

Jenkinson, M., & Smith, S. (2001). A global optimisation method for robust affine registration of brain images. *Medical Image Analysis*, *5*(2), 143–156. https://doi.org/10.1016/S1361-8415(01)00036-6

Jensen, O., Kaiser, J., & Lachaux, J.-P. (2007). Human gamma-frequency oscillations associated with attention and memory. *Trends in Neurosciences*, *30*(7), 317–24. https://doi.org/10.1016/j.tins.2007.05.001

Jia, X., & Kohn, A. (2011). Gamma Rhythms in the Brain. *PLoS Biology*, *9*(4), e1001045. https://doi.org/10.1371/journal.pbio.1001045

Kamm, C. P., Uitdehaag, B. M., Polman, C. H., & Kamm, C. (2014). E-Mail Multiple Sclerosis: Current Knowledge and Future Outlook. *Eur Neurol*, *72*, 132–141. https://doi.org/10.1159/000360528

Kannurpatti, S. S., Biswal, B. B., & Hudetz, A. G. (2003). Baseline physiological state and the fMRI-BOLD signal response to apnea in anesthetized rats. *NMR in Biomedicine*, *16*(5), 261–268. https://doi.org/10.1002/nbm.842

Kastrup, A., Krüger, G., Glover, G. H., & Moseley, M. E. (1999). Assessment of cerebral oxidative metabolism with breath holding and fMRI. *Magnetic Resonance in Medicine*, *42*(3), 608–611. https://doi.org/10.1002/(SICI)1522-2594(199909)42:3<608::AID-MRM26>3.0.CO;2-I

Kennan, R. P., Zhong, J., & Gore, J. C. (1994). Intravascular susceptibility contrast mechanisms in tissues. *Magnetic Resonance in Medicine*, *31*(1), 9–21. https://doi.org/10.1002/mrm.1910310103

Ki, J. J., Kelly, S. P., & Parra, L. C. (2016). Attention Strongly Modulates Reliability of Neural Responses to Naturalistic Narrative Stimuli. *The Journal of Neuroscience : The Official Journal of the Society for Neuroscience*, *36*(10), 3092–101. https://doi.org/10.1523/JNEUROSCI.2942-15.2016

Kielar, A., Deschamps, T., Chu, R. K. O., Jokel, R., Khatamian, Y. B., Chen, J. J., & Meltzer, J. A. (2016). Identifying Dysfunctional Cortex: Dissociable Effects of Stroke and Aging on Resting State Dynamics in MEG and fMRI. *Frontiers in Aging Neuroscience*, *8*, 40. https://doi.org/10.3389/fnagi.2016.00040

Kilavik, B. E., Zaepffel, M., Brovelli, A., MacKay, W. A., & Riehle, A. (2013). The ups and downs of beta oscillations in sensorimotor cortex. *Experimental Neurology*, *245*, 15–26. https://doi.org/10.1016/J.EXPNEUROL.2012.09.014

Klaver, R., De Vries, H. E., Schenk, G. J., & Geurts, J. J. G. (2013a). Grey matter damage in multiple sclerosis: a pathology perspective. *Prion*, *7*(1), 66–75. https://doi.org/10.4161/pri.23499

Klaver, R., De Vries, H. E., Schenk, G. J., & Geurts, J. J. G. (2013b). Grey matter damage in multiple sclerosis. *Prion*, *7*(1), 66–75.

https://doi.org/10.4161/pri.23499

Kothari, R., Bokariya, P., Singh, S., & Singh, R. (2016). A Comprehensive Review on Methodologies Employed for Visual Evoked Potentials. *Scientifica*, *2016*, 1–9. https://doi.org/10.1155/2016/9852194

Kurtzke, J. F. (1983). Rating neurologic impairment in multiple sclerosis: an expanded disability status scale (EDSS). *Neurology*, *33*(11), 1444–52. Retrieved from http://www.ncbi.nlm.nih.gov/pubmed/6685237

Lahnakoski, J. M., Glerean, E., Jääskeläinen, I. P., Hyönä, J., Hari, R., Sams, M., & Nummenmaa, L. (2014). Synchronous brain activity across individuals underlies shared psychological perspectives. *NeuroImage*, *100*, 316–324. https://doi.org/10.1016/J.NEUROIMAGE.2014.06.022

Lajoie, I., Nugent, S., Debacker, C., Dyson, K., Tancredi, F. B., Badhwar, A. P., … Hoge, R. D. (2017). Application of calibrated fMRI in Alzheimer's disease. *NeuroImage: Clinical*, *15*, 348–358. https://doi.org/10.1016/j.nicl.2017.05.009

Lankinen, K., Saari, J., Hari, R., & Koskinen, M. (2014). Intersubject consistency of cortical MEG signals during movie viewing. *NeuroImage*, *92*, 217–224. https://doi.org/10.1016/J.NEUROIMAGE.2014.02.004

Lankinen, K., Saari, J., Hlushchuk, Y., Tikka, P., Parkkonen, L., Hari, R., & Koskinen, M. (2018). Consistency and similarity of MEG- and fMRI-signal time courses during movie viewing. *NeuroImage*, *173*, 361–369. https://doi.org/10.1016/J.NEUROIMAGE.2018.02.045

Lapointe, E., Li, D. K. B., Traboulsee, A. L., & Rauscher, A. (2018). What Have We Learned from Perfusion MRI in Multiple Sclerosis? *AJNR. American Journal of Neuroradiology*, *39*(6), 994–1000. https://doi.org/10.3174/ajnr.A5504

Lavi, S., Gaitini, D., Milloul, V., & Jacob, G. (2006). Impaired cerebral CO2 vasoreactivity: association with endothelial dysfunction. *American Journal of Physiology. Heart and Circulatory Physiology*, *291*(4), H1856–H1861. https://doi.org/10.1152/ajpheart.00014.2006

Lega, B. C., Jacobs, J., & Kahana, M. (2012). Human hippocampal theta oscillations and the formation of episodic memories. *Hippocampus*, *22*(4), 748–761. https://doi.org/10.1002/hipo.20937

Leithner, C., & Royl, G. (2014). The oxygen paradox of neurovascular coupling. *Journal of Cerebral Blood Flow and Metabolism : Official Journal of the International Society of Cerebral Blood Flow and Metabolism*, *34*(1), 19–29. https://doi.org/10.1038/jcbfm.2013.181

Leon, A. C., Davis, L. L., & Kraemer, H. C. (2011). The role and interpretation of pilot studies in clinical research. *Journal of Psychiatric Research*, *45*(5), 626–9. https://doi.org/10.1016/j.jpsychires.2010.10.008

Li, L., Chopp, M., Nejad-Davarani, S. P., Jafari-Khouzani, K., Patel, S. C., Budaj, J., … Jiang, Q. (2014). Perfusion and Diffusion Abnormalities of Multiple Sclerosis Lesions and Relevance of Classified Lesions to Disease Status NIH Public Access. *J Neurol Neurophysiol*, (12), 12. https://doi.org/10.4172/2155-9562.S12-012

Li, Y.-C., Chen, C.-C., & Chen, J.-H. (2011). Impact of Visual Repetition Rate on Intrinsic Properties of Low Frequency Fluctuations in the Visual Network. *PLoS ONE*, *6*(5), e18954. https://doi.org/10.1371/journal.pone.0018954

Lin, A.-L., Fox, P. T., Hardies, J., Duong, T. Q., & Gao, J.-H. (2010). Nonlinear coupling between cerebral blood flow, oxygen consumption, and ATP production in human visual cortex. *Proceedings of the National Academy of Sciences of the United States of America*, *107*(18), 8446–51. https://doi.org/10.1073/pnas.0909711107

Lindroos, M. M., Borra, R. J., Parkkola, R., Virtanen, S. M., Lepomäki, V., Bucci, M., … Majamaa, K. (2009). Cerebral oxygen and glucose metabolism in patients with mitochondrial m.3243A>G mutation. *Brain*, *132*(12), 3274–3284. https://doi.org/10.1093/brain/awp259

Liu, P., De Vis, J. B., & Lu, H. (2018). Cerebrovascular reactivity (CVR) MRI with CO2 challenge: A technical review. *NeuroImage*. https://doi.org/10.1016/j.neuroimage.2018.03.047

Liu, T. T., & Wong, E. C. (2005). A signal processing model for arterial spin labeling functional MRI. *NeuroImage*, *24*(1), 207–215. https://doi.org/10.1016/J.NEUROIMAGE.2004.09.047

Logothetis, N. K. (2002). The neural basis of the blood-oxygen-level-dependent functional magnetic resonance imaging signal. *Philosophical Transactions of the Royal Society of London. Series B, Biological Sciences*, *357*(1424), 1003–37. https://doi.org/10.1098/rstb.2002.1114

Logothetis, N. K., Pauls, J., Augath, M., Trinath, T., & Oeltermann, A. (2001). Neurophysiological investigation of the basis of the fMRI signal. *Nature*, *412*(6843), 150–157. https://doi.org/10.1038/35084005

Lublin, F. D., Reingold, S. C., Cohen, J. A., Cutter, G. R., Sørensen, P. S., Thompson, A. J., … Polman, C. H. (2014). Defining the clinical course of multiple sclerosis: the 2013 revisions. *Neurology*, *83*(3), 278–86. https://doi.org/10.1212/WNL.0000000000000560

Lucchinetti, C. F., Popescu, B. F. G., Bunyan, R. F., Moll, N. M., Roemer, S. F., Lassmann, H., … Ransohoff, R. M. (2011). Inflammatory Cortical Demyelination in Early Multiple Sclerosis. *New England Journal of Medicine*, *365*(23), 2188–2197. https://doi.org/10.1056/NEJMoa1100648

Lutti, A., Dick, F., Sereno, M. I., & Weiskopf, N. (2014). Using high-resolution quantitative mapping of R1 as an index of cortical myelination. https://doi.org/10.1016/j.neuroimage.2013.06.005

Lycke, J., Wikkelsö, C., Bergh, A. C., Jacobsson, L., & Andersen, O. (1993). Regional cerebral blood flow in multiple sclerosis measured by single photon emission tomography with technetium-99m hexamethylpropyleneamine oxime. *European Neurology*, *33*(2), 163–7. https://doi.org/10.1159/000116926

Magazzini, L., Muthukumaraswamy, S. D., Campbell, A. E., Hamandi, K., Lingford-Hughes, A., Myers, J. F. M., … Singh, K. D. (2016). Significant reductions in human visual gamma frequency by the gaba reuptake inhibitor tiagabine revealed by robust peak frequency estimation. *Human Brain Mapping*, *37*(11), 3882–3896. https://doi.org/10.1002/hbm.23283

Mark, C. I., & Bruce Pike, G. (2012). Indication of BOLD-specific venous flow-volume changes from precisely controlled hyperoxic vs. hypercapnic calibration. *Journal of Cerebral Blood Flow & Metabolism*, *32*, 709–719. https://doi.org/10.1038/jcbfm.2011.174

Marshall, O., Chawla, S., Lu, H., Pape, L., & Ge, Y. (2016). Cerebral blood flow modulation insufficiency in brain networks in multiple sclerosis: A hypercapnia MRI study. *Journal of Cerebral Blood Flow and Metabolism : Official Journal of the International Society of Cerebral Blood Flow and Metabolism*, *36*(12), 2087–2095. https://doi.org/10.1177/0271678X16654922

Marshall, O., Lu, H., Brisset, J.-C., Xu, F., Liu, P., Herbert, J., … Ge, Y. (2014). Impaired cerebrovascular reactivity in multiple sclerosis. *JAMA Neurology*, *71*(10), 1275–81. https://doi.org/10.1001/jamaneurol.2014.1668

Masamoto, K., Vazquez, A., Wang, P., & Kim, S.-G. (2008). Trial-by-trial relationship between neural activity, oxygen consumption, and blood flow responses. *NeuroImage*, *40*(2), 442–450. https://doi.org/10.1016/j.neuroimage.2007.12.011

Mathewson, K. E., Lleras, A., Beck, D. M., Fabiani, M., Ro, T., & Gratton, G. (2011). Pulsed Out of Awareness: EEG Alpha Oscillations Represent a Pulsed-Inhibition of Ongoing Cortical Processing. *Frontiers in Psychology*, *2*, 99. https://doi.org/10.3389/fpsyg.2011.00099

Mayhew, S. D., Macintosh, B. J., Dirckx, S. G., Iannetti, G. D., & Wise, R. G. (2010). Coupling of simultaneously acquired electrophysiological and haemodynamic responses during visual stimulation. *Magnetic Resonance Imaging*, *28*(8), 1066–1077. https://doi.org/10.1016/j.mri.2010.03.027

McSwain, S. D., Hamel, D. S., Smith, P. B., Gentile, M. A., Srinivasan, S., Meliones, J. N., & Cheifetz, I. M. (2010). End-tidal and arterial carbon dioxide measurements correlate across all levels of physiologic dead space. *Respiratory*

Care, *55*(3), 288–93. Retrieved from http://www.ncbi.nlm.nih.gov/pubmed/20196877

Merola, A., Germuska, M. A., Murphy, K., & Wise, R. G. (2018). Assessing the repeatability of absolute CMRO2, OEF and haemodynamic measurements from calibrated fMRI. *NeuroImage*, *173*, 113–126. https://doi.org/10.1016/J.NEUROIMAGE.2018.02.020

Merola, A., Murphy, K., Stone, A. J., Germuska, M. A., Griffeth, V. E. M., Blockley, N. P., … Wise, R. G. (2016). Measurement of oxygen extraction fraction (OEF): An optimized BOLD signal model for use with hypercapnic and hyperoxic calibration. *NeuroImage*, *129*, 159–174. https://doi.org/10.1016/J.NEUROIMAGE.2016.01.021

Millett, D. (2001). Hans Berger: From Psychic Energy to the EEG. *Perspectives in Biology and Medicine*, *44*(4), 522–542. https://doi.org/10.1353/pbm.2001.0070

Mintun, M. A., Lundstrom, B. N., Snyder, A. Z., Vlassenko, A. G., Shulman, G. L., & Raichle, M. E. (2001). *Blood flow and oxygen delivery to human brain during functional activity: Theoretical modeling and experimental data* (Vol. 98). Retrieved from www.pnas.orgcgidoi10.1073pnas.111164398

Mühlau, M., Buck, D., Förschler, A., Boucard, C. C., Arsic, M., Schmidt, P., … Ilg, R. (2013). White-matter lesions drive deep gray-matter atrophy in early multiple sclerosis: Support from structural MRI. *Multiple Sclerosis Journal*, *19*(11), 1485–1492. https://doi.org/10.1177/1352458513478673

Mukamel, R., Gelbard, H., Arieli, A., Hasson, U., Fried, I., & Malach, R. (2005). Coupling between neuronal firing, field potentials, and FMRI in human auditory cortex. *Science (New York, N.Y.)*, *309*(5736), 951–954. https://doi.org/10.1126/science.1110913

Mumford, J. A. (2012). A power calculation guide for fMRI studies. *Social Cognitive and Affective Neuroscience*, *7*(6), 738–42. https://doi.org/10.1093/scan/nss059

Murta, T., Chaudhary, U. J., Tierney, T. M., Dias, A., Leite, M., Carmichael, D. W., … Lemieux, L. (2017). Phase–amplitude coupling and the BOLD signal: A simultaneous intracranial EEG (icEEG) - fMRI study in humans performing a finger-tapping task. *NeuroImage*, *146*, 438–451. https://doi.org/10.1016/J.NEUROIMAGE.2016.08.036

Muthukumaraswamy, S. D., & Singh, K. D. (2008). Spatiotemporal frequency tuning of BOLD and gamma band MEG responses compared in primary visual cortex. *NeuroImage*, *40*(4), 1552–1560. https://doi.org/10.1016/j.neuroimage.2008.01.052

Muthukumaraswamy, S. D., & Singh, K. D. (2009). Functional decoupling of BOLD and gamma-band amplitudes in human primary visual cortex. *Human Brain*

Mapping, *30*(7), 2000–2007. https://doi.org/10.1002/hbm.20644

Muthukumaraswamy, S. D., & Singh, K. D. (2013). Visual gamma oscillations: The effects of stimulus type, visual field coverage and stimulus motion on MEG and EEG recordings. *NeuroImage*, *69*, 223–230. https://doi.org/10.1016/j.neuroimage.2012.12.038

Muthukumaraswamy, S. D., Singh, K. D., Swettenham, J. B., & Jones, D. K. (2010). Visual gamma oscillations and evoked responses: Variability, repeatability and structural MRI correlates. *NeuroImage*, *49*(4), 3349–3357. https://doi.org/10.1016/j.neuroimage.2009.11.045

Narayana, P. A., Zhou, Y., Hasan, K. M., Datta, S., Sun, X., & Wolinsky, J. S. (2014). Hypoperfusion and T1-hypointense lesions in white matter in multiple sclerosis. *Multiple Sclerosis Journal*, *20*(3), 365–373. https://doi.org/10.1177/1352458513495936

Neumann, H. (2003). Molecular mechanisms of axonal damage in inflammatory central nervous system diseases. *Current Opinion in Neurology*, *16*(3), 267–73. https://doi.org/10.1097/01.wco.0000073926.19076.29

Nichols, T. E., & Holmes, A. P. (2001). *Nonparametric Permutation Tests For Functional Neuroimaging: A Primer with Examples*. Retrieved from https://www.fil.ion.ucl.ac.uk/spm/doc/papers/NicholsHolmes.pdf

Niessing, J., Ebisch, B., Schmidt, K. E., Niessing, M., Singer, W., & Galuske, R. A. W. (2005). Hemodynamic Signals Correlate Tightly with Synchronized Gamma Oscillations. *Science*, *309*(5736), 948–951. https://doi.org/10.1126/science.1110948

Nimmrich, V., Draguhn, A., & Axmacher, N. (2015). Neuronal Network Oscillations in Neurodegenerative Diseases. *NeuroMolecular Medicine*, *17*(3), 270–284. https://doi.org/10.1007/s12017-015-8355-9

Nolte, G. (2003). The magnetic lead field theorem in the quasi-static approximation and its use for magnetoencephalography forward calculation in realistic volume conductors. *Physics in Medicine and Biology*, *48*(22), 3637–3652. https://doi.org/10.1088/0031-9155/48/22/002

Noseworthy, J. H., Lucchinetti, C., Rodriguez, M., & Weinshenker, B. G. (2000). Multiple Sclerosis. *New England Journal of Medicine*, *343*(13), 938–952. https://doi.org/10.1056/NEJM200009283431307

Nummenmaa, L., Glerean, E., Viinikainen, M., Jaaskelainen, I. P., Hari, R., & Sams, M. (2012). Emotions promote social interaction by synchronizing brain activity across individuals. *Proceedings of the National Academy of Sciences*, *109*(24), 9599–9604. https://doi.org/10.1073/pnas.1206095109

Nyhus, E., & Curran, T. (2010). Functional role of gamma and theta oscillations in

episodic memory. *Neuroscience & Biobehavioral Reviews*, *34*(7), 1023–1035. https://doi.org/10.1016/j.neubiorev.2009.12.014

O'gorman, C., Lucas, R., & Taylor, B. (2012). Environmental Risk Factors for Multiple Sclerosis: A Review with a Focus on Molecular Mechanisms. *Int. J. Mol. Sci*, *13*, 11718–11752. https://doi.org/10.3390/ijms130911718

Ogawa, S., & Lee, T.-M. (1990). Magnetic resonance imaging of blood vessels at high fields:In vivo andin vitro measurements and image simulation. *Magnetic Resonance in Medicine*, *16*(1), 9–18. https://doi.org/10.1002/mrm.1910160103

Ogawa, S., Lee, T. M., Kay, A. R., & Tank, D. W. (1990). Brain magnetic resonance imaging with contrast dependent on blood oxygenation. *Proceedings of the National Academy of Sciences of the United States of America*, *87*(24), 9868–72. Retrieved from http://www.ncbi.nlm.nih.gov/pubmed/2124706

Okell, T. W., Chappell, M. A., Kelly, M. E., & Jezzard, P. (2013). Cerebral blood flow quantification using vessel-encoded arterial spin labeling. *Journal of Cerebral Blood Flow and Metabolism : Official Journal of the International Society of Cerebral Blood Flow and Metabolism*, *33*(11), 1716–24. https://doi.org/10.1038/jcbfm.2013.129

Oostenveld, R., Fries, P., Maris, E., & Schoffelen, J.-M. (2011). FieldTrip: Open source software for advanced analysis of MEG, EEG, and invasive electrophysiological data. *Computational Intelligence and Neuroscience*, *2011*, 156869. https://doi.org/10.1155/2011/156869

Ota, M., Sato, N., Nakata, Y., Ito, K., Kamiya, K., Maikusa, N., … Kunugi, H. (2013). Abnormalities of cerebral blood flow in multiple sclerosis: A pseudocontinuous arterial spin labeling MRI study. *Magnetic Resonance Imaging*, *31*(6), 990–995. https://doi.org/10.1016/J.MRI.2013.03.016

Paling, D., Golay, X., Wheeler-Kingshott, C., Kapoor, R., & Miller, D. (2011). Energy failure in multiple sclerosis and its investigation using MR techniques. *Journal of Neurology*, *258*(12), 2113–2127. https://doi.org/10.1007/s00415-011-6117-7

Paling, D., Petersen, E. T., Tozer, D. J., Altmann, D. R., Am, C., Kingshott, W.-, … Golay, X. (2013). Cerebral arterial bolus arrival time is prolonged in multiple sclerosis and associated with disability. *Journal of Cerebral Blood Flow & Metabolism*, *34*, 34–42. https://doi.org/10.1038/jcbfm.2013.161

Papadaki, E. Z., Mastorodemos, V. C., Amanakis, E. Z., Tsekouras, K. C., Papadakis, A. E., Tsavalas, N. D., … Maris, T. G. (2012). White matter and deep gray matter hemodynamic changes in multiple sclerosis patients with clinically isolated syndrome. *Magnetic Resonance in Medicine*, *68*(6), 1932–1942. https://doi.org/10.1002/mrm.24194

Pasley, B. N., Inglis, B. A., & Freeman, R. D. (2007). Analysis of oxygen metabolism

implies a neural origin for the negative BOLD response in human visual cortex. *NeuroImage*, *36*(2), 269–276. https://doi.org/10.1016/j.neuroimage.2006.09.015

Penner, I., Raselli, C., Stöcklin, M., Opwis, K., Kappos, L., & Calabrese, P. (2009). The Fatigue Scale for Motor and Cognitive Functions (FSMC): validation of a new instrument to assess multiple sclerosis-related fatigue. *Multiple Sclerosis Journal*, *15*(12), 1509–1517. https://doi.org/10.1177/1352458509348519

Perry, G., Randle, J. M., Koelewijn, L., Routley, B. C., & Singh, K. D. (2015). Linear tuning of gamma amplitude and frequency to luminance contrast: Evidence from a continuous mapping paradigm. *PLoS ONE*, *10*(4), 1–14. https://doi.org/10.1371/journal.pone.0124798

Peruzzo, D., Castellaro, M., Calabrese, M., Veronese, E., Rinaldi, F., Bernardi, V., … Bertoldo, A. (2013). Heterogeneity of cortical lesions in multiple sclerosis: an MRI perfusion study. *Journal of Cerebral Blood Flow & Metabolism*, *33*, 457–463. https://doi.org/10.1038/jcbfm.2012.192

Petcharunpaisan, S., Ramalho, J., Castillo, M., & Carmichael, O. (2010). Arterial spin labeling in neuroimaging. *World J Radiol*, *2*(10), 384–398. https://doi.org/10.4329/wjr.v2.i10.384

Petzold, G. C., & Murthy, V. N. (2011). Review Role of Astrocytes in Neurovascular Coupling. *Neuron*, *71*, 782–797. https://doi.org/10.1016/j.neuron.2011.08.009

Phillips, A. A., Chan, F. H., Zheng, M. M. Z., Krassioukov, A. V, & Ainslie, P. N. (2015). Neurovascular coupling in humans: Physiology, methodological advances and clinical implications. *Journal of Cerebral Blood Flow and Metabolism : Official Journal of the International Society of Cerebral Blood Flow and Metabolism*, 0271678X15617954. https://doi.org/10.1177/0271678X15617954

Polman, C. H., Reingold, S. C., Banwell, B., Clanet, M., Cohen, J. A., Filippi, M., … Wolinsky, J. S. (2011). Diagnostic criteria for multiple sclerosis: 2010 revisions to the McDonald criteria. *Annals of Neurology*, *69*(2), 292–302. https://doi.org/10.1002/ana.22366

Popescu, V., Schoonheim, M. M., Versteeg, A., Chaturvedi, N., Jonker, M., Xavier de Menezes, R., … Vrenken, H. (2016). Grey Matter Atrophy in Multiple Sclerosis: Clinical Interpretation Depends on Choice of Analysis Method. *PloS One*, *11*(1), e0143942. https://doi.org/10.1371/journal.pone.0143942

Powers, W. J., Hirsch, I. B., & Cryer, P. E. (1996). *Effect of stepped hypoglycemia on regional cerebral blood flow response to physiological brain activation*. Retrieved from www.physiology.org/journal/ajpheart

Proudfoot, M., Woolrich, M. W., Nobre, A. C., Turner, M. R., & Turner, M. (n.d.). Magnetoencephalography. https://doi.org/10.1136/practneurol

Pu, Y., Cheyne, D. O., Cornwell, B. R., & Johnson, B. W. (2018). Non-invasive Investigation of Human Hippocampal Rhythms Using Magnetoencephalography: A Review. *Frontiers in Neuroscience*, *12*, 273. https://doi.org/10.3389/fnins.2018.00273

R Core Team. (2017). *R: A Language and Environment for Statistical Computing*. *R Foundation for Statistical Computing* (Vol. 1). https://doi.org/10.1007/978-3-540-74686-7

Raichle, M. E., & Gusnard, D. A. (2002). Appraising the brain's energy budget. *Proceedings of the National Academy of Sciences of the United States of America*, *99*(16), 10237–9. https://doi.org/10.1073/pnas.172399499

Rao, H., Wang, J., Tang, K., Pan, W., & Detre, J. A. (2007). Imaging brain activity during natural vision using CASL perfusion fMRI. *Human Brain Mapping*, *28*(7), 593–601. https://doi.org/10.1002/hbm.20288

Rashid, W., Parkes, L. M., Ingle, G. T., Chard, D. T., Toosy, A. T., Altmann, D. R., … Miller, D. H. (2004). Abnormalities of cerebral perfusion in multiple sclerosis. *Journal of Neurology, Neurosurgery, and Psychiatry*, *75*(9), 1288–93. https://doi.org/10.1136/jnnp.2003.026021

Rocca, M. A., & Filippi, M. (2007). Functional MRI in Multiple Sclerosis. *Journal of Neuroimaging*, *17*, 36S–41S. https://doi.org/10.1111/j.1552-6569.2007.00135.x

Sakamoto, S., Ikeda, H., Tsuyuguchi, N., Uda, T., Okumura, E., Asakawa, T., … Miki, Y. (2016). MEG Frequency Analysis Depicts the Impaired Neurophysiological Condition of Ischemic Brain. *PLOS ONE*, *11*(12), e0168588. https://doi.org/10.1371/journal.pone.0168588

Sbardella, E., Petsas, N., Tona, F., & Pantano, P. (2015). Resting-State fMRI in MS: General Concepts and Brief Overview of Its Application. https://doi.org/10.1155/2015/212693

Schall, J. D. (2009). Frontal Eye Fields. *Encyclopedia of Neuroscience*, 367–374. https://doi.org/10.1016/B978-008045046-9.01111-6

Scheeringa, R., Fries, P., Petersson, K.-M., Oostenveld, R., Grothe, I., Norris, D. G., … Bastiaansen, M. C. M. (2011). Neuronal dynamics underlying high- and low-frequency EEG oscillations contribute independently to the human BOLD signal. *Neuron*, *69*(3), 572–83. https://doi.org/10.1016/j.neuron.2010.11.044

Scheffer-Teixeira, R., Belchior, H., Leão, R. N., Ribeiro, S., & Tort, A. B. L. (2013). On high-frequency field oscillations (>100 Hz) and the spectral leakage of spiking activity. *The Journal of Neuroscience : The Official Journal of the Society for Neuroscience*, *33*(4), 1535–9. https://doi.org/10.1523/JNEUROSCI.4217-12.2013

Schmithorst, V. J., Hernandez-Garcia, L., Vannest, J., Rajagopal, A., Lee, G., & Holland, S. K. (2014). Optimized simultaneous ASL and BOLD functional

imaging of the whole brain. *Journal of Magnetic Resonance Imaging : JMRI*, *39*(5), 1104–17. https://doi.org/10.1002/jmri.24273

Schoonheim, M. M., Geurts, J. J. G., Landi, D., Douw, L., van der Meer, M. L., Vrenken, H., … Stam, C. J. (2013). Functional connectivity changes in multiple sclerosis patients: A graph analytical study of MEG resting state data. *Human Brain Mapping*, *34*(1), 52–61. https://doi.org/10.1002/hbm.21424

Schridde, U., Khubchandani, M., Motelow, J. E., Sanganahalli, B. G., Hyder, F., & Blumenfeld, H. (2008). Negative BOLD with large increases in neuronal activity. *Cerebral Cortex (New York, N.Y. : 1991)*, *18*(8), 1814–27. https://doi.org/10.1093/cercor/bhm208

Senior, C., Russell, T., & Gazzaniga S., M. (2006). *Methods in Mind*. *The MIT Press, Massachusetts Institute of Technology*. MIT Press.

Sheth, S. A., Nemoto, M., Guiou, M., Walker, M., Pouratian, N., & Toga, A. W. (2004). Linear and Nonlinear Relationships between Neuronal Activity, Oxygen Metabolism, and Hemodynamic Responses. *Neuron*, *42*(2), 347–355. https://doi.org/10.1016/S0896-6273(04)00221-1

Shulman, R. G., Rothman, D. L., Behar, K. L., & Hyder, F. (2004). Energetic basis of brain activity: implications for neuroimaging. *TRENDS in Neurosciences*, *27*(8). https://doi.org/10.1016/j.tins.2004.06.005

Shulman, R. G., Rothman, D. L., & Hyder, F. (2007). A BOLD search for baseline. *NeuroImage*, *36*(2), 277–81. https://doi.org/10.1016/j.neuroimage.2006.11.035

Siegert, R. J. (2005). Depression in multiple sclerosis: a review. *J Neurol Neurosurg Psychiatry*, *76*, 469–475. https://doi.org/10.1136/jnnp.2004.054635

Singh, K. D., Barnes, G. R., & Hillebrand, A. (2003). Group imaging of task-related changes in cortical synchronisation using nonparametric permutation testing. *NeuroImage*, *19*(4), 1589–1601. https://doi.org/10.1016/S1053-8119(03)00249-0

Singh, K. D., Barnes, G. R., Hillebrand, A., Forde, E. M. E., & Williams, A. L. (2002). Task-Related Changes in Cortical Synchronization Are Spatially Coincident with the Hemodynamic Response. *NeuroImage*, *16*(1), 103–114. https://doi.org/10.1006/NIMG.2001.1050

Sisto, D., Trojano, M., Vetrugno, M., Trabucco, T., Iliceto, G., & Sborgia, C. (2005). Subclinical Visual Involvement in Multiple Sclerosis: A Study by MRI, VEPs, Frequency-Doubling Perimetry, Standard Perimetry, and Contrast Sensitivity. *Investigative Opthalmology & Visual Science*, *46*(4), 1264. https://doi.org/10.1167/iovs.03-1213

Smith, K. J., & Lassmann, H. (2002a). The role of nitric oxide in multiple sclerosis. *The Lancet. Neurology*, *1*(4), 232–41. https://doi.org/10.1016/S1474-4422(02)00102-3

Smith, K. J., & Lassmann, H. (2002b). The role of nitric oxide in multiple sclerosis. *The Lancet Neurology*, *1*(4), 232–241. https://doi.org/10.1016/S1474-4422(02)00102-3

Smith, S. M. (2002). Fast robust automated brain extraction. *Human Brain Mapping*, *17*(3), 143–155. https://doi.org/10.1002/hbm.10062

Smith, S. M., & Brady, J. M. (1997). SUSAN—A New Approach to Low Level Image Processing. *International Journal of Computer Vision*, *23*(1), 45–78. https://doi.org/10.1023/A:1007963824710

Smith, S. M., De Stefano, N., Jenkinson, M., & Matthews, P. M. (n.d.). Normalized accurate measurement of longitudinal brain change. *Journal of Computer Assisted Tomography*, *25*(3), 466–75. Retrieved from http://www.ncbi.nlm.nih.gov/pubmed/11351200

Smith, S. M., Zhang, Y., Jenkinson, M., Chen, J., Matthews, P. M., Federico, A., & De Stefano, N. (2002). Accurate, Robust, and Automated Longitudinal and Cross-Sectional Brain Change Analysis. *NeuroImage*, *17*(1), 479–489. https://doi.org/10.1006/NIMG.2002.1040

Spano, V. R., Mandell, D. M., Poublanc, J., Sam, K., Battisti-Charbonney, A., Pucci, O., … Mikulis, D. J. (2013). cO 2 Blood Oxygen level-dependent Mr Mapping of cerebrovascular reserve in a clinical Population: Safety, Tolerability, and Technical Feasibility 1. *Radiology.Rsna.Org n Radiology*, *266*(2). https://doi.org/10.1148/radiol.12112795

Spencer, J. I., Bell, J. S., & DeLuca, G. C. (2018). Vascular pathology in multiple sclerosis: reframing pathogenesis around the blood-brain barrier. *Journal of Neurology, Neurosurgery, and Psychiatry*, *89*(1), 42–52. https://doi.org/10.1136/jnnp-2017-316011

Stanimirovic, D. B., & Friedman, A. (2012). Pathophysiology of the neurovascular unit: disease cause or consequence? *Journal of Cerebral Blood Flow & Metabolism*, *32*(7), 1207–1221. https://doi.org/10.1038/jcbfm.2012.25

Steen, C., D'haeseleer, M., Hoogduin, J. M., Fierens, Y., Cambron, M., Mostert, J. P., … De Keyser, J. (2013). Cerebral white matter blood flow and energy metabolism in multiple sclerosis. *Multiple Sclerosis Journal*, *19*(10), 1282–1289. https://doi.org/10.1177/1352458513477228

Stys, P. K., Zamponi, G. W., van Minnen, J., & Geurts, J. J. G. (2012). Will the real multiple sclerosis please stand up? *Nature Reviews Neuroscience*, *13*(7), 507–514. https://doi.org/10.1038/nrn3275

Sun, P., Guo, J., Guo, S., Chen, J., He, L., Fu, S., & Ptito, M. (2014). BOLD Signal Change and Contrast Reversing Frequency: An Event-Related fMRI Study in Human Primary Visual Cortex. https://doi.org/10.1371/journal.pone.0099547

Sun, X., Tanaka, M., Kondo, S., Okamoto, K., & Hirai, S. (1998). Clinical significance of reduced cerebral metabolism in multiple sclerosis: A combined PET and MRI study. *Annals of Nuclear Medicine*, *12*(2), 89–94. https://doi.org/10.1007/BF03164835

Swettenham, J. B., Muthukumaraswamy, S. D., & Singh, K. D. (2009). Spectral properties of induced and evoked gamma oscillations in human early visual cortex to moving and stationary stimuli. *Journal of Neurophysiology*, *102*(2), 1241–53. https://doi.org/10.1152/jn.91044.2008

Swettenham, J. B., Muthukumaraswamy, S. D., & Singh, K. D. (2013). BOLD Responses in Human Primary Visual Cortex are Insensitive to Substantial Changes in Neural Activity. *Frontiers in Human Neuroscience*, *7*, 76. https://doi.org/10.3389/fnhum.2013.00076

Tallon-Baudry, C., & Bertrand, O. (1999). Oscillatory gamma activity in humans and its role in object representation. *Trends in Cognitive Sciences*, *3*(4), 151–162. https://doi.org/10.1016/S1364-6613(99)01299-1

Tan, H.-R. M., Gross, J., & Uhlhaas, P. J. (2016). MEG sensor and source measures of visually induced gamma-band oscillations are highly reliable. *NeuroImage*, *137*, 34–44. https://doi.org/10.1016/J.NEUROIMAGE.2016.05.006

Tekgöl Uzuner, G., & Uzuner, N. (2016). Neurovascular coupling in patients with relapsing-remitting multiple sclerosis. *Clinical Neurology and Neurosurgery*, *146*, 24–28. https://doi.org/10.1016/j.clineuro.2016.04.020

Tewarie, P., Schoonheim, M. M., Schouten, D. I., Polman, C. H., Balk, L. J., Uitdehaag, B. M. J., … Stam, C. J. (2015). Functional brain networks: Linking thalamic atrophy to clinical disability in multiple sclerosis, a multimodal fMRI and MEG Study. *Human Brain Mapping*, *36*(2), 603–618. https://doi.org/10.1002/hbm.22650

Tewarie, P., Schoonheim, M. M., Stam, C. J., van der Meer, M. L., van Dijk, B. W., Barkhof, F., … Hillebrand, A. (2013). Cognitive and Clinical Dysfunction, Altered MEG Resting-State Networks and Thalamic Atrophy in Multiple Sclerosis. *PLoS ONE*, *8*(7), e69318. https://doi.org/10.1371/journal.pone.0069318

Tewarie, P., Steenwijk, M. D., Tijms, B. M., Daams, M., Balk, L. J., Stam, C. J., … Hillebrand, A. (2014). Disruption of structural and functional networks in long-standing multiple sclerosis. *Human Brain Mapping*, *35*(12), 5946–5961. https://doi.org/10.1002/hbm.22596

Thompson, A. J., Banwell, B. L., Barkhof, F., Carroll, W. M., Coetzee, T., Comi, G., … Cohen, J. A. (2018). Diagnosis of multiple sclerosis: 2017 revisions of the McDonald criteria. *The Lancet Neurology*, *17*, 162–173. https://doi.org/10.1016/

Tomassini, V., d'Ambrosio, A., Petsas, N., Wise, R. G., Sbardella, E., Allen, M., …

Pozzilli, C. (2016). The effect of inflammation and its reduction on brain plasticity in multiple sclerosis: MRI evidence. *Human Brain Mapping*, *37*(7), 2431–2445. https://doi.org/10.1002/hbm.23184

Tomassini, V., Matthews, P. M., Thompson, A. J., Fuglo, D., Geurts, J. J., Johansen-Berg, H., … Palace, J. (2012). Neuroplasticity and functional recovery in multiple sclerosis. *Nat Rev Neurol*, *8*(11), 635–646. https://doi.org/10.1038/nrneurol.2012.179

Toosy, A. T., Mason FRACP, D. F., & Miller FMedSci, D. H. (2014). *Optic neuritis*. *The Lancet Neurology* (Vol. 13). https://doi.org/10.1016/S1474-4422(13)70259-X

Torkildsen, Ø., Myhr, K.-M., & Bø, L. (2016). Disease-modifying treatments for multiple sclerosis - a review of approved medications. *European Journal of Neurology*, *23 Suppl 1*(Suppl 1), 18–27. https://doi.org/10.1111/ene.12883

Trapp, B. D., & Stys, P. K. (2009). Virtual hypoxia and chronic necrosis of demyelinated axons in multiple sclerosis. *The Lancet. Neurology*, *8*(3), 280–91. https://doi.org/10.1016/S1474-4422(09)70043-2

Tukey, J. W. (John W. (1977). *Exploratory data analysis*. Addison-Wesley Pub. Co.

Tzourio-Mazoyer, N., Landeau, B., Papathanassiou, D., Crivello, F., Etard, O., Delcroix, N., … Joliot, M. (2002). Automated Anatomical Labeling of Activations in SPM Using a Macroscopic Anatomical Parcellation of the MNI MRI Single-Subject Brain. *NeuroImage*, *15*(1), 273–289. https://doi.org/10.1006/NIMG.2001.0978

Uhlhaas, P. J., & Singer, W. (2006). Neural synchrony in brain disorders: relevance for cognitive dysfunctions and pathophysiology. *Neuron*, *52*(1), 155–68. https://doi.org/10.1016/j.neuron.2006.09.020

Uhlhaas, P. J., & Singer, W. (2010). Abnormal neural oscillations and synchrony in schizophrenia. *Nature Reviews Neuroscience*, *11*(2), 100–113. https://doi.org/10.1038/nrn2774

Urback, A. L., MacIntosh, B. J., & Goldstein, B. I. (2017). Cerebrovascular reactivity measured by functional magnetic resonance imaging during breath-hold challenge: A systematic review. *Neuroscience & Biobehavioral Reviews*, *79*, 27–47. https://doi.org/10.1016/J.NEUBIOREV.2017.05.003

Ureshi, M., Matsuura, T., & Kanno, I. (2004). Stimulus frequency dependence of the linear relationship between local cerebral blood flow and field potential evoked by activation of rat somatosensory cortex. *Neuroscience Research*, *48*(2), 147–153. https://doi.org/10.1016/J.NEURES.2003.10.014

Utevsky, A. V, Smith, D. V, & Huettel, S. A. (2014). Precuneus is a functional core of the default-mode network. *The Journal of Neuroscience : The Official Journal of the Society for Neuroscience*, *34*(3), 932–40.

https://doi.org/10.1523/JNEUROSCI.4227-13.2014

Uzuner, N., Ozkan, S., & Cinar, N. (2007). Cerebrovascular reactivity in multiple sclerosis patients. *Multiple Sclerosis*, *13*(6), 737–741. https://doi.org/10.1177/1352458506074645

Vafaee, M. S., & Gjedde, T. (2000a). *Model of Blood-Brain Transfer of Oxygen Explains Nonlinear Flow-Metabolism Coupling During Stimulation of Visual Cortex*. Retrieved from http://journals.sagepub.com/doi/pdf/10.1097/00004647-200004000-00012

Vafaee, M. S., & Gjedde, T. (2000b). *Model of Blood-Brain Transfer of Oxygen Explains Nonlinear Flow-Metabolism Coupling During Stimulation of Visual Cortex*. Retrieved from http://journals.sagepub.com/doi/pdf/10.1097/00004647-200004000-00012

Vafaee, M. S., Meyer, E., Marrett, S., Paus, T., Evans, A. C., & Gjedde, A. (1999). Frequency-Dependent Changes in Cerebral Metabolic Rate of Oxygen during Activation of Human Visual Cortex. *Journal of Cerebral Blood Flow & Metabolism*, *19*(3), 272–277. https://doi.org/10.1097/00004647-199903000-00005

Van der Meer, M. L., Tewarie, P., Schoonheim, M. M., Douw, L., Barkhof, F., Polman, C. H., … Hillebrand, A. (2013). Cognition in MS correlates with resting-state oscillatory brain activity: An explorative MEG source-space study. *NeuroImage: Clinical*, *2*, 727–734. https://doi.org/10.1016/J.NICL.2013.05.003

Van Veen, B. D., Van Drongelen, W., Yuchtman, M., & Suzuki, A. (1997). Localization of brain electrical activity via linearly constrained minimum variance spatial filtering. *IEEE Transactions on Biomedical Engineering*, *44*(9), 867–880. https://doi.org/10.1109/10.623056

Vidal-Jordana, A., Sastre-Garriga, J., Pérez-Miralles, F., Pareto, D., Rio, J., Auger, C., … Montalban, X. (2016). Brain Volume Loss During the First Year of Interferon-Beta Treatment in Multiple Sclerosis: Baseline Inflammation and Regional Brain Volume Dynamics. *Journal of Neuroimaging*, *26*(5), 532–538. https://doi.org/10.1111/jon.12337

Vitorino, R., Hojjat, S., Cantrell, C. G., Zhang, L., Lee, L., Connor, P. O., … Aviv, R. I. (2017). *Multiple Sclerosis with Cognitive Decline*. Retrieved from https://www.ncbi.nlm.nih.gov/pmc/articles/PMC5116278/pdf/nihms775767.pdf

Wang, J., Aguirre, G. K., Kimberg, D. Y., Roc, A. C., Li, L., & Detre, J. A. (2003). Arterial spin labeling perfusion fMRI with very low task frequency. *Magnetic Resonance in Medicine*, *49*(5), 796–802. https://doi.org/10.1002/mrm.10437

Ward, L. M. (2003). Synchronous neural oscillations and cognitive processes. *Trends in Cognitive Sciences*, *7*(12), 553–559. https://doi.org/10.1016/j.tics.2003.10.012

Warnert, E. A. H., Harris, A. D., Murphy, K., Saxena, N., Tailor, N., Jenkins, N. S., … Wise, R. G. (2014). In vivo assessment of human brainstem cerebrovascular function: a multi-inversion time pulsed arterial spin labelling study. *Journal of Cerebral Blood Flow and Metabolism : Official Journal of the International Society of Cerebral Blood Flow and Metabolism*, *34*(6), 956–63. https://doi.org/10.1038/jcbfm.2014.39

Warnock, G., Özbay, P. S., Kuhn, F. P., Nanz, D., Buck, A., Boss, A., & Rossi, C. (2018). Reduction of BOLD interference in pseudo-continuous arterial spin labeling: towards quantitative fMRI. *Journal of Cerebral Blood Flow and Metabolism*, *38*(5), 847–856. https://doi.org/10.1177/0271678X17704785

Werring, D. J., Bullmore, E. T., Toosy, A. T., Miller, D. H., Barker, G. J., MacManus, D. G., … Thompson, A. J. (2000). Recovery from optic neuritis is associated with a change in the distribution of cerebral response to visual stimulation: a functional magnetic resonance imaging study. *Journal of Neurology, Neurosurgery, and Psychiatry*, *68*(4), 441–9. https://doi.org/10.1136/JNNP.68.4.441

Westbrook, C., Roth, C. K., & Talbot, J. (Writer on magnetic resonance imaging). (2011). *MRI in practice*. Wiley-Blackwell.

Whittaker, J. R., Driver, I. D., Bright, M. G., & Murphy, K. (2016). The absolute CBF response to activation is preserved during elevated perfusion: Implications for neurovascular coupling measures. *NeuroImage*, *125*, 198–207. https://doi.org/10.1016/j.neuroimage.2015.10.023

Whittingstall, K., Bartels, A., Singh, V., Kwon, S., & Logothetis, N. K. (2010). Integration of EEG source imaging and fMRI during continuous viewing of natural movies. *Magnetic Resonance Imaging*, *28*(8), 1135–1142. https://doi.org/10.1016/J.MRI.2010.03.042

Whittingstall, K., & Logothetis, N. K. (2009). Frequency-band coupling in surface EEG reflects spiking activity in monkey visual cortex. *Neuron*, *64*(2), 281–9. https://doi.org/10.1016/j.neuron.2009.08.016

Wise, R. G., Harris, A. D., Stone, A. J., & Murphy, K. (2013). Measurement of OEF and absolute CMRO2: MRI-based methods using interleaved and combined hypercapnia and hyperoxia. *NeuroImage*, *83*, 135–47. https://doi.org/10.1016/j.neuroimage.2013.06.008

Wong, E. C., Buxton, R. B., & Frank, L. R. (1998). *Quantitative Imaging of Perhsion Using a Single Subtraction (QUIPSS and QUIPSS 11)*. Retrieved from http://mri-q.com/uploads/3/4/5/7/34572113/wong_quippsii_mrm_1998.pdf

Worsley, K. J. (2001). *Functional MRI: An introduction to methods*. *Functional MRI: An introduction to methods*. https://doi.org/10.1093/acprof

Wu, W.-C., Fernández-Seara, M., Detre, J. A., Wehrli, F. W., & Wang, J. (2007). A theoretical and experimental investigation of the tagging efficiency of pseudocontinuous arterial spin labeling. *Magnetic Resonance in Medicine*, *58*(5), 1020–1027. https://doi.org/10.1002/mrm.21403

Wuerfel, J., Bellmann-Strobl, J., Brunecker, P., Aktas, O., McFarland, H., Villringer, A., & Zipp, F. (2004). Changes in cerebral perfusion precede plaque formation in multiple sclerosis: a longitudinal perfusion MRI study. *Brain*, *127*(1), 111–119. https://doi.org/10.1093/brain/awh007

Yablonskiy, D. A. (2011). Cerebral metabolic rate in hypercapnia: Controversy continues. *Journal of Cerebral Blood Flow and Metabolism*, *31*(7), 1502–1503. https://doi.org/10.1038/jcbfm.2011.32

Zappe, A. C., Uludağ, K., Oeltermann, A., Uğurbil, K., & Logothetis, N. K. (2008). The influence of moderate hypercapnia on neural activity in the anesthetized nonhuman primate. *Cerebral Cortex*, *18*(11), 2666–2673. https://doi.org/10.1093/cercor/bhn023

Zhang, Y., Brady, M., & Smith, S. (2001). Segmentation of brain MR images through a hidden Markov random field model and the expectation-maximization algorithm. *IEEE Transactions on Medical Imaging*, *20*(1), 45–57. https://doi.org/10.1109/42.906424

Zheng, D., LaMantia, A. S., & Purves, D. (1991). Specialized vascularization of the primate visual cortex. *The Journal of Neuroscience : The Official Journal of the Society for Neuroscience*, *11*(8), 2622–9. https://doi.org/10.1523/JNEUROSCI.11-08-02622.1991

Zhu, Z., Zumer, J. M., Lowenthal, M. E., Padberg, J., Recanzone, G. H., Krubitzer, L. A., … Disbrow, E. A. (2009). The relationship between magnetic and electrophysiological responses to complex tactile stimuli. *BMC Neuroscience*, *10*(4). https://doi.org/10.1186/1471-2202-10-4

Zivadinov, R., Reder, A. T., Filippi, M., Minagar, A., Stüve, O., Lassmann, H., … Khan, O. (2008). Mechanisms of action of disease-modifying agents and brain volume changes in multiple sclerosis. *Neurology*, *71*(2), 136–44. https://doi.org/10.1212/01.wnl.0000316810.01120.05

Zumer, J. M., Brookes, M. J., Stevenson, C. M., Francis, S. T., & Morris, P. G. (2010). Relating BOLD fMRI and neural oscillations through convolution and optimal linear weighting. *NeuroImage*, *49*(2), 1479–1489. https://doi.org/10.1016/J.NEUROIMAGE.2009.09.020